Next-generation single-photon sources using two-dimensional hexagonal boron nitride

Tobias Vogl

A thesis submitted for the degree of
Doctor of Philosophy of
The Australian National University

Australian National University

April 2019

What we observe is not nature itself, but nature exposed to our method of questioning.

Werner Karl Heisenberg

Declarations

This thesis is an account of research undertaken between April 2016 and April 2019 at the Department of Quantum Science, Research School of Physics and Engineering, The Australian National University, Canberra, Australia.

Except where acknowledged in the customary manner, the material presented in this thesis is, to the best of my knowledge, original and has not been submitted in whole or part for a degree in any university.

Tobias Vogl
April 2019

Contribution to published work

This thesis is presented as a series of papers which have been published in, or submitted to peer-reviewed journals. The bibliographic details of published and submitted works appearing in this thesis are given below. The extent of the contribution to the research and the authorship of each paper have been truthfully stated, and permission from each author has been sought to include the published material in this thesis.

1. **Tobias Vogl**, Yuerui Lu, and Ping Koy Lam, *Room temperature single photon source using fiber-integrated hexagonal boron nitride*, J. Phys. D: Appl. Phys. 50, 295101 (2017)
   Status: In press
   Contribution: Experiments (90%), Manuscript (70%)

2. **Tobias Vogl**, Geoff Campbell, Ben C. Buchler, Yuerui Lu, and Ping Koy Lam, *Fabrication and Deterministic Transfer of High-Quality Quantum Emitters in Hexagonal Boron Nitride*, ACS Photonics 5, 2305-2312 (2018)
   Status: In press
   Contribution: Experiments (90%), Manuscript (70%)

3. **Tobias Vogl**, Kabilan Sripathy, Ankur Sharma, Prithvi Reddy, James Sullivan, Joshua R. Machacek, Linglong Zhang, Fouad Karouta, Ben C. Buchler, Marcus W. Doherty, Yuerui Lu, and Ping Koy Lam, *Radiation tolerance of two-dimensional material-based devices for space applications*, Nature Communications 10, 1202 (2019)
   Status: In press
   Contribution: Experiments (70%), Simulations (70%), Manuscript (70%)

4. **Tobias Vogl**, Ruvi Lecamwasam, Ben C. Buchler, Yuerui Lu, and Ping Koy Lam, *Space-compatible cavity-enhanced single-photon generation with hexagonal boron nitride*, arXiv:1902.03019 (2019)
   Status: Published as an as soon as publishable article in ACS Photonics
   https://pubs.acs.org/doi/10.1021/acsphotonics.9b00314
   Contribution: Experiments (90%), Simulations (60%), Manuscript (70%)

5. **Tobias Vogl**, Marcus W. Doherty, Ben C. Buchler, Yuerui Lu, and Ping Koy Lam, *Atomic localization of quantum emitters in multilayer hexagonal boron nitride*, Nanoscale 11, 14362-14371 (2019)
   Status: In press
   Contribution: Experiments (90%), Simulations (90%), Manuscript (70%)

Tobias Vogl
April 2019

The original declaration endorsed by the supervisory panel can be found in the Appendix A.6.

Publications not included in this thesis

1. Ankur Sharma, Miheng Dong, Yuhan Zhang, Jing Wen, Linglong Zhang, Robert Halbich, **Tobias Vogl**, Kun Liang, Hieu T. Nguyen, Fan Wang, Alessandro Troisi, Daniel Macdonald, Haibo Ma, Ping Koy Lam, Xinran Wang, and Yuerui Lu, *Supertransport of Excitons in Atomically Thin Organic Semiconductors at the 2D Quantum Limit*
   Status: Under review in Nature Communications

2. **Tobias Vogl**, Yuerui Lu, and Ping Koy Lam, *Single-photon test of extended quantum theories using two-dimensional materials*
   Status: In preparation

3. Simone Piacentini, **Tobias Vogl**, Giacomo Corrielli, Ping Koy Lam, and Roberto Osellame, *Space qualification of ultrafast laser written integrated waveguide optics*
   Status: In preparation

Acknowledgements

My journey toward the doctorate would not have been possible without the help of many people whom I want to express my sincere gratitude and appreciation here.

First, I would like to offer my special thanks to Ping Koy Lam, chair of my supervisory panel and primary doctoral advisor. At the start of my PhD you asked me if I want to explore using two-dimensional materials for quantum optics, an opportunity and challenge which I happily accepted. You allowed me to guide the project into whatever direction I thought was promising and provided the necessary funding to properly carry out the experiments. I am deeply grateful for your support, guidance and for sharing your broad knowledge in quantum physics with me during the past three years. I wish to thank Yuerui (Larry) Lu as well, who introduced me to the field of 2D materials and got me up to speed very quickly, even though I did not know much about 2D materials when I started. Your knowledge of the field is incredible and you provided many explanations behind effects I saw in the experiments. Finally on my supervisory panel is also Ben Buchler, whose critical questions always made me think and I believe this made me a better physicist.

I would also like to thank the entire quantum optics group for always being available for a scientific discussion, or when a helping hand was needed. This of course includes my office mates (past and present), Aaron Tranter, Anthony Leung, Daniel Higginbottom, Jesse Everett, Jinyong Ma, Kabilan Sripathy, Karun Paul, and Pierre Vernaz-Gris, who made the time in the office a lot more enjoyable, not to mention Geoff Campbell, Oliver Thearle, Ruvi Lecamwasam, and Sarah Lau who regularly stopped by for a chat and a funny story. I also have to thank the group admins, Amanda Haines and Lynne Christians, for dealing with all the administrative issues and ordering of parts and components for my experiments, thereby keeping my life as a researcher easy.

Then there are a lot of fruitful collaborations within the Australian National University which I would like to acknowledge. This includes Jiong Yang, Ankur Sharma, Jiajie Pei, Yi Zhu and Ahmed Raza from Larry's group who showed me how to exfoliate, identify, transfer and characterize 2D materials. There are many people from the Department of Materials Engineering, including Khu Vu, Hendry Chan, Ziyuan Li, Kun Peng and Dipankar Chugh, who trained me to use their equipment. A special thanks goes to Hoe Tan for granting me access to the time-resolved photoluminescence setup and Lan Fu for discussions on polymers and Fourier transform spectroscopy. I would also like to thank Prithvi Reddy for carrying out some of my density functional calculations. Another special thanks goes to Marcus Doherty for guiding me through density functional theory and all theoretical physics problems I came across in the past few years. I am particularly grateful for James Sullivan and Joshua Machacek who opened their positron setup twice to let me conduct my space qualification experiments, even though I initially promised that I will only need a single irradiation. The space qualification study would not have been possible without the help of Rob Elliman and Tom Ratcliff, who not only helped with the ion accelerator, but had useful discussions with me about ion-matter interactions as well. I also thank the Australian National Fabrication Facility (ANFF) for access to their nano- and microfabrication facilities, particularly Li Li for assistance with the FIB, Kaushal Vora for

aiding with the sputter system, RTA, and ellipsometer, and Fouad Karouta for helping with the plasma systems. Without the ANFF, none of my experiments would have been possible. I appreciate the mechanical workshop and the electronics unit of the Research School of Physics and Engineering for providing solutions to the problems I was facing during my experiments.

Also, thank you very much to everyone who proof-read my thesis and fought against my notoriously long German sentence structure, I know that was not easy.

I would also like to express my gratitude to Harald Weinfurter, Immanuel Bloch, and Alexander Högele who held great lectures on quantum communication and quantum computing, quantum optics, and advanced solid-state physics at the Ludwig Maximilians Universität München. The knowledge you taught me forms the basis of this thesis. I also thank David Hunger for fruitful discussions on cavity integration of solid-state quantum emitters.

Next, I have to thank my current collaborators at the National University of Singapore, Chorng Haur Sow, Alex Ling, Christian Nijhuis, and Thorin Duffin, as well as Roberto Osellame and Giacomo Corrielli from the Politecnico di Milano.

Finally, all of this would not have been possible without the scholarship support from the Australian National University and the research funding from the Australian Research Council.

The use of the optics ComponentLibrary by Alexander Franzen under the terms of the Creative Commons Attribution-NonCommercial 3.0 License (CC BY-NC 3.0), https://creativecommons.org/licenses/by-nc/3.0/ is acknowledged.

Zum Schluss geht noch ein besonderer Dank an Eva, die geduldig im 16259 km entfernten München auf mich gewartet hat und mich trotzdem immer bei allem unterstützt hat. Auch meiner Familie möchte ich danken, dafür, dass ihr immer für mich da seid.

Abstract

With the second quantum revolution unfolding, the realization of optical quantum technologies will transform future information processing, communication, and sensing. One of the crucial building blocks of quantum information architectures is a single-photon source. Promising candidates for such quantum light sources are quantum dots, trapped ions, color centers in solid-state crystals, and sources based on heralded spontaneous parametric down-conversion. The recent discovery of optically active defects hosted by 2D materials has added yet another class to the solid-state quantum emitters. Stable quantum emitters have been reported in semiconducting transition metal dichalcogenides (TMDs) and in hexagonal boron nitride (hBN). Owing to the large band gap, the energy levels of defects in hBN are well isolated from the band edges. In contrast to TMDs, this allows for operation at room temperature and prevents non-radiative decay, resulting in a high quantum yield. Unlike NV centers in diamond and other solid-state quantum emitters in 3D systems, the 2D crystal lattice of hBN allows for an intrinsically ideal extraction efficiency.

In this thesis, recent advances in developing this new type of emitter are described. In the first experiment, quantum emitters hosted by hBN are attached by van der Waals force to the core of multimode fibers. The system features a free space and fiber-coupled single-photon generation mode. The results can be generalized to waveguides and other on-chip photonic quantum information processing devices, thus providing a path toward integration with photonic networks. Next, the fabrication process, based on a microwave plasma etching technique, is substantially improved, achieving a narrow emission linewidth, high single-photon purity, and a significant reduction of the excited state lifetime. The defect formation probability is influenced by the plasma conditions, while the emitter brightness correlates with the annealing temperature.

Due to their low size, weight and power requirements, the quantum emitters in hBN are promising candidates as light sources for long-distance satellite-based quantum communication. The next part of this thesis focuses on the feasibility of using these emitters as a light source for quantum key distribution. The necessary improvement in the photon quality is achieved by coupling an emitter with a microcavity in the Purcell regime. The device is characterized by a strong increase in spectral and single-photon purity and can be used for realistic quantum key distribution, thereby outperforming efficient state-of-the-art decoy state protocols. Moreover, the complete source is integrated on a 1U CubeSat, a picoclass satellite platform encapsulated within a cube of length 10 cm. This makes the source among the smallest, fully self-contained, ready-to-operate single-photon sources in the world. The emitters are also space-qualified by exposure to ionizing radiation. After irradiation with γ-rays, protons and electrons, the quantum emitters show negligible change in photophysics. The space certification study is also extended to other 2D materials, suggesting robust suitability for use of these nanomaterials for space instrumentation.

Finally, since the nature of the single-photon emission is still debated and highly controversial, efforts are made to locate the defects with atomic precision. The positions at which the defects form correlate with the fabrication method. This allows one to engineer

the emitters to be close to the surface, where high-resolution electron microscopy can be utilized to identify the chemical defect.

The results so far prove that quantum emitters in hBN are well suited for quantum information applications and can also be integrated on satellite platforms. A device based around this technology would thus provide an excellent building block for a worldwide quantum internet, where metropolitan fiber networks are connected through satellite relay stations.

Contents

List of Figures

List of Tables

Chapter 1

Introduction

It was the year 1900 when Max Planck proposed the hypothesis of discrete energies of light. Even though Planck himself questioned his conclusion at first, the work inspired the field of quantum mechanics. This lead to the first quantum revolution, with the invention of the transistor, the laser, and the atomic clock. Today we observe the second quantum revolution unfolding, with the development of quantum communication, quantum sensors, quantum simulators and quantum computing. Just last year, the European Union launched its Quantum Technologies Flagship,[1] a large-scale and long-term initiative to advance these technologies from the laboratories to industrial applications.

The paradoxical laws of physics at the microscopic scale include the superposition principle, entanglement, non-commuting operators, and no-cloning. Exploiting these laws forms the foundation of quantum computing and quantum communication. The key area of the latter, and arguably the closest to large-scale commercialization, is quantum cryptography.

Modern conventional cryptography relies on unproven mathematical assumptions, such as the computational complexity of factorization or computing the discrete logarithm. Public-key cryptography exploits these one-way functions, which can be computed in polynomial time for every input, but any polynomial time algorithm attempting to invert the image of a random input succeeds with negligible probability. Famous examples include the RSA algorithm or Elliptic Curve Diffie-Hellman key exchange. These schemes use a public key for encryption and a secret key for decryption. While it is technically possible to calculate the secret from the public key, the use of a one-way function makes this unfeasible. The assumption of the implemented function being one-way, however, is only an assumption which could be contradicted over night, if an efficient solution to the underlying algorithm becomes public. Moreover, a sufficiently large quantum computer can solve all these problems with polynomial resources. It is thus essential to find alternatives to public-key cryptography.

One such alternative is quantum cryptography, whose security, for the first time in the history of code making and code breaking, relies only on fundamental laws of quantum physics. As long as these laws hold, quantum cryptography is provably secure, independent from resources available to any eavesdropper. The research on quantum cryptography, or more precisely quantum key distribution (QKD), is a very active research field, further catalyzed by the first space-to-ground quantum key exchange performed by the Micius satellite in 2017. Expensive components and the requirement of direct point-to-point connections, however, hamper the widespread use of QKD. In addition, imperfect implementations allow loopholes which have to be carefully characterized and closed. It

[1] https://qt.eu/

were precisely these loopholes which gave credence to the opinion that QKD can never outperform quantum-resistant or post-quantum cryptography, which resulted in an initially low acceptance of QKD. This attitude is flawed for the following reasons: On the one hand, QKD allows for perfect backward and forward secrecy, and the eavesdropping attempt must take place at the time of key exchange. Simply monitoring and storing all internet traffic as the National Security Agency (NSA) does for later decryption with more efficient algorithms or quantum computers is thus not possible. On the other hand, it cannot be proven that post-quantum cryptography is truly quantum-resistant. Just because at the moment there is no quantum or even classical algorithm known that can break post-quantum cryptography does not mean it does not exist. Post-quantum cryptography is thus another bet on the unknown, just like RSA was 40 years ago. It is, however, undeniable that someday in the not too distant future the current public-key cryptographic systems will collapse. Its replacement will likely be a hybrid system, where the most sensitive data is encrypted with QKD and other data secured with post-quantum cryptography. The NSA's Information Assurance Directorate stated, they

> *"will initiate a transition to quantum-resistant algorithms in the not too distant future."*[2]

Starting this transition immediately is crucial since its implementation on a large scale takes time. For comparison, it took more than a decade to replace DES with AES, and these are similar algorithms.

Going into more detail, the security of QKD is based on the no-cloning theorem, stating that no unknown quantum state can be measured perfectly. Furthermore, its security is also based on the Heisenberg uncertainty relation, specifying that not all properties of a quantum system can be measured simultaneously. Thus, if only a single quantum system is sent at a time, it is impossible to copy or readout its state. Photons are an ideal information carrier for quantum cryptography, as they travel at the speed of light and can be transmitted over long distances. This, however, requires the generation of single-photons, a highly non-trivial task. An ideal single-photon source (SPS) emits the single-photon Fock state on demand at a high repetition rate (with a high degree of indistinguishability), allows for (application-specific) spectral tuning and efficient extraction of the single-photons. In addition, for practical applications it should operate at room temperature, be mass-producible (meaning different sources have the same properties), and be easily integratable into application-specific environments. Due to the lack of such an ideal SPS, the vast majority of QKD implementations use weak coherent states, with mean photon numbers much smaller than 1 to reduce the amount of multiphoton states. Nevertheless, great progress in the development of single-photon sources has been made, most notably quantum dots, trapped ions, color centers in solids, and single-photon sources based on heralded parametric spontaneous down-conversion. Achieving near-ideal properties in all mentioned categories simultaneously remains a technical challenge.

The recent discovery of fluorescent defects in two-dimensional (2D) materials has added yet another class of quantum emitters to the solid-state color centers. A 2D material is defined as a solid where the bonding energies of atoms in two dimensions are of comparable strength and much stronger compared to the third dimension. In-plane the atoms are covalently bound, while multiple layers are stacked together with van der Waals bonds. These crystals can be as thin as one atomic layer or be heterostructures consisting of multiple layers. The first isolated 2D material was semimetallic graphene, soon followed by

[2] https://www.nsa.gov/

numerous other 2D materials, including semiconducting transition metal dichalcogenides (TMDs) and insulating hexagonal boron nitride (hBN). Compared to their bulk counterparts, the reduced dimensionality can change their properties significantly. For example, TMDs undergo a transition from an indirect to a direct band gap semiconductor in the limit of a monolayer.

Point defects in these 2D materials introduce additional energy levels into the electronic band structure. These states act as localized trap sites for charge carriers. The trapped charge carrier can be excited in a photoluminescence experiment and after a finite time it will return to its initial ground state under emission of a single-photon. Stable quantum emitters have been reported in the TMDs WSe_2, WS_2, $MoSe_2$ and MoS_2. The optical transition energies for these emitters, however, are located in close vicinity to the electronic bands. Thus, cryogenic cooling below 15 K is required to resolve the zero-phonon line. For room temperature single-photon emission, defects hosted by large band gap materials such as hBN are more ideal, as the energy levels are well isolated. Moreover, a large band gap prevents non-radiative decay, allowing for high quantum efficiencies and thus high single-photon luminosities. Quantum emitters in 2D materials have several advantages over emitters in 3D systems. The 2D lattice allows for an intrinsically ideal extraction efficiency, as none of the emitters are surrounded by high refractive index materials. Thus, the collection of single-photons is not limited by Fresnel or total internal reflection. The chemical and thermal stability of the host materials also assists the stability and durability of the defects, which have shown long-term stable operation over an extremely large temperature range. The confinement of the emitters in 2D also allows for easy integration with fiber networks or waveguides. All these characteristics make hBN and 2D materials in general a promising candidate for a practical single-photon source.

This thesis describes the full development of such a single-photon source, presented as a series of publications. The first part introduces the basic ideas and concepts that were used throughout this thesis and in the publications. As this work bridges two very different research fields, a brief introduction to both quantum optics in Chap. 2 and solid-state physics in Chap. 3 is given. However, in doing so the focus lies mostly on the aspects important for this work, leaving full coverage of the fields to the literature. A review of quantum emitters in 2D materials is given in Chap. 4. Chap. 5 introduces important computational methods and experimental techniques. Chap. 6 through 10 include the publications, which have been published or are under review in peer-reviewed journals. Each of these chapters starts with a foreword linking the publications and placing the work in context. Chap. 6 starts with the integration of quantum emitters with multimode fibers. Chap. 7 discusses the optimization of the fabrication parameters and the enhancement of the single-photon emitter quality. After this work, the focus was shifted toward exploring the use of the single-photon emitters for satellite-based quantum communication. Since space environments differ substantially from Earth a full space-certification of the emitters was carried out. This is described in Chap. 8. The improvement of the quantum emitters through the fabrication optimization, especially the increase in spectral purity, also allows one to integrate the emitter with a microcavity on a satellite platform. The results of this study are presented in Chap. 9. As the nature of the defects remains unknown and controversial, Chap. 10 attempts to assist the identification by atomic localization of the quantum emitters. Finally, Chap. 11 provides an overall conclusion of the thesis.

Part I

Theoretical framework

Chapter 2

Quantum optics

In the early 20th century, physicists began what Serge Haroche later called "unveiling the quantum"[1]. Max Planck's hypothesis of discrete energies of light[2, 3], Albert Einstein's explanation of the photoelectric effect[4], and Niels Bohr's theory of quantized energy levels of atoms[5] are only some of the major breakthroughs in the development of quantum mechanics. The subsequent study of the interaction between light and matter engaged many physicists. Historically, this is referred to as the first and second quantization, though this designation may be misleading. The second quantization is rather an expansion of quantum theory to find a quantum mechanical description for classical field equations. Numerous experiments have confirmed quantum mechanical predictions with impressive conformance, making quantum theory the most successful theory of physics.

This chapter provides a brief introduction to quantum optics and derives for this thesis important concepts from classical field equations. The approach is mostly following methods of the second quantization and Roy Glauber's quantum optics theory[6–8], leaving a full review of the field to the literature[1, 9].[1]

2.1 Classical radiation fields

The Maxwell equations in vacuum are given by

$$\nabla \cdot \vec{E} = 0 \tag{2.1}$$

$$\nabla \cdot \vec{B} = 0 \tag{2.2}$$

$$\nabla \times \vec{E} = -\frac{\partial \vec{B}}{\partial t} \tag{2.3}$$

$$\nabla \times \vec{B} = \frac{1}{c^2}\frac{\partial \vec{E}}{\partial t} \tag{2.4}$$

A common approach is to express electric and magnetic fields in these differential equations in terms of potentials ϕ for the electric and $\vec{A}$ for the magnetic field. The invariance of these under certain transformations allows one to choose a gauge. In the absence of source terms, the Coulomb gauge $\nabla \cdot \vec{A} = 0$ is used such that the associated fields are given by

$$\vec{E} = -\frac{\partial \vec{A}}{\partial t} \tag{2.5}$$

$$\vec{B} = \nabla \times \vec{A} \tag{2.6}$$

[1] This chapter is mostly based on notes of Prof. Immanuel Bloch's lecture on Quantum Optics 2014/15 at the Ludwig Maximilians Universität München.

Substituting these into equation 2.4 yields the wave equation for the vector potential

$$\nabla^2 \vec{A} - \frac{1}{c^2}\frac{\partial^2 \vec{A}}{\partial t^2} = 0 \tag{2.7}$$

where the identity $\nabla \times (\nabla \times \vec{A}) = \nabla(\nabla \cdot \vec{A}) - \nabla^2 \vec{A}$ and the Coulomb gauge was used. This approach decouples the differential equations and is equivalent to the original Maxwell equations. The wave equation can be solved with the plane wave ansatz

$$\vec{A}_{\vec{k},\alpha} = \vec{\epsilon}_{\vec{k},\alpha} A_{\vec{k},\alpha} e^{i(\vec{k}\vec{r}-\omega t)} \tag{2.8}$$

where $A_{\vec{k},\alpha}$ is the complex amplitude and $\vec{\epsilon}_{\vec{k},\alpha}$ is a unit vector determining the polarization of the radiation mode. Note that $|\vec{k}| = k = \frac{2\pi}{\lambda}$, $\omega = ck$, and $\alpha = 1, 2$ denotes the polarization index in an arbitrarily chosen orthogonal basis set. In general, the polarization can be any (normalized) complex linear combination of these states. The general solution for the vector potential can be expanded in the basis of $A_{\vec{k},\alpha}$:

$$\vec{A}(\vec{r},t) = \sum_{\vec{k},\alpha} \vec{\epsilon}_{\vec{k},\alpha} \left(A_{\vec{k},\alpha} e^{i(\vec{k}\vec{r}-\omega t)} + A^*_{\vec{k},\alpha} e^{-i(\vec{k}\vec{r}-\omega t)} \right) \tag{2.9}$$

The complex conjugate is required to ensure that $\vec{A}(\vec{r},t)$ and consequently also $\vec{E}(\vec{r},t)$ and $\vec{B}(\vec{r},t)$ are real valued. The electric and magnetic fields are thus given by

$$\vec{E}(\vec{r},t) = -\frac{\partial \vec{A}(\vec{r},t)}{\partial t} = \sum_{\vec{k},\alpha} i\omega \vec{\epsilon}_{\vec{k},\alpha} \left(A_{\vec{k},\alpha} e^{i(\vec{k}\vec{r}-\omega t)} - A^*_{\vec{k},\alpha} e^{-i(\vec{k}\vec{r}-\omega t)} \right) \tag{2.10}$$

$$\vec{B}(\vec{r},t) = \nabla \times \vec{A}(\vec{r},t) = \sum_{\vec{k},\alpha} i\vec{k} \times \vec{\epsilon}_{\vec{k},\alpha} \left(A_{\vec{k},\alpha} e^{i(\vec{k}\vec{r}-\omega t)} - A^*_{\vec{k},\alpha} e^{-i(\vec{k}\vec{r}-\omega t)} \right) \tag{2.11}$$

It is worth noting that infinite space allows a continuous distribution of $\vec{k}$, but in a finite volume only discrete wave vectors are possible. This is the situation of a radiation mode confined within a cavity (see Sec. 2.5). The total energy H of the radiation field contained in a volume V can be calculated by integrating the energy density over the volume:

$$H = \int_V dV \left(\frac{\epsilon_0}{2} |\vec{E}|^2(\vec{r},t) + \frac{1}{2\mu_0} |\vec{B}|^2(\vec{r},t) \right) = \sum_{\vec{k},\alpha} V \epsilon_0 \omega^2 \left(A_{\vec{k},\alpha} A^*_{\vec{k},\alpha} + A^*_{\vec{k},\alpha} A_{\vec{k},\alpha} \right) \tag{2.12}$$

where $\epsilon_0 \mu_0 = c^{-2}$, $\omega = ck$, and periodic boundary conditions have been used.[2]

2.2 Quantum harmonic oscillator

Quantum mechanics postulates that the energy levels of an harmonic oscillator are quantized. The Hamiltonian of such oscillator with mass m and resonant (angular) frequency ω is given by

$$\hat{\mathcal{H}} = \frac{\hat{p}^2}{2m} + \frac{1}{2} m\omega^2 \hat{x}^2 \tag{2.13}$$

[2] Using these conditions, the fields vanish at the boundaries of V.

where the position and momentum operators $\hat{x}$ and $\hat{p}$ satisfy the commutation relation $[\hat{x}, \hat{p}] = i\hbar$. It is convenient to define the ladder operators:

$$\hat{a} = \frac{1}{\sqrt{2m\hbar\omega}}(m\omega\hat{x} + i\hat{p}) \tag{2.14}$$

$$\hat{a}^\dagger = \frac{1}{\sqrt{2m\hbar\omega}}(m\omega\hat{x} - i\hat{p}) \tag{2.15}$$

which satisfy the commutation relation $\left[\hat{a}, \hat{a}^\dagger\right] = 1$. The ladder operators are not hermitian and therefore not observables. The position and momentum operators expressed in terms of the ladder operators are

$$\hat{x} = \sqrt{\frac{\hbar}{2m\omega}}\left(\hat{a} + \hat{a}^\dagger\right) \tag{2.16}$$

$$\hat{p} = \sqrt{\frac{m\hbar\omega}{2}}i\left(\hat{a}^\dagger - \hat{a}\right) \tag{2.17}$$

so the corresponding Hamiltonian reads

$$\hat{\mathcal{H}} = \frac{\hbar\omega}{2}\left(\hat{a}^\dagger\hat{a} + \hat{a}\hat{a}^\dagger\right) = \hbar\omega\left(\hat{a}^\dagger\hat{a} + \frac{1}{2}\right) \tag{2.18}$$

The last equation used the commutation relation of the ladder operators. The operator $\hat{a}^\dagger\hat{a}$ can be defined as the number operator $\hat{n}$. In contrast to the ladder operators, the number operator is hermitian and therefore an observable as

$$\hat{n}^\dagger = (\hat{a}^\dagger\hat{a})^\dagger = \hat{a}^\dagger\hat{a} = \hat{n} \tag{2.19}$$

shows. The number operator has eigenstates $|n\rangle$ satisfying the eigenvalue equation

$$\hat{n}\,|n\rangle = n\,|n\rangle \tag{2.20}$$

which implies that the eigenstates of $\hat{\mathcal{H}}$ are also $|n\rangle$:

$$\hat{\mathcal{H}}\,|n\rangle = \hbar\omega\left(\hat{n} + \frac{1}{2}\right)|n\rangle = \hbar\omega\left(n + \frac{1}{2}\right)|n\rangle \tag{2.21}$$

Therefore, the eigenvalue or energies of the quantum harmonic oscillator are

$$E_n = \hbar\omega\left(n + \frac{1}{2}\right) \tag{2.22}$$

where E_0 is the zero point energy.

2.3 Quantization of the electromagnetic field

The mathematical description of the quantum harmonic oscillator can be used to quantize the electromagnetic field. Every radiation mode $\vec{k}, \alpha$ is associated with a quantized harmonic oscillator. Therefore, a photon is an excitation quantum of the oscillator in the corresponding radiation mode. The ladder operators act on the number states in the

following way:

$$\hat{a}_{\vec{k},\alpha}\left|n_{\vec{k},\alpha}\right\rangle = \sqrt{n_{\vec{k},\alpha}}\left|n_{\vec{k},\alpha}-1\right\rangle \tag{2.23}$$

$$\hat{a}^{\dagger}_{\vec{k},\alpha}\left|n_{\vec{k},\alpha}\right\rangle = \sqrt{n_{\vec{k},\alpha}+1}\left|n_{\vec{k},\alpha}+1\right\rangle \tag{2.24}$$

Therefore, $\hat{a}_{\vec{k},\alpha}$ destroys a photon, $\hat{a}^{\dagger}_{\vec{k},\alpha}$ creates a photon, and $\hat{n}_{\vec{k},\alpha}$ counts the number of photons in mode $\vec{k},\alpha$. The former two are often referred to as the annihilation and creation operators, respectively. The number states are called Fock states and have a fixed photon number in their radiation mode. The Hamiltonian of the total radiation field is the sum over all modes:

$$\hat{\mathcal{H}} = \sum_{\vec{k},\alpha}\hat{\mathcal{H}}_{\vec{k},\alpha} = \sum_{\vec{k},\alpha}\hbar\omega\left(\hat{n}_{\vec{k},\alpha}+\frac{1}{2}\right) = \sum_{\vec{k},\alpha}\frac{\hbar\omega}{2}\left(\hat{a}_{\vec{k},\alpha}\hat{a}^{\dagger}_{\vec{k},\alpha}+\hat{a}^{\dagger}_{\vec{k},\alpha}\hat{a}_{\vec{k},\alpha}\right) \tag{2.25}$$

When comparing the classical field energy in Eqn. 2.12 with the quantum mechanical Hamiltonian the following replacement for the fields can be made:

$$A_{\vec{k},\alpha} \rightarrow \sqrt{\frac{\hbar}{2V\epsilon_0\omega}}\hat{a}_{\vec{k},\alpha} \tag{2.26}$$

$$A^{*}_{\vec{k},\alpha} \rightarrow \sqrt{\frac{\hbar}{2V\epsilon_0\omega}}\hat{a}^{\dagger}_{\vec{k},\alpha} \tag{2.27}$$

It should be mentioned that this quantization assumes the field to be confined in a cavity with finite volume V (see also Sec. 2.1). This implies that the concept of quantized radiation or a photon cannot be defined in free space outside of a cavity. In the physical picture, free space is an infinitely large cavity. This does not lead to any divergences, as the photon density of states varies with the volume, and thus this cancels in any physical observable. Substituting the replacements into Eqn. 2.10 and 2.11 yields the operator for the electric and the magnetic field:

$$\hat{E}(\vec{r},t) = \sum_{\vec{k},\alpha} i\sqrt{\frac{\hbar\omega}{2V\epsilon_0}}\vec{\epsilon}_{\vec{k},\alpha}\left(\hat{a}_{\vec{k},\alpha}e^{i(\vec{k}\vec{r}-\omega t)} - \hat{a}^{\dagger}_{\vec{k},\alpha}e^{-i(\vec{k}\vec{r}-\omega t)}\right) \tag{2.28}$$

$$\hat{B}(\vec{r},t) = \sum_{\vec{k},\alpha} i\sqrt{\frac{\hbar}{2V\epsilon_0\omega}}\vec{k}\times\vec{\epsilon}_{\vec{k},\alpha}\left(\hat{a}_{\vec{k},\alpha}e^{i(\vec{k}\vec{r}-\omega t)} - \hat{a}^{\dagger}_{\vec{k},\alpha}e^{-i(\vec{k}\vec{r}-\omega t)}\right) \tag{2.29}$$

For simplicity the dimensionless phase $\chi = -\vec{k}\vec{r}+\omega t-\frac{\pi}{2}$ is defined, such that $ie^{i(\vec{k}\vec{r}-\omega t)} = e^{-i\chi}$. In addition, it is convenient to express $\hat{E}(\vec{r},t)$ in units of $\sqrt{\frac{2\hbar\omega}{V\epsilon_0}}$ and $\hat{B}(\vec{r},t)$ in units of $\sqrt{\frac{2\hbar}{V\epsilon_0\omega}}$, so the simplified field operators read

$$\hat{E}(\vec{r},t) = \frac{1}{2}\sum_{\vec{k},\alpha}\vec{\epsilon}_{\vec{k},\alpha}\left(\hat{a}_{\vec{k},\alpha}e^{-i\chi} - \hat{a}^{\dagger}_{\vec{k},\alpha}e^{i\chi}\right) \tag{2.30}$$

$$\hat{B}(\vec{r},t) = \frac{1}{2}\sum_{\vec{k},\alpha}\vec{k}\times\vec{\epsilon}_{\vec{k},\alpha}\left(\hat{a}_{\vec{k},\alpha}e^{-i\chi} - \hat{a}^{\dagger}_{\vec{k},\alpha}e^{i\chi}\right) \tag{2.31}$$

Indeed, integrating the energy density over the volume yields the Hamiltonian of the radiation field (in SI units):

$$\int_V dV \left(\frac{\epsilon_0}{2} \hat{E}^2(\vec{r},t) + \frac{1}{2\mu_0} \hat{B}^2(\vec{r},t) \right) = \sum_{\vec{k},\alpha} \hbar\omega \left(\hat{a}^\dagger_{\vec{k},\alpha} \hat{a}_{\vec{k},\alpha} + \frac{1}{2} \right) = \hat{\mathcal{H}} \tag{2.32}$$

2.4 Field states

The concept of Fock states as the eigenstates of the number operator was introduced in the previous section. Fock states are orthonormal and form a basis. The expectation value of the radiation field Hamiltonian for the vacuum or ground state of the radiation field is

$$\left\langle \hat{\mathcal{H}} \right\rangle = \left\langle 0 \left| \hat{\mathcal{H}} \right| 0 \right\rangle = \sum_{\vec{k},\alpha} \frac{\hbar\omega}{2} \tag{2.33}$$

Each mode has a finite zero point energy resulting in an infinite vacuum energy. This problem requires renormalization, which is done in quantum field theory, but often it is sufficient to consider energy differences with respect to the ground state. In the following analysis, only a single radiation mode is considered. The expectation value of the electric field for the Fock state vanishes, which means it is a non-classical or quantum field state and cannot be represented by a classical field. The variance $(\Delta\hat{E})^2$, however, does not vanish, as

$$(\Delta\hat{E})^2 = \left\langle \hat{E}^2 \right\rangle - \left\langle \hat{E} \right\rangle^2 = \frac{1}{4} \left\langle n \left| \hat{a}\hat{a}^\dagger + \hat{a}^\dagger\hat{a} \right| n \right\rangle = \frac{1}{2} \left(n + \frac{1}{2} \right) \tag{2.34}$$

shows. This means even the vacuum has fluctuations, but the average is zero. The states of light, whose expectation value corresponds to classical electromagnetic radiation fields are coherent states, which can be described with a single complex parameter α:

$$|\alpha\rangle = e^{-\frac{1}{2}|\alpha|^2} \sum_n \frac{\alpha^n}{\sqrt{n!}} |n\rangle \tag{2.35}$$

Coherent states are eigenstates of the annihilation operator with eigenvalue α, are normalized, and have a mean photon number of $|\alpha|^2$. The probability of a mode actually containing n photons when the system is in state $|\alpha\rangle$ is given by

$$P(n) = |\langle n \,|\, \alpha \rangle|^2 = \frac{|\alpha|^{2n}}{n!} e^{-|\alpha|^2} = P_{\bar{n}}(n) \tag{2.36}$$

which is precisely the probability mass function of the Poisson distribution with a mean $\bar{n} = |\alpha|^2$. The photon number variance is

$$(\Delta n)^2 = \left\langle \alpha \left| \hat{a}^\dagger\hat{a}\hat{a}^\dagger\hat{a} \right| \alpha \right\rangle - \left\langle \alpha \left| \hat{a}^\dagger\hat{a} \right| \alpha \right\rangle^2 = |\alpha|^2 = \langle \hat{n} \rangle = \bar{n} \tag{2.37}$$

where the commutation relation has been used such that $\hat{a}^\dagger\hat{a}\hat{a}^\dagger\hat{a} = \hat{a}^\dagger(\hat{a}^\dagger\hat{a}+1)\hat{a}$. Therefore, the photon number fluctuates with the square root of the mean photon number. This phenomenon, called Shot noise, is purely quantum, as a classical field does not exhibit such intensity fluctuations. Since the output of a laser is a coherent state, this means that the intensity stability of a laser is fundamentally limited by Shot noise. The relative

fluctuations

$$\frac{\Delta n}{\bar{n}} = \frac{1}{\sqrt{\bar{n}}} \tag{2.38}$$

can be minimized in the classical limit of $n \gg 1$. It is worth noting the Fock state is not Shot noise limited, meaning the variance of the number operator vanishes. Thus, a single-photon source, which outputs the single-photon Fock state $|1\rangle$, is also not Shot noise limited. The expectation value of the electric field is

$$\left\langle \alpha \left| \hat{E} \right| \alpha \right\rangle = \frac{1}{2} \left(\alpha e^{-i\chi} - \alpha^* e^{i\chi} \right) \tag{2.39}$$

which can be simplified using $\alpha = |\alpha| e^{i\phi}$ and $e^{-i\chi} = i e^{i(\vec{k}\vec{r} - \omega t)}$ such that Euler's formula can be applied. The expectation value for $\hat{E}$ is then $|\alpha| \sin(-\vec{k}\vec{r} + \omega t - \phi)$. Hence, coherent states are indeed states of light whose expectation value corresponds to classical waves.

2.5 Quantized light-atom interactions

A quantized radiation field interacting with a two-level system (TLS) is the typical situation in cavity quantum electrodynamics (QED). An example is a single atom interacting with a radiation mode in a cavity (see Fig. 2.1). This model was introduced as an idealization of light-matter interactions in free space. In the following section only a single radiation mode with angular frequency ω is considered with the vacuum field energy set to zero (it does not contribute to the dynamics). The transition energy of the TLS from its excited state $|2\rangle$ to its ground state $|1\rangle$ is $\hbar\omega_{21}$. To simplify the calculations, the ground state energy of the atom is chosen to be zero as well. Similar to the ladder operators for the electric field, atomic ladder operators can be defined as

$$\hat{\sigma} = |1\rangle\langle 2| \tag{2.40}$$

$$\hat{\sigma}^\dagger = |2\rangle\langle 1| \tag{2.41}$$

resulting in the Hamiltonian of the atom being

$$\hat{\mathcal{H}}_A = \hbar\omega_{21} \hat{\sigma}^\dagger \hat{\sigma} \tag{2.42}$$

The interaction between the dipole of the atom and the radiation field is given by

$$\hat{\mathcal{H}}_I = -\hat{d}\hat{E} \tag{2.43}$$

The dipole operator can be written as

$$\hat{d} = e\hat{r} = \sum_{i,j} |i\rangle \underbrace{\langle i| \, e\hat{r} \, |j\rangle}_{\vec{d}_{ij}} \langle j| \overset{\text{TLS}}{=} \vec{d}_{12} \left(|1\rangle\langle 2| + |2\rangle\langle 1| \right) = \vec{d}_{12} \left(\hat{\sigma} + \hat{\sigma}^\dagger \right) \tag{2.44}$$

For the sake of simplicity the atom is assumed to rest at the center of the cavity. In the Schrödinger picture the time dependence is shifted to the state vectors, while operators

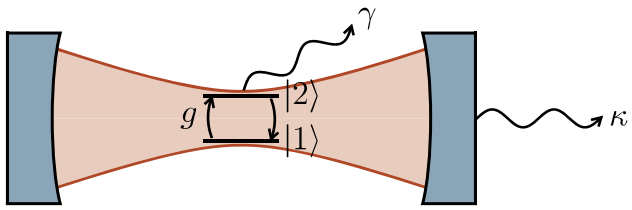

Figure 2.1: A simple conceptual model of cavity QED. A two-level system (e.g. an atom) is coupled with the radiation field in a cavity. Its ground $|1\rangle$ and excited state $|2\rangle$ couple to the radiation field with coupling strength g. κ is the loss rate of cavity photons and γ the excited state decay rate through spontaneous emission. While the atom-field coupling is coherent, spontaneous emission and cavity losses are incoherent dynamics.

and observables are time-independent. The interaction Hamiltonian then reads

$$\begin{aligned}\hat{\mathcal{H}}_I &= -\vec{d}_{12}\left(\hat{\sigma}+\hat{\sigma}^\dagger\right)\cdot\sqrt{\frac{\hbar\omega}{2V\epsilon_0}}\vec{\epsilon}\left(\hat{a}-\hat{a}^\dagger\right) = \\ &= -\underbrace{\vec{d}_{12}\cdot\vec{\epsilon}\sqrt{\frac{\omega}{2V\epsilon_0\hbar}}}_{g}\hbar\left(\hat{\sigma}\hat{a}-\hat{\sigma}\hat{a}^\dagger+\hat{\sigma}^\dagger\hat{a}-\hat{\sigma}^\dagger\hat{a}^\dagger\right)\end{aligned} \tag{2.45}$$

where the coupling strength g was defined. The terms $\hat{\sigma}\hat{a}$ and $\hat{\sigma}^\dagger\hat{a}^\dagger$ are energy non-conserving. Neglecting these amounts to the rotating wave approximation. The remaining terms $\hat{\sigma}\hat{a}^\dagger$ and $\hat{\sigma}^\dagger\hat{a}$ correspond to emission of a photon with the atom transitioning from the excited to its ground state and absorption of a photon with the atom transitioning from ground to excited state, respectively. The complete Jaynes-Cummings Hamiltonian[3] is the sum of the three contributions (the Hamiltonian for the radiation field is derived in Eqn. 2.32):

$$\hat{\mathcal{H}}_{JC} = \underbrace{\hbar\omega_{21}\hat{\sigma}^\dagger\hat{\sigma}}_{\hat{\mathcal{H}}_A} + \underbrace{\hbar\omega\hat{a}^\dagger\hat{a}}_{\hat{\mathcal{H}}_R} + \underbrace{\hbar g\left(\hat{\sigma}\hat{a}^\dagger-\hat{\sigma}^\dagger\hat{a}\right)}_{\hat{\mathcal{H}}_I} \tag{2.46}$$

To calculate the time evolution of the system it is convenient to switch to the interaction picture, in which both states and operators are time-dependent. The Jaynes-Cummings Hamiltonian can be decomposed into a non-interacting and interacting part, such that

$$\hat{\mathcal{H}}_{JC} = \underbrace{\hat{\mathcal{H}}_A+\hat{\mathcal{H}}_R}_{\hat{\mathcal{H}}_0} + \underbrace{\hat{\mathcal{H}}_I}_{\hat{\mathcal{H}}'} \tag{2.47}$$

In the interaction picture the interaction Hamiltonian becomes

$$\hat{\mathcal{H}}'_I(t) = e^{\frac{i}{\hbar}\hat{\mathcal{H}}_0 t}\hat{\mathcal{H}}' e^{-\frac{i}{\hbar}\hat{\mathcal{H}}_0 t} \tag{2.48}$$

[3]It is important to note that in the literature the interaction Hamiltonian is often defined as $\hbar g\left(\hat{\sigma}\hat{a}^\dagger+\hat{\sigma}^\dagger\hat{a}\right)$. This is a convention which does not change the observables and expectation values associated with them. In fact, in Minkowski spacetime all representations are unitary equivalent. In curved spacetime (general relativity), however, this is not generally valid anymore[10].

and the state vector is written as

$$|\psi_I(t)\rangle = e^{\frac{i}{\hbar}\hat{\mathcal{H}}_0 t}\,|\psi_S(t)\rangle \tag{2.49}$$

The indices I and S denote the corresponding operator or state in the interaction or Schrödinger picture, respectively. Note that for any operator $\hat{O}$ and state vector $|\psi(t)\rangle$ the equation

$$\left\langle \psi_S(t) \,\middle|\, \hat{O}_S \,\middle|\, \psi_S(t) \right\rangle = \left\langle \psi_S(t) \,\middle|\, e^{-\frac{i}{\hbar}\hat{\mathcal{H}}_0 t} e^{\frac{i}{\hbar}\hat{\mathcal{H}}_0 t} \hat{O}_S e^{-\frac{i}{\hbar}\hat{\mathcal{H}}_0 t} e^{\frac{i}{\hbar}\hat{\mathcal{H}}_0 t} \,\middle|\, \psi_S(t) \right\rangle = \left\langle \psi_I(t) \,\middle|\, \hat{O}_I \,\middle|\, \psi_I(t) \right\rangle \tag{2.50}$$

holds. Both pictures are therefore equivalent. The interaction Hamiltonian can be calculated with the Baker-Campbell-Hausdorff formula[4] and the fact that $\hat{a}$ and $\hat{\sigma}$ commute:[5]

$$\hat{\mathcal{H}}_I'(t) = \hbar g \left(\hat{\sigma}\hat{a}^\dagger e^{i(\omega-\omega_{21})t} - \hat{\sigma}^\dagger \hat{a} e^{-i(\omega-\omega_{21})t} \right) \tag{2.51}$$

The frequency difference between the light field and the atomic transition is the detuning $\Delta = \omega - \omega_{21}$. The time evolution of the state vector $|\psi_I(t)\rangle$ is governed by the time-dependent Schrödinger equation

$$i\hbar \frac{\partial}{\partial t} |\psi_I(t)\rangle = \hat{\mathcal{H}}_I'(t)\,|\psi_I(t)\rangle \tag{2.52}$$

which is solved by the ansatz

$$|\psi_I(t)\rangle = \sum_n c_{1,n+1}(t)\,|n+1,1\rangle + c_{2,n}(t)\,|n,2\rangle \tag{2.53}$$

The interaction Hamiltonian links the states $|n+1,1\rangle \longleftrightarrow |n,2\rangle$ through a coherent exchange of energy quanta. When the atom transitions $|2\rangle \longrightarrow |1\rangle$, the field gets one additional photon $|n\rangle \longrightarrow |n+1\rangle$ and vice versa. Inserting the ansatz into the Schödinger equation yields (in vector representation)

$$\begin{pmatrix} \dot{c}_{1,n+1}(t) \\ \dot{c}_{2,n}(t) \end{pmatrix} = \begin{pmatrix} -ig\sqrt{n+1}e^{i\Delta t} c_{2,n}(t) \\ ig\sqrt{n+1}e^{-i\Delta t} c_{1,n+1}(t) \end{pmatrix} \tag{2.54}$$

In the resonant case $\Delta = 0$ the coupled first-order differential equations can be transformed to uncoupled second-order differential equations. Choosing the atom to be in the ground state and the field in state $n+1$ at time $t = 0$ allows these equations to be easily solved with a cosine ansatz

$$\begin{pmatrix} c_{1,n+1}(t) \\ c_{2,n}(t) \end{pmatrix} = \begin{pmatrix} \cos(g\sqrt{n+1}t) \\ i\sin(g\sqrt{n+1}t) \end{pmatrix} \tag{2.55}$$

[4] $e^{\alpha\hat{X}}\hat{Y}e^{-\alpha\hat{X}} = \hat{Y} + \alpha[\hat{X},\hat{Y}] + \frac{\alpha^2}{2!}[\hat{X},[\hat{X},\hat{Y}]] + \ldots$

[5] This allows one to calculate the terms individually, e.g.
$[\hat{a}^\dagger\hat{a},\hat{a}] = \hat{a} \rightsquigarrow e^{i\omega t\hat{a}^\dagger\hat{a}}\hat{a}e^{-i\omega t\hat{a}^\dagger\hat{a}} = \hat{a} + (i\omega t)\hat{a} + \frac{(i\omega t)^2}{2!}\hat{a} + \cdots = \hat{a}e^{i\omega t}$ and similar for $\hat{\sigma}$.

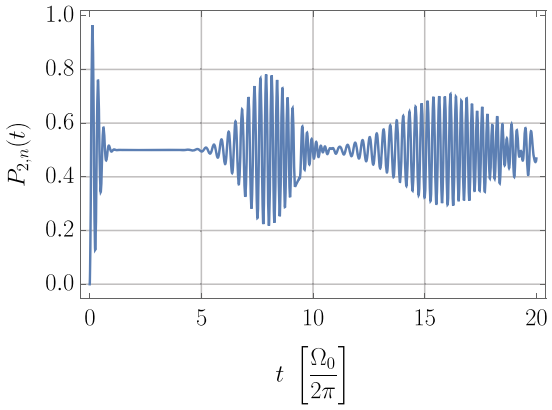

Figure 2.2: Collapse and revival of Rabi oscillations. The system is interacting with a coherent state with $|\alpha|^2 = 15$. The Rabi oscillations are a superposition of many oscillations with quantized frequencies. At $t = 0$ the system is in the ground state and all oscillations are in phase. At a later time, they dephase (collapse) and even later they rephase (revival) at least partially.

The absolute square of these coefficients give the populations in each state:

$$P_{1,n+1}(t) = \cos^2(g\sqrt{n+1}t) = \frac{1}{2}(1 + \cos(2g\sqrt{n+1}t)) \tag{2.56}$$

$$P_{2,n}(t) = \sin^2(g\sqrt{n+1}t) = \frac{1}{2}(1 - \cos(2g\sqrt{n+1}t)) \tag{2.57}$$

Therefore, the population oscillates between both states with $\Omega_n = 2g\sqrt{n+1}$, the quantized Rabi frequency.[6] It is worth noting that even for $n = 0$ (i.e. no photons in the field mode) Rabi oscillations occur. This is called vacuum Rabi oscillations, and is a pure quantum mechanical effect. The generalized Rabi frequency (i.e. with a finite detuning) is given by

$$\Omega_n^\Delta = \sqrt{\Omega_n^2 + \Delta^2} \tag{2.58}$$

If the two-level system in the cavity interacts with a coherent light field, the probability of finding the atom in the excited state modifies to

$$P_{2,n}(t) = \sum_n^\infty \frac{|\alpha|^2 e^{-|\alpha|^2}}{n!} \frac{1}{2}(1 - \cos(\Omega_0\sqrt{n+1}t)) \tag{2.59}$$

since a coherent state is a superposition of Fock states with a Poisson distributed mean photon number (see Sec. 2.4). $P_{2,n}(t)$ is shown in Fig. 2.2 for $|\alpha|^2 = 15$. At $t = 0$ the atom is in the ground state and all oscillations are in phase. At a later time, they dephase due to dispersion of Rabi frequencies in the field (collapse). The collapse time is the time when the Rabi frequencies $\Omega_{\bar{n}+\Delta n}$ and $\Omega_{\bar{n}-\Delta n}$ are π-out of phase and can be estimated with $\tau_c \approx \frac{\pi}{\Omega_0}$. Eventually, the oscillations of Rabi frequencies Ω_n and Ω_{n+1} rephase (are 2π-out of phase) and revival of the oscillations happens at revival time $\tau_r \approx 4|\alpha|\tau_c$.

[6] A semiclassical treatment of a TLS evolving in the presence of a light field yields similar dynamics with a non-quantized Rabi frequency $\Omega_0 = \frac{\vec{d}_{12}\vec{E}}{\hbar}$.

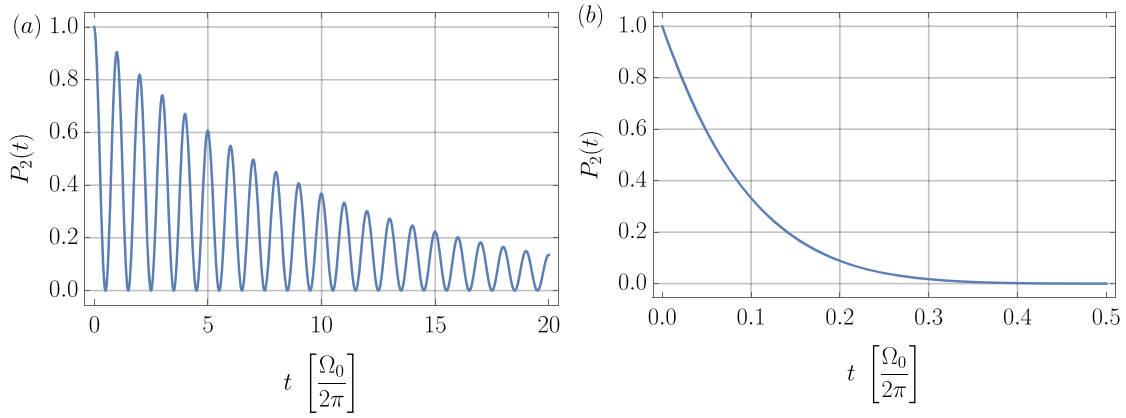

Figure 2.3: Rabi oscillations of the excited state population of an atom in a cavity. (a) In the damped regime with $g = 5(\kappa + \gamma)$ Rabi oscillations are still observable. (b) In the overdamped (Purcell) regime with $5g = (\kappa + \gamma)$ no full Rabi cycle can be observed. In both cases a photon is ultimately emitted by the cavity.

2.6 Weak coupling

The quantized light-atom interactions derived in the previous section can be observed in cavity QED systems (see Fig. 2.1). Experimentally, this has been realized for Rydberg atoms coupled to superconducting microwave resonators[11, 12], ultracold atoms coupled to optical cavities[13–16], quantum dots in photonic crystal cavities[17–19], and on-chip superconducting qubits in circuit cavity QED[20]. Characteristic for the dynamics is how the coupling strength g compares to the loss mechanisms of the cavity, the spontaneous emission rate γ and the cavity loss rate κ. While the atom-field coupling is coherent, spontaneous emission and cavity losses are incoherent dynamics. In the simple case of vacuum Rabi oscillations (no light field and assuming the atom starts in the excited state), the incoherent dynamics add damping of the form $\frac{1}{\kappa+\gamma}$. In the strong coupling regime, where $g \gg (\kappa+\gamma)$, many Rabi oscillations can be observed before the photon is eventually lost to the environment. This situation is shown in Fig. 2.3(a). In the weak coupling regime, where $g \ll (\kappa + \gamma)$ the oscillation is overdamped, as shown in Fig. 2.3(b). In the latter case, the cavity appears to act as the environment for the atom, whose excited state population spontaneously decays. This spontaneous decay occurs at a much faster rate than in free space and is known as the Purcell effect.

The Purcell effect can be exploited to modify the spontaneous emission rate of a single-photon emitter (which is an effective two-level system). Another way to interpret this effect is that the cavity reduces the number of modes the TLS can couple to, thereby enhancing the resonant modes. The ratio of cavity-coupled to free space emission rate is defined as the Purcell factor F_p. The rates can be calculated using the quantum master equation, Wigner-Weisskopf theory of spontaneous emission, or Fermi's golden rule, which is probably the most intuitive method. According to the latter, the transition rate from the initial (excited) state $|2, 0\rangle$ to final (ground) state $|1, 1\rangle$ under the emission of a photon is given by

$$\Gamma_{21} = \frac{2\pi}{\hbar^2}|\langle 2, 0|\hat{d}\hat{E}|1, 1\rangle|^2\rho(\omega) \tag{2.60}$$

where $\langle 2,0|\hat{d}\hat{E}|1,1\rangle$ is the transition matrix element and $\rho(\omega)$ is the density of states. The matrix element can be calulated using the interaction Hamiltonian from Eqn. 2.46:

$$|\langle 2,0|\hat{d}\hat{E}|1,1\rangle|^2 = |\langle 2,0|\hbar g(\hat{\sigma}\hat{a}^\dagger - \hat{\sigma}^\dagger\hat{a})|1,1\rangle|^2 = \hbar^2 g^2 |\langle 2,0|2,0\rangle|^2 = \hbar^2 g^2 = \frac{|\vec{d}_{12}\cdot\vec{\epsilon}|^2\hbar\omega}{2V\epsilon_0} \tag{2.61}$$

For a randomly oriented dipole in free space $|\vec{d}_{12}\cdot\vec{\epsilon}|^2$ averages to $\frac{d_{12}^2}{3}$ where $|\vec{d}_{12}| = d_{12}$. The density of states in free space is given by $\rho(\omega) = \frac{V\omega^2}{\pi^2 c^3}$,[7] so the transition rate is

$$\Gamma_{21} = \frac{2\pi}{\hbar^2}\frac{d_{12}^2\hbar\omega}{6V\epsilon_0}\frac{V\omega^2}{\pi^2c^3} = \frac{d_{12}^2\omega^3}{3\hbar\pi\epsilon_0 c^3} = \frac{1}{\tau_r} \tag{2.62}$$

where the radiative lifetime τ_r was introduced. For non-ideal two-level systems, non-radiative decay paths exist as well.

As already mentioned, if the emitter is confined in a cavity with finite volume, the transition rate changes. While a cavity has many resonant modes, for this calculation it is assumed only one of these resonant modes is close to the atomic transition. Therefore, the overlap integral of the photonic density of states of the cavity and electronic density of states of the atom vanishes for all other modes.[8] The photonic density of states of a cavity with resonance frequency ω_c and linewidth $\Delta\omega_c = \kappa + \gamma$ is of the form of a normalized Lorentzian

$$\rho(\omega) = \frac{2}{\pi}\frac{\Delta\omega_c}{4(\omega-\omega_c)^2 + \Delta\omega_c^2} \tag{2.63}$$

The matrix element can be calculated in a similar fashion to the free space case, however, the term $|\vec{d}_{12}\cdot\vec{\epsilon}|^2$ does not average to $\frac{d_{12}^2}{3}$ anymore. Rather, the dipole orientation can be accounted for by introducing the dimensionless factor

$$\xi^2 = \frac{|\vec{d}_{12}\cdot\vec{\epsilon}|^2}{|\vec{d}_{12}|^2|\vec{\epsilon}|^2} = \frac{|\vec{d}_{12}\cdot\vec{\epsilon}|^2}{d_{12}^2} \tag{2.64}$$

To obtain the last equality, the normalization of the polarization vector has been assumed. In an experiment, this overlap of transition dipole and cavity mode has to be optimized such that $\xi^2 \to 1$. At resonance the density of states simplifies to

$$\rho(\omega = \omega_{21} = \omega_c) = \frac{2}{\pi}\frac{1}{\Delta\omega_c} = \frac{2}{\pi}\frac{\omega_c}{\Delta\omega_c\omega_c} = \frac{2}{\pi}\frac{Q}{\omega_c} \tag{2.65}$$

[7] Assuming the electric field being confined in a box with edge length L, then boundary conditions require $k_i L = 2\pi n_i$ for all dimensions $i = x, y, z$ with $n_i \in \mathbb{N}$, such that the field vanishes at the boundaries. Therefore, only discrete values of k are allowed, resulting in a finite number of k-states $\rho(k)dk$ between $k + dk$. In 3D this number is the volume in k-space of the spherical shell between radius k and $k + dk$ divided by the volume per k state $\left(\frac{2\pi}{L}\right)^3$. Thus, $\rho(k)dk = \frac{4\pi k^2 L^3}{(2\pi)^3}dk = \frac{Vk^2}{2\pi^2}dk$. Mapping this into frequency space gives $\rho(\omega)d\omega = 2\rho(k)dk \rightsquigarrow \rho(\omega) = 2\rho(k)\frac{dk}{d\omega}$. The factor of 2 is due to both possible polarizations for each k-state. Using $\omega = ck$ allows one to calculate the final result $\rho(\omega) = \frac{V\omega^2}{\pi^2c^3}$. Note that in the physical picture, free space is an infinitely large cavity.

[8] This approximation is valid since the natural linewidth of an atom is much narrower than typical cavity linewidths. In cases where this is not true, a large free spectral range can ensure that this approximation is still valid. This is typical for a room temperature solid-state quantum emitter in a cavity and exploited in Chap. 9.

where the quality factor of the cavity $Q = \frac{\omega_c}{\Delta\omega_c}$ was introduced. With Fermi's golden rule this results in the transition rate in the cavity at resonance being

$$\Gamma_{21} = \frac{2\pi}{\hbar^2}\frac{d_{12}^2\xi^2\hbar\omega}{3V\epsilon_0}\frac{2Q}{\pi\omega} = \frac{2d_{12}^2\xi^2 Q}{\hbar V\epsilon_0} \tag{2.66}$$

The Purcell factor is then the ratio of cavity to free space transition rate

$$F_p = \frac{\Gamma_{21}^{\text{cav}}}{\Gamma_{21}^{\text{free}}} = \frac{2d_{12}^2\xi^2 Q}{\hbar V\epsilon_0}\frac{3\hbar\pi\epsilon_0 c^3}{d_{12}^2\omega^3} = \frac{6\pi Q\xi^2}{V}\underbrace{\frac{c^3}{\omega^3}}_{=\frac{1}{k^3}=\frac{\lambda^3}{8\pi^3}} = \frac{3}{4\pi^2}\lambda^3\frac{Q}{V}\xi^2 \tag{2.67}$$

which is the well known formula for the Purcell factor. It is obvious that for a large Purcell factor a high quality factor and a small mode volume is required. This has been experimentally demonstrated for quantum dots and solid-state quantum emitters in microcavities[21]. It is worth noting, that the cavity only affects the density of states along its axis, so there is still emission into non-resonant modes. This can, however, be minimized with a large Purcell factor. It is also important to remember that the derived formula is strictly only valid in the limit where the dipole transition is much narrower than the cavity linewidth. Otherwise, the Purcell factor requires the calculation of the exact overlap integral of photonic density of states $\rho_{\text{p}}(\omega)$ and electronic density of states $\rho_{\text{e}}(\omega)$. It has the form

$$\int_0^\infty d\omega' \rho_{\text{p}}(\omega')\rho_{\text{e}}(\omega') \tag{2.68}$$

An easier approximation in this case is to introduce the effective or reduced quality factor

$$Q_{\text{eff}} = \frac{\lambda}{\Delta\lambda_{\text{cav}} + \Delta\lambda_{\text{em}}} \tag{2.69}$$

where the dynamics are dominated by the linewidth of the emitter $\Delta\lambda_{\text{em}}$. In the limit of $\Delta\lambda_{\text{em}} \ll \Delta\lambda_{\text{cav}}$ the reduced quality factor becomes the normal cavity quality factor Q.

2.7 Coherence and correlations

The ability of light to interfere is described by coherence. A light field is said to be coherent, if it sustains a fixed phase relation between the electric field at a given location and different times (temporal coherence), or at different locations at a given time (spatial coherence). The coherence time t_c is the average time during which the phase relation remains constant. Usually this is defined as the time after which the coherence or first-order correlation function decreased to $\frac{1}{e}$ and in general it depends on the spectral shape of the light. For a Lorentzian-shaped profile with linewidth $\Delta\gamma$ this is

$$t_c = \frac{1}{\Delta\gamma} \tag{2.70}$$

This can be related to a coherence length $l_c = ct_c$, which is the average propagation distance over which the phase relation remains constant. The coherence length affects the interference visibility of an interferometer. By implication this also means that coherence can be probed with an interferometer, e.g. a Mach-Zehnder interferometer (see Fig. 2.4(a)).

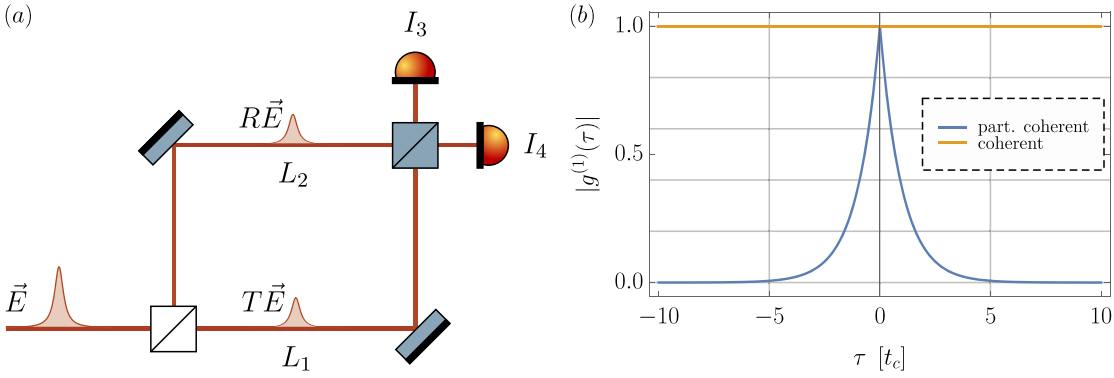

Figure 2.4: (a) Mach-Zehnder interferometer with input light field $\vec{E}$. The field is split into $T\vec{E}$ in arm L_1 and $R\vec{E}$ in arm L_2. The light field interferes at a second beam splitter, with detectors in both outputs. (b) First-order correlation function for partially (blue) and perfectly coherent (orange) light. The time is in units of the coherence time t_c. The partially coherent light source assumes a Lorentzian broadening mechanism.

The beam splitters have reflection and transmission coefficients R and T, respectively.[9] The electric field at detector 4 at time t is

$$\vec{E}_4(t) = RT\vec{E}\left(t_2 = t - \frac{L_2}{c}\right) + TR\vec{E}\left(t_1 = t - \frac{L_1}{c}\right) \tag{2.71}$$

Since the detector can only measure optical intensities and no fields, the intensity reads

$$I_4(t) = \frac{1}{2}\epsilon_0 c|\vec{E}_4(t)|^2 = \frac{1}{2}\epsilon_0 c|R|^2|T|^2\left(|\vec{E}4(t_1)|^2 + |\vec{E}(t_2)|^2 + 2\Re\{\vec{E}^*(t_1)\vec{E}(t_2)\}\right) \tag{2.72}$$

Averaging over $T' \gg t_c$ yields

$$\langle I_4(t)\rangle = \frac{1}{2}\epsilon_0 c|R|^2|T|^2\left(\left\langle|\vec{E}4(t_1)|^2\right\rangle + \left\langle|\vec{E}(t_2)|^2\right\rangle + 2\Re\left\{\left\langle\vec{E}^*(t_1)\vec{E}(t_2)\right\rangle\right\}\right) \tag{2.73}$$

Introducing the time delay $\tau = \frac{L_1 - L_2}{c}$ between t_1 and t_2 allows one to express the correlation using just one variable:

$$\left\langle\vec{E}^*(t)\vec{E}(t+\tau)\right\rangle = \frac{1}{T'}\int dt\vec{E}^*(t)\vec{E}(t+\tau) \tag{2.74}$$

which is defined as the first-order correlation function. It is useful to assume constant input intensities and normalize the correlation function to this, such that the normalized first-order correlation function is given by

$$g^{(1)}(\tau) = \frac{\left\langle\vec{E}^*(t)\vec{E}(t+\tau)\right\rangle}{\left\langle\vec{E}^*(t)\vec{E}(t)\right\rangle} = \frac{\left\langle\vec{E}^*(t)\vec{E}(t+\tau)\right\rangle}{\left\langle|\vec{E}(t)|^2\right\rangle} \tag{2.75}$$

Thus, the normalized intensity at detector 4 reads

$$\langle I_4(t)\rangle = 2|R|^2|T|^2\left(1 + \Re\{g^{(1)}(\tau)\}\right) \tag{2.76}$$

[9] $R, T \in \mathbb{C}$ to account for the phase shift of R. Energy conservation requires $|R|^2 + |T|^2 = 1$.

It is obvious that for $g^{(1)}(\tau) = 0$ the intensity at detector 4 (and consequently also at detector 3) is constant. Therefore, the first-order correlation function determines the interference visibility of the interferometer.[10]

As mentioned above, the coherence will be lost after some time $t > t_c$ which is a consequence of the finite linewidth of the light source. The light field can be modeled as a sum of single radiation modes from an ensemble of N sources with varying phase factors $e^{i\phi_j(t)}$. These phase factors are uncorrelated, i.e. $\left\langle e^{-i\phi_j(t)} e^{i\phi_k(t+\tau)} \right\rangle = 0$ for $j \neq k$. For the Lorentzian-shaped profile (e.g. collision broadened light source) the probability that an emitter has no collisions during the time interval $[\tau, \tau + d\tau]$ is given by

$$P(\tau)d\tau = \frac{1}{t_c} e^{-\frac{\tau}{t_c}} \tag{2.77}$$

The integral

$$\int_\tau^\infty d\tau' P(\tau') = e^{-\frac{\tau}{t_c}} \tag{2.78}$$

is thus the probability that no collision occured up to time τ. Each collision is going to introduce a frequency shift (hence the finite linewidth) with a random phase change. The light field at a fixed location can be written as

$$\vec{E}(t) = \vec{E}_0 e^{-i\omega t} \sum_j^N e^{i\phi_j(t)} \tag{2.79}$$

Finally, the first-order correlation function modifies to

$$\begin{aligned} \left\langle \vec{E}^*(t)\vec{E}(t+\tau) \right\rangle &= |\vec{E}_0|^2 e^{-i\omega\tau} \sum_j^N \left\langle e^{i\phi_j(t+\tau) - i\phi_j(\tau)} \right\rangle = \\ &= |\vec{E}_0|^2 e^{-i\omega\tau} N \left\langle e^{i\phi_k(t+\tau) - i\phi_k(\tau)} \right\rangle = \\ &= |\vec{E}_0|^2 e^{-i\omega\tau} N \int_\tau^\infty d\tau' P(\tau') = |\vec{E}_0|^2 N e^{-i\omega\tau - \frac{\tau}{t_c}} \end{aligned} \tag{2.80}$$

where the fact that all emitters are equal has been used. Normalizing this gives

$$g^{(1)}(\tau) = e^{-i\omega\tau - \frac{|\tau|}{t_c}} \tag{2.81}$$

The degree of coherence is $|g^{(1)}(\tau)|$. Monochromatic light has $|g^{(1)}(\tau)| = 1$, so it is perfectly coherent. Light with $|g^{(1)}(\tau)| < 1$ is called partially coherent. The degree of coherence for such light sources is shown in Fig. 2.4(b). Since $|g^{(1)}(t_c)| = \frac{1}{e}$ the above definition of the coherence time actually makes sense. The coherence time also restricts potential applications of a single-photon source, the shorter it is, the fewer applications the source is useful for. The case $|g^{(1)}(\tau)| = 0$ corresponds to incoherent light. It should be noted that perfectly monochromatic light does not exist, so it follows that $g^{(1)}(\infty) = 0$ for all light sources.

[10] The interference visibility is defined as $V = \frac{I^{\max} - I^{\min}}{I^{\max} + I^{\min}}$. For $I = \text{const.} \rightsquigarrow V = 0$.

2.8 Quantized correlation functions

The first-order correlation function correlates fields and was derived in the previous section. The second-order correlation function correlates intensities and is defined as

$$g^{(2)}(\tau) = \frac{\langle E^*(t)E^*(t+\tau)E(t+\tau)E(t+\tau)\rangle}{\langle |E(t+\tau)|^2\rangle \langle |E(t)|^2\rangle} \tag{2.82}$$

In general, the electric field carries also spatial dependence on $\vec{r}$. For the quantized correlation functions the classical fields have to be replaced with their quantized versions. To simplify the equations only a single radiation mode (with infinite coherence time) is considered and the quantized electrical field (see Eqn. 2.30) is split into its hermitian conjugate parts:

$$\hat{E}(\vec{r},t) = \frac{1}{2}\left(\hat{a}e^{-i\chi(\vec{r},t)} - \hat{a}^\dagger e^{i\chi(\vec{r},t)}\right) = \hat{E}^+(\vec{r},t) + \hat{E}^-(\vec{r},t) \tag{2.83}$$

with $\hat{E}^+(\vec{r},t) = \frac{1}{2}\left(\hat{a}e^{-i\chi(\vec{r},t)}\right)$ and $\hat{E}^-(\vec{r},t) = -\frac{1}{2}\left(\hat{a}^\dagger e^{i\chi(\vec{r},t)}\right)$. The classical average $\langle\cdots\rangle$ is replaced with the expectation value $\langle\psi\,|\cdots|\,\psi\rangle$. Thus

$$\left\langle \hat{E}^-(\vec{r}_1,t_1)\hat{E}^+(\vec{r}_2,t_2)\right\rangle = -\frac{1}{4}\left\langle \psi \,\middle|\, \hat{a}^\dagger\hat{a} \,\middle|\, \psi\right\rangle e^{i(\chi(\vec{r}_1,t_1)-\chi(\vec{r}_2,t_2))} \tag{2.84}$$

so the first-order correlation function is given by[11]

$$g^{(1)}(\vec{r}_1,t_1,\vec{r}_2,t_2) = \frac{\left\langle \hat{E}^-(\vec{r}_1,t_1)\hat{E}^+(\vec{r}_2,t_2)\right\rangle}{\left\langle \hat{E}^-(\vec{r}_1,t_1)\hat{E}^+(\vec{r}_1,t_1)\right\rangle^{\frac{1}{2}}\left\langle \hat{E}^-(\vec{r}_2,t_2)\hat{E}^+(\vec{r}_2,t_2)\right\rangle^{\frac{1}{2}}} = e^{i(\chi(\vec{r}_1,t_1)-\chi(\vec{r}_2,t_2))} \tag{2.85}$$

For $\vec{r}_1 = \vec{r}_2$ and setting $t_1 = 0 \rightsquigarrow t_2 = \tau$ yields $g^{(1)}(\tau) = e^{i\omega\tau}$ and $|g^{(1)}(\tau)| = 1$, the classical result. This means a pure state of a single mode is always coherent. For a non-pure state (e.g. a thermal state) with density matrix $\hat{\rho}$ the expectation value is given by

$$\left\langle \hat{E}^-(\vec{r}_1,t_1)\hat{E}^+(\vec{r}_2,t_2)\right\rangle = \mathrm{tr}\left(\hat{E}^-(\vec{r}_1,t_1)\hat{E}^+(\vec{r}_2,t_2)\hat{\rho}\right) \tag{2.86}$$

For the quantized-second order correlation function the same replacements can be made:

$$g^{(2)}(\vec{r}_1,t_1,\vec{r}_2,t_2) = \frac{\left\langle \hat{E}^-(\vec{r}_1,t_1)\hat{E}^-(\vec{r}_2,t_2)\hat{E}^+(\vec{r}_1,t_1)\hat{E}^+(\vec{r}_2,t_2)\right\rangle}{\left\langle \hat{E}^-(\vec{r}_1,t_1)\hat{E}^+(\vec{r}_1,t_1)\right\rangle\left\langle \hat{E}^-(\vec{r}_2,t_2)\hat{E}^+(\vec{r}_2,t_2)\right\rangle} = \frac{\left\langle \hat{a}^\dagger\hat{a}^\dagger\hat{a}\hat{a}\right\rangle}{\left\langle \hat{a}^\dagger\hat{a}\right\rangle^2} \tag{2.87}$$

It is obvious that all phase factors cancel (that means $g^{(2)}$ is independent of $\vec{r}$ and t). Using the commutation relation, the normal ordering can be broken:[12]

$$g^{(2)} = \frac{\langle\hat{n}^2\rangle - \langle\hat{n}\rangle}{\langle\hat{n}\rangle^2} = \frac{(\Delta n)^2 + \langle\hat{n}\rangle^2 - \langle\hat{n}\rangle}{\langle\hat{n}\rangle^2} = 1 + \frac{(\Delta n)^2 - \langle\hat{n}\rangle}{\langle\hat{n}\rangle^2} \tag{2.88}$$

[11] Note that $\frac{-1}{\sqrt{-1}\sqrt{-1}} = \frac{-1}{i^2} = 1$.

[12] $\hat{a}^\dagger\hat{a}^\dagger\hat{a}\hat{a} = \hat{a}^\dagger\left(\hat{a}\hat{a}^\dagger - 1\right)\hat{a} = \hat{a}^\dagger\hat{a}\hat{a}^\dagger\hat{a} - \hat{a}^\dagger\hat{a} = \hat{n}^2 - \hat{n}$

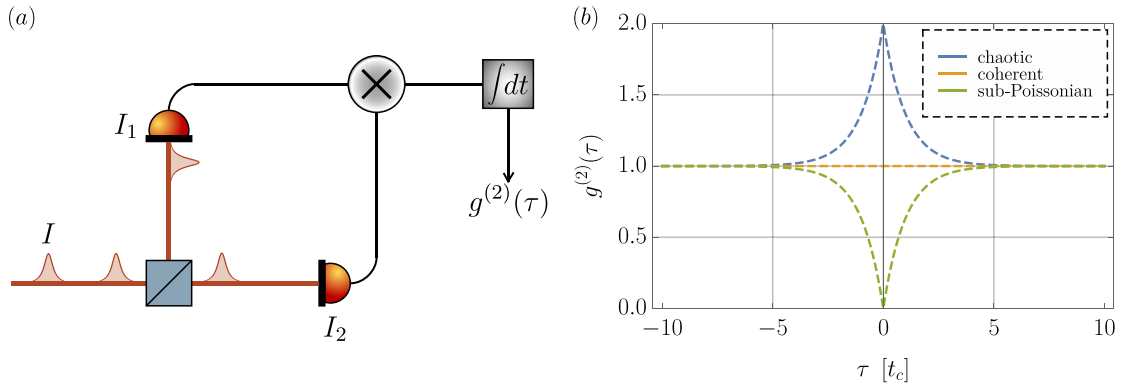

Figure 2.5: (a) HBT-type interferometer with input intensity I. The beam splitter splits the wave packets, which are successively detected by two detectors. The arrival times get correlated, and integration over many events allows one to construct the $g^{(2)}(\tau)$. (b) Second-order correlation function for a chaotic, coherent, and sub-Poissonian light source. The time delay is in units of the coherence time t_c. The chaotic light source (blue) assumes a Lorentzian broadening mechanism (e.g. collision broadening) and shows bunching. For a laser (orange) the arrival time of photons is randomly distributed. A two-level system (green) emits anti-bunched light.

Recalling variance and expectation value for Fock and coherent states (see Sec. 2.4) gives

$$g^{(2)} = 1 - \frac{1}{n} < 1 \quad \forall\, |n\rangle \tag{2.89}$$

$$g^{(2)} = 1 \quad \forall\, |\alpha\rangle \tag{2.90}$$

While $g^{(2)} = 1$ for coherent states is the same outcome a classical field would produce, $g^{(2)} < 1$ is a result only possible for quantized fields (for classical fields $g^{(2)} \geq 1$).[13]

In practice, a multimode description is required, since photons have to be described as wave packets with a finite frequency bandwidth $\Delta\omega$. This is directly related with the temporal extension Δt of the photon through a Fourier transform, such that

$$\Delta\omega\Delta t \sim 1 \tag{2.91}$$

The exact transform-limit depends on the temporal or spectral shape of the photon. In the photon picture, the value $g^{(2)}(\tau)$ is the conditional probability of detecting a second photon at time τ after the detection of a first photon at time $t = 0$. Thus, $g^{(2)}(0)$ is the probability that two or more photons are emitted at the same time. Experimentally, this second-order correlation function can be measured with an HBT (Hanbury Brown and Twiss)-type interferometer (see Fig. 2.5(a)). The photon correlations can be classified in three categories:

1. $g^{(2)}(0) > 1$, $g^{(2)}(0) > g^{(2)}(\tau)$: chaotic or super-Poissonian light (photon bunching)

2. $g^{(2)}(0) = g^{(2)}(\tau) = 1$: coherent light

[13] Eqn. 2.89 is the reason why in the literature $g^{(2)} < \frac{1}{2}$ is often used as a criterion if a single-photon emitter is present, since for $n \geq 2$ the inequality $g^{(2)} > \frac{1}{2}$ holds. This, however, only implies that the projection onto the single-photon Fock state $|1\rangle$ is not vanishing. Moreover, $g^{(2)}$ is different from the single-photon purity, as it omits the fraction of vacuum in the state. When evaluating a single-photon source, it is thus important to consider the value of $g^{(2)}$ as well as the the ratio of single-photons to vacuum[22].

3. $g^{(2)}(0) < 1$, $g^{(2)}(0) < g^{(2)}(\tau)$: sub-Poissonian light (photon anti-bunching)

Examples of these correlations are shown in Fig. 2.5(b). In general, the coherence time can be obtained through both $g^{(1)}(\tau)$ and $g^{(2)}(\tau)$ measurements, but it is much easier to do this with the HBT-type interferometer. This is because the Mach-Zehnder interferometer requires length stability much smaller than the wavelength. In contrast, the HBT-type interferometer only requires length stability much smaller than the coherence length, so it is much more robust.

2.9 Interferometers

In the previous sections, the concepts of coherence and correlation functions were introduced. As it was derived, interferometers are an essential tool to obtain information about coherence of light or photon correlations. In case of quantized fields, the interferometers have to be described quantum mechanically as well.

A classical beam splitter (BS) with input fields E_1, E_2 and output fields E_3, E_4 (omitting vector notation) can be described with a matrix:

$$\begin{pmatrix} E_3 \\ E_4 \end{pmatrix} = \begin{pmatrix} R & T \\ T & R \end{pmatrix} \begin{pmatrix} E_1 \\ E_2 \end{pmatrix} \tag{2.92}$$

The beam splitter has the complex transmission and reflection coefficients T and R, respectively. Energy conversation requires $|E_1|^2 + |E_2|^2 = |E_3|^2 + |E_4|^2$ and thus $|R|^2 + |T|^2 = 1$ and $RT^* + TR^* = 0$ (this can be seen easily by substituting the square of Eqn. 2.92 into the energy conversation). Expressing the coefficients as $R = |R|e^{i\phi_R}$ and $T = |T|e^{i\phi_T}$ yields

$$|R||T|e^{i\phi_R - i\phi_T} + |T||R|e^{i\phi_T - i\phi_R} = 0 \tag{2.93}$$

which is fulfilled for $\phi_T - \phi_R = \frac{\pi}{2}$. Since only relative phases matter, the common convention is to set $\phi_T = 0$. The quantum mechanical beam splitter can be described in a similar way with the annihilation operators

$$\begin{pmatrix} \hat{a}_3 \\ \hat{a}_4 \end{pmatrix} = \begin{pmatrix} R & T \\ T & R \end{pmatrix} \begin{pmatrix} \hat{a}_1 \\ \hat{a}_2 \end{pmatrix} \tag{2.94}$$

Inverting the matrix yields

$$\begin{pmatrix} \hat{a}_1 \\ \hat{a}_2 \end{pmatrix} = \begin{pmatrix} R^* & T^* \\ T^* & R^* \end{pmatrix} \begin{pmatrix} \hat{a}_3 \\ \hat{a}_4 \end{pmatrix} \tag{2.95}$$

The input state can be constructed with the creation operator acting on the vacuum state: $\hat{a}_1^\dagger \otimes \hat{\mathbb{1}}_2 \, |0\rangle_1 \otimes |0\rangle_2 = |1\rangle_1 \otimes |0\rangle_2 = |10\rangle_{12}$ which creates a single photon in the input mode 1 and none in mode 2. To keep the equations clear, a compact notation was introduced and only relevant modes are denoted. With $R = \frac{i}{\sqrt{2}}$ and $\frac{1}{\sqrt{2}}$ for a 50:50 beam splitter, the input state can be written as

$$|10\rangle_{12} = R\,|10\rangle_{34} + T\,|01\rangle_{34} \overset{\text{50:50 BS}}{=} \frac{1}{\sqrt{2}}(i\,|10\rangle_{34} + |01\rangle_{34}) \tag{2.96}$$

The state is a superposition state and for a 50:50 beam splitter both field modes are maximally entangled (see Sec. 2.10). As expected

$$\langle \hat{n}_3 \rangle = \left\langle 01 \left| \hat{a}_3^\dagger \hat{a}_3 \right| 10 \right\rangle_{12} = \left\langle 01 \left| (R^* \hat{a}_1^\dagger + T^* \hat{a}_2^\dagger)(R\hat{a}_1 + T\hat{a}_2) \right| 10 \right\rangle_{12} = |R|^2 \tag{2.97}$$

$$\langle \hat{n}_4 \rangle = |T|^2 \tag{2.98}$$

However, the correlations between both output ports vanish:

$$\langle \hat{n}_3 \hat{n}_4 \rangle = \left\langle 01 \left| (R^* \hat{a}_1^\dagger + T^* \hat{a}_2^\dagger)(R\hat{a}_1 + T\hat{a}_2)(T^* \hat{a}_1^\dagger + R^* \hat{a}_2^\dagger)(T\hat{a}_1 + R\hat{a}_2) \right| 10 \right\rangle_{12} = 0 \tag{2.99}$$

In the particle picture this is not surprising: the photon is either in output 3 or 4. For classical fields, such anti-correlation is not possible ($g^{(2)}(\tau) \geq 1$ for classical fields).
The formalism can be applied to the quantized Mach Zehnder interferometer (MZI) or to the Hong-Ou-Mandel effect. The input state above was $|10\rangle_{12}$, but what happens for an initial state $|11\rangle_{12}$, i.e. a photon in each input?

$$\begin{aligned}
|11\rangle_{12} &= \hat{a}_1^\dagger \hat{a}_2^\dagger |00\rangle_{12} = (R\hat{a}_3^\dagger + T\hat{a}_4^\dagger)(T\hat{a}_3^\dagger + R\hat{a}_4^\dagger) |00\rangle_{34} = \\
&= (R\hat{a}_3^\dagger + T\hat{a}_4^\dagger)(T |10\rangle_{34} + R |01\rangle_{34}) = \\
&= \sqrt{2}RT |20\rangle_{34} + R^2 |11\rangle_{34} + T^2 |11\rangle_{34} + \sqrt{2}TR |02\rangle_{34} = \\
&\overset{\text{50:50 BS}}{=} \frac{i}{\sqrt{2}} |20\rangle_{34} - \frac{1}{2} |11\rangle_{34} + \frac{1}{2} |11\rangle_{34} + \frac{i}{\sqrt{2}} |02\rangle_{34} = \\
&= \frac{i}{\sqrt{2}} (|20\rangle_{34} + |02\rangle_{34})
\end{aligned} \tag{2.100}$$

For a 50:50 beam splitter, the amplitudes of one photon in each output mode cancel and the resulting output state is maximally entangled (see Sec. 2.10). It is thus possible to generate entangled states from single-photons. This form of two-photon interference is known as the Hong-Ou-Mandel effect. This works, however, only for identical photons in each input. The two-photon interference visibility is a measure for indistinguishability of photons.

The MZI (see Fig. 2.4(a)) can be seen as a generalized beam splitter. Two inputs result in two outputs, however, each arm of the MZI adds a phase shift to the reflection and transmission coefficients:

$$\begin{pmatrix} \hat{a}_3 \\ \hat{a}_4 \end{pmatrix} = \begin{pmatrix} R' & T' \\ T' & R'' \end{pmatrix} \begin{pmatrix} \hat{a}_1 \\ \hat{a}_2 \end{pmatrix} \tag{2.101}$$

with

$$R' = R^2 e^{ikL_2} + T^2 e^{ikL_1} \tag{2.102}$$

$$T' = RT(e^{ikL_1} + e^{ikL_2}) \tag{2.103}$$

$$R'' = T^2 e^{ikL_2} + R^2 e^{ikL_1} \tag{2.104}$$

From Eqn. 2.98 it is clear that for the quantized MZI

$$\langle \hat{n}_4 \rangle = |T'|^2 = |R|^2 |T|^2 (2 + e^{ik(L_1 - L_2)} + e^{-ik(L_1 - L_2)}) = 4|R|^2 |T|^2 \cos\left(\frac{k}{2}(L_1 - L_2)\right) \tag{2.105}$$

where the trigonometric identity $1 + \cos(2x) = 2\cos^2(x)$ was used. This result can also be obtained using a classical treatment of the MZI and is thus not surprising. However, the input state was a non-classical single-photon Fock state! Thus, a single-photon can interfere with itself. This can only be understood in the wave picture of the photon, where the photon is in a superposition state of both paths in the interferometer.

2.10 Qubits and entanglement

So far only single quantum systems have been considered. Quantum mechanics allows further non-classical correlations, if multipartite states are considered. For this it is convenient to introduce the computational basis states

$$|0\rangle = \begin{pmatrix} 1 \\ 0 \end{pmatrix} \qquad \text{and} \qquad |1\rangle = \begin{pmatrix} 0 \\ 1 \end{pmatrix} \tag{2.106}$$

In analogy to classical information processing these are called logical qubits (quantum bits). Qubits are simply vectors in a complex Hilbert space. Any operation on a single qubit can be decomposed into a linear combination of the Pauli matrices

$$\hat{X} = \hat{\sigma}_x = \begin{pmatrix} 0 & 1 \\ 1 & 0 \end{pmatrix}, \qquad \hat{Y} = \hat{\sigma}_y = \begin{pmatrix} 0 & -i \\ i & 0 \end{pmatrix}, \qquad \hat{Z} = \hat{\sigma}_z = \begin{pmatrix} 1 & 0 \\ 0 & -1 \end{pmatrix} \tag{2.107}$$

The computational basis states are eigenstates of Z, and rotating these states by 45° yields the eigenstates of $\hat{X}$:

$$|\pm\rangle = \frac{1}{\sqrt{2}} \left(|0\rangle \pm |1\rangle \right) \tag{2.108}$$

For multipartite states (this could be e.g. two photons A and B), the compact notation $|\psi\rangle_A \otimes |\phi\rangle_B = |\psi\phi\rangle$ is introduced for the following.

A multipartite state is entangled if it cannot be factorized, i.e. the state cannot be written as a product of single-particle states: $|\Psi\rangle_{AB} \neq |\psi\rangle_A \otimes |\phi\rangle_B$. Examples for entangled states are the four Bell states

$$\left|\Phi^{\pm}\right\rangle = \frac{1}{\sqrt{2}} \left(|00\rangle \pm |11\rangle \right) \tag{2.109}$$

$$\left|\Psi^{\pm}\right\rangle = \frac{1}{\sqrt{2}} \left(|01\rangle \pm |10\rangle \right) \tag{2.110}$$

The Bell states are also maximally entangled[23]. Entangled states can be produced experimentally through branched photon cascades (e.g. the decay of the 6^1S_0 state in Ca via 4^1P_1 to 4^1S_0), spontaneous parametric down-conversion in nonlinear crystals, or two-photon interference (see Sec. 2.9). A direct consequence of entangled states is that while the measurement result on each of the sub-systems is *a priori* random, the result on the other sub-system is always perfectly correlated. This also holds in every measurement basis, since

$$\left|\Phi^{+}\right\rangle = \frac{1}{\sqrt{2}} \left(|00\rangle + |11\rangle \right) = \frac{1}{\sqrt{2}} \left(|{+}{+}\rangle + |{-}{-}\rangle \right) \tag{2.111}$$

follows with the definition of $|\pm\rangle$ (similar for the other Bell states). The state is thus entangled in every basis. This is not possible with classical correlations: for example, if the state $|00\rangle$ or $|11\rangle$ is measured in the $\hat{Z}$ basis, the results on both sub-systems are perfectly correlated. In the $\hat{Z}$ basis, however, the results will be random, while for entangled states the results are still perfectly correlated. This is even true for spacetime-like separated measurements: a measurement on system A determines instantaneously the result of the measurement on B. This is what Albert Einstein once called "spooky action at a distance" and leads to the famous EPR paradox (Einstein-Podolsky-Rosen paradox)[24]. Since $\hat{X}$ and $\hat{Z}$ do not commute, it is impossible to measure both observables simultaneously.[14] However, even for spacetime-like separated systems, the measurement results are correlated after a measurement. EPR therefore concluded that quantum mechanics is incomplete and a more complete theory contains hidden (yet undiscovered) variables which determine the results.

EPR introduced requirements a complete theory should fulfill: (1) A theory is realistic if the measurement outcome is fixed before a measurement. (2) A theory is local if measurements outside a systems light cone cannot influence measurements in the system. The question, then, is whether a theory can be both local and realistic, i.e. a local realistic theory with hidden variables.

Suppose a local realistic theory (LRT) has a local hidden parameter set λ, which predetermines the measurement outcomes at A and B. It is only required that this set is normalized (i.e. $\int d\lambda P(\lambda) = 1$). Without loss of generality, the measurements could be detection of photon pairs in any basis along two directions $\vec{\alpha}_{1,2}$ for A and $\vec{\beta}_{1,2}$ for B with outcomes

$$a(\vec{a}_1, \lambda) = a_1 = \pm 1 \tag{2.112}$$
$$a(\vec{a}_2, \lambda) = a_2 = \pm 1 \tag{2.113}$$
$$b(\vec{b}_1, \lambda) = b_1 = \pm 1 \tag{2.114}$$
$$b(\vec{b}_2, \lambda) = b_2 = \pm 1 \tag{2.115}$$

The outcomes correspond to detection $(+1)$ or no detection (-1). The quantity

$$\begin{aligned} S_{\mathrm{LRT}} &= \left| \int d\lambda P(\lambda) \left[(a_1 + a_2) b_1 + (a_2 - a_1) b_2 \right] \right| \leq \\ &\leq \underbrace{\left| \int d\lambda P(\lambda) \right|}_{=1} \underbrace{\left| [(a_1 + a_2) b_1 + (a_2 - a_1) b_2] \right|}_{=2} = 2 \end{aligned} \tag{2.116}$$

Therefore, $S_{\mathrm{LRT}} \leq 2$. This is known as the CHSH (Clauser-Horne-Shimony-Holt) inequality and is an upper bound for any correlation of measurement results within a LRT.

The quantum mechanical measurement directions can be written as $\vec{\alpha}_{1,2}\vec{\sigma}$ and $\vec{\beta}_{1,2}\vec{\sigma}$ with $\vec{\sigma} = (\hat{\sigma}_x, \hat{\sigma}_y, \hat{\sigma}_z)^T$. Choosing the photons to be in state $|\Psi^-\rangle$ and the measurement

[14] This is a consequence of the Heisenberg uncertainty relation.

directions

$$\vec{\alpha}_1 = (0,0,1)^T \tag{2.117}$$
$$\vec{\alpha}_2 = (1,0,0)^T \tag{2.118}$$
$$\vec{\beta}_1 = -\frac{1}{\sqrt{2}}(1,0,1)^T \tag{2.119}$$
$$\vec{\beta}_2 = \frac{1}{\sqrt{2}}(-1,0,1)^T \tag{2.120}$$

yields the expectation values

$$\begin{aligned}\left\langle \Psi^- \middle| \vec{\alpha}_1\vec{\beta}_1 \middle| \Psi^- \right\rangle &= \frac{1}{2}\left\langle 01-10 \middle| \hat{\sigma}_z \otimes \frac{-1}{\sqrt{2}}(\hat{\sigma}_x + \hat{\sigma}_z) \middle| 01-10 \right\rangle = \\ &= \frac{-1}{2\sqrt{2}}\left\langle 01-10 \middle| \hat{\sigma}_z \otimes \hat{\mathbb{1}} \middle| 00-11-01-10 \right\rangle = \\ &= \frac{-1}{2\sqrt{2}}\left\langle 01-10 \middle| \hat{\mathbb{1}} \otimes \hat{\mathbb{1}} \middle| 00+11+01-10 \right\rangle = \\ &= \frac{-1}{2\sqrt{2}}\left(\langle 01-10 | 01-10\rangle + \langle 01-10 | 00+11\rangle\right) = \frac{-1}{\sqrt{2}}\end{aligned} \tag{2.121}$$
$$\left\langle \Psi^- \middle| \vec{\alpha}_1\vec{\beta}_2 \middle| \Psi^- \right\rangle = \frac{-1}{\sqrt{2}} \tag{2.122}$$
$$\left\langle \Psi^- \middle| \vec{\alpha}_2\vec{\beta}_1 \middle| \Psi^- \right\rangle = \frac{-1}{\sqrt{2}} \tag{2.123}$$
$$\left\langle \Psi^- \middle| \vec{\alpha}_2\vec{\beta}_2 \middle| \Psi^- \right\rangle = \frac{1}{\sqrt{2}} \tag{2.124}$$

so the CHSH parameter for this particular setting reads

$$S_{\mathrm{QM}} = \left|\left\langle \vec{\alpha}_1\vec{\beta}_1 \right\rangle + \left\langle \vec{\alpha}_2\vec{\beta}_1 \right\rangle + \left\langle \vec{\alpha}_2\vec{\beta}_2 \right\rangle - \left\langle \vec{\alpha}_1\vec{\beta}_2 \right\rangle\right| = \left|-\frac{1}{\sqrt{2}} - \frac{1}{\sqrt{2}} - \frac{1}{\sqrt{2}} - \frac{1}{\sqrt{2}}\right| = 2\sqrt{2} > 2 \tag{2.125}$$

This shows that quantum mechanics predicts a violation of the CHSH inequality. Therefore, quantum mechanics allows stronger correlations than would be possible with any local realistic theory with (local) hidden variables. This has been verified recently in loophole-free implementations of such tests for local realism[25–28]. It is worth noting, this only forbids local realistic theories. Whether quantum mechanics should be interpreted as a local, non-realistic theory (Copenhagen interpretation) or as a non-local, realistic theory (de Broglie–Bohm theory) remains a philosophical question.

2.11 Applications

2.11.1 Quantum communication

The laws of quantum mechanics allow remarkable opportunities. Harnessing quantum phenomena has countless appclications and promises to revolutionize the field of information processing through quantum communication[29] and quantum computing[30]. Qubits, which have already been introduced in the previous section, are central to quantum information processing. Undoubtedly, the biggest part of quantum communication is quantum

key distribution. This is, however, only a method of generating random strings at distant locations, which can be used for symmetric encryptions as the Advanced Encryption Standard (AES) or the One-Time Pad (OTP). Without going into detail, the latter is information theoretically secure. QKD together with OTP forms quantum cryptography. Hereafter, two QKD protocols are introduced.

The security of QKD is based on fundamental laws of quantum mechanics: no-cloning and the Heisenberg uncertainty relation. The former is a consequence of the linearity of quantum mechanics and can easily be seen by *reductio ad absurdum*. Suppose a unitary operator $\hat{O}$ exists that transforms any arbitrary state $|\psi\phi\rangle$ into $|\psi\psi\rangle$. For $|\psi\rangle = \alpha\,|0\rangle + \beta\,|1\rangle$ with $|\alpha|^2 + |\beta|^2 = 1$ it follows that

$$\hat{O}(\alpha\,|0\phi\rangle + \beta\,|1\phi\rangle) = \alpha\,|00\rangle + \beta\,|11\rangle \neq \alpha^2\,|00\rangle + \alpha\beta\,|01\rangle + \beta\alpha\,|10\rangle + \beta^2\,|11\rangle = |\psi\psi\rangle \tag{2.126}$$

which is fulfilled for any $\alpha \wedge \beta \neq 0, 1$. Therefore, it is impossible to clone any unknown state.[15]

The first QKD protocol was BB84 developed by Charles Bennett and Gilles Brassard in 1984[31]. The scheme uses the polarization states[16] in mutually conjugated bases,[17] e.g. $\hat{X}$ and $\hat{Z}$. The sender (Alice) sends single-photons with a randomly chosen polarization and the receiver (Bob) measures in a randomly chosen basis ($\hat{X} \vee \hat{Z}$). Both mutually agree that each state corresponds to a certain logical bit value. If Bob measures in the eigenbasis of the sent state, his result is perfectly correlated, while if he measures in the conjugated basis the result will be random. Alice and Bob repeat this procedure until they have exchanged enough qubits. After the measurements, Alice and Bob announce publicly through an authenticated channel in which basis the state was encoded or measured, respectively, and keep only events with coinciding bases. This is referred to as key sifting and reduces the number of qubits by 50%. Alice and Bob have now two equal bit strings or keys. Any eavesdropper (Eve) carrying out an intercept-and-resend-attack[18] will introduce errors to this bit string. Eve can only guess Alice's basis choice correctly with 50% probability, so in half of all events she forwards the wrong state to Bob, who has then a chance of 50% to measure the correct state. Suppose Alice sends $|0\rangle$, Eve measures along $\hat{X}$ (i.e. projects onto $|\pm\rangle$) and Bob measures along $\hat{Z}$ (i.e. projects onto $|0\rangle/|1\rangle$):

$$|0\rangle_A \rightarrow \begin{cases} |\langle + \,|\, 0\rangle_E|^2 = \frac{1}{2} \rightarrow \begin{cases} |\langle 0 \,|\, +\rangle_B|^2 = \frac{1}{2} & \text{correct} \\ |\langle 1 \,|\, +\rangle_B|^2 = \frac{1}{2} & \text{false} \end{cases} \\ |\langle - \,|\, 0\rangle_E|^2 = \frac{1}{2} \rightarrow \begin{cases} |\langle 0 \,|\, -\rangle_B|^2 = \frac{1}{2} & \text{correct} \\ |\langle 1 \,|\, -\rangle_B|^2 = \frac{1}{2} & \text{false} \end{cases} \end{cases} \tag{2.127}$$

Thus, this introduces an overall error of 25%. Alice and Bob can simply compare random bit values and estimate this quantum bit error ratio (QBER), which automatically reveals

[15] However, it is possible to clone an unknown state in a known basis, since a projection in the eigenbasis are always deterministic.

[16] The original BB84 protocol was proposed using polarization encoding. However, it works equivalently with any other degree of freedom of light (or technically also with other information carrier).

[17] Two bases are mutually conjugated if the probability of measuring an eigenstate of one basis in the other basis has equal probability for all outcomes. For example the Pauli operators are all mutually conjugated.

[18] Eve intercepts the photons, measures in a randomly chosen basis ($\hat{X} \vee \hat{Z}$) and according to the measurement result, prepares a new state that is forwarded to Bob.

the presence of the eavesdropper. The only assumption was that Eve is bound by the fundamental laws of quantum mechanics (i.e. she can only perform unitary operations), so the security of QKD is guaranteed by quantum physics. Realistic devices, however, differ from their ideal theoretical description, so it is crucial to understand these differences.

It is essential that Alice sends single-photon states, otherwise Eve could store a single-photon from multiphoton pulses in a quantum memory, while blocking single-photon states. Once the basis choices are announced Eve could measure the stored photon and gain full information without introducing any noise. Due to the lack of a practical single-photon source, it is common to make use of weak coherent states (see Sec. 2.4). To reduce the amount of multiphoton states in the Poisson distribution, a low mean photon number $\bar{n} \ll 1$ is required, resulting in most pulses actually being empty (vacuum does not transmit information). While there exist sophisticated protocols that mitigate this effect and allow higher mean photon numbers[32], none of these can outperform a true single-photon source. In addition, the states must be indistinguishable in all degrees of freedom in which the key is not encoded, since measurement operators of other degrees of freedom commute with the polarization measurement operator. Furthermore, it is also possible to extract information from the used hardware, e.g. by analyzing the breakdown flash of single-photon detectors[33], detector blinding[34, 35], or detection efficiency mismatch[36, 37]. Once these sidechannels are known, a patch can be implemented, but this requires careful characterization. Practical devices also have a finite natural error rate, due to imperfect state preparation, basis mismatch, or detector dark counts. Since it is impossible to distinguish an error occurred due to the presence of an eavesdropper from a natural error, one has to attribute all errors to a potential eavesdropper. There exist classical post-processing algorithms which can correct these errors and eliminate any suspected information leakage. This works as long as the mutual information of Alice and Bob is larger than the mutual information of the environment and Bob or Alice.

Of the other QKD protocols the E91 protocol proposed by Artur Ekert in 1991 is described[38]. In this protocol Alice and Bob share a pair of entangled photons. Similar to the tests of local realism (see Sec. 2.10), Alice measures along $\hat{Z}_0$, $\hat{Z}_{22.5}$, and $\hat{Z}_{45}$ and Bob along $\hat{Z}_0$, $\hat{Z}_{22.5}$, and $\hat{Z}_{-22.5}$ ($\hat{Z}_\phi$ denotes the $\hat{Z}$ basis rotated by ϕ). The key is encoded in $\hat{Z}_0$ and the measurement results in $\hat{Z}_{22.5}$, $\hat{Z}_{45}$, and $\hat{Z}_{-22.5}$ have to violate the CHSH inequality. Any attack determines local hidden variables resulting in the CHSH inequality not being violated. This allows for device-independent QKD, where the hardware needs not to be trusted. Fully device-independent QKD can achieve unconditional security with realistic devices.

Other quantum communication protocols include quantum teleportation[39], superdense coding[40], and entanglement swapping[41]. Quantum teleportation allows one to transmit a quantum state from one location to another using an entangled state as a resource. Superdense coding allows one to transmit two classical bit of information with only one qubit, also using a previously shared entangled state as a resource. Entanglement swapping allows one to entangle photons that never interacted.

There have been numerous implementations of QKD in fiber or free space quantum channels[42–44]. Most notably is the recent demonstration of a satellite-to-ground quantum key exchange[45], which holds the record for the longest distance exchange. The other quantum communication protocols mentioned have also been demonstrated experimentally with success[46–48].

2.11.2 Quantum computing

Beyond quantum key distribution, the other key application for a single-photon source is photonic quantum computing[49, 50]. The idea of a quantum computer dates back to Richard Feynman who postulated that a quantum system can simulate the evolution of a quantum system with linear resources. A quantum computation consists of a set of operations on qubits, whose state is readout in the end through a measurement. Single-qubit gates only act on a single qubit. Common single-qubit gates are the Pauli operators. Since $\hat{X}$ flips the computational basis states it is often referred to as logical NOT, analogously to classical computing. $\hat{Z}$ is a phase gate introducing a phase of π between the computational basis states. Another important gate is the hermitian Hadamard gate with the matrix representation

$$\hat{H} = \frac{1}{\sqrt{2}} \begin{pmatrix} 1 & 1 \\ 1 & -1 \end{pmatrix} \tag{2.128}$$

This gate transforms the $\hat{X}$ to $\hat{Z}$ and vice versa and also their basis states.[19] Two-qubit gates act on two qubits, most notable are the SWAP gate (which swaps both qubits) and controlled unitary (CU) gates $\hat{\mathbb{1}} \otimes \hat{U}$, which apply the unitary operation $\hat{U}$ on the target qubit if the control qubit is in state $|1\rangle$ (and the identity if the control qubit is in state $|0\rangle$). All N-qubit operations can be decomposed into single- and two-qubit operations. This is important, as it allows universal quantum computing with only a set of universal single- and two-qubit gates. The Pauli gates and CNOT are an example of a universal set.

The first quantum algorithm was the Deutsch-Jozsa algorithm[51], which determines if a binary function $f_i : \{0, 1\} \to \{0, 1\}$ is balanced or constant. The four cases are

$$f_1(x) = 0 \vee f_2(x) = 1 \forall x \to f_i = \text{constant} \tag{2.129}$$

$$f_3(0) = 0 \wedge f_3(1) = 1 \vee f_4(0) = 1 \wedge f_4(1) = 0 \to f_i = \text{balanced} \tag{2.130}$$

The classical solution is to evaluate f twice, however, using quantum parallelism a quantum computer only requires a single evaluation. The function can be defined as a unitary gate acting on one qubit of a two-qubit state:

$$\hat{U}_{f_i} |x\rangle|w\rangle = |x\rangle|w \oplus f_i(x)\rangle \tag{2.131}$$

where $\oplus$ is the sum modulo 2 (or the XOR operation) and can be implemented with $\hat{\mathbb{1}}$, $\hat{X}$, CNOT, Z-CNOT, for $i = 1, 2, 3, 4$, respectively. After initializing the quantum computer in state $|00\rangle$, the algorithm applies the NOT gate on qubit 2 (giving $|01\rangle$), the Hadamard gate on both qubits, and then $\hat{U}_f$:

$$|\psi\rangle = \hat{U}_f \hat{H}_1 \hat{H}_2 |01\rangle = \frac{1}{2} \hat{U}_f (|00\rangle - |01\rangle + |10\rangle - |11\rangle) = \tag{2.132}$$

$$= \frac{1}{2} (|0, f(0)\rangle - |0, 1 \oplus f(0)\rangle + |1, f(1)\rangle - |1, 1 \oplus f(1)\rangle) \tag{2.133}$$

[19] $\hat{H}\hat{X}\hat{H} = \hat{Z} \leftrightarrow \hat{H}\hat{Z}\hat{H} = \hat{X}$.

The final state of the quantum computer $|\psi\rangle$ can be factorized, depending on f_i:

$$f(0) = f(1)(\text{constant}) : |\psi\rangle = \frac{1}{2}(|0\rangle + |1\rangle)(|f(0)\rangle - |1 \oplus f(0)\rangle) \tag{2.134}$$

$$f(0) = 1 \oplus f(1)(\text{balanced}) : |\psi\rangle = \frac{1}{2}(|0\rangle - |1\rangle)(|f(0)\rangle - |1 \oplus f(0)\rangle) \tag{2.135}$$

Applying the Hadamard gate to qubit 1 transforms its state to $|0\rangle$ or $|1\rangle$ for the constant or balanced function, respectively. A simple measurement in the computational basis then allows one to deterministically distinguish if f is constant or balanced. Note that the function was only applied once. The Deutsch-Jozsa algorithm has been experimentally realized on an ion-trap quantum computer[52]. While this algorithm has no practical use, it was the first to demonstrate quantum advantage. Other algorithms with quantum advantage include Grover's algorithm, which searches through unstructured databases[53] or Shor's algorithm, which finds a prime factor of an integer[54]. The latter has massive implications for conventional public-key cryptography (see Chap. 1). As of today, there exists a large "zoo of quantum algorithms",[20] with 14 algebraic and number theoretic, 34 oracular, and 12 simulation algorithms.

The criteria, a useful quantum computer must fulfill were summarized by David DiVincenzo[55]:

1. A quantum computer needs a set of well-defined and scalable qubits.
2. It must be possible to initialize the quantum computer to a known state (such as $|0\rangle \cdots |0\rangle$).
3. It must be possible to perform quantum operations on the qubits (ideally with a universal set, but application specific sets would be useful as well).
4. The decoherence time must be small compared to the computational time.
5. The final state of the quantum computer (i.e. the result of the computation) has to be able to be readout.

In reality, every physical implementation will have a final error probability, but if all combined fidelities surpass a certain threshold, quantum error correction allows fault-tolerant quantum computing.

There are several approaches to implement these, most notably in ion traps[56], nuclear spins[57], superconducting circuits[58], cavity QED systems[59], and photonic circuits using flying qubits[60]. In spite of large research efforts, none of these systems achieved quantum supremacy, i.e. could not perform a computation beyond the capabilities of a practical classical supercomputer. For a photonic quantum computer, the crucial components are two-qubit gates, since photons do not interact and need a mediator. This non-linear interaction makes it difficult to build photonic two-photon gates. Single-qubit gates, however, are simply phase retarders and are available with linear optical components. The exception is the one-way quantum computer[61], which shifts the difficulty to create large entangled resource states (e.g. cluster states), but then uses only linear optics. This system destroys the computational resource by a measurement after the computation and is hence termed "one-way". A deterministic source of indistinguishable single-photons could easily create large cluster states. The one-way computer has been demonstrated experimentally[62].

[20] http://quantumalgorithmzoo.org/

Chapter 3

Solid-state physics

3.1 Crystal structure and lattices

A crystal consists of ordered atoms in the solid phase with short and long range periodicity.[1] The condensation of atoms into the solid phase through bonding reduces the total energy of the crystal. The stronger the atomic bond, the larger the reduction of the total energy. This results in a more stable crystal, as this energy is required to break the bonds. Ultimately, this is reflected by the crystal melting temperature. The different types of atomic bondings are summarized in Tab. 3.1, where Coulomb or dipole-dipole interactions provide attractive potentials for the bonding of atoms. The Coulomb potential makes metallic, covalent, and ionic bondings relatively strong, with bond energies typically $1 - 10\,\mathrm{eV}$. Transition metals have particularly strong bonds, since they have additional

[1] This chapter is mostly based on notes of Prof. Alexander Högele's lecture on Advanced Solid-State Physics 2014/15 at the Ludwig Maximilians Universität München.

Table 3.1: Summary of crystal bonding types. Metallic bonds have full electron delocalization, where positive atomic kernels reside in a negatively charged electron cloud. This screens the Coulomb potential and reduces the bond energy. Covalent bonds have a partial electron transfer, a shared electron, and the valence states hybridize (e.g. sp^2 in graphene) to maximize the bond energy. Transition metals have metallic and covalent bonds, resulting in particularly large bond energies. Ionic bonds have almost full electron transfer to the more electronagative partner. Hydrogen bonds are dipole-dipole interactions between permanent dipoles, while van der Waals bonds are dipole-dipole interactions between induced dipoles (via charge fluctuations in neutral bonding partners).

Type	Example Allotrope/Compound	Interaction	Typ. E_{bond} [eV]	T_{melt} [K]
Metallic	Li, W/CuSn	Coulomb	$1 - 10$	454 (Li) 3695 (W)
Covalent	Si/GaAs	Coulomb $\sim r^{-1}$	$5 - 10$	1687 (Si) 1511 (GaAs)
Ionic	-/NaCl	Coulomb $\sim r^{-1}$	$5 - 10$	1074 (NaCl)
Hydrogen	H_2O (ice)/-	Dipole $\sim r^{-3}$	0.1	273 (ice)
van der Waals	Ne/CH_4	Dipole $\sim r^{-6}$	$0.01 - 0.1$	24 (Ne) 91 (CH_4)

covalent bonds of the d-shell electrons. Bondings resulting from dipole-dipole interactions are hydrogen bonds (permanent dipoles) and van der Waals bonds (induced dipoles). The bond lengths are typically of the order of a few Å. The attraction potentials are countered by very short-ranged repulsive potentials (e.g. Lennard-Jones potential). This accounts for the Pauli exclusion principle and prevents the collapse of molecules and solids.

In a crystal each atom resides at specific periodic lattice points in space. The crystal structure can be described as a primitive unit cell and the lattice. A primitive unit cell is thereby the smallest volume that, if repeated periodically at the lattice points, forms the crystal. An example is the Wigner-Seitz cell, which is constructed by perpendicular boundaries in the middle of interconnects to next-neighbors. The lattice types can be classified into the 14 Bravais lattices in 3D (1 triclinic, 2 monoclinic, 4 orthorombic, 2 tetragonal, 1 trigonal, 1 hexagonal, and 3 cubic). Each Bravais lattice has a set of basis lattice vectors $(\vec{a}_1, \vec{a}_2, \vec{a}_3)$, such that the complete Bravais lattice is given by all linear combinations of the basis vectors, with the n-th point given by

$$\vec{R}_n = n_1\vec{a}_1 + n_2\vec{a}_2 + n_3\vec{a}_3, \quad n_i \in \mathbb{Z} \tag{3.1}$$

The lattices are invariant under certain symmetry operations, which greatly simplifies calculations of the crystal properties. In 2D, the hexagonal lattice is the most common lattice (see Sec. 3.5). The same chemical elements or compounds can also exist in different crystal structures, or crystal phases, depending on temperature and pressure in the phase diagram. A famous example is carbon which naturally occurs in the forms of diamond, graphite, or lonsdaleite.

The periodic lattice in real space is related to a periodic lattice in reciprocal space through a Fourier transform of the electronic density:

$$\rho(\vec{r}) = \rho(\vec{r} + \vec{R}_n) = \sum_m \rho(\vec{K}_m) e^{i\vec{K}_m\cdot(\vec{r}+\vec{R}_n)} = \sum_m \rho(\vec{K}_m) e^{i\vec{K}_m\cdot\vec{r}} \tag{3.2}$$

where $e^{i\vec{K}_m\cdot\vec{R}_n} = 1$ is implied by the fact that the equation must hold for all n. The translation vector in reciprocal space is given by

$$\vec{K}_m = m_1\vec{b}_1 + m_2\vec{b}_2 + m_3\vec{b}_3, \quad m_i \in \mathbb{Z} \tag{3.3}$$

with the basis lattice vectors of the reciprocal lattice given by

$$\vec{b}_i = 2\pi \frac{\vec{a}_j \times \vec{a}_k}{\vec{a}_i \cdot (\vec{a}_j \times \vec{a}_k)} \tag{3.4}$$

From this definition it follows that $\vec{a}_i \cdot \vec{b}_j = 2\pi\delta_{ij}$. The Wigner-Seitz cell of the reciprocal lattice is called the Brillouin zone and constructed similarly.

3.2 Lattice vibration and phonons

In a crystal, the atoms rest at their lattice positions at $T = 0\,\mathrm{K}$. Crystals with finite temperature, however, exhibit mechanical lattice excitations which give rise to bulk crystal properties such as specific heat, thermal conductivity, and thermal expansion. The atoms move around their equilibrium position in a sum of attractive and repulsive potentials (see Fig. 3.1). The solid-state Hamiltonian is split into a kinetic ion energy term and an effective

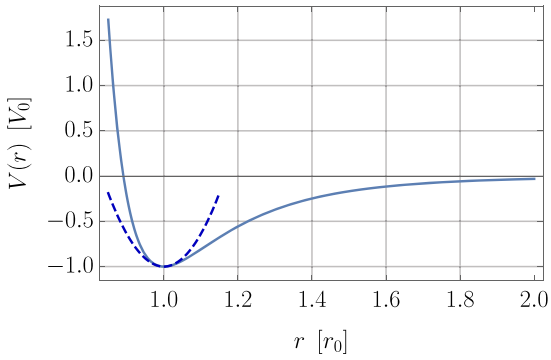

Figure 3.1: Lennard-Jones potential of the form of $V(r) = \frac{A}{r^{12}} - \frac{B}{r^6}$ in units of $V(r_0) = V_0$. The equilibrium position is at $r = r_0$. The dashed curve is the Taylor expansion to second-order and has the form of r^2 (harmonic potential).

ion potential $V_{\text{ion}}^{\text{eff}}(r)$ which incorporates the kinetic electron energy and the electron-ion interaction term.[2] This effective potential can be obtained by a Taylor expansion:

$$V(r)|_{r_0} = \underbrace{V(r_0)}_{\text{set to 0}} + \underbrace{\frac{\partial V}{\partial r}\bigg|_{r_0}}_{\substack{=0 \text{ at} \\ \text{equilibrium} \\ \text{position}}} \frac{(r-r_0)}{1!} + \frac{\partial^2 V}{\partial r^2}\bigg|_{r_0} \frac{(r-r_0)^2}{2!} + \cdots \approx c\frac{(r-r_0)^2}{2} \tag{3.5}$$

where the crystal ground state energy $V(r_0)$ can be set to 0 and the constant c is the second derivative of $V(r)$ at position r_0. The restoring force to this harmonic potential is

$$F(r) = -\nabla_r V(r) = -c(r - r_0) \tag{3.6}$$

To calculate the modes of vibrational excitations, the following approximations have to be made:

1. The coupling potential is harmonic. This neglects next-to-nearest neighbor interactions and is reflected by taking the expansion to its second-degree Taylor polynomial.

2. The ion and electron motion is decoupled, i.e. electrons follow the ions adiabatically and the ions react slowly to the electrons. This can be justified by the Born-Oppenheimer approximation[3] and simplifies the solid-state problem to motion of electrons in a stationary lattice and motion of ions in a uniform charge space.

For simplicity the crystal is modeled as a linear harmonic chain, with every atom connected to its nearest neighbor by a spring with spring constant c (see Fig. 3.2(a), top). The rest position of each atom with mass m is separated by the lattice constant $a = r_0$. The equation of motion for the n-th atom at position u_n is given by

$$m\frac{\partial^2 u_n}{\partial t^2} = -c(u_n - u_{n+1}) - c(u_n - u_{n-1}) = c(u_{n+1} + u_{n-1} - 2u_n) \tag{3.7}$$

which is solved by the plane wave ansatz $u_n(t) = f_n e^{-i(\omega t - q(r - r_n))}$. In 1D the lattice vector r_n is simply na. Substituting this ansatz into the equation of motion yields the dispersion

[2] Spin and external effects are neglected.
[3] Due to the large difference between ion and electron mass this approximation is valid.

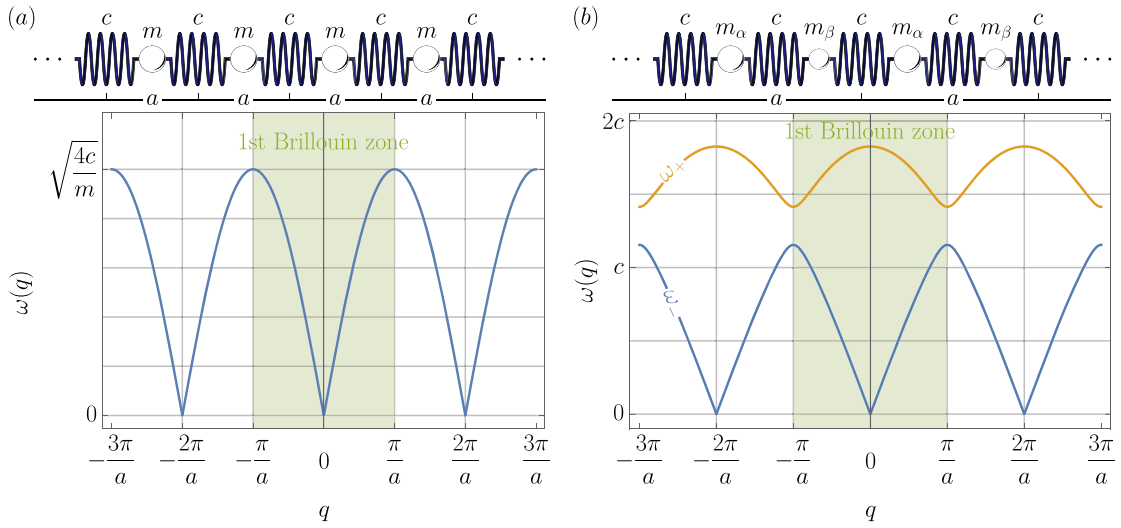

Figure 3.2: (a) The crystal is modeled as a linear harmonic chain. Every atom has mass m and is connected to its nearest neighbor through a spring with spring constant c. The Wigner-Seitz cell (or Brillouin zone) has size a. The dispersion relation (in units of $\sqrt{\frac{4c}{m}}$) has only a single branch. (b) The model can be extended to a primitive unit cell with two different atom species with masses m_α, m_β. Every atom is connected to its nearest neighbor through springs with spring constant c and the Wigner-Seitz cell (or Brillouin zone) of size a contains two atoms. The dispersion relation (in units of c) branches into a high and a low frequency mode. The shown dispersion relation assumes $m_\alpha = 1.5m_\beta$, similar to the mass ratio in a NaCl crystal.

relation of acoustic modes (see Fig. 3.2(a)):

$$-m\omega^2 = c\left(e^{iqa} + e^{-iqa} - 2\right) = -4c\sin^2\left(\frac{qa}{2}\right) \rightsquigarrow \omega(q) = \sqrt{\frac{4c}{m}}\left|\sin\left(\frac{qa}{2}\right)\right| \tag{3.8}$$

The model above assumed there is only a single atom species in the primitive unit cell of the 1D chain. This can be replaced with two different atoms at positions u_n, v_n and with masses m_α, m_β. The atoms are connected again by springs with spring constant c (see Fig. 3.2(b), top). This results in coupled equations of motion:

$$m_\alpha \frac{\partial^2 u_n}{\partial t^2} = -c(u_n - v_n) - c(u_n - v_{n-1}) = c(v_n + v_{n-1} - 2u_n) \tag{3.9}$$

$$m_\beta \frac{\partial^2 n_n}{\partial t^2} = -c(v_n - u_{n+1}) - c(v_n - u_n) = c(u_{n+1} + u_n - 2v_n) \tag{3.10}$$

which is solved by two plane waves with

$$u_n(t) = f_n^\alpha e^{-i(\omega t - q(r - r_n))} \tag{3.11}$$

$$v_n(t) = f_n^\beta e^{-i(\omega t - q(r - r_n))} \tag{3.12}$$

Periodicity allows one to set $f_n^\alpha = f_\alpha \forall n$ and $f_n^\beta = f_\beta \forall n$. Substituting this into the equations of motion yields

$$-m_\alpha\omega^2 f_\alpha = c\left(f_\beta + f_\beta e^{-iqa} - 2f_\alpha\right) \tag{3.13}$$

$$-m_\beta\omega^2 f_\beta = c\left(f_\alpha e^{iqa} + f_\alpha - 2f_\beta\right) \tag{3.14}$$

Table 3.2: Comparison of photons to phonons.

	Photon	Phonon
Frequency	ω_k	ω_q
Energy	$\hbar\omega_k$	$\hbar\omega_q$
Momentum	$\hbar k$	$\hbar q$
Dispersion	$\omega_k = ck$	$\omega_q = \omega(q)$
Polarization	π, σ	LA, TA, LO, TO

Solving these simultaneous equations yields[4]

$$\omega_\pm^2 = c\left(\frac{1}{m_\beta} + \frac{1}{m_\alpha}\right) \pm c\sqrt{\left(\frac{1}{m_\beta} + \frac{1}{m_\alpha}\right)^2 - \frac{4}{m_\alpha m_\beta}\sin^2\left(\frac{qa}{2}\right)} \tag{3.15}$$

The result is two characteristic frequencies $\omega_\pm$. These correspond to two branches in the dispersion relation $\omega_\pm(q)$ (see Fig. 3.2(b)). This links the energy of a vibrational (out-of-equilibrium) excitation ($\sim \omega$) to its quasi-momentum ($\sim q$). Due to the frequency of ω_+ typically being in the infrared spectrum (and thus excitable with infrared light), this mode is referred to as the optical branch and ω_- is referred to as the acoustic branch, as the excitation propagates similar to a sound wave. Due to the periodicity, it is sufficient to consider only the 1st Brillouin zone $-\frac{\pi}{a} \leq q \leq \frac{\pi}{a}$ (reduced scheme).

Even the linear chain has a polarization. In the acoustic branch for $q = 0$ (long wavelength limit), all atoms of the basis are in-phase and the primitive unit cells move against each other (longitudinal acoustic (LA) polarization). The speed of sound is given by the group velocity $v_\mathrm{g} = \frac{\partial\omega_-}{\partial q}\big|_0$. At the edges of the 1st Brillouin zone $v_\mathrm{g} = 0$, so higher frequency waves are standing waves that do not propagate. In this case the lighter atom is at the node of the vibration and does not move (transverse acoustic (TA) polarization). In the optical branch for $q = 0$, the basis atoms move in opposite directions and are π-out-of-phase (longitudinal optical (LO) polarization). Finally, at the edges of the 1st Brillouin zone the heavier atoms are at the nodes of the vibration and do not move (transverse optical (TO) polarization).

In Sec. 2.3, it was derived that confining the electromagnetic field in a finite volume leads to field quantization. Similarly, confining the lattice excitation to finite crystal dimensions leads to quantization of q. This can be described by periodic boundary conditions (e.g. Born-von Karman boundary condition), which implies a discrete set of $q_m = \frac{2\pi}{aN}m$, where N is the number of atoms in the chain. In analogy to the excitation quanta of the electromagnetic field, the photon, a quasi-particle can be introduced for the lattice vibration quanta, the phonon.[5] A comparison of the quantities characterizing photons to the quantities characterizing phonons is given in Tab. 3.2. As will be shown hereafter, phonons can couple to other quasi-particles in a solid. The concept of phonons can also be

[4]Solving Eqn. 3.13 for f_α yields $f_\alpha = c\frac{1+e^{-iqa}}{2c-m_\alpha\omega^2}f_\beta$ which can be substituted into Eqn. 3.14. This yields the equation $-m_\beta\omega^2(-m_\alpha\omega^2 + 2c) = c^2(e^{iqa} + 2 + e^{-iqa}) - 2c(-m_\alpha\omega^2 + 2c)$ which is quadratic in (ω^2) and can thus be easily solved with the pq-formula. The result is shown in Eqn. 3.15.

[5]More generally, the system can be modeled by an ensemble of N decoupled harmonic oscillators by introducing normal coordinates Q_i and P_i which satisfy the commutation relation $[Q_i, P_j] = i\hbar\delta_{ij}$. The Hamiltonian can be rewritten as $\mathcal{H} = \sum_i \frac{p_i^2}{2m} + \frac{1}{2}m\omega^2\sum_{i,j;i=j\pm1}(x_i - x_j)^2 = \sum_k \frac{P_k P_{-k}}{2m} + m\omega_k^2 Q_k Q_{-k}$, which has eigenvalues $E_{n,k} = \hbar\omega_k\left(n + \frac{1}{2}\right)$.

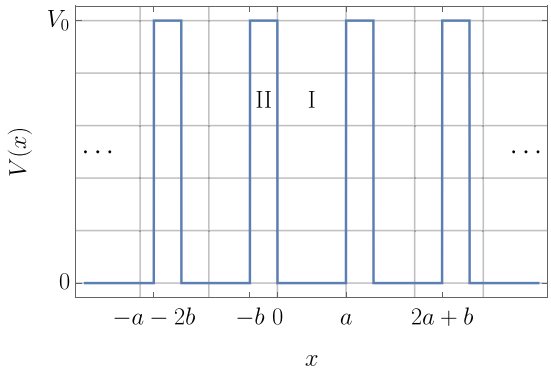

Figure 3.3: The Kronig-Penney potential has the form of square wells with $V(x) = 0$ for $0 < x < a$ (region I) and $V(x) = V_0$ for $-b < x < 0$ (region II), and is periodically repeated.

used to quantitatively describe phenomena like specific heat, thermal expansion, thermal conductivity, and interactions of lattice excitations (phonon-phonon coupling).

3.3 Electronic band structure

Simple molecules such as H_2 with two electrons can be calculated relatively easily, even though no analytical solution exists. In contrast, $1\,\mathrm{cm}^3$ of Si contains $\sim 2 \times 10^{23}$ valence electrons, a many-body problem impossible to solve, since the wavefunction of each electron has contributions from those of all others. Solid-state physics makes two central assumptions to simplify this problem: First, the independent electron approximation, which assumes that the electron wavefunction can be separated into single-electron wavefunctions with electrons in an effective (average) potential. Second, this effective potential is periodic, which is known as Bloch's theorem and justified by the periodic structure of crystalline materials. The crystal electrons with mass $m = m_\mathrm{e}$ are then described by Bloch wavefunctions $\psi(\vec{k}, \vec{r}) = e^{i\vec{k}\cdot\vec{r}} u_{\vec{k}}(\vec{r})$, which are eigenstates of the Hamiltonian

$$\mathcal{H} = -\frac{\hbar^2 \nabla^2_{\vec{r}}}{2m} + V(\vec{r}) = -\frac{\hbar^2 \nabla^2_{\vec{r}}}{2m} + V(\vec{r} + \vec{R}_n) \tag{3.16}$$

The amplitude function has the periodicity of the lattice: $u_{\vec{k}}(\vec{r}) = u_{\vec{k}}(\vec{r} + \vec{R}_n)$. The dispersion of the energy eigenvalues of the Hamiltonian is described by the band structure. For a simple periodic potential in 1D consisting of square wells of width a, periodicity $a+b$, and a barrier height of V_0 (see Fig. 3.3), this can be calculated with the Kronig-Penney model. The time-independent Schrödinger equation $\mathcal{H}\psi = E\psi$ can be written as

$$\begin{aligned} \psi'' + \frac{2mE}{\hbar^2}\psi = 0 \qquad & 0 < x < a \\ \psi'' + \frac{2m(E - V_0)}{\hbar^2}\psi = 0 \qquad & -b < x < 0 \end{aligned} \tag{3.17}$$

Assuming $E < V_0$ the definitions $\alpha^2 = \frac{2mE}{\hbar^2}$ and $\beta^2 = \frac{2m(E-V_0)}{\hbar^2}$ can be made. According to Bloch's theorem the wavefunction can be written as

$$\psi(x) = u_K(x) e^{iKx} \tag{3.18}$$

Differentiating this twice yields

$$\psi'(x) = u'_K(x)e^{iKx} + iKu_K(x)e^{iKx} \tag{3.19}$$
$$\psi''(x) = u''_K(x)e^{iKx} + 2iKu'_K(x) - K^2u_K(x)e^{iKx} \tag{3.20}$$

Substituting this into the Schrödinger equation yields

$$\begin{aligned}(\alpha^2 - K^2)u_{K,\mathrm{I}}(x) + 2iKu'_{K,\mathrm{I}}(x) + u''_{K,\mathrm{I}}(x) = 0\\ -(\beta^2 + K^2)u_{K,\mathrm{II}}(x) + 2iKu'_{K,\mathrm{II}}(x) + u''_{K,\mathrm{II}}(x) = 0\end{aligned} \tag{3.21}$$

For the Bloch amplitude the ansatz $u_K(x) = e^{mx}$ can be made, so

$$\begin{aligned}(\alpha^2 - K^2) + 2imK + m^2 = 0 \rightsquigarrow m_\pm = -iK \pm i\alpha\\ -(\beta^2 + K^2) + 2imK + m^2 = 0 \rightsquigarrow m_\pm = -iK \pm \beta\end{aligned} \tag{3.22}$$

The general solution is then given by

$$\begin{aligned}u_{K,\mathrm{I}}(x) = A_+e^{i(\alpha-K)x} + A_-e^{-i(\alpha+K)x}\\ u_{K,\mathrm{II}}(x) = B_+e^{(\beta-iK)x} + B_-e^{-(\beta+iK)x}\end{aligned} \tag{3.23}$$

The constants A_i and B_i can be obtained by using the boundary conditions:

$$u_{K,\mathrm{I}}(0) = u_{K,\mathrm{II}}(0) \rightsquigarrow A_+ + A_- = B_+ + B_- \tag{3.24}$$
$$u'_{K,\mathrm{I}}(0) = u'_{K,\mathrm{II}}(0) \rightsquigarrow i(\alpha - K)A_+ - i(\alpha + K)A_- = (\beta - iK)B_+ - (\beta + iK)B_- \tag{3.25}$$
$$u_{K,\mathrm{I}}(a) = u_{K,\mathrm{II}}(-b) \rightsquigarrow A_+e^{i(\alpha-K)a} + A_-e^{-i(\alpha+K)a} = B_+e^{-(\beta-iK)b} + B_-e^{(\beta+iK)b} \tag{3.26}$$
$$\begin{aligned}u'_{K,\mathrm{I}}(a) = u'_{K,\mathrm{II}}(-b) \rightsquigarrow i(\alpha - K)A_+e^{i(\alpha-K)a} - i(\alpha + K)A_-e^{-i(\alpha+K)a} =\\ = (\beta - iK)B_+e^{-(\beta-iK)b} - (\beta + iK)B_-e^{(\beta+iK)b}\end{aligned} \tag{3.27}$$

which looks complicated at first, however, with the definitions

$$c_1 = i(\alpha - K),\ c_2 = -i(\alpha + K),\ c_3 = \beta - iK,\ c_4 = -(\beta + iK) \tag{3.28}$$

it can be rewritten into

$$\begin{pmatrix} 1 & 1 & -1 & -1\\ c_1 & c_2 & -c_3 & -c_4\\ e^{c_1a} & e^{c_2a} & -e^{-c_3b} & -e^{-c_4b}\\ c_1e^{c_1a} & c_2e^{c_2a} & -c_3e^{-c_3b} & -c_4e^{-c_4b}\end{pmatrix}\begin{pmatrix}A_+\\A_-\\B_+\\B_-\end{pmatrix} = \begin{pmatrix}0\\0\\0\\0\end{pmatrix} \tag{3.29}$$

These simultaneous equations have a non-trivial solution if and only if the determinant of the matrix is 0:

$$\det\begin{vmatrix} 1 & 1 & 1 & 1\\ c_1 & c_2 & c_3 & c_4\\ e^{c_1a} & e^{c_2a} & e^{-c_3b} & e^{-c_4b}\\ c_1e^{c_1a} & c_2e^{c_2a} & c_3e^{-c_3b} & c_4e^{-c_4b}\end{vmatrix} \stackrel{!}{=} 0 \tag{3.30}$$

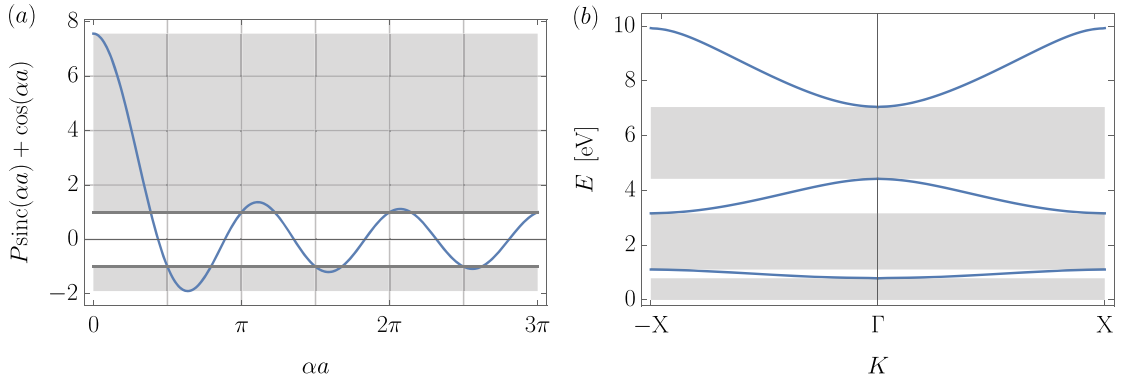

Figure 3.4: (a) Eqn. 3.33 as a function of αa. If $|P\,\mathrm{sinc}(\alpha a) + \cos(\alpha a)| \geq 1$ the electron wavefunction does not exist (gray-shaded area). Since $\alpha^2 = \frac{2mE}{\hbar^2}$ this limits E to certain values. Here $a = 5\,\text{Å}$, $b = 1\,\text{Å}$, $V_0 = 10\,\text{eV}$, and $m = 9.109 \times 10^{-31}\,\text{kg} \rightsquigarrow P = 6.562$. (b) The resulting band structure shows gaps with forbidden energy values. The band edges occur at high-symmetry points of the lattice, namely at the center of the Brillouin zone Γ ($K = 0$), or at the Brillouin zone edges ±X ($K = \pm\frac{\pi}{a+b}$), where $P\,\mathrm{sinc}(\alpha a) + \cos(\alpha a) = \pm 1$.

It is helpful to evaluate this with a symbolic simultaneous equation solver, leading to the equation

$$\frac{\beta^2 - \alpha^2}{2\alpha\beta}\sin(\alpha a)\sinh(\beta b) + \cos(\alpha a)\cosh(\beta b) = \cos(Ka + Kb) \tag{3.31}$$

Since $-1 \leq \cos(Ka + Kb) \leq 1$ it is obvious there exist certain values of E for which Eqn. 3.31 is not satisfied, so Eqn. 3.29 has no solution. The electron wavefunction does not exist in these cases. In the limit $V_0 \gg E$ one finds $b \to 0$ (this is to keep the barrier strength $V_0 b$ finite), so

$$\beta^2 - \alpha^2 = \frac{2m}{\hbar^2}(V_0 - 2E) \approx \frac{2mV_0}{\hbar^2},\ \sinh(\beta b) \to \beta b,\ \cosh(\beta b) \to 1 \tag{3.32}$$

Eqn. 3.31 simplifies to

$$\frac{mV_0}{\hbar^2\alpha\beta}\sin(\alpha a)\beta b + \cos(\alpha a) = \frac{mV_0 ab}{\hbar^2}\,\mathrm{sinc}(\alpha a) + \cos(\alpha a) = \cos(Ka + Kb) \tag{3.33}$$

The factor $P = \frac{mV_0 ab}{\hbar^2}$ is called the barrier scattering power and is a measure of the attraction of the crystal electrons to the ions on the lattice sites. Eqn. 3.33 is plotted in Fig. 3.4(a) and shows that for certain αa there exists no solution to Eqn. 3.29. Since $\alpha^2 = \frac{2mE}{\hbar^2}$, the electron wavefunction does not exist for all values of E. These forbidden energies give rise to band gaps in the band structure (see Fig. 3.4(b)).

Apart from the Kronig-Penney model, there exist many other methods to calculate the band structure, such as tight-binding or quasi-free electrons. Modern calculations often use the pseudopotential method, with the most sophisticated *ab initio* pseudopotentials being able to predict static ground-state properties of very complex crystals (see also density functional theory in Sec. 5.1.1).

The band structure describes the energy dispersion relation $E(K)$ of crystal electrons and is a result of the symmetric crystal geometry. The last (with electrons) occupied

Table 3.3: Comparison of various band gaps[63].

Material	E_g [eV]	Nature of the band gap
Diamond (insulator)	5.47	indirect
Graphene (semi-metal)	0	-
Si	1.12	indirect
Ge	0.66	indirect
GaP	2.26	indirect
GaAs	1.43	direct
InP	1.35	direct
CdS	2.42	direct

energy band is called the valence band (VB), the first unoccupied energy band is called the conduction band (CB). The energy difference between both bands is called the band gap. The band structure is non-parabolic in general, however, near the band edges the dispersion relation of the valence/conduction band can be Taylor expanded into a parabolic dispersion:

$$E(K) = E_{\mathrm{v,c}} + \underbrace{\frac{\partial E_{\mathrm{v,c}}}{\partial K}}_{=0} K + \frac{\partial^2 E_{\mathrm{v,c}}}{\partial K^2}\frac{K^2}{2} + \cdots \approx E_{\mathrm{v,c}} + \frac{\hbar^2 K^2}{2m^*} \tag{3.34}$$

with $\frac{1}{m^*} = \frac{\partial^2 E_{\mathrm{v,c}}}{\hbar^2 \partial K^2}$. States near the band edges, which are the most relevant in semiconductors as they are responsible for optical and transport phenomena, can thus be treated as free electrons with an effective mass m^* (all Coulomb interactions with the crystal potential are contained within m^*).

The Fermi energy E_F is the energy up to which all states are occupied with electrons at zero temperature. For metals the Fermi energy falls within the conduction band, while for semiconductors it lies within the band gap E_g. This means at $T = 0\,\mathrm{K}$ all semiconductors are insulators, as there is no electron in the conduction band contributing to a current. At finite temperature electrons are promoted from the valence to the conduction band,[6] leaving behind positively charged vacancies or holes in the valence band. Electron-hole pairs can form hydrogen-like bound states and these quasi-particles are referred to as excitons. They can transport energy without transporting net charge and are useful for the description of charge transport and optical phenomena.

Semiconductors have typical band gaps of the order of $1 - 2\,\mathrm{eV}$, while insulators have band gaps $> 3\,\mathrm{eV}$ (see Tab. 3.3). An important classification of semiconductors is whether their band gap is direct or indirect. For a direct band gap semiconductor (like GaAs) the conduction band minimum and valence band maximum are at the same point in the 1st Brillouin zone (see Fig. 3.5(a)). Indirect semiconductors (like Si) in turn have their CB minimum and VB maximum at different points in the 1st Brillouin zone (see Fig. 3.5(b)). One consequence is that electron-hole recombination requires a phonon for momentum conservation, which makes recombination a second-order process. Thus, indirect semiconductors are inefficient light emitters. Excitons coupling to phonons give rise to a zero-phonon line (ZPL) and the phonon sideband (PSB) in the optical emission spectrum

[6] In general, the band gap is temperature dependent, with the empirical expression $E_g(T) = E_g(0) - \frac{\alpha T^2}{\beta + T}$, where α and β are material constants.

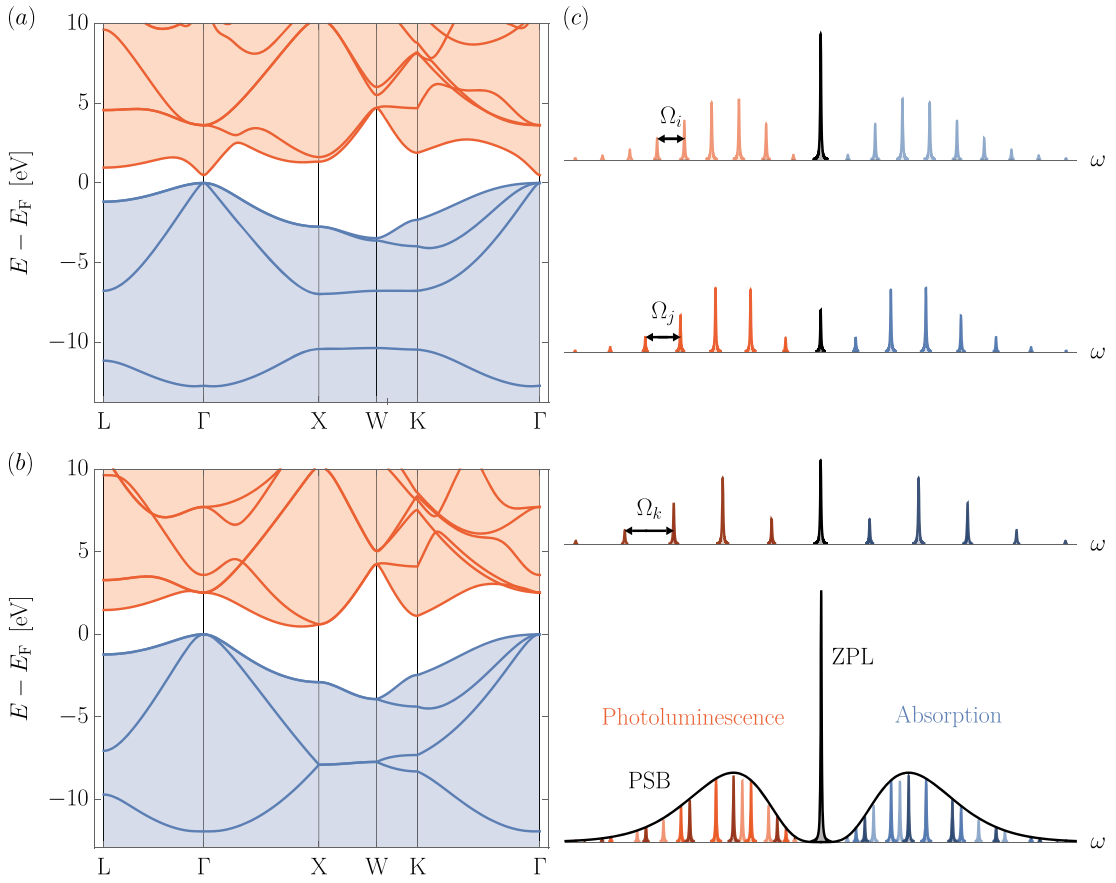

Figure 3.5: (a) Band structure of GaAs routed along the high-symmetry points in the Brillouin zone. GaAs is a direct band gap semiconductor. The CB (blue) maximum and VB (red) minimum are both at the Γ point. (b) Band structure of Si routed along the high-symmetry points in the Brillouin zone. Si is an indirect band gap semiconductor. The CB (blue) maximum is at the Γ point, while the VB (red) minimum is near the X point. Both band structures have been calculated using density functional theory (see Sec. 5.1.1). (c) The optical absorption and emission spectra show sidebands due to exciton-phonon coupling. Each phonon mode i, j, k is quantized, but the overlap of all phonon modes seems continuous. The shape of the zero-phonon line is that of a Lorentzian, while the phonon modes are Poisson distributed.

(see Fig. 3.5(c)). The amount of emission into the ZPL is characterized by the Debye-Waller factor α, so $(1 - \alpha)$ of the emission happens via phonons.

It is worth noting that there is a difference in electronic and optical band gap, precisely the exciton binding energy. While in most semiconductors this is very small (i.e. there is little interaction between electrons and holes), in two-dimensional semiconductors (see Sec. 3.5) this exciton binding energy can be large ($\sim 1\,\mathrm{eV}$)[64].

3.4 Defects

So far, only pristine crystals with perfect symmetry and periodicity have been considered. Realistic crystals, however, always have a finite defect density. Defects can be classified into bulk, planar, line, and point defects, of which only the latter are considered hereafter. Point defects can be further classified into

1. Vacancies: A vacancy is a missing atom in the lattice.

2. Substitutional defects: A substitutional defect is a different atom species replacing an atom at a lattice point.

3. Interstitial defects: An interstitial defect is an additional atom in between lattice points. This can be a crystal atom or another element. In most crystals, the defect formation energy for interstitial defects is large, so these defects play only a minor role.

4. Antisites: In compounds, an antisite defect is an atom of one species occupying the lattice point where usually another atom species is located.

5. Point-like complexes: There can also be combinations of the above, forming point-like complexes. A famous example is the NV-center in diamond, which is a vacancy and a neighboring carbon atom replaced with a nitrogen atom.

For point defects the following notation (similar to the Kröger-Vink notation) is introduced: $\mathrm{D}_{\mathrm{A}}^{c}$, where D is the substitutional atom (V for vacancy) replacing A at its lattice point and c is the charge of the defect. For example a negatively charged arsenic vacancy in GaAs has the notation $\mathrm{V}_{\mathrm{As}}^{-1}$ or an indium atom replacing a gallium atom has the notation $\mathrm{In}_{\mathrm{Ga}}^{0}$. Complexes are simply concatenated and for allotropes no index is required (hence NV in diamond). Defects without a specific charge state are assumed to be neutral.

The fundamental defect concentration at temperature T can be calculated by minimizing the Gibbs free energy of the system, given by

$$G_{\mathrm{F}} = H - TS \tag{3.35}$$

The method can be applied to generalized defects, but for simplicity a vacancy is considered hereafter. The enthalpy $H = E_{\mathrm{f}} + pV$ has the positive terms of the defect formation energy, E_{f}, and the work required to move an atom initially occupying the lattice site to the surface, pV. These terms prevent defect formation. The entropy $S = S_{\mathrm{v}} + S_{\mathrm{mix}}$ includes the vacancy entropy, S_{v}, and crystal entropy due to the disorder introduced by the vacancy, S_{mix}. The entropy promotes defect formation. For a crystal containing N_{v} vacancies and N atoms (i.e. it has $N + N_{\mathrm{v}}$ lattice sites) the Gibbs free energy is given by

$$\begin{aligned} G_{\mathrm{F}} &= N_{\mathrm{v}}E_{\mathrm{f}} + p\Omega N_{\mathrm{v}} - T\left(s_{\mathrm{v}}N_{\mathrm{v}} - k_{\mathrm{B}}\left[N\log\left(\frac{N}{N+N_{\mathrm{v}}}\right) + N_{\mathrm{v}}\log\left(\frac{N_{\mathrm{v}}}{N+N_{\mathrm{v}}}\right)\right]\right) = \\ &= N_{\mathrm{v}}(E_{\mathrm{f}} + p\Omega - Ts_{\mathrm{v}}) - k_{\mathrm{B}}(N(\log(N) - \log(N+N_{\mathrm{v}})) + N_{\mathrm{v}}(\log(N_{\mathrm{v}}) - \log(N+N_{\mathrm{v}})) \end{aligned} \tag{3.36}$$

where Ω is the volume of a lattice site and s_{v} is the entropy change due to a formation of a single vacancy. In the thermodynamic equilibrium

$$\frac{\partial G_{\mathrm{F}}}{\partial N_{\mathrm{v}}} = E_{\mathrm{f}} + p\Omega - Ts_{\mathrm{v}} + k_{\mathrm{B}}T\log\left(\frac{N_{\mathrm{v}}}{N+N_{\mathrm{v}}}\right) \stackrel{!}{=} 0 \tag{3.37}$$

Since the concentration of vacancies is $c_{\mathrm{v}} = \frac{N_{\mathrm{v}}}{N+N_{\mathrm{v}}}$, the concentration is given by

$$c_{\mathrm{v}} = e^{\frac{s_{\mathrm{v}}}{k_{\mathrm{B}}}} e^{\frac{p\Omega}{k_{\mathrm{B}}T}} e^{-\frac{E_{\mathrm{f}}}{k_{\mathrm{B}}T}} \approx e^{-\frac{E_{\mathrm{f}}}{k_{\mathrm{B}}T}} \tag{3.38}$$

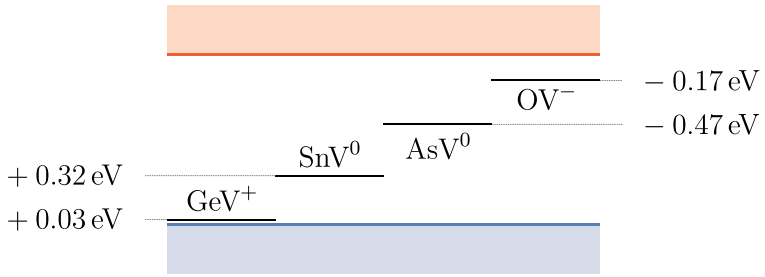

Figure 3.6: Electronic structure of defects in silicon. The energy difference is measured from the nearest band edge[65]. The GeV^+ defect has a shallow level in the band structure, since its energy difference from the conduction band is on the order of the thermal energy k_BT at room temperature. Since the energy levels of the other defects are well isolated from the band edges, these defects are called deep defects.

In most cases, the first two exponential factors do not contribute significantly, so they can be set to 1. This defect concentration is a fundamental limit, and every crystal has at least this defect concentration.[7] At room temperature, defect concentrations are much higher than this fundamental limit and the type of defect, as well as the defect concentration depends on the crystal fabrication technique and growth conditions.

Many electrical and optical crystal properties, such as electrical charge transport and emission spectra, are influenced by defects. Defects or impurities can also be beneficial and are often artificially introduced (referred to as doping). In a Si crystal a silicon atom can be replaced by an arsenic atom, adding an extra electron to the conduction band (n-type doping). In contrast, if a Si atom is replaced by a boron atom an extra hole is added to the valence band (p-type doping). Thus, it is possible to tailor electrical properties of a semiconductor. Defects can also introduce new energy levels into the band gap. In case of As_{Si} or $Ge_{Si}V_{Si}^+$ these levels are close to the band edges, which is why these are shallow defects (see Fig. 3.6). Other defects can also have deep levels, which are well isolated from the bands (e.g. N_{Si} or $As_{Si}V_{Si}$[65]). Quantitatively, shallow and deep defects are characterized by the energy difference between the band edges and the defect states. This energy difference is small (large) compared to the thermal energy k_BT for shallow (deep) defects. Deep defect states act as local charge carrier traps. This is exploited for single-photon generation, when the trapped charge carrier is excited from the ground to an excited state, and as the excited state decays, a single-photon is emitted (see Chap. 4).

The introduced defect levels can be quantitatively understood even with the simple Kronig-Penney model (see Sec. 3.3), where the defect alters the potential locally. A substitutional defect makes a particular well deeper or shallower and/or changes the width of a particular potential well or barrier. In general, defects distort the crystal lattice locally, meaning that the bond lengths around the defect change to minimize the total energy of the crystal. For example, the oxygen atom of the O_S defect in a WS_2 crystal relaxes toward the transition metal. The W – O bond length is 2.07 Å, while the W – S bond length is 2.42 Å. Practically, however, defect levels are calculated using density functional theory (as has been done for the O_S defect in WS_2[66], for details see Chap. 8).

[7] Defects can also form spontaneously and in the thermodynamic equilibrium $c_v(N + N_v)$ defects will have formed.

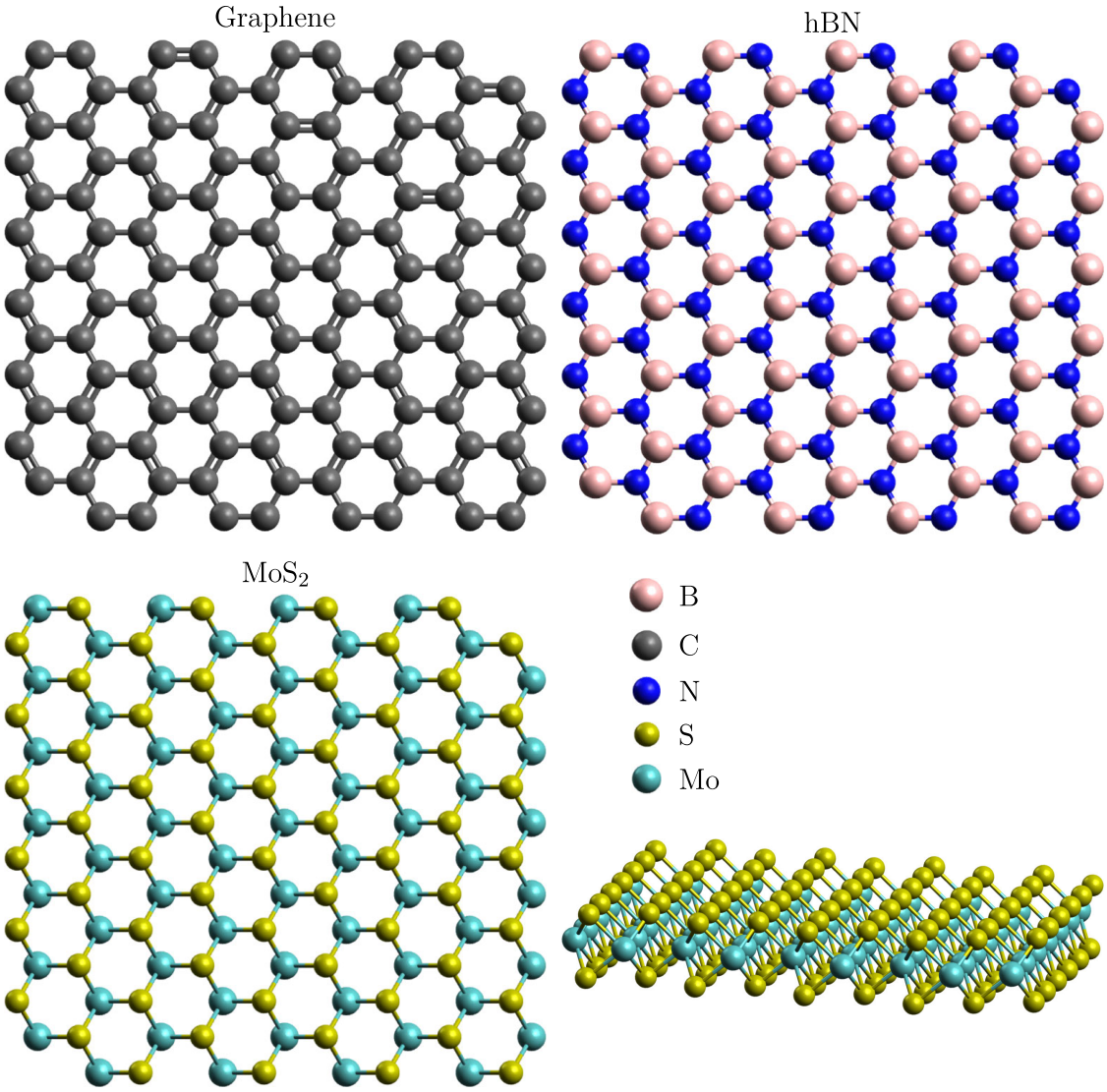

Figure 3.7: Atomic structure of graphene, hBN, and MoS_2. Atoms in monolayer graphene and hBN are all in one plane. For TMDs (like MoS_2) a monolayer consists of three atomic layers.

3.5 2D materials

Condensed matter physics is the most active field within physics today.[8] In recent decades low-dimensional structures, such as quantum wells, wires, and dots became of broad interest. A new class of materials emerged in 2004, when Konstantin Novoselov and Andre Geim isolated singlelayer carbon sheets[67]. This work inspired the field of two-dimensional (2D) materials and was awarded with the 2010 Nobel prize in physics.[9] In a 2D material, the atoms are covalently bonded in-plane, while multiple layers are stacked with van der Waals bonds. The ultimate limit is the monolayer which consists of only one atomic layer. The 2D geometry restricts the motion of electrons essentially in-plane with little charge transfer between multiple layers. This allows for unique properties and applications, some of which are introduced in the following section. A more detailed overview on the field of

[8] From 2012 to 2018 condensed matter physics had continuously the most submissions to the arXiv.
[9] https://www.nobelprize.org/prizes/physics/2010/summary/

2D materials can be found in recent reviews[68–70].

3.5.1 Graphene

The most widely studied 2D material is graphene, a stable carbon allotrope in which carbon atoms are packed in an hexagonal (honeycomb) lattice (see Fig. 3.7). Graphene is known for its record intrinsic electron mobility, exceeding $2 \times 10^5\,\mathrm{cm^2V{-}1s^{-1}}$[71], benefiting electrical applications of graphene. The electron transport in graphene is governed by the relativistic Dirac equation, with the charge carriers showing phenomena otherwise characteristic for two-dimensional Dirac fermions[72]. A record-breaking thermal conductivity up to $5.30 \times 10^3\,\mathrm{W\,mK^{-1}}$ further benefits electrical applications, as it allows for excellent thermal management[73]. The electrical and thermal conductivity comes together with optical transparency[74], opening up countless applications, including displays or defrosters in aircraft windshields. Another particularly elegant application is DNA sequencing, where a DNA molecule passing through a nanopore in graphene alters ionic currents running through graphene[75]. Graphene's large mechanical strength is manifested in a giant Young's modulus of 1 TPa[76]. The quantum hall effect is also observable in graphene, even at room temperature[77]. All these unique features earned graphene the reputation of a wonder material. However, graphene's applications in photonics and optoelectronics are limited due to the semi-metallic zero band gap nature. While band gap engineering can open a small band gap (for example a band gap opens in bilayer graphene when an electric field is applied[78], or in monolayer graphene after nano-patterning[79]), many other 2D materials have an intrinsically non-zero band gap.

3.5.2 Transition metal dichalcogenides

Transition metal dichalcogenides (TMDs) are semiconducting 2D materials with band gaps in the visible spectrum ($\sim 1.6 - 2.0\,\mathrm{eV}$). TMDs are compounds of the form MX_2, where M is a transition metal (M=Mo, W, ...) and X is from the group of the chalcogenides (X=S, Se, ...). Monolayers exist, however, unlike graphene (which is truly one atomic layer), TMDs crystallize in an X−M−X sandwich structure (see Fig. 3.7). The M−X bonds are covalent bonds. Monolayer MoS_2 is an excellent material for atomically thin field-effect transistors, with current ON/OFF ratios exceeding 10^8 and carrier mobilities $> 200\,\mathrm{cm^2V^{-1}s^{-1}}$[80]. Possible applications also include valleytronics, which exploit the fact that some materials have multiple minima in the conduction band at different points in k-space, making these valleys individually addressable with circularly polarized light[81]. Interestingly, TMDs transition from indirect to direct band gap semiconductors when thinning from bi- to monolayer thickness[82–84]. This can be observed either with theoretical band structure calculations (see Fig. 3.8(a, b)), or in an experiment, when comparing the photoluminescence from a mono- to a bilayer (see Fig. 3.8(c)). Owing to the direct band gap transition, many monolayer TMDs are excellent light emitters[85] (see Fig. 3.8(d)), allowing for atomically thin active laser materials in semiconductor nanocavity lasers[86]. TMDs also allow for a variety of quasi-particles beyond excitons, most notably trions or charged excitons[87] and biexcitons or bound excitons[88]. Excitons have a typical Bohr radius $\sim 1\,\mathrm{nm}$. Trions and biexcitons are larger with typical Bohr radii $\sim 2 - 3$ and $\sim 4 - 5\,\mathrm{nm}$, respectively. Recently, even charged biexcitons have been demonstrated, and it was possible to switch between charged and neutral biexciton electrically[89]. This provides routes toward control of many-body quantum phenomena in TMDs. Strong exciton-polariton coupling at room temperature has been realized in monolayer TMDs

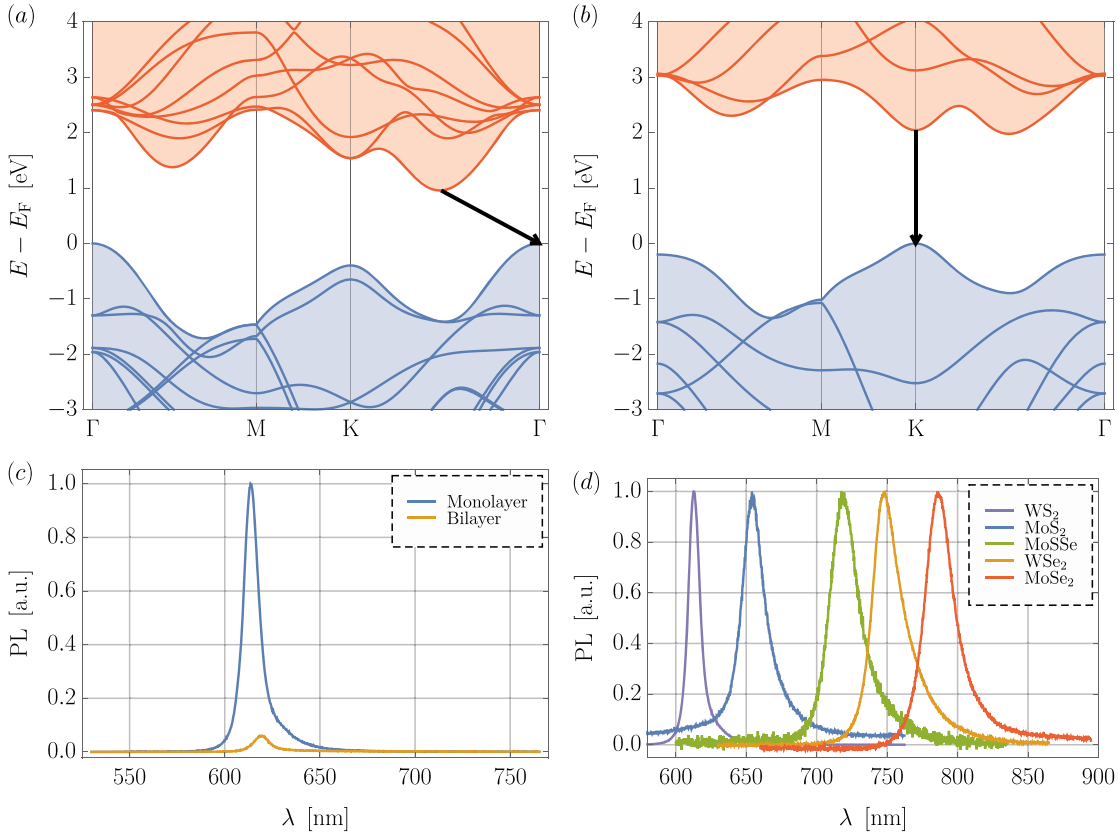

Figure 3.8: (a) The band structure of bilayer WS_2 routed along the high-symmetry points in the Brillouin zone reveals an indirect band gap transition. (b) The band structure of monolayer WS_2 routed along the high-symmetry points in the Brillouin zone reveals a direct band gap transition. (c) Photoluminescence spectrum of mono- and bilayer WS_2. With the exciton peak at 613 nm, the monolayer emits 20× stronger than the bilayer with its exciton peak at 619 nm. The lines are asymmetric due to the presence of excitons and trions and the trion binding energy red-shifts its emission peak. The much stronger photoluminescence is explained by the fact that WS_2 transitions to a direct band gap semiconductor when thinned down to a monolayer. (d) Photoluminescence spectrum of various TMDs measured at room temperature.

embedded within monolithic cavities[90, 91]. This provides a path towards exploitation of nonlinear effects and polaritonic devices. While the mechanical stability is inferior to graphene, TMDs still have a remarkably large Young's modulus around 270 GPa[92], exceeding that of steel. Closely related to the X−M−X family are the X−M−Y TMDs, which have one of the chalcogen layers replaced with a different chalcogen layer.[10] An example is MoSSe, which has similar properties to MoS_2 and $MoSe_2$, but its band gap is between both.

3.5.3 Hexagonal boron nitride

Hexagonal boron nitride (hBN) is a 2D material with a similar atomic structure to graphene, but with alternating boron and nitrogen atoms (see Fig. 3.7). The mechanical and thermal properties of hBN are similar to that of graphene[93], resulting in a large

[10] Due to the two sides, these are also called Janus monolayers, named after the roman god with two faces.

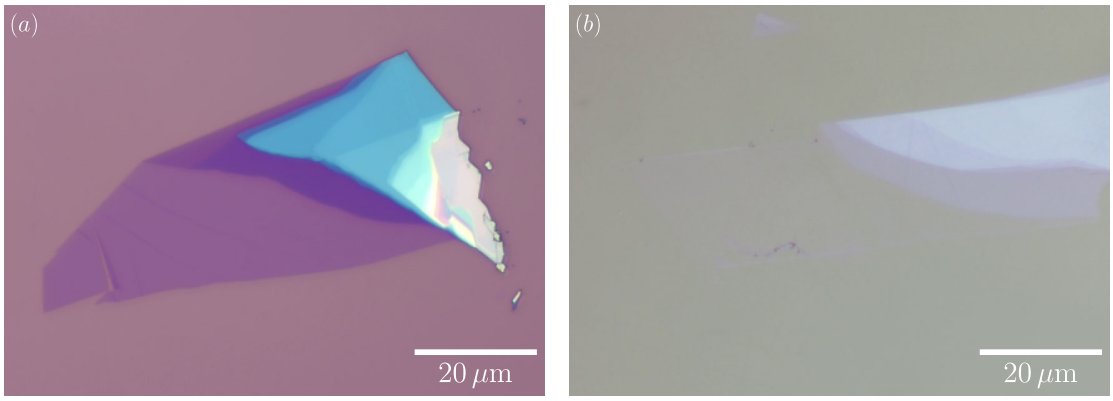

Figure 3.9: (a) Microscope image of a MoS_2 monolayer on 270 nm SiO_2 on Si. The monolayer is visible as the lightest shade of purple. The next darker shades are a bilayer, trilayer, and so on. (b) On a 350 μm SiC substrate, the monolayer is barely visible and has almost no optical contrast.

thermal and chemical stability. Its electrical properties, however, differ considerably. The band gap of hBN is 6 eV[94], which is why hBN is often used as an insulating layer in 2D heterostructures, where multiple 2D materials are stacked together[95]. In a graphene-hBN-metal heterostructure it was possible to probe the ultimate plasmon confinement limit down to the length scale of just one atom[96]. Encapsulating monolayer TMDs suppresses inhomogeneous broadening of the exciton linewidth[97], or provides excellent protection from any coupling to the environment in field-effect transistors[98]. The thermal conductivity is very large for an insulating material and varies with layer number[99], meaning that hBN-graphene heterostructures still have a large combined thermal conductivity. Owing to the large band gap, defect levels in hBN are deep and well isolated from the band edges, which allows for room temperature quantum emission[100]. In contrast, single-photon emission in TMDs requires cryogenic cooling[101–105]. The optical contrast of hBN is poor with a zero-crossing in the visible spectrum, making the fabrication of monolayer particularly difficult[106].

3.5.4 Fabrication

Beyond graphene, TMDs, and hBN there are many more 2D materials, with 1500+ materials computationally predicted[107], many of which are yet to be synthesized. The most common techniques to fabricate mono- or multilayer 2D materials are mechanical exfoliation and chemical and physical vapor deposition (CVD and PVD). Mechanical exfoliation utilizes shear forces to break the van der Waals bonds. Since the in-plane covalent bonds are much stronger than these bonds stacking the layers together, crystals predominantly break between layers. Using successive thinning with adhesive tapes, Novoselov *et al.* demonstrated that with this fairly simple method it is possible to produce monolayers of remarkable high quality[67], at the expense of a time-consuming exfoliate-and-characterize process. During chemical vapor deposition and similar techniques, precursors react at high temperatures to grow the specific material. This process can be highly optimized through an appropriate choice of catalyst, growth conditions, and precursor and carrier gases. The defects in 2D materials produced with either method, however, typically differs. It was found the dominant defect in mechanically exfoliated or CVD-grown MoS_2 crystals is the sulfur vacancy, while samples grown with PVD have the molybdenum antisite as the pre-

dominant defect[108].

It is also possible to combine CVD growth and mechanical exfoliation to produce large-scale monolayers (5 cm in diameter)[109], much larger than typical diameters $\sim 100\,\mu$m which are routinely achieved with the other methods. Beyond growth and exfoliation, plasma etching has recently became a common technique to reliably fabricate monolayers with a high throughput[110, 111].

As already mentioned, hBN has a particularly low optical contrast. The optical contrast of monolayer graphene or TMDs, while considerably higher than that of hBN, is also tiny, owing to the crystal thickness of just a few Å. The optimal substrate choice, however, can artificially increase the optical contrast of 2D materials. One such choice is ~ 270 nm SiO_2 on Si (see Fig. 3.9(a)), which provides excellent optical contrast for monolayered 2D materials. On pure SiC, in contrast, a monolayer is barely visible (see Fig. 3.9(b)).

Chapter 4

Quantum emitters in 2D materials

Near-future optical quantum information processing[50] relies on sources of pure and indistinguishable single-photons (see Sec. 2.11). Promising candidates include quantum dots[112–114], trapped ions[115], color centers in solids[116] and single-photon sources based on heralded spontaneous parametric down-conversion[117]. The recent discovery of fluorescent defects in 2D materials has added yet another class of quantum emitters to the solid-state color centers, attracting considerable attention among the research community. Quantum emitters in 2D have the distinct advantage, in contrast to their 3D counterparts, of not being surrounded by any high refractive index materials. This in turn prevents total internal and Fresnel reflection of emitted single-photons, leading to an intrinsically ideal extraction efficiency. Specifically engineer the environment, as has been done for NV centers in diamond, is thus not necessary[118].

The general concept of the single-photon emission mechanism is illustrated in Fig. 4.1, where a laser non-resonantly excites a quantum system to some excited vibronic state. While more complex to achieve, this initial excitation can also be accomplished by electrical pumping. The vibronic excitation relaxes non-radiatively to an excited electronic state $|2\rangle$, which, as it decays to the ground state $|1\rangle$, emits a single-photon with energy $\hbar(\omega_2 - \omega_1)$. This relaxation usually happens on ultrafast timescales on the order of picoseconds, while the lifetime of the excited electronic state is typically on the order of nanoseconds. Such level structure is introduced by point defects into the band structure (see Sec. 3.4). Since the defect is located at a specific lattice site, one speaks of a localized exciton. The emission has non-classical second-order correlations, with the correlation function vanishing at zero time-delay (see Fig. 2.5(b)). In reality, however, the level structure is more complicated than this idealized picture. In addition to the ground and excited electronic state, there are intermediate states which usually have long decay times (long compared to the lifetime of $|2\rangle$). These intermediate states are unwanted since they can decay non-radiatively and their slow transition makes an emitter dark for its duration, contributing to photoluminescence fluctuations and decreasing single-photon luminosity.

The following chapter introduces quantum emitters in 2D materials, with the focus on defects hosted by hBN. A recent review provides a broader overview of the field[119].

4.1 Quantum emitters in transition metal dichalcogenides

Stable quantum emission from defects in 2D materials has been initially reported in the transition metal dichalcogenide WSe_2 at cryogenic temperatures below 15 K[101–105]. At room temperature, the optical band gap of monolayer WSe_2 is 1.66 eV with a free exciton linewidth of 17 meV and a charged exciton at 1.63 eV (see Fig. 3.8(d)). At cryo-

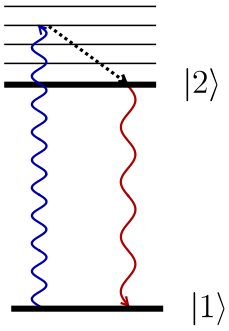

Figure 4.1: Concept of single-photon emission in an idealized two-level system (two electronic states). A high-energy photon from the laser field excites a vibrational mode which decays non-radiatively into an electronic excited state on ultrafast timescales. This excited state further decays radiatively under the emission of a single-photon.

genic temperatures, both the exciton and trion peak shift roughly 100 meV into the blue with the emergence of spatially localized, strong and narrow peaks in the spectrum at around 1.71 eV (50 to 80 meV below the free exciton) with linewidths ranging from 0.1 to 2 meV[101–105]. Second-order correlation functions confirmed that this emission has a non-zero overlap with the single-photon Fock state. The excited state lifetimes range from 1.5 to 2.5 ns. As is generally the case for all emission from 2D materials, the emitter lifetime is strongly dependent on the substrate[101]. This can be explained by the different dielectric environment, leading to an effective Purcell effect (see Chap. 9 for a quantitative calculation of this effect). Important for quantum information processing is that the single-photon emission has a well-defined polarization[101]. In recent years, the list of quantum emitters was successively expanded by WS_2[120,121], $MoSe_2$[122,123], and MoS_2[124]. The quantum emitters are hosted either by PVD grown[104] or mechanically exfoliated monolayers[101–103, 105]. While the locations of the emitters on grown samples are fully random, emitters on exfoliated samples form predominantly near the edges. The spectral diffusion is power-dependent and varies from emitter to emitter, where some emitters have spectral wandering $< 200\,\mu$eV, but others have much larger spectral diffusion > 1 meV[102]. Important for practical applications is that the emitters can be also excited all-electrically in graphene-hBN-TMD heterostructures, without loss of photon quality[120]. Both the emitters in PVD grown as well as mechanically exfoliated samples originate from naturally occurring defects. It is also possible to induce trap states into the band gap by stress. This has been demonstrated by depositing monolayer WSe_2 and WS_2 on nanopillars, which leads to deterministic formation of stress-induced single-photon emitters[121, 125]. Quantum emitters in WSe_2 have also been integrated with dielectric microcavities[126] and plasmonic nanocavity arrays[127, 128], where the latter achieved a very strong Purcell enhancement[128]. Quantum emitters in WSe_2 also exhibit Zeeman splitting under magnetic fields[102–105].

4.2 Quantum emitters in hexagonal boron nitride

Due to the optical transition energy being located in close proximity to the electronic band gap, resolving the zero-phonon line for the shallow defects in TMDs at room temperature

is impossible. More advantageous is the use of a wide band gap material, where the defect levels introduced into the band structure are well isolated from the energy bands.

The demonstration of quantum emission from defects hosted by WSe_2 was shortly followed by a report of single-photon emission from defects hosted by mono- and multilayer hBN[100]. The large band gap of hBN allows one to resolve the zero phonon line at room temperature and thwarts non-radiative recombination of the localized exciton. Thus, single-photon emitters in hBN have an intrinsically high quantum efficiency which leads to ultrabright emission.[1] Apart from operation at room temperature and brightness, the quantum emitters in hBN share many properties with their counterparts in TMDs: they exhibit an in-plane dipole resulting in linear polarization, large emission into the ZPL (indicating weak electron-phonon coupling), and have similar photostability[119]. The in-plane dipole can, but does not necessarily coincide with the excitation dipole[100, 129]. While the degree of linear polarization is typically high, depending on the fabrication of the crystal, the layer containing the chemical defect may not be perfectly perpendicular to the substrate. Therefore, this results in a z-component of the dipole.[2]

4.2.1 Emitter fabrication and characteristics

The single-photon emitters in the initial report originated from naturally occurring defects[100]. The following works enhanced the defect formation synthetically through chemical[130] or plasma etching[131, 132], laser[133], γ-ray[66], ion[134] and electron irradiation[134, 135] or near-deterministic stress-induced activation[136]. The latter is similar to previous works on WSe_2 and WS_2[121, 125], but operates through a fundamentally different single-photon emission mechanism compared to the other emitters. It has been pointed out that it is unclear whether any emitters are actually created with these methods or if preexisting, optically inactive defects are simply activated during the processing[119]. The latter could happen via modification or restructuring of the crystal environment. With a few exceptions[129], most defects form at (or near) the edges, or at locations, where the crystal already has cracks. Defect formation at these positions is preferred, as the required defect formation energy there is low (compared to the defect formation energy well within the crystal). This could be indicative of new defects being actually created during the processing. Subsequent to the emitter fabrication is usually a thermal annealing step, performed at high temperatures $\sim 850°C$ in various atmospheres[137]. The defect diffusion during this annealing is expected to be low[138].

Independent of the fabrication method, the emitter photophysics vary strongly, not only from defect to defect hosted by different hBN crystals, but also for defects on the same host crystal. Most notably, this is pronounced by ZPLs covering a wide range in the UV[139] and visible spectrum[137, 140, 141]. The excited state lifetimes vary from 20 down to 0.3 ns[131, 142], but as already mentioned, the emitter lifetime is substrate dependent. The shorter lifetime is more desirable, as this allows for efficient post-selection to mediate the effect of detector dark counts in practical quantum information processing. In addition, a long lifetime limits the brightness fundamentally. Recent progress in growth of hBN allows one to selectively grow emitters with predefined ZPLs through CVD[143] or atmospheric pressure CVD[144]. Importantly, depending on the growth conditions the ZPL

[1] Ultrabright means that single-photon counting modules detect MHz rates without collecting the emission with an immersion objective or Purcell enhancement. These rates are also not corrected for detector efficiency or transmission losses through the optical path toward the detector.

[2] This happens for example during mechanical exfoliation, where the terminating layers on both sides in multilayer hBN get shattered, or during the drop cast method of multilayer hBN flakes in ethanol[100].

can be predominantly localized in a spectral window within $550-600\,\mathrm{nm}$ or $600-650\,\mathrm{nm}$.

The single-photon emission from hBN was found to be remarkably robust. This is mostly governed by the thermal and chemical stability of hBN. The temperatures at which the single-photon emitters can operate range from $4\,\mathrm{K}$ (liquid He temperature)[140] to $800\,\mathrm{K}$[145]. When heated to $T = 800\,\mathrm{K}$, the lifetime as well as second-order correlation function remains invariant, suggesting that no new relaxation channels open. In addition to temperature stability, the emitters have also temporal stability over months, with no significant change in photophysics[131]. It was not even necessary to encapsulate the emitters to achieve this temporal stability, they can simply be stored in air at room temperature. The photostability, however, varies strongly from defect to defect. In general, the photostability depends on the laser excitation wavelength and laser power. The higher the excitation photon energy or power, the larger the photobleaching[141]. This suggests that the local crystal environment is modified, induced by the excitation laser. The problem of photostability can be countered with a two-laser co-excitation scheme, which strongly reduces photoluminescence fluctuations[146]. This can be explained by the fact that the additional laser repumps the population from any intermediate, slowly decaying state back into the excited state, which has a fast, radiative decay. Thus, this also increases the single-photon luminosity, as more excitations decay radiatively. The spectral diffusion can be almost entirely eliminated by appropriate surface passivation using Al_2O_3[147].

For practical applications, tuning of the emission is desirable, as this could specifically tailor the optical emission properties to match the application-specific requirements. Furthermore, understanding tuning dynamics provides insight on the emitter itself (see also next section). Spectral tuning has been achieved using either strain, electric fields, or pressure. Using strain on different emitters revealed tuning bandwidths from -3.1 to $+6\,\mathrm{meV}$ per % strain applied to the substrate[148]. The linear Stark tuning using electrical fields is larger with up to $5.4\,\mathrm{nm}$ per $\mathrm{GV\,m^{-1}}$ which corresponds to $15\,\mathrm{meV}$ per $\mathrm{GV\,m^{-1}}$ (a quadratic and V-shaped Stark effect was also observed)[149]. This is comparable to the linear Stark shift of the NV center in diamond ZPL with $6.3\,\mathrm{THz}$ per $\mathrm{GV\,m^{-1}}$ (corresponding to $26\,\mathrm{meV}$ per $\mathrm{GV\,m^{-1}}$)[150]. The tuning using pressure is up to $15\,\mathrm{meV\,GPa^{-1}}$, with most pressure tuning coefficients being below $6\,\mathrm{meV\,GPa^{-1}}$[151]. Interestingly, the pressure tuning is anomalous, as some emitters show an initial red-shift at lower pressure with a subsequent blue-shift at higher pressure.

Beyond optical excitation using one or more lasers, quantum emission from hBN has been triggered by cathodoluminescence schemes[139, 152]. An all-electrical excitation scheme similar to the one demonstrated for TMDs[120] is not accessible due to the insulating nature of hBN. It was proposed to electrically trigger UV emission from the band gap of hBN which in turn could excite the quantum emitters[119]. This excitation, however, relies on an inefficient second-order process which requires strong UV light due to the large detuning between UV excitation and visible defect emission. The incident UV power required would lead to strong photobleaching.

4.2.2 Nature of the emission and theoretical modeling

The generally accepted model for the quantum emission from 2D materials is based on a localized exciton. As described in Sec. 3.4, fluorescent point-like defects introduce trap states into the band gap, thus acting as an effective two-level system. In defiance of several attempts to identify the origin of the fluorescence using group theory analysis and *ab*

inito density functional theory[153–155], the exact nature of the defects remains controversial and is debated among the research community. Possible defect candidates include the C_BV_N, V_BC_N, V_NN_B, and V_B defects. It was recently noted, however, that widely used generalized gradient functionals can perform poorly and lead to misassignment of the defect states, hence, hybrid or long-range corrected functionals should be applied[156]. Moreover, calculated defects can have multiple transitions coinciding with the variety of experimentally observed ZPLs, making these assignments prone to errors. Density functional theory calculations often assume monolayered supercells due to the exponential scaling with the number of atoms and limited computational resources, while most experimental works use multilayer hBN. For reasons which are not yet fully understood, the spectral emission shape of quantum emitters hosted by mono- and multilayer hBN differ substantially[100].

On the experimental side, research efforts toward the identification of the responsible defect has been made, but so far the results are still inconclusive and further investigations are necessary[152, 157]. In general, the variations in ZPL position cannot be explained by local strain or Stark shifts (hBN is piezoelectric[136]) of a single optical transition line. The expected shifts alone are too small to account for the variety of ZPLs ($< 1\,\mathrm{meV}$, see previous section). Of particular note is that the ZPLs seem to bunch in groups around 560 nm[131], 590 nm[143], 640 nm[100, 137] and 714 nm[137]. It is believed that a specific point-like defect is responsible for each of these groups with the crystal lattice locally strained or changed otherwise, thus explaining the spread around these wavelengths. This hypothesis is supported by the similar vibronic bandshape of these defects, indicating they belong to the same symmetry group. It is worth noting there are occasional ZPLs which do not fall into either of these categories. It is likely that these originate from surface contaminants. Moreover, the bandshape of these differ from the bandshape typical for other emitters in the three groups, which supports this conjecture. A detailed analysis of this is presented in Chap. 10[158]. It is also definitely known that the power saturation behavior is that of an idealized two-level system (a point-like defect has) and the defects exhibit an in-plane dipole, as polarization-resolved photoluminescence shows. The latter indicates the defect has symmetry C_{2v} or lower, and the molecular orbitals involved in the transition are either both in-plane or both out-of-plane. Given other experimental observations, it is more likely they are in-plane. Such a low symmetry defect is formed by an interstitial or by distorting a vacancy or substitutional. Another option is a combination of two or more vacancies, interstitials or substitutionals.

4.2.3 Integration with photonic structures

A straightforward path for improving the performance of a spontaneous emission process is to use the Purcell effect by coupling the emitter to an optical resonator[21]. The optical resonator reduces the number of modes the emitter can couple to, thereby enhancing emission into the resonant modes. This even works in the "bad-emitter" regime, when the emitter linewidth is larger than the cavity linewidth[159]. Furthermore, all cavity QED theory (see Sec. 2.5) still applies, even though the emitter coupled to the cavity is, in this case, a defect in a solid rather than an atom. The dipole transition of the defect acts as a similar effective two-level system.

In addition to the work on cavity-integration of emitters in TMDs, quantum emitters hosted by hBN have been coupled to plasmonic nanocavities as well, achieving a single-photon source with a particularly low second-order correlation function[160]. Hexagonal

boron nitride can also be used to fabricate photonic crystal cavities, however, this makes the required spectral matching between optical cavity mode and emitter difficult[161]. The coupling of emitters with a dielectric cavity was recently achieved and is described in Chap. 9[162].

It is also possible to integrate the emitters directly with fibers. This can be achieved by transferring an hBN flake hosting a quantum emitter to a tapered fiber using a tungsten tip driven by a piezo positioner[142]. The overall system collection efficiency was 10%. The same system collection efficiency can be achieved by attaching the hBN flake by van der Waals force onto the core of a multimode fiber[163]. The advantage of the latter is that it does not increase the emitter lifetime. An alternative approach is to directly combine the cavity with the fiber. The fiber tip surface is shaped to be concave using a CO_2 laser pulse and subsequently coated to be highly reflecting[164]. This system achieves a high finesse, small mode volume, and features single-photon collection with the fiber. This has been demonstrated for NV and SiV centers in diamond coupled to these fiber microcavities[165, 166].

4.2.4 Applications

Although most researchers agree that quantum emitters in hBN provide a number of unique opportunities, the performance still lags behind state-of-the-art single-photon sources. Moreover, the reported single-photon quality is not sufficient for practical quantum information processing, giving rise to the question whether this can be achieved at room temperature at all. Without the advantage of room temperature operation, quantum emitters in hBN will hardly be able to compete with quantum dots.

The cavity-integrated emitter described in Chap. 9, however, demonstrated for the first time that single-photon emission from defects in hBN can indeed be useful for at least quantum key distribution, out-performing conventionally used protocols on short and medium distances. The work, however, questioned if the performance can be pushed toward indistinguishable single-photons, a requirement for optical quantum computing[162]. Even strongly dephasing emitters can achieve a good indistinguishability if coupled with a cavity that features a high quality factor[167]. The achieved spectral narrowing was already down to 200 GHz from 5 THz, but for indistinguishable single-photons with $> 90\%$ visibility, the required linewidth is ~ 100 MHz. Since the linewidth of a cavity with cavity length L is given by

$$\Delta\nu = \frac{\Delta\nu_{\mathrm{FSR}}}{\mathcal{F}} \tag{4.1}$$

where the free spectral range is given by $\Delta\nu_{\mathrm{FSR}} = \frac{c}{2L}$ and the cavity finesse $\mathcal{F} = -\frac{\pi}{\log(R)}$ is determined by the mirror reflectivities R (assumed to be equal for both cavity mirrors). Substituting this into Eqn. 4.1 yields

$$\Delta\nu = -\frac{c\log(R)}{2\pi L} \tag{4.2}$$

Thus, a narrow linewidth requires highly reflecting mirrors (which is limited by fabrication) or a long cavity. Enlarging the cavity length, however, reduces the free spectral range. If the free spectral range is less than the free space linewidth of 5 THz, the cavity would simply sample the free space emission spectrum, resulting in a comb-shaped spectrum. Indistinguishability requires filtering one peak, which means a great loss in efficiency. This

could only be resolved with further development in photonic crystal cavities, which could achieve higher quality factors and thus a narrower cavity linewidth. It is worth noting, that under resonant excitation at low temperatures, the linewidth is less than 1 GHz, broadened by spectral diffusion to 6.3 GHz[168]. Furthermore, it was reported recently that under resonant excitation, even at room temperature, Fourier transform limited emission lines can be observed, with linewidths of 60 MHz, independent of temperature[169]. This would allow for indistinguishable single-photons at room temperature even without a cavity. It is still an open discussion why such behavior is possible at all and why this has not been observed in the similar previous experiment[168].

Quantum cryptography, however, does not require this kind of indistinguishability. The single-photon sources are ideal for QKD, as they can be fully integrated within a cube with edge length of 10 cm[162], making them interesting for satellite-based quantum key distribution. Their feasibility is confirmed by the temperature stability over a range of 800 K[145], long-term stable operation over months[131], as well as resistance to space radiation[66]. The quantum emitters in hBN are particularly useful here due to the spread of optical transition lines. One can choose a defect with a ZPL coinciding with one of the Fraunhofer lines in the solar spectrum. Narrow filtering around this line allows one to operate a QKD system at daylight, as the background from sun light is suppressed[170]. Other color centers in solid-state crystals have their ZPL fixed, so these cannot be used in this way. In addition, the intrinsically ideal out-coupling efficiency and high quantum efficiency is of particular benefit for single-photon QKD. For fiber-based quantum links, however, optical transitions in the telecom bands (1330 or 1550 nm) are required, where fibers have low loss coefficients. This has not been demonstrated for any quantum emitter in 2D materials.

While initial investigations found no magnetic field dependency of the emission[147], the recent discovery of an optically addressable spin of quantum emitters in hBN at room temperature makes this platform also interesting for sensing applications[171]. This effect was highly anisotropic, and thus consistent with a spin-dependent crossing between singlet and triplet states.

Part II

Next-generation single-photon sources

Chapter 5

Methodology

5.1 Computational Methods

5.1.1 Density Functional Theory

For the development of density functional theory (DFT), Walter Kohn was awarded with the 1998 Nobel prize in chemistry.[1] Density functional theory is currently one of the most successful computational methods to calculate the electronic structure of matter. Part of the reason for this is its versatile applicability, ranging from atoms, molecules and solid-state crystals to quantum fluids. The initial method of DFT has been successively refined to include for example spin effects, superconductivity, time-dependency, or the use of pseudopotentials. With DFT, it is possible to predict a great variety of crystal properties, including the band structure, density of states, phonon dispersion and transport phenomena, structural relaxation, total energy, forces, stress and piezoelectrizity, phase stability, and many more. Since DFT has been used to calculate the band structures in Chap. 3, 8, and 10, the fundamental principles are introduced in this section. More complete reviews can be found in the literature[172–174].

5.1.1.1 Formalism

The fundamental principle of DFT is trying to reduce the problem of solving the $3N$-dimensional Schrödinger equation to a 3-dimensional one (assuming N crystal electrons). Starting with the Born-Oppenheimer approximation, the electrons are assumed to move in a slowly-varying (adiabatic) potential of the ions (whose positions are described by the lattice vector $\vec{R}$). The time-independent Schrödinger equation simplifies to

$$\hat{H}\psi = \left[-\sum_{i}^{N} \frac{\hbar^2 \nabla_i^2}{2m_\mathrm{e}} + \sum_{i}^{N} V(\vec{r}_i; \vec{R}) + \sum_{i<j}^{N} U(\vec{r}_i, \vec{r}_j) \right] \psi = E\psi \tag{5.1}$$

The crystal ions obey the vibronic equation and their interactions with the electrons are contained within the external potential $V(\vec{r}_i; \vec{R})$. The electron wavefunction (in the Born-Oppenheimer approximation) is a function of the position of each electron and depends on the positions of the nuclei only parametrically:

$$\psi = \psi(\vec{r}_1, \ldots, \vec{r}_N; \vec{R}) \tag{5.2}$$

[1] https://www.nobelprize.org/prizes/chemistry/1998/summary/

The interaction potential $U(\vec{r}_i, \vec{r_j})$ prevents separability into single-electron wavefunctions. Simpler approaches such as the Hartree-Fock method solve this many-body Schrödinger equation with a wave function approach by expanding the electron wavefunction in a single Slater determinant[175]. This has the advantage of exact representation of electron exchange interactions, but at the cost of ignoring electron correlation and greater computational complexity. On the other hand, DFT offers inclusion of correlation and computational efficiency at the cost of imprecise evaluation of electron exchange.

Central to density functional theory approach is the electron density $\rho(\vec{r})$, defined as the integral over the coordinates of all electrons except one, given by

$$\rho(\vec{r}) = N \int dr_2^3 \cdots \int dr_N^3 |\psi(\vec{r}, \vec{r}_2, \ldots, \vec{r}_N; \vec{R})|^2 \tag{5.3}$$

Therefore, according to Born's rule, $\rho(\vec{r})$ is the probability of finding any of the N electrons within the finite volume element $d\vec{r}$. This approach allows one to map the many-body problem onto a single-body problem without electron-electron interactions (see below). This electron density is an observable, meaning it can be measured experimentally through e.g. X-ray diffraction. For any given ground-state density $\rho_0(\vec{r})$, inverting the definition allows one to obtain the ground-state wavefunction $\psi_0(\vec{r}_1, \ldots, \vec{r}_N; \vec{R})$, where the wavefunction is expressed as a functional of ρ_0. This is known as the Hohenberg-Kohn theorem[176]. A direct consequence of this is that the crystal ground-state energy is also a functional of ρ_0. The energy associated with any density functional is given by

$$E[\rho] = T[\rho] + U[\rho] + \underbrace{\int d^3r V(\vec{r}; \vec{R})\rho(\vec{r})}_{=V[\rho]} \tag{5.4}$$

where $T[\rho]$ is the kinetic energy term and $U[\rho]$ is the electron-electron interaction term from the Hamiltonian. The problem is now minimizing $E[\rho]$ with respect to ρ, which will yield the ground-state energy and density, and thus all other ground-state observables. $T[\rho]$ and $U[\rho]$ are universal functionals, while $V[\rho]$ depends on the specific crystal or system. The minimization problem can be solved with the Kohn-Sham equations[177]. For this the electron-electron interaction and the external lattice potential is replaced with an effective external potential V_{eff} in which the electrons move (mean-field approximation), making the Schrödinger equation particularly easy to solve as the system has been transferred into a non-interacting system. Solving the Schrödinger equation yields the single-particle wavefunctions or Kohn-Sham orbitals $\psi_i(\vec{r}; \vec{R})$. These are, however, only fictional wavefunctions. The effective electron density is

$$\rho_{\text{eff}}(\vec{r}) = \sum_i^N |\psi_i(\vec{r}; \vec{R})|^2 \tag{5.5}$$

The effective single-particle potential is given by

$$V_{\text{eff}}(\vec{r}) = V(\vec{r}; \vec{R}) + \underbrace{\int d^3r' \frac{e^2 \rho_{\text{eff}}(\vec{r}')}{|\vec{r} - \vec{r}'|}}_{\text{Hartree term}} + \underbrace{V_{\text{XC}}[\rho_{\text{eff}}(\vec{r})]}_{\text{exchange-correlation}} \tag{5.6}$$

The Hartree term describes electron-electron Coulomb repulsion and the exchange correlation describes all many-body interactions. Both terms are a functional of $V_{\text{eff}}(\vec{r})$, and

Pseudopotential	E_g [eV]
LDA-HL[181]	0.46
LDA-PZ[182]	0.47
GGA-BLYP[183, 184]	0.78
GGA-BPW91[183, 185]	0.61
GGA-PBE[186]	0.58
GGA-PBES[187]	0.47
GGA-RPBE[188]	0.63
GGA-XLYP[184, 189]	0.81
Experiment[63]	1.12

Table 5.1: Comparison of the performance of density functional theory pseudopotentials. The underlying crystal calculated is Si. All calculations reproduce the indirect band gap nature of Si correctly, however, the magnitude of the band gap is severely underestimated, when comparing to the experimental value.

thus of $\psi_i(\vec{r};\vec{R})$, so solving the Kohn-Sham equations must be done iteratively (or in a self-consistent way), until the results converge. This means the electron density does not change more than the convergence criterion after the k-th iteration step.

5.1.1.2 Limitations

The major drawback of using DFT is that the exchange-correlation functionals in general are unknown. Practical implementations of DFT use approximations to describe the exchange-correlation. Widely used are the local-density approximation (LDA), generalized gradient approximation (GGA) or Meta-GGA. Many DFT calculators allow the use of a great variety of predefined pseudopotentials to describe the exchange-correlation potential[174]. Whether a pseudopotential describes the crystal electrons well depends on the specific problem, so great care is required when using these.

These limitations of DFT become clear when looking at strongly correlated systems, band gaps, or optical phenomena (like excitonic features). In particular, DFT severely underestimates the quasiparticle band gap[178]. Moreover, depending on the specific pseudopotential used in a calculation, the band gap calculated with DFT can substantially vary, as Tab. 5.1 shows. Nevertheless, DFT provides a good trade-off between computational efficiency and accuracy. Hybrid functionals or GW corrections can also yield more accurate results[179, 180].

5.1.1.3 Implementation in the Atomistix ToolKit

There exist many implementations of density functional theory. For this thesis, all DFT calculations were done using the Atomistix ToolKit (ATK)[190, 191] with the Virtual NanoLab front end or the Vienna Ab initio Simulation Package (VASP)[192, 193].[2] ATK models electronic properties of closed and open quantum systems within the framework of DFT using numerical linear combination of atomic orbitals basis sets. The self-consistent calculation of the Kohn-Sham equations and the electron density was introduced in the previous sections. For open systems, ATK calculates the density matrix using non-equilibrium Green's functions, while for closed (or periodic) systems it is calculated by diagonalization of the Kohn-Sham Hamiltonian. ATK is equipped with a large variety of predefined functionals and a crystal database, allowing one to build up any arbitrary heterostructure. While still relatively new, ATK has already an impressive functionality.

In the following section, the methodological and numerical details of the DFT simula-

[2] VASP has only been used in Chap. 8[66], all other calculations use ATK.

tions in this thesis are outlined.[3] The band structure of GaAs and Si (see Fig. 3.5(a, b)) have been calculated using a $8 \times 8 \times 8$ Monkhorst-Pack reciprocal space grid. First, the geometry was optimized such that all forces were $< 0.01\,\mathrm{eV\,\AA^{-1}}$. For the face-centered cubic (fcc) lattice of GaAs and Si the calculated lattice constants are 5.6537 and 5.4306 Å, respectively. The used pseudopotentials are norm-conserving with non-linear core correction to describe the core electrons. The exchange-correlation energy was described by the Perdew-Burke-Ernzerhof for Solids (PBES) functional in the generalized gradient approximation[187]. Since GaAs and Si have strong covalent bonds, a double zeta polarized basis set ensures accurate results for these crystals. The band structure is routed along the high symmetry points in k-space. The resulting band gaps are 0.5 and 0.48 eV for GaAs and Si, respectively, showing DFT severely underestimates the band gap in the LDA or GGA.

The band structures of mono- and bilayer WS_2 (see Fig. 3.8(a, b)) are calculated in a similar fashion, but with a $21 \times 21 \times 1$ and $21 \times 21 \times 21$ Monkhorst-Pack grid, respectively. The bilayer supercell contains six atoms, while the unit cell for the monolayer only contains three atoms. The optimized lattice constants are $a = 3.1532$ and $c = 12.323\,\mathrm{\AA}$.[4]

Finally, Tab. 5.1 was calculated with $21 \times 21 \times 21$ Monkhorst-Pack grids, and the only difference between each calculation is simply the exchange-correlation. All other simulation parameters are the same as above.

5.1.2 Finite-Difference Time-Domain method

The finite-difference time-domain (FDTD) method is a finite-element technique for numerically solving Maxwell's equations or modeling electrodynamics. FDTD simulations solve the differential equations in the time-domain using finite-difference approximations. This allows one to calculate the evolution of the fields as they evolve in time as well as to include a wide range of frequencies within a single simulation. Key element of FDTD is the central finite-difference approximation which can be obtained from a Taylor expansion, with the result:[5]

$$\left.\frac{\partial f(x)}{\partial x}\right|_{x_0} = \frac{f\left(x_0 + \frac{\Delta x}{2}\right) - f\left(x_0 - \frac{\Delta x}{2}\right)}{\Delta x} + \mathcal{O}(\Delta x^2) \approx \frac{f\left(x_0 + \frac{\Delta x}{2}\right) - f\left(x_0 - \frac{\Delta x}{2}\right)}{\Delta x} \tag{5.7}$$

While it is possible to construct higher-order central finite-differences, choosing Δx sufficiently small yields accurate results, accurate to $\mathcal{O}(\Delta x^2)$. This approximation was exploited by Kane Yee in the first FDTD algorithm[195]: Starting with Maxwell's equations, all derivatives in Ampére's and Faraday's law are replaced with their central finite-difference approximations. Space and time are also discretized, such that electric and magnetic fields are discretized over a finite mesh. The resulting difference equations can be solved to obtain updated electric and magnetic fields, that can be evaluated for the next time step. The electric field evaluated at a given time updates the magnetic field at the next time step. In the same way the magnetic field updates the electric field. These steps are repeated iteratively until the transient of steady-state solution is obtained (convergence). Modern implementations of the FDTD method allow one to inject a source and to choose specific boundary conditions like perfectly matched layers (PMLs), which absorb

[3] Limited to Chap. 3 and 5, as the publications have these details in their Methods sections.

[4] Note that the supercell with $c = 12.323$ Å contains two atomic layers, so the monolayer thickness would be 6.162 Å, close to the experimental value of ~ 6 Å[194].

[5] This expression is obtained by subtracting the Taylor expansion of $f\left(x_0 - \frac{\Delta}{2}\right)$ from $f\left(x_0 + \frac{\Delta}{2}\right)$ and solving for the first partial derivative.

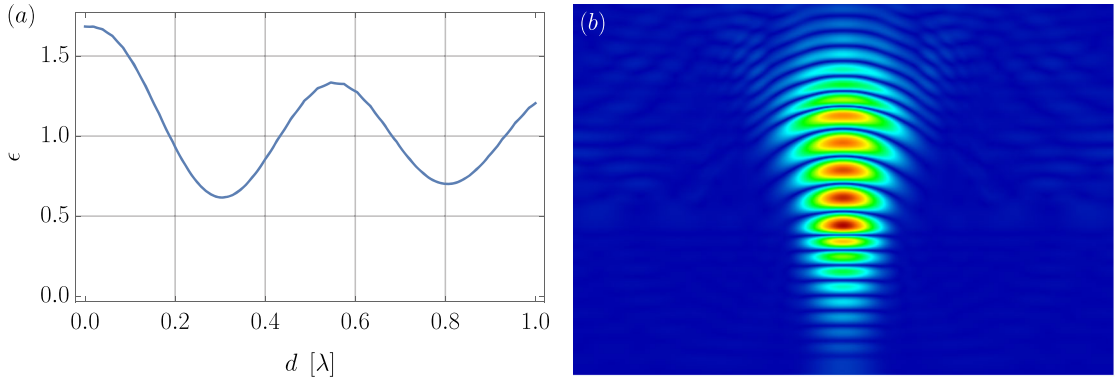

Figure 5.1: (a) FDTD simulation of the Purcell enhancement ϵ of a dipole emitter near a dielectric surface as a function of distance to this surface (in units of the wavelength). The dielectric environment consists of a highly-reflective mirror, which modifies the photonic density of states, resulting in modulation of the emission behavior. (b) FDTD simulation of the electric field profile of a dipole emitter in a confocal cavity, used to enhance a single-photon emitter hosted by hBN. The details of the simulations are presented in Chap. 9[162].

any incident electromagnetic waves. PMLs are often used as the electric and magnetic fields are calculated at every mesh point in space, so limiting this space is required to account for the finite accessible memory.

The FDTD method can be easily parallelized, and is thus well suited for use on supercomputers. It is accurate and robust, handling nonlinear materials naturally. As already mentioned, it is applicable to a wide range of frequencies in a single simulation, meaning if a resonance frequency is not known, it can easily be obtained by injecting a broadband pulse and recording the spectrally-resolved response. FDTD allows one to define any material, geometry and light source and is thus very versatile. Since the time-evolution of the fields is recorded, animations of the electric and magnetic fields can be created easily. The major drawbacks include the requirement of a fine mesh, resulting in the trade-off between accuracy, memory requirements and computational simulation time. In general, the mesh has to be finer than the wavelength and any geometrical features of the materials. The latter is especially computationally expensive on curved surfaces, or when a simulation has large and small features. This limits the numerical accuracy, but can at least be partially countered by using a dynamic mesh depending on the local environment.

In this thesis, FDTD simulations have been used to calculate exciton lifetimes as a function of varying dielectric environments and emission mode profiles. Examples for these are shown in Fig. 5.1. The software used was Lumerical FDTD Solutions, a commercial-grade simulator based on the finite-difference time-domain method[196].

5.2 Experimental techniques

5.2.1 Scanning electron microscopy with a focused ion beam

Due to diffraction, the resolution of an optical microscope is fundamentally limited by the wavelength of the light that is used to probe a sample, a fact that is known as the Abbe limit. Matter waves in turn, can have much shorter wavelengths than visible light. For

this discovery Louis de Broglie was awarded with the 1929 Nobel prize in physics.[6] The de Broglie wavelength is given by

$$\lambda_{\mathrm{dB}} = \frac{h}{p} \tag{5.8}$$

Thus, for electrons it takes an accelerating voltage of only 150 V to reach a wavelength of 0.1 nm. This fact is exploited in a scanning electron microscope (SEM), a technique that was awarded with the 1986 Nobel prize in physics.[7] In an SEM, the sample is scanned with a focused electron beam and the response is recorded as a function of electron beam position. This response can be of the form of secondary electrons, back-scattered electrons, characteristic X-rays, light (cathodoluminescence), or transmitted electrons and contains information about the surface topography and composition of the underlying sample.

A similar operation principle is used for a focused ion beam (FIB), which is usually equipped with dual electron and ion beams, where the electron beam is used for ultrahigh resolution imaging (as it is less invasive than the ion beam) and the ion beam is used for nanofabrication. One of the most common ion species for FIB are Ga^+ ions from a liquid metal ion source. While a FIB can be used to image a sample similar to an SEM,[8] it can additionally restructure the sample, either by localized deposition or milling. The requirement for using any such charged particle beam is that the sample must be conductive and kept under vacuum. For non-conductive samples, it is common to coat it with a thin conductive coating (Au or Pd/Au), or to neutralize the ions after the acceleration, beam steering and focusing phase with an electron beam. In this thesis, the used FIB was a FEI Helios 600 NanoLab, with a resolution of 0.8 nm for the electron beam (at 30 keV) and 2.5 nm for the ion beam (at 30 keV).

5.2.2 Sputter deposition

Sputter coating belongs to the class of physical vapor deposition methods used to grow thin films. The technique is versatile and applicable to metals as well as to dielectrics (such as oxides and nitrides). During sputtering a high DC or 13.56 MHz RF discharge (for conductive or non-conductive targets, respectively) is applied to create an argon plasma (argon is used since, as a noble gas, it does not chemically react). During sputtering the Ar^+ ions are accelerated through a potential gradient and bombard the target material or cathode. This makes the surface atoms of the target volatile (creating a vapor), which are then transported as such to the sample holder or substrate, resulting in the deposition of a thin film of the target material.[9] When depositing oxides or nitrides (insulating dielectrics), the composition of the target may change during the vapor transport of the atoms resulting in a non-stoichiometric material deposition. To maintain stoichiometry or to alter it in a certain direction one may consider adding reactive gases like O_2 or N_2, which enable reactive sputtering. This is a commonly used technique to alter the composition of the sputtered materials with respect to the original target and is a chemical process. Furthermore, a high vacuum prior to the deposition is essential, since otherwise undesired residual gases get incorporated within the thin film. In general, sputtering is a complex process with many parameters influencing the growth quality and rate, but in

[6] https://www.nobelprize.org/prizes/physics/1929/summary/

[7] https://www.nobelprize.org/prizes/physics/1986/summary/

[8] In a FIB apparatus the electron beam is used for imaging. It is possible to use the ion beam for imaging as well, however, the focused ion beam can damage the sample.

[9] In reality the entire vacuum chamber is coated with the target material.

turn this also allows one to tune and control the process. In this thesis, the used hardware was an AJA sputter coater system featuring three 1000 W DC and three 600 W RF guns.

Another deposition technique used in this thesis is electron beam evaporation (Temescal BJD-2000), where a target metal is bombarded in high vacuum with an electron beam. The electrons heat the target above its melting temperature, resulting in a gas cloud of the target atoms successively coating substrate with a thin film of the material.

5.2.3 Plasma processing

Plasma etching is a nanofabrication technique, where one or more gases are submitted to a certain potential in a vacuum causing the partial ionization of the gases. Commonly, plasma tools use an RF generator operating at 13.56 MHz and the simplest configuration is a capacitively coupled plasma, where the feed gases are injected between two electrodes with the RF electrical field applied and maintained at low pressure. This ionizes the gases, thereby creating the plasma. The technique creates a negative bias voltage (DC bias) on the lower electrode where typically the samples are placed and etched. Hence, positive ions build up kinetic energy that is transferred to the sample. This energy can be critical to initiate the etching process, especially to break the bonds of the substrate atoms. High density plasma reactors use typically two power sources: one to create the plasma remotely (away) from the lower electrode and the second applied to the lower electrode that induces the DC bias voltage to the lower electrode. The main advantage of such a reactor is the independent control of plasma density and dc bias voltage enabling low damage etching processes. Electron cyclotron resonance (ECR) power sources operate at 2.45 GHz and high density microwave plasma systems like these typically achieve $\sim$ 100 times denser plasmas than others excited at 13.56 MHz. Another type of high density plasma system is the inductively coupled plasma (ICP), where the gas is excited by magnetically-induced electric currents. ICP systems make use of power sources operating at 13.56 MHz and do not require the strong magnets needed by ECR machines to confine the plasma.

Plasma etching is a chemical dry-etching method that is material-selective and can be tuned to etch in an isotropic or anisotropic way[197]. Depending on the specific process parameters, it is viable to achieve surface modification without direct etching of the underlying material.[10] This fact has been exploited in this thesis and is basis for many plasma processes, allowing one to specifically engineer and tailor material properties. The involved plasma processes have been optimized and are, in general, strongly machine-dependent, conditioned by the plasma generator, chamber geometry, or gas pump. In this thesis, the used microwave plasma was a PVA TePla with O_2 and CF_4 dual etch capability and the ICP system was a Samco RIE-400iP for etching with fluorides, chlorides, Ar, O_2, and H_2.

5.2.4 Time-resolved photoluminescence spectroscopy

Photoluminescence (PL) spectroscopy is a technique where a sample is excited non-resonantly with a high-energy laser.[11] After the excitation relaxes to its initial state, a photon containing information about the sample is emitted. The extractable information depends on the laser and the detection scheme. In this thesis, time-resolved photoluminescence (TRPL) spectroscopy was employed, where a linearly-polarized excitation laser emits ultrashort pulses (frequency-doubled to 522 nm, 300 fs pulse length at a repetition

[10] For instance, a low power O_2 plasma makes surfaces hydrophilic, whereas a CF_3/CF_4 plasma results in a hydrophobic surface.

[11] High-energy here means that the photon energy must be larger than that of the underlying transition.

rate of 20.8 MHz). The PL emission is collected in-reflection through the same high numerical aperture objective (100×/0.9). The excitation laser is split into trigger and excitation pulse, thus providing the exact time when the sample is excited. A single-photon avalanche diode (SPAD) from Micro Photon Devices provides the arrival time of the photoluminescence photon (time-correlated single-photon counting). The latter correlation is given by a PicoHarp 300. The excitation lifetime can be extracted from fitting the decay curve in the TRPL data.[12] In this thesis, the used setup allows one to couple the PL via a grating either onto the SPAD or a CCD camera, allowing one to extract temporal and spectral information of the photoluminescence. The setup is equipped with nanopositioning stages allowing one to map the PL response with 200 nm spatial resolution and a cryostat for cooling the sample down to the temperature of liquid helium (4.2 K).

5.2.5 HBT-type interferometry

The HBT-type interferometer was introduced in Sec. 2.8 and can be used to measure the second-order correlation function. The HBT-type interferometer is a very simple apparatus consisting only of a beam splitter and two detectors (see Fig. 2.5(a)). When photon number resolving detectors are used, the measurement of $g^{(2)}(\tau)$ is exact, otherwise the measured correlations only approximate $g^{(2)}(\tau)$[198].[13] While such photon number resolving detectors have been demonstrated in proof-of-principle experiments[199], they are not yet commercially available (even though it is possible to gain information about the photon number within a pulse from standard SPADs[200]).

Standard SPADs can distinguish vacuum from non-vacuum states. For an HBT interferometer with such detectors, the correlation function

$$\gamma^{(2)}(0) = \frac{P_{01}}{P_0 \times P_1} \tag{5.9}$$

can be defined as the conditional probability P_{01} that both detectors measure non-vacuum within the same time interval or time bin, divided by the product of the probabilities that any detectors measured non-vacuum (in this time interval) $P_0 \times P_1$. P_0 and P_1 are independent of each other. It can be shown that Eqn. 5.9 is equal to

$$\begin{aligned}\gamma^{(2)}(0) &= \frac{\sum_{n=2}^{\infty}\left[1-(1-\eta_0 R)^n-(a-\eta_1 T)^n+(1-\eta_0 R-\eta_1 T)^n\right]P(n)}{\sum_{n=1}^{\infty}\left[1-(1-\eta_0 R)^n\right]P(n)\times\sum_{n=1}^{\infty}\left[1-(1-\eta_1 T)^n\right]P(n)} = \\ &= \frac{2P(2)+6P(3)\left(1-\frac{1}{2}\eta_0 R-\frac{1}{2}\eta_1 T\right)+\mathcal{O}(4)}{\left(P(1)+2P(2)\left(1-\frac{1}{2}\eta_0 R\right)+\mathcal{O}(3)\right)\times\left(P(1)+2P(2)\left(1-\frac{1}{2}\eta_1 T\right)+\mathcal{O}(3)\right)}\end{aligned} \tag{5.10}$$

where η_0 and η_1 are the detection efficiencies of the detectors incorporating all losses, R (T) are the reflection (transmission) coefficients of the beam splitter, and $P(n)$ is the probability of the photon source to emit n photons[198]. In the limit of $\eta_0, \eta_1 \ll 1$ or $P(1) \gg P(n \geq 2)$,[14] this expression is a good approximation for $g^{(2)}(0)$. It is worth noting, that in the latter limit, $\gamma^{(2)}(0)$ becomes independent of R, T, η_0, η_1 as Eqn. 5.10 shows. In other words, $\gamma^{(2)}(0)$ still approximates $g^{(2)}(0)$ well when $R \neq T$ and $\eta_0 \neq \eta_1$.

[12] When the TRPL data is deconvoluted from the instrument response function, the system achieves a temporal resolution of ~ 3 ps.

[13] In fact, a single photon number resolving detector would be sufficient for exact measurement of $g^{(2)}(\tau)$.

[14] For photons originating from a physical process, it is reasonable to assume a monotonically decreasing function for higher-orders, implying $P(2) \gg P(n > 2)$.

Chapter 6

Room temperature single photon source using fiber-integrated hexagonal boron nitride

6.1 Foreword

With the general framework of quantum optics and solid-state physics established in the previous chapters, it is now possible to describe single-photon sources in two-dimensional materials, their role for robust quantum information processing, and the background required to engineer and tailor such sources. The developments achieved during this thesis are detailed in the following chapters.

A particular problem from which many single-photon sources suffer is a poor extraction and collection efficiency of the generated photons. Among the highly-efficient single-photon sources, quantum dots excel, reporting extraction efficiencies around $65-66\%$[201, 202]. It took huge research efforts to engineer these quantum dots to achieve this performance. A key element for this was the direct integration of the quantum dot within an optical resonator. Other solid-state emitters, such as color centers, are less intuitive to integrate with a cavity, as the cavity and emitter cannot be grown together for a monolithic device. As already mentioned, quantum emitters in 2D have the decisive advantage that, in contrast to their counterparts in 3D, the emitters are not surrounded by any high refractive index materials. This prevents total internal and Fresnel reflection and allows, at least in principle, for an intrinsically ideal extraction efficiency. The in-plane dipole results in an out-of-plane emission, shifting the problem solely to collecting the single-photons.[1] In addition, the 2D lattice makes it particularly easy to attach 2D materials hosting quantum emitters to any surface with van der Waals forces. These forces are typically very weak (see Tab. 3.1), but the large 2D crystal area makes the total force considerably large, such that the materials can be attached indefinitely.

This has been exploited in the work presented in this chapter, where a single-photon emitter hosted by hBN has been attached by van der Waals force to the core of a multimode fiber. The system achieves a single-photon collection efficiency of 10.15% and can be pumped via free space or directly via the fiber. The single-photons can be collected with the fiber or via free space. This work has been published in J. Phys. D: Appl. Phys. **50**, 29510 (2017). All graphics have been recreated to match the style of this thesis.

[1] This is a lot easier than extracting and collecting the single-photons efficiently at the same time.

Room temperature single photon source using fiber-integrated hexagonal boron nitride

Tobias Vogl[1], Yuerui Lu[2], and Ping Koy Lam[1]

[1] *Centre for Quantum Computation and Communication Technology, Department of Quantum Science, Research School of Physics and Engineering, The Australian National University, Acton ACT 2601, Australia*

[2] *Research School of Engineering, The Australian National University, Acton ACT 2601, Australia*

Abstract

Single-photons are a key resource for quantum optics and optical quantum information processing. The integration of scalable room temperature quantum emitters into photonic circuits remains to be a technical challenge. Here we utilize a defect center in hexagonal Boron Nitride (hBN) attached by Van der Waals force onto a multimode fiber as a single-photon source. We perform an optical characterization of the source in terms of spectrum, state lifetime, power saturation and photostability. A special feature of our source is that it allows for easy switching between fiber-coupled and free space single-photon generation modes. In order to prove the quantum nature of the emission we measure the second-order correlation function $g^{(2)}(\tau)$. For both fiber-coupled and free space emission, the $g^{(2)}(\tau)$ dips below 0.5 indicating operation in the single-photon regime. The results so far demonstrate the feasibility of 2D material single-photon sources for scalable photonic quantum information processing.

J. Phys. D: Appl. Phys. **50**, 29510 (2017).

6.2 Introduction

The field of two-dimensional (2D) materials has gained much interest during the past few years[1, 2]. Due to their excellent electronic and optical properties, 2D materials offer significant potentials for both industrial technologies and scientific studies. Although most research on 2D materials is targeting graphene[3, 4] due to its high tensile strength and electrical properties, such as an intrinsic record high electron mobility, the material's application to optics is limited due to the lack of a band gap. It was recently discovered that monolayer transition metal dichalcogenides (TMDs) can host quantum emitters at cryogenic temperatures[5–9]. The defect alters the electronic crystal structure or, more precisely, introduces sub-states within the band gap that typically lie close to the valence or conduction band. For materials with a large band gap, transition levels with greater energy differences to the bands can occur. This in turn allows defect emission to be distinct from photoluminescence (PL) emission at room temperature as demonstrated in the insulating 2D material hexagonal Boron Nitride (hBN)[10].

In spite of the pivotal role single-photon sources (SPSs) play in many quantum information processing and quantum communication applications[11–13], and the huge efforts made in order to investigate different types of SPSs, building an *ideal* single-photon source remains challenging. Among the desired properties of a single-photon source are (I) a vanishing second-order correlation function $g^{(2)}(\tau = 0) \to 0$, (II) a high indistinguishability of the emitted photons, (III) spectral control of the emission (meaning a narrow linewidth

and tuning of the center wavelength), (IV) a high brightness and (V) a high coupling efficiency, while (VI) still being able to integrate the source into various environments. Progress has been made on several different types of single-photon sources: in SPSs based on heralded spontaneous parametric down-conversion it was possible to achieve simultaneously outstanding results for most of (I)-(V)[14–18] at the expense of requiring single-photon avalanche diodes (SPADs) for heralding and high power excitation lasers. Recent demonstrations of single-photon emission from quantum dots caught up with state-of-the-art results in especially (I) and (II) and also in (VI), (V)[19–22]. However, quantum dots require cooling to liquid helium temperatures making them infeasible for some of the applications. Another extensively studied direction is NV-centers in diamond and similar systems[23]. In contrast a SPS in a 2D material offers versatile integrability and an intrinsic out-coupling efficiency of unity, while at the same time being cost-effective, easy-to-handle and can operate at room temperature and normal pressure.

Here we report a room temperature single-photon source using atomically-thin hBN flakes attached to the end face of a high-NA multimode fiber excited by PL. Our setup allows easy switching between fiber-coupled and free space operation. We demonstrate the quantum nature for both modes and approximate the collection efficiency of the fiber.

6.3 Experimental results

6.3.1 Device fabrication

First, few-layer hBN flakes are mechanically exfoliated to gel foil (Gel-Pak WF-40-X4) from bulk crystal (acquired from HQGraphene) using 3M scotch tape, and then optically identified with a microscope. In order to enhance the optical contrast of the hBN flakes the latter is done under red light[24]. Still, due to the zero-crossing of the optical contrast of hBN in the visible spectrum, this sets a limit to the minimally achievable layer thickness (typically $4 - 5\,\mathrm{nm}$). The thickness is calculated by comparing the optical contrast with atomic force microscopy measurements from a previous experiment. In the following the sample undergoes a series of oxygen plasma and thermal treatments, in order to introduce and activate the color centers[25]. We have tried a variety of different settings and found the best results with a 3-stage process: Initially, the flakes are are treated for 1 min at a plasma power of 100 W and an oxygen flow of 300 sccm and then for 10 min at 500 W at 600 sccm oxygen flow. During the third step the sample is baked at 160°C for 30 min. We found that higher temperatures (with the sample on a Si/SiO_2 substrate) yield higher brightnesses, however, the used polymer foil is not suitable for higher temperatures. In an intermediate step after the annealing the flakes are characterized in a micro-photoluminescence system (μPLS) with a DPSS laser at a wavelength of 522 nm continuously exciting the sample in a confocal microscope. As the photon energy is below the band gap of hBN ($E_g > 5\,\mathrm{eV}$[24]), delocalized excitonic emission is prevented making it possible to address distinct defect centers in a photoluminescence experiment. The flakes are scanned to identify regions with a high PL response as shown in Figure 6.1(a) marked with D1, D2 and D3. For each position a full spectrum is recorded. The regions with a high PL intensity are regions where the defect centers are localized. If the flake is found not to host a defect center the plasma treatment is repeated. In the final fabrication step, appropriate flakes are transferred by dry contact onto the cleaved end of a high-NA multimode fiber with a pure silica core (core diameter $d_{core} = 200\,\mu\mathrm{m}$, $NA = 0.5$). To

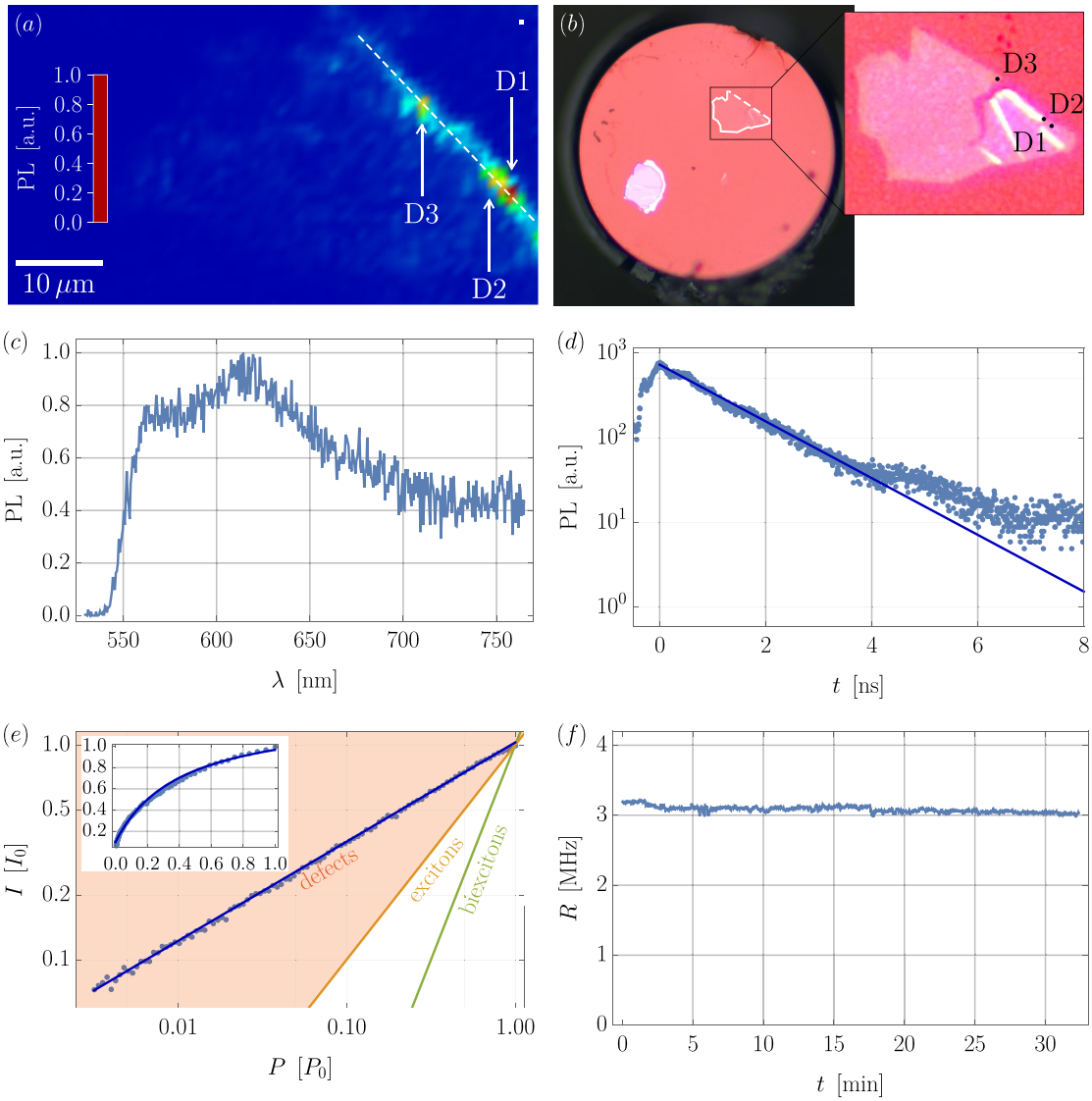

Figure 6.1: Characterization of the hBN flake on the fiber. (a) μPL scan of the flake revealing the presence of suspected defects labeled D1, D2 and D3. The small white box in the top right corner indicates the resolution (0.5 μm) of the μPL scan. (b) Optical microscope image of the hBN flake on the fiber under red light with 500× magnification. The flake is framed in white with the edge with the defects dashed (see white line in (a)). The top right magnification shows a contrast-enhanced image of the flake with the approximate positions D1-D3 marked with dots. (c) Spectrum measured at D1 acquired in-reflection from the flake by excitation with a laser at 522 nm. (d) Time-resolved photoluminescence of D1 reveals an effective decay time of $\tau = 1.93$ ns. (e) Log-Log-plot of the saturation of the PL intensity as a function of laser excitation power. A slope $\alpha < 1$ (red-shaded area) indicates defect emission, while a slope of $\alpha = 1$ (orange line) would indicate free excitonic emission and a slope of $\alpha = 2$ (green line) biexcitonic emission. The slope in this measurement ($\alpha = 0.46$) confirms the defect nature of the emission. (f) The single-photon count rate as a function of time demonstrates a photostability better $\sigma_{\mathrm{PL}}/\overline{R}_{\mathrm{PL}} < 1.3\,\%$. Integration time for each point is 1 s.

ensure depositing the flake at the center of the fiber core, the fiber is illuminated through the back end during the transfer process. It is just as much pressure applied such that the

air gap between the fiber and the polymer foil closes by itself. After 4 min the polymer foil is removed and with around 70 % probability the flake will be transferred to the fiber. The applied pressure and contact time strongly influence this success probability. However, even after an unsuccessful transfer these steps can be repeated. Using this transfer method, the flakes are attached by Van der Waals force to the fiber. Figure 6.1(b) shows a microscope image under red light of the transferred flake on the end of the fiber. The magnified part shows a post-processed contrast-enhanced image of the area of interest with the approximate positions of D1-D3 marked with dots. The flake thickness is approximately 5 nm, which corresponds to about 12 atomic layers.

6.3.2 Characterization

After transferring the flakes onto the fiber, the flakes are fully characterized, with all measurements being carried out at room temperature. Preliminary measurements showed a low background noise originating from the fiber which was traced back to Raman scattering[26]. To eliminate this background the flakes are excited under an angle such that the pump light is not guided anymore. The PL response is checked again in order to confirm that the defect survived the transfer process. The following analysis is limited to the defect marked with D1 in Figure 6.1(a), as this defect showed the highest brightness. It is not clear why some defects show a higher brightness than others, the brightness can vary from defect to defect (and including from flake to flake) by a factor of up to 4.7, while more than 80 different samples have been tested. However, although not reproducible for each individual defect, a bright defect can always be re-created by fabricating and testing more samples. The spectrum of the emission of D1 is shown in Figure 6.1(c). As can be seen the spectrum is rather broad as reported in [10] with the maximum PL intensity peaking at 616 nm. Time-resolved PL (TRPL) with the laser in pulsed mode and a pulse length of 300 fs at a repetition rate of 20.8 MHz reveals an effective state lifetime of $\tau = 1.93$ ns extracted from a fit of a single exponential decay function (see Figure 6.1(d)). The effective state lifetime satisfies

$$\frac{1}{\tau} = \frac{1}{\tau_r} + \frac{1}{\tau_{nr}} \tag{6.1}$$

with τ_r and τ_{nr} being the radiative and non-radiative decay time. Note that this state lifetime sets a physical limit onto minimal timing jitter and also on the maximal repetition frequency of the source. Although we did not measure the lifetime of every defect we tested, we found that the excited state lifetime as well as spectral shape of the emission can vary from defect to defect. However, there is no correlation between brightness and lifetime or spectrum so far. Future investigations together with theoretical modeling will give more insight into the nature of the defect. To find the ideal excitation power a saturation measurement has been done. The PL intensity I as a function of the excitation power P (see Figure 6.1(e), small inset) can be described by

$$I\,(P) = \frac{I_{sat} \cdot P}{P + P_{sat}} + I_d \tag{6.2}$$

where I_{sat} and P_{sat} are the saturation intensity and power respectively and I_d is the dark count intensity. From a fit we find the saturation power to be $P_{sat} = 38.2\,\mu$W. With a focused laser spot size diameter of 0.67 μm this amounts to an intensity of 2.71 kW/cm^2 which is found to be below the damage threshold for the flakes. We measured the damage

threshold by increasing the laser intensity up to 2.18 MW/cm^2 (average intensity from a pulsed laser with a duty cycle of $6.24 \cdot 10^{-6}$) and exposed the sample for a minute. We note that this is just a lower bound for the damage threshold, as we did not increase the laser power until it actually damaged the sample. However, if the power dependence is plotted on a Log-Log-scale, the nature of the emission can be determined: The slope $\alpha = 1$ means, the emission originates from a free exciton, a slope close to 2 indicates biexcitonic emission, while a slope less than one confirms emission from localized excitons (in Figure 6.1(e) the red-shaded area)[27]. For our source the slope is $\alpha = 0.46$ confirming the presence of a defect. Finally, the photostability of the emission is investigated by continuously exciting the defect D1 and recording the single-photon count rate. Figure 6.1(f) shows an average count rate of $\overline{R}_{\mathrm{PL}} = 3.09 \times 10^6\,\mathrm{s}^{-1}$ and a standard deviation of $\sigma_{\mathrm{PL}} = 40.1 \times 10^3\,\mathrm{s}^{-1}$. The fluctuations follow an expected Poisson distribution. We intensity-stabilized the laser diode such that the fluctuations of the laser are small compared to the fluctuations of the single-photon count rate. The devices are stable for at least > 4 months if stored at room temperature and normal pressure as the first device fabricated is still operational and we could not find a significant change (less than 7 %) in single-photon count rate or correlation function (see below). This proves that the source is able to operate on long timescales also under field conditions and paves the way for integration into future experiments.

6.3.3 Correlation function measurements

In order to confirm the true quantum nature of the emitted photons the second-order correlation function is measured using a Hanbury Brown and Twiss-type (HBT) interferometer with the setup used as shown in Figure 6.2(a). A laser beam is split into a pump beam and a reference beam which is utilized for alignments. The pump beam is expanded and then coupled into a home-built confocal microscope, with the fiber-end with the defect loaded at the diffraction-limited focal spot of a microscope objective (Olympus MPlanFL N 50x/0.8). The setup only utilizes off-the-shelf components and a standard laser diode. Other than in the usual in-reflection geometry, where the excitation and collection of the emission is done via the objective, here, in a first experiment the defect is excited via the objective, but the emission is directly collected with the fiber. Then, at the other end of the fiber, the light is collimated and possible remains of the pump light are filtered out. The light is then split by a 50:50 beam splitter and finally detected by two SPADs (PerkinElmer SPCM-AQR-16). The special feature of this experiment is that the photons can be generated in the same setup into the fiber or into free space, just by flipping four mirrors and re-positioning the longpass filter used to filter out the pump light (see Figure 6.2(b)). Thus, this setup offers to switch easily between free space single-photon generation and fiber-coupled single-photon generation. Note that the reference beam (see above) is also coupled into the HBT interferometer which then automatically couples the free space emission into the detectors. The results for fiber-coupled and free space operation are shown in Figure 6.2(c) and 6.2(d), respectively. The second order correlation function can be described with

$$g^{(2)}(\tau) = 1 - A_1 \exp\left(-\left|\frac{\tau - \mu}{t_1}\right|\right) + A_2 \exp\left(-\left|\frac{\tau - \mu}{t_2}\right|\right) \tag{6.3}$$

with A_1 and A_2 being the antibunching and bunching amplitude respectively and t_1 and t_2 being the characteristic antibunching and bunching time respectively. The parameter μ corrects for slightly different optical and electrical path lengths in the HBT interferometer.

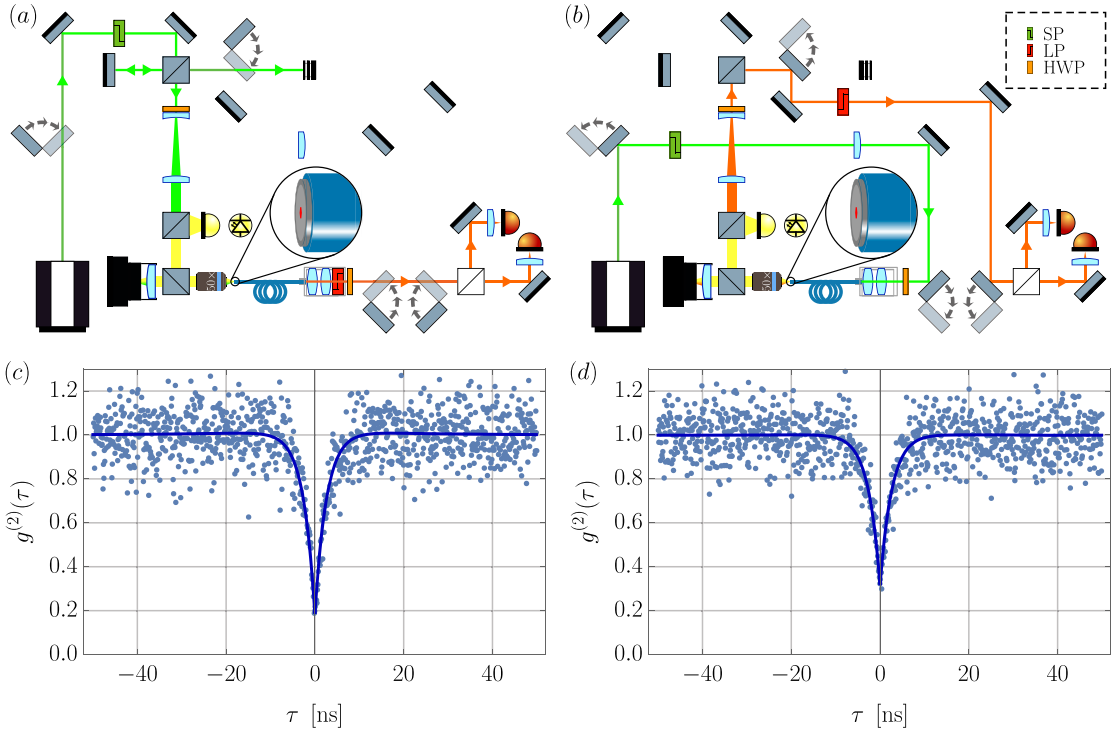

Figure 6.2: Measurements of the second-order correlation function. (a) Setup for operation in fiber-coupled-mode. For easing the coupling of the free space collection the laser is split into reference and pump beam. The pump light is then expanded and coupled into a confocal microscope with the fiber end with the hBN flake loaded at the focal point (small inset, the position of the hBN flake is indicated by a red hexagon). The light is then spectrally filtered and collimated. Finally, the emitted photons are detected in an HBT-type interferometer. (b) Setup for operation in free space-mode. By flipping the four flip mirrors, the defect can be excited via the fiber and the photons can be collected via free space. SP: Shortpass filter, LP: Longpass filter, HWP: Half wave plate. (c) $g^{(2)}(\tau)$ as measured at the fiber output. (d) $g^{(2)}(\tau)$ as measured with free space collection.

Also $g^{(2)}(\tau)$ has been normalized such that $g^{(2)}(\tau) \to 1$ for $\tau \to \infty$. From the fit we extract a $g^{(2)}(0) = 0.18 \pm 0.04$ for fiber-coupled operation and a $g^{(2)}(0) = 0.34 \pm 0.03$ for free space operation clearly indicating that the source is operating in the single-photon regime. The differences in the $g^{(2)}$ for free space and fiber-coupled operation can be explained by the fact that it is harder to address the distinct defect while pumping through the back end of the fiber and performing a free space readout.

6.3.4 Collection efficiency

We now turn to a calculation of the collection efficiency for the fiber. Contrary to an NV-center embedded in the high refractive index material of bulk diamond, this source has an intrinsic out-coupling efficiency of unity as no total internal reflection is restricting the efficiency to collect the emission. While the emission is often assumed to be isotropic into 4π, polarization-resolved PL from quantum emitters showed that the emitters typically exhibit an in-plane dipole[5, 10]. For an ideal dipole oriented perpendicular to the collection direction the fraction of the collected photons η_ϕ by an optical component with

an acceptance angle $\phi = 2\sin^{-1}(NA)$ (full angle) is calculated using antenna theory:

$$\eta_\phi = T_0 \cdot (T_1 + T_2 \cdot T_3) \tag{6.4}$$

where

$$T_0 = \frac{\phi}{2\pi} \tag{6.5}$$

$$T_1 = \frac{1}{2\pi}(2\phi - \sin(2\phi)) \tag{6.6}$$

$$T_2 = \frac{4}{\pi}\sqrt{\cos^{-2}(\phi/2) - 1} \tag{6.7}$$

$$T_3 = \left(1 + \tan^2(\phi/2)\sqrt{\cos^{-2}(\phi/2) - 1}\right)^{-2} \tag{6.8}$$

The distance between collection optics and emitter is assumed to be small compared to the diameter of the optics. For a numerical aperture $NA = 0.5$ we find a collection efficiency of $\eta_\phi = 10.15\%$.[2] Note that with this configuration the fiber has overfilled launch conditions making it sensitive to bending loss.

6.4 Conclusion

Aside from the measurements carried out with the TRPL setup the defect was excited with a laser in continuous wave mode. This yields of course single-photons in continuous wave mode which are not useful for quantum information processing. Using a short-pulsed excitation laser will allow testing the single-photon source in a real quantum information experiment. In order to maintain the compactness of the single-photon source a short-pulsed vertical-cavity surface-emitting laser (VCSEL) can be utilized. It is also possible to transfer the hBN onto the input port of a waveguide chip which would include the source directly on chip. We note that the difficulty of transferring onto a waveguide is the same as transferring onto a fiber.

In future experiments we will also test other materials and other specific defect types as well as different sample thicknesses and defect activation methods as it is then possible to achieve a narrower spectrum this way[10]. The defect then can be placed in between two distributed Bragg reflectors (DBRs), which suppresses noise and thus improves the $g^{(2)}(\tau = 0)$, enhances the directionality of the emission and cleans the spectrum.

In conclusion, we fabricated a fiber-integrated single-photon source in few-layered hBN. The emitted single-photons can be collected via free space- or fiber-coupled-mode just by switching the pump direction. Our setup shows the versatility of the source, as it is operational at room temperature. Measurements of the second-order correlation function dipping below 0.5 indicates that the source is operating in the quantum regime. Although these results are already promising, improvements suggested above making use of advantages of having the emitter in a cavity will improve the single-photon properties. This will then pave the way for high quality single-photon quantum information experiments with integrated photonics.

Note added: While preparing this manuscript we became aware of a recent similar

[2] It was later pointed out that the dielectric environment (air - hBN - silica) leads to a modified dipole emission pattern, which also affects the collection efficiency (see e.g. Figure 10.3(e) and (f)). A new FDTD simulation taking this into account revealed the actual system collection efficiency is 11.80%.

work from the groups of I. Aharonovich and S. Takeuchi[28].

Acknowledgments

This work was funded by the Australian Research Council (CE110001027, FL150100019, and DE140100805). We thank the ACT Node of the Australian National Fabrication Facility for access to their nano- and microfabrication facilities, particularly Naeem Shahid for technical support with the plasma system. We would also like to thank Hark Hoe Tan for access to the TRPL system.

References

[1] S. Z. Butler, S. M. Hollen, L. Cao, Y. Cui, J. A. Gupta, H. R. Gutiérrez, T. F. Heinz, S. S. Hong, J. Huang, A. F. Ismach, E. Johnston-Halperin, M. Kuno, V. V. Plashnitsa, R. D. Robinson, R. S. Ruoff, S. Salahuddin, J. Shan, L. Shi, M. G. Spencer, M. Terrones, W. Windl, and J. E. Goldberger, *Progress, Challenges, and Opportunities in Two-Dimensional Materials Beyond Graphene*, ACS Nano, **7** 2898–2926, 2013.

[2] A. Gupta, T. Sakthivel, and S. Seal, *Recent development in 2D materials beyond graphene*, Prog. Mater. Sci., **73** 44–126, 2015.

[3] A. K. Geim and K. S. Novoselov, *The rise of graphene*, Nat. Mater., **6** 183–191, 2007.

[4] K. S. Novoselov, V. I. Fal'ko, L. Colombo, P. R. Gellert, M. G. Schwab, and K. Kim, *A roadmap for graphene*, Nature, **490** 192–200, 2012.

[5] P. Tonndorf, R. Schmidt, R. Schneider, J. Kern, M. Buscema, G. A. Steele, A. Castellanos-Gomez, H. S. J. van der Zant, S. M. de Vasconcellos, and R. Bratschitsch, *Single-photon emission from localized excitons in an atomically thin semiconductor*, Optica, **2** 347–352, 2015.

[6] A. Srivastava, M. Sidler, A. V. Allain, D. S. Lembke, A. Kis, and A. Imamoğlu, *Optically active quantum dots in monolayer WSe2*, Nat. Nanotechnol., **10** 491–496, 2015.

[7] Y.-M. He, G. Clark, J. R. Schaibley, Y. He, M.-C. Chen, Y.-J. Wei, X. Ding, Q. Zhang, W. Yao, X. Xu, C.-Y. Lu, and J.-W. Pan, *Single quantum emitters in monolayer semiconductors*, Nat. Nanotechnol., **10** 497–502, 2015.

[8] M. Koperski, K. Nogajewski, A. Arora, V. Cherkez, P. Mallet, J.-Y. Veuillen, J. Marcus, P. Kossacki, and M. Potemski, *Single photon emitters in exfoliated WSe2 structures*, Nat. Nanotechnol., **10** 503–506, 2015.

[9] C. Chakraborty, L. Kinnischtzke, K. M. Goodfellow, R. Beams, and A. N. Vamivakas, *Voltage-controlled quantum light from an atomically thin semiconductor*, Nat. Nanotechnol., **10** 507–511, 2015.

[10] T. T. Tran, K. Bray, M. J. Ford, M. Toth, and I. Aharonovich, *Quantum emission from hexagonal boron nitride monolayers*, Nat. Nanotechnol., **11** 37–41, 2016.

[11] P. Kok, W. J. Munro, K. Nemoto, T. C. Ralph, J. P. Dowling, and G. J. Milburn, *Linear optical quantum computing with photonic qubits*, Rev. Mod. Phys., **79** 135–174, 2007.

[12] N. Gisin, G. Ribordy, W. Tittel, and H. Zbinden, *Quantum cryptography*, Rev. Mod. Phys., **74** 145–195, 2002.

[13] X. Ma, X. Yuan, Z. Cau, B. Qi, and Z. Zhang, *Quantum random number generation*, npj Quantum Inf., **2** 16021, 2016.

[14] A. Fedrizzi, T. Herbst, A. Poppe, T. Jennewein, and A. Zeilinger, *A wavelength-tunable fiber-coupled source of narrowband entangled photons*, Opt. Express, **15** 15377–15386, 2007.

[15] Q. Wang, W. Chen, G. Xavier, M. Swillo, T. Zhang, S. Sauge, M. Tengner, Z.-F. Han, G.-C. Guo, and A. Karlsson, *Experimental Decoy-State Quantum Key Distribution with a Sub-Poissionian Heralded Single-Photon Source*, Phys. Rev. Lett., **100** 090501, 2008.

[16] T. Zhong, X. Hu, F. N. C. Wong, K. K. Berggren, T. D. Roberts, and P. Battle, *High-quality fiber-optic polarization entanglement distribution at 1.3μm telecom wavelength*, Opt. Lett., **35** 1392–1394, 2010.

[17] X.-L. Wang, L.-K. Chen, W. Li, H.-L. Huang, C. Liu, C. Chen, Y.-H. Luo, Z.-E. Su, D. Wu, Z.-D. Li, H. Lu, Y. Hu, X. Jiang, C.-Z. Peng, L. Li, N.-L. Liu, Y.-A. Chen, C.-Y. Lu, and J.-W. Pan, *Experimental Ten-Photon Entanglement*, Phys. Rev. Lett., **117** 210502, 2016.

[18] M. Rambach, A. Nikolova, T. J. Weinhold, and A. G. White, *Sub-megahertz linewidth single photon source*, APL Photonics, **1** 096101, 2016.

[19] D. Heinze, D. Breddermann, A. Zrenner, and S. Schumacher, *A quantum dot single-photon source with on-the-fly all-optical polarization control and timed emission*, Nat. Commun., **6** 8473, 2015.

[20] X. Ding, Y. He, Z.-C. Duan, N. Gregersen, M.-C. Chen, S. Unsleber, S. Maier, C. Schneider, M. Kamp, S. Höfling, C.-Y. Lu, and J.-W. Pan, *On-Demand Single Photons with High Extraction Efficiency and Near-Unity Indistinguishability from a Resonantly Driven Quantum Dot in a Micropillar*, Phys. Rev. Lett., **116** 020401, 2016.

[21] N. Somaschi, V. Giesz, L. D. Santis, J. C. Loredo, M. P. Almeida, G. Hornecker, S. L. Portalupi, T. Grange, C. Antón, J. Demory, C. Gómez, I. Sagnes, N. D. Lanzilotti-Kimura, A. Lemaítre, A. Auffeves, A. G. White, L. Lanco, and P. Senellart, *Near-optimal single-photon sources in the solid state*, Nat. Photon., **10** 340–345, 2016.

[22] R. S. Daveau, K. C. Balram, T. Pregnolato, J. Liu, E. H. Lee, J. D. Song, V. Verma, R. Mirin, S. W. Nam, L. Midolo, S. Stobbe, K. Srinivasan, and P. Lodahl, *Efficient fiber-coupled single-photon source based on quantum dots in a photonic-crystal waveguide*, arXiv:1610.08670, 2016.

[23] T. M. Babinec, B. J. M. Hausmann, M. Khan, Y. Zhang, J. R. Maze, P. R. Hemmer, and M. Lončar, *A diamond nanowire single-photon source*, Nat. Nanotechnol., **5** 195–199, 2010.

[24] R. V. Gorbachev, I. Riaz, R. R. Nair, R. Jalil, L. Britnell, B. D. Belle, E. W. Hill, K. S. Novoselov, K. Watanabe, T. Taniguchi, A. K. Geim, and P. Blake, *Hunting for Monolayer Boron Nitride: Optical and Raman Signatures*, Small, **7** 465–468, 2011.

[25] C. W. Nam and S. Ashok, *ECR hydrogen plasma treatment of Si: defect activation under thermal anneal*, Proc. ICSICT **4** 565–567, 1995.

[26] S. P. Singh, R. Gangwar, and N. Singh, *Nonlinear scattering effects in optical fibers*, Prog. Electromagn. Res., **74** 379–405, 2007.

[27] Y. Miyauchi, M. Iwamura, S. Mouri, T. Kawazoe, M. Ohtsu, and K. Matsuda, *Brightening of excitons in carbon nanotubes on dimensionality modification*, Nat. Photon., **7** 715–719, 2013.

[28] A. W. Schell, H. Takashima, T. T. Tran, I. Aharonovich, and S. Takeuchi, *Coupling quantum emitters in 2D materials with tapered fibers*, arXiv:1701.02696, 2017.

Chapter 7

Fabrication and Deterministic Transfer of High-Quality Quantum Emitters in Hexagonal Boron Nitride

7.1 Foreword

The previous chapter presented the early work of integrating a quantum emitter hosted by hBN with a multimode fiber. This was already an important milestone toward practical applications, as it shows how easily these emitters can be integrated with photonic networks. The direct integration with fibers reduces the complexity of fiber-based quantum key distribution, as the quantum light source is already on the fiber. In addition, the approach can be applied directly to waveguides, allowing for the fabrication of on-chip single-photon sources for photonic quantum processors.

A problem that will inhibit any such applications is the broadband emission spectrum, the long excited state lifetime, and the poor single-photon purity. It is worth noting, that the excited state lifetime is already much shorter than is typical for other solid-state color centers (e.g. the negatively charged NV center in diamond has a decay time of $\sim 20\,\mathrm{ns}$[203]). Thus, with decay times $\sim 2\,\mathrm{ns}$, the reported emitters in hBN already have a one order of magnitude faster decay, but an even faster decay is desirable. This in turn allows for efficient post-selection to suppress single-photon detector dark counts, making quantum information processing more robust, as well as enabling fundamentally higher repetition rates.

The emitters have been fabricated using a plasma process. This chapter presents the full optimization of the fabrication cycle. This includes varying the plasma conditions as well as the subsequent rapid thermal annealing. The process, however, cannot be applied to crystals transferred to fiber tips. Therefore, a transfer process for the optimized emitters was developed, allowing one to transfer and use the emitters again on any arbitrary substrate, including fibers and waveguides. To study significant changes in photophysics owing to the different fabrication parameters, the fabrication of a great number of emitters was required. This is due to the fact that in general, the photophysics of quantum emitters in hBN strongly varies, with the optical properties randomly distributed. While the reason for this is not yet fully understood, Chap. 10 gives a more in-depth investigation into this. One of the key results of this study is that the photophysics do not correlate with the fabrication parameters. Nevertheless, the performance was improved

significantly, establishing the foundation for the following works toward practical quantum information processing in the following chapters. This work has been published in and is here reprinted (adapted) with permission from ACS Photonics **5**, 2305-2312 (2018). All graphics have been recreated to match the style of this thesis.

Fabrication and Deterministic Transfer of High-Quality Quantum Emitters in Hexagonal Boron Nitride

Tobias Vogl[1], Geoff Campbell[1], Ben C. Buchler[1], Yuerui Lu[2], and Ping Koy Lam[1]

[1] *Centre for Quantum Computation and Communication Technology, Department of Quantum Science, Research School of Physics and Engineering, The Australian National University, Acton ACT 2601, Australia*

[2] *Research School of Engineering, The Australian National University, Acton ACT 2601, Australia*

Abstract

Color centers in solid-state crystals have become a frequently used system for single-photon generation, advancing the development of integrated photonic devices for quantum optics and quantum communication applications. In particular, defects hosted by two-dimensional (2D) hexagonal boron nitride (hBN) are a promising candidate for next-generation single-photon sources, due to its chemical and thermal robustness and high brightness at room temperature. The 2D crystal lattice of hBN allows for a high extraction efficiency and easy integration into photonic circuits. Here we develop plasma etching techniques with subsequent high temperature annealing to reliably create defects. We show how different fabrication parameters influence the defect formation probability and the emitter brightness. A full optical characterization reveals the higher quality of the created quantum emitters, represented by a narrow spectrum, short excited state lifetime and high single-photon purity. We also investigated the photostability on short and very long time scales. We utilize a wet chemically assisted transfer process to reliably transfer the single-photon sources onto arbitrary substrates, demonstrating the feasibility for the integration into scalable photonic quantum information processing networks.

7.2 Introduction

Since the rediscovery of graphene[1], the field of two-dimensional (2D) materials[2, 3] has attracted great interest due to its possible applications in electronics[4], optoelectronics and photonics[5] as well as advanced sensing[6] and uses in biophysics[7]. More recently, the insulating 2D material hexagonal boron nitride (hBN) has drawn the attention of many researchers due to its ability to host high luminosity room temperature single-photon sources (SPSs)[8]. In particular, the outstanding chemical and thermal stability of hBN leads to excellent robustness of the single quantum emitters, which have demonstrated long-term stable operation[9]. In addition, unlike NV centers in diamond, monolayered 2D material based single-photon sources have an almost ideal out-coupling efficiency of unity, as none of the emitters are surrounded by any high refractive index material and are not affected by Fresnel or total internal reflection[10].

The single-photon generation mechanism is based on trapping sites at point defects in the crystal lattice, which introduce energy states in the electronic band gap. While this is the generally accepted model, the exact nature of the defects remains unresolved and controversial. First-principles calculations using density functional theory and group theory

analysis have already given some insight into the energy level structure[11, 12]. However, the diversity of zero phonon lines (ZPLs), which vary from defect to defect, spanning the full visible spectrum[13] down to the UV[14] shows that deeper analysis and further experimental investigations are necessary.

Single-photon sources are important for quantum optics, quantum communication[15] and optical quantum computing[16]. These fields allow for the realization of unconditionally secure communication and efficient solutions for mathematically hard problems and simulations that are intractable for even the most powerful classical supercomputers. Protocols in these quantum information processing schemes require narrower emission linewidths and shorter excited state lifetimes of the trapped excitons than reported so far for single-photons in hBN at room temperature. Protocols of particular interest include quantum key distribution with single-photons (such as BB84[15]) or single-photon interferometry[17]. Optical quantum computing requires transform limited single-photons with lifetime-bandwidth products on the order of 1[16]. To date, single-photons generated from 2D materials have lifetime-bandwidth products ranging from 6×10^3 to 2×10^4 above the transform limit at room temperature[8, 13, 18–20]. First attempts of engineering the defect formation have been successful, using either ion irradiation[21], chemical etching[22] or plasma etching[9].

In this article, we describe methods to enhance the yield of particularly high quality single-photon emitters in mechanically exfoliated hBN. The primary defect creation mechanism is oxygen plasma etching[9], while the defect activation relies on high temperature thermal annealing[8]. We investigate how plasma parameters and annealing temperatures influence the formation probability and brightness of the quantum emitters and fully characterize their optical properties in terms of spectral distribution, excited state lifetime, power-dependence and photostability on short and prolonged time scales. Finally, we employ a universally applicable wet chemical transfer method for transferring the single-photon sources onto arbitrary substrates, allowing for an easy integration into photonic circuits and networks.

7.3 Device fabrication

Starting with bulk crystal hexagonal boron nitride, multilayer flakes are mechanically exfoliated onto a viscoelastic foil. Using contrast-enhanced microscopy, thin flakes are selected by optical contrast and transferred by dry contact[23] to a Si substrate with a 280 nm thermally grown insulating capping layer (SiO_2). The flake thickness is measured by phase-shift interferometry (PSI), where the optical path length (OPL) through the flake is converted to physical thickness via rigorous coupled-wave analysis (RCWA) simulations[24]. By measuring the physical flake thickness of a few flakes using atomic force microscopy (AFM), the RCWA simulations of the OPL yield the refractive index of hBN of 1.849(134) for green light, which matches well previous results[25]. Knowing the exact refractive index allows for extrapolating the RCWA simulations, so that they serve as a conversion measure between OPL and physical thickness. A microscope image of an example flake is shown in Figure 7.1(a), together with the corresponding PSI map in Figure 7.1(b). However, for hBN on Si/SiO_2 the RCWA simulations yield only reliable results for (physical) flake thicknesses < 40 nm, as the simulations give an ambiguous outcome for optical path lengths of > 50 nm, as shown in Figure 7.1(c). Thus, larger flake thicknesses are measured using AFM. We studied a large variety of flake thicknesses and found crystals with step heights ranging from 4 nm to roughly 100 nm were capable of hosting a

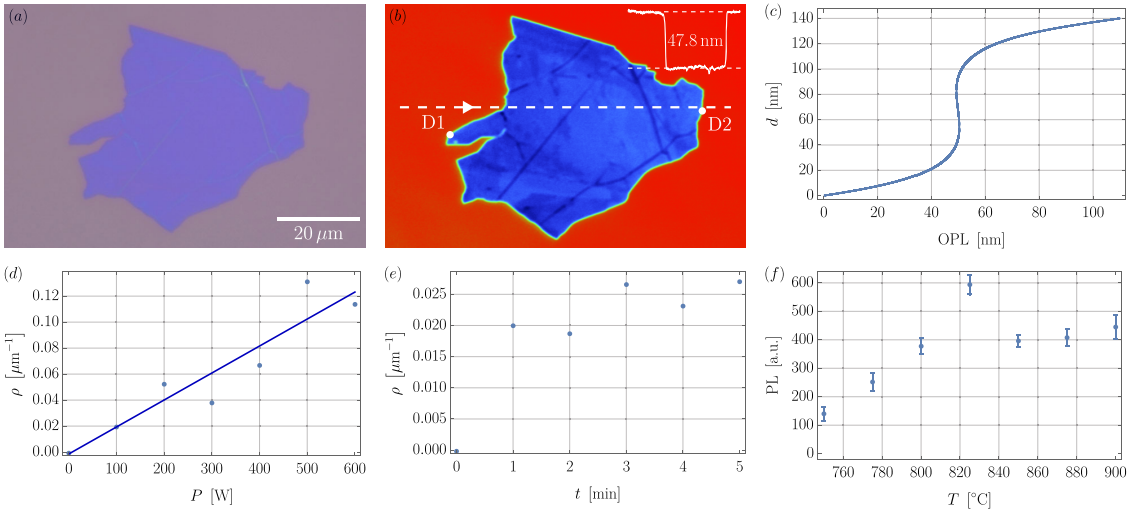

Figure 7.1: Fabrication parameters. (a) Optical microscope image of an hBN crystal. (b) PSI image of the crystal. The small inset shows the OPL difference along the dashed line. (c) RCWA simulations of the physical thickness d as a function of OPL for hBN on Si/SiO_2, calibrated with AFM and PSI measurements. For OPLs around 50 nm the simulations become ambiguous. (d) The linear defect density increases linearly with the plasma power. The plasma time was 1 min. (e) At a constant plasma power of 100 W the linear defect density remains approximately constant for different plasma times. (f) Influence of the annealing temperature on the average ZPL brightness. The error bars denote the standard deviation.

single-photon emitter.

In order to create the defects, the flakes are treated with an oxygen plasma and thermally annealed to activate the color centers under an argon atmosphere. In the interest of maximizing the quantum emitter yield per flake as well as optimizing the single-photon spectral properties, we varied the plasma power, plasma time, and annealing temperature. After plasma etching and thermal annealing the hBN samples are optically characterized in a confocal micro-photoluminescence (μPL) system scanning each flake and mapping the PL response. With the laser excitation wavelength being at 522 nm ($E = 2.38$ eV), the photon energy is well below the band gap of hexagonal boron nitride ($E_g = 5.955$ eV[26]), preventing any delocalized free excitonic emission. With the photon energy of the laser being more than a factor of 2 below band gap and keeping the excitation power well below saturation (see the next section), multiphoton excitation does not play a major role. As pure hexagonal boron nitride is optically inactive in the visible spectrum, regions with a large PL response are considered as candidates for hosting single-photon emitters. During this confocal mapping, a spectrum has been taken for each scanning position. All measurements have been carried out at room temperature.

For the sake of a fair comparison we define the average linear density of emitters per edge length $\rho = N/L$, as larger flakes are more likely to host defects, independent of the initial plasma parameters. We did not choose to take the areal density as the emitters are almost exclusively created at the boundaries of the flakes. This is a result of a low defect formation energy at the edges of the flake. We studied plasma powers varying from 100 to 600 W generated from a microwave field with total plasma times ranging from 1 to 5 min. At this stage in the process, all samples have been subsequently annealed at 850°C. Figure 7.1(d) shows the linear density per unit edge length as a function of plasma power, which exhibits a linear increase in defect density with plasma power (see fit). This can be

explained by the fact that at higher powers the plasma is denser, leading to the formation of more defects. When keeping the plasma power constant at 100 W and varying the plasma times as shown in Figure 7.1(e), the linear defect density remains approximately constant. This is due to etching effects in the oxygen plasma, which is not only creating the defects, but also etching the hBN flakes layer by layer. Even though the etching rate is power-dependent, a single layer is etched faster than the time scales investigated here, so longer plasma times tend to remove already formed defects. It is worth noting, however, that the plasma field is highly anisotropic (conditioned by the gas pump, plasma generator and chamber geometry) and the plasma power varies across the plasma chamber, with the field weakening toward the center of the chamber. Thus, we tried to position the substrates always at the same distance from the chamber walls, but repeating this experiment in a different plasma chamber will require using different plasma powers than the ones reported here.

For the next part of this study we kept the plasma power constant at 100 W for 1 min and varied the subsequent annealing temperature from 750 to 900°C under an inert argon atmosphere. Annealing under vacuum reduces the defect yield drastically. As the defects are created during the interaction with the plasma and are only optically activated and stabilized during the annealing, we use the average brightness of the ZPL as a figure of merit for a good annealing temperature, while the excitation laser power was kept constant (see Figure 7.1(f)). The practically usable interval of annealing temperatures spans from 800 to 850°C, similar to previously reported annealing temperatures[8, 13, 27]. Lower annealing temperatures lead to weak ZPLs, where the defects are not fully optically activated, while higher annealing temperatures cause the defects to diffuse too much. Especially the latter effect is present for long annealing times as well; hence we employed rapid thermal annealing (RTA) instead of standard furnace annealing. We note that unlike in previous reports[8,13], annealing in a tube furnace did not yield any bright and stable single-photon emitters in our experiments.

7.4 Optical characterization

We now turn to a full characterization of the single-photon emitters. The sample crystal shown in Figure 7.1(a) hosts two defects, with their positions labeled D1 and D2 in Figure 7.1(b). The spectrum of D1 is shown in Figure 7.2(a) and from a fit we extract the ZPL at a wavelength of 553.23 (5) nm and a linewidth of 2.82 (10) nm. Unless stated otherwise, we use a 95 % confidence interval for the uncertainties, calculated using Monte Carlo simulation methods. This defect emitted 82.4 % into its ZPL. Using a Hanbury Brown and Twiss (HBT)-type interferometer, we measure the second-order correlation function (see Figure 7.2(b)), with $g^{(2)}(\tau = 0)$ dipping to 0.330(28), obtained by fitting a three-level system with ground and excited states as well as a metastable shelving state:

$$g^{(2)}(\tau) = 1 - Ae^{-|\tau-\mu|/t_1} + Be^{-|\tau-\mu|/t_2} \tag{7.1}$$

where t_1 and t_2 are the excited and metastable state lifetimes, respectively, μ accounts for different electrical and optical path lengths in the HBT interferometer, and A and B are the anti-bunching and bunching amplitudes. The experimental data have been normalized such that for very long time delays $g^{(2)}(\tau \to \infty) = 1$. In all correlation function measurements no background correction has been applied, as these measurements are not yet dark count limited; the dark counts from the used detectors are very low compared

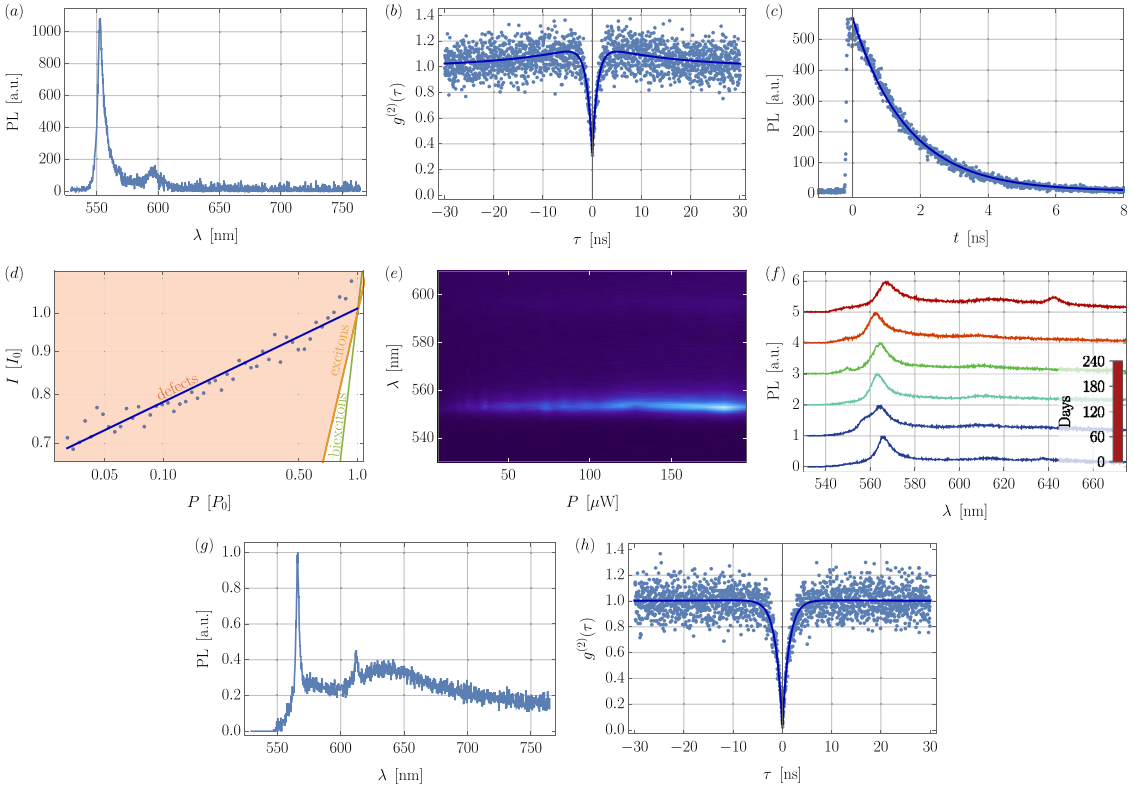

Figure 7.2: Optical characterization of fabricated defects. (a) Spectrum measured in-reflection after an ultrasteep longpass filter (opening at 530 nm) coupled into a high-resolution spectrometer. Excited at a wavelength of 522 nm, the ZPL is at 553.23(5) nm with a linewidth of 2.82(10) nm. (b) Second-order correlation function dipping at zero time delay to 0.330(28) (obtained from fit). (c) Time-resolved photoluminescence using an ultrashort pulsed laser, revealing an excited state lifetime of $\tau = 1.123(7)$ ns. (d) Log-log-plot of the photoluminescence response as a function of excitation power. The red-shaded area (slope $\alpha < 1$) indicates emission from defects, while the orange line ($\alpha = 1$) corresponds to free excitonic emission and the green line ($\alpha = 2$) biexcitonic emission. The slope $\alpha = 0.350(54) < 1$ of the linear fit confirms defect emission. (e) Spectrally resolved power-dependence measurement. The emitter showed some power-dependent photobleaching. (f) Long-term stability of a defect over a duration of 8 months (normalized and vertically offset for clarity). The center of the ZPL remains stable within ±2.5 nm, while its linewidth increases with time. (g) Spectrum of the best single-photon emitter we found with a ZPL at 566.04(4) nm and a linewidth of 1.31(7) nm. 8.7 % of the emission is into the ZPL. (h) The second order correlation of the defect with the spectrum shown in (g) dips to 0.033(47) at zero time delay.

to the single-photon count rate (see Methods). The μPL system is equipped with an ultrashort pulsed laser with a 300 fs pulse length at a repetition rate of 20.8 MHz, allowing us to measure the exciton lifetime as well, with the lifetime of D1 shown in Figure 7.2(c). A fit of a single exponential decay reveals an excited state lifetime τ of 1.123(7) ns. The shelving state lifetime is not accessible from this measurement due to its weak transition and longer lifetime. However, the decay time is consistent with the correlation function measurements: From the fit of the $g^{(2)}$ function we obtain $t_1 = 1.100(134)$ ns and $t_2 = 15.441(4168)$ ns (all other fit parameters are summarized in the Supporting Information S1). Together with its linewidth $\Delta\nu = \frac{c\Delta\lambda}{\lambda^2}$ this yields a lifetime-bandwidth product of 3102, still far above the transform limit, but better than any reported emitter in hBN so

far. In addition we measured the PL intensity as a function of excitation power, which is described by

$$I(P) = \frac{I_{sat} \cdot P}{P + P_{sat}} + I_d \tag{7.2}$$

with I_{sat} and P_{sat} being the saturation intensity and power, respectively, and I_d is the dark count intensity. From a fit we extract $P_{sat} = 142.6(685)\,\mu$W. Together with a focal spot diameter of $0.67\,\mu$m and a duty cycle of 6.24×10^{-6} this amounts to a peak intensity of $1.62\,\mathrm{GW\ cm^{-2}}$, which is still below the damage threshold. Figure 7.2(d) shows this measurement together with the fit on a log-log-scale, which confirms the defect nature of the emission: A slope of $\alpha = 1$ indicates free excitonic emission (orange line), while $\alpha = 2$ reveals the presence of biexcitons (green line) and $\alpha < 1$ verifies trapped excitons from a defect (red-shaded area)[28]. The power-dependence of D1 has a slope of $\alpha = 0.350(54)$, clearly in the defect emitter region. Furthermore, we measured the power-dependent photostability, which is shown in Figure 7.2(e). Defect D1 showed some power- as well as time-dependent photobleaching. The power-dependent photobleaching causes the deviations from the linear fit in Figure 7.2(d) and is also the reason for the large confidence interval on P_{sat}. However, we have also found emitters that were photostable. Finally, we also look at the long-term stability, meaning repeating all measurements above for a subset of samples over a time span of more than 8 months. In between measurements the samples were stored under normal atmosphere in air. Figure 7.2(f) shows the spectra for different days, all normalized and offset vertically for clarity. With the center of the ZPL being constant within ± 2.5 nm, its linewidth increases over time from 4.38(13) nm to 6.61(25) nm. Other optical properties such as τ, α and $g^{(2)}(0)$ are varying as well, without showing a clear trend in the case of α and $g^{(2)}(0)$ (see Supporting Information S2), while τ shortens with an increase in linewidth (see also the next section). The variations can be explained by the fact that 2D materials typically oxidize in an ambient environment. The stability in air is ultimately controlled by the oxygen dissociative absorption barrier and is also affected by defects present. As the host crystal is very thin and the interactions within the crystal are strong, already small variations can cause large changes in the photophysical properties. Isolating the crystal from any coupling to the environment, such as through encapsulation, can improve the long-term stability, but the influence of the encapsulation layer must be investigated. Nevertheless, the defects maintain their single-photon emission properties on short and very long time scales and at the same time keep the photophysical properties (for a 2D material) constant within the reported limits.

7.5 Correlating optical properties

The optical properties as described in the previous section are by no means representative for all defects, but are typical photophysical properties. The optical properties in terms of spectral distribution, excited state lifetime, power-dependence, photostability, and second-order correlation function vary not only from flake to flake but also from defect to defect hosted by the same flake. As reported previously[13], the ZPLs cover the full visible spectrum below the excitation photon energy. In our experiments the quantum emitter ZPLs span a range from 550 to 720 nm, with the lower limit set by a longpass filter used to filter out the excitation laser and the upper limit set by the spectrometer bandwidth.

The linewidths vary from as low as 1.31(7) nm (see Figure 7.2(g)) to 11.6(4) nm at room temperature, while the exciton lifetimes span a smaller range from 294(3) ps to 1.32(1) ns[1]. This is more than 1 order of magnitude faster than any previously reported excited state lifetime in hBN; in fact, all of the defects have shorter lifetimes than the fastest previously reported ones (see also Supporting Information S4). The single-photon purities characterized by $g^{(2)}(0)$ vary from 0.033(47) to 0.480(38) (excluding any emitter with $g^{(2)}(0) > 0.5$, which are considered ensembles). A single-photon purity with $g^{(2)}(0) = 0.033(47)$ (see Figure 7.2(h)) in hBN is only matched by emitters coupled to plasmonic nanocavity arrays[29], with $g^{(2)}(0) = 0.02 - 0.04$. This defect has a time-bandwidth product of 1389. The slopes of the power saturation vary from 0.290(56) to 0.942(43) for different defects. Across all defects, the optical properties are randomly distributed with the exception of the zero phonon line, which with a 53 % chance is between 550 and 570 nm (see Supporting Information S4).

The natural question then arises whether there is any correlation between the optical properties and especially between the optical properties and the fabrication parameters or geometrical features of the host crystal flakes. By studying a large variety of flakes and cross-correlating optical properties, we found that a narrow linewidth correlates with a longer excited state lifetime, even though the single-photons are still above the transform limit (see Supporting Information S3). The smallest time-bandwidth product was 807 at room temperature, which is 1 order of magnitude smaller than any previously reported value. The mean of 3782 for this product shows the higher quality of the emitters, compared to emitters fabricated by other methods[8, 13, 18–20]. So far it seems that neither the fabrication parameters nor the physical crystal thickness at the defect position has any influence on the emission spectra, lifetimes, purities or α. The latter demonstrates that the interaction of the in-plane dipole with surrounding layers is probably small. Even though it remains obscure why defects formed by plasma etching of the host crystals perform better and have particularly short lifetimes, we have seen that this process reliably creates a large number of higher quality single-photon emitters (see also Supporting Information S4). In total we studied more than 300 flakes hosting more than 200 defects. Each flake hosted between 0 and 7 defects, with the average number being 2.55 (not counting the flakes hosting no defect).

7.6 Deterministic transfer of quantum emitters

Finally, we demonstrate a deterministic transfer of the quantum emitters onto arbitrary substrates. The Si/SiO_2 substrates, on which the hBN flakes are bonded by van der Waals force, are good for characterization, but from an application point of view, the single-photon emitter must be integrated into photonic devices or networks. It is possible to transfer the flakes directly from the polymer foil onto the photonic device before plasma treatment and thermal annealing, but as the defects are formed at random positions this is not favorable. Furthermore, the high annealing temperature may damage integrated single-photon devices. For monolayer transition metal dichalcogenides (TMDs) it has been demonstrated that stress induced by nanopillars allows the formation and precise positioning of quantum emitter arrays[30]. Here we employ a wet chemical transfer method developed to transfer TMDs from SiO_2 onto other substrates[31]. The technique is

[1] 1.31 nm linewidth and 1.32 ns lifetime are not from the same defect, the same holds for 11.6 nm and 294 ps.

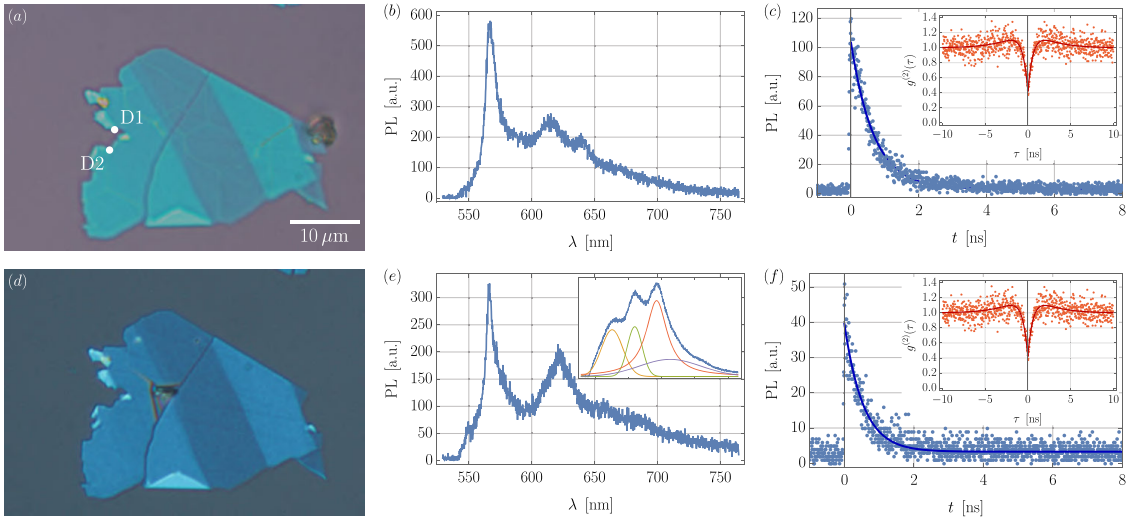

Figure 7.3: Deterministic transfer of a quantum emitter. (a, d) Optical microscope image before and after the transfer at 1000× magnification. The locations of defects D1 and D2 are marked with white dots. (b, e) Spectrum of D2 before and after the transfer. The ZPL peaks at 567.61(8) nm, which is marginally blue-shifted to 567.39(13) nm after the transfer. The small inset in (e) shows the spectrum before the plasma cleaning: From a fit four peaks can be extracted, which can be assigned to PVP (orange), NVP (green) and PVA (red). The horizontal axis has the same scale as the large spectrum, while its vertical axis is on a much larger scale. (c, f) Time-resolved photoluminescence response before and after the transfer. The excited state lifetime is $\tau = 468(8)$ ps and is shortened to $\tau = 375(15)$ ps after the transfer. The purity remains approximately constant (small insets), with $g^{(2)} = 0.416(55)$ and $g^{(2)} = 0.433(57)$ before and after the transfer, respectively.

based on using a two-component polymer mediator, which consists of polyvinylpyrrolidone (PVP) / N-vinylpyrrodoline (NVP) and poly(vinyl alcohol) (PVA), where the PVP/NVP provides good adhesion to the crystal while the PVA reinforces the mechanical strength of the PVP film. However, as the hBN flakes have considerably more layers compared to monolayered crystals, we adapted the polymer concentrations (see Methods). The solutions are spin coated onto the sample, and the resulting polymer carpet can be pressed onto a new viscoelastic foil, from which it can be transferred to its new substrate. Then the PVP/NVP dissolves easily in water.

After the transfer all hBN crystals exhibited a strong broadband PL emission with peak maxima at 575.5, 609.6, 642.5 and 662.9 nm (see Figure 7.3(e), small inset), making it impossible to resolve the single-photon ZPL. This PL was traced back to polymer chains remaining on the hBN, with PVP peaking around 576.4 nm, NVP peaking around 605.2 nm, and PVA peaking around 619.6 nm. The hBN red-shifts the PVA peak, explaining the third large background peak. The polymers adhered to the hBN even after soaking in distilled water for 14 h at elevated temperatures of 60°C for accelerated solution, meaning that the adhesion of the polymer to the hBN is stronger than its solubility in water. The solubility in other polar protic solvents (mostly alcohols) turned out to be too low as well. Finally, using low power oxygen plasma cleaning, the polymers can be fully removed. However, great care must be taken such that the hBN itself is not etched. It shall be mentioned that the 2D materials community developed a great toolbox of other transfer techniques, for example utilizing different polymers for the pick-up[32]. Using different polymers for the transfer might not introduce fluorescent residues.

We characterized the single-photon emission properties before and after a full transfer cycle. The example flake presented here hosted two defects, which both have survived the transfer. An optical microscope image prior to the transfer is shown in Figure 7.3(a), with both defects marked with yellow dots labeled D1 and D2. The spectrum and lifetime before the transfer process are shown in Figure 7.3(b) and (c), respectively. The small inset in (c) is the second-order correlation function. Prior to contact with the polymers the ZPL was at 567.61(8) nm with a linewidth of 4.99(17) nm and the lifetime was 468(8) ps with $g^{(2)}(0) = 0.416(55)$. After the full transfer process including plasma cleaning, the microscope image shows additional cracks in the host crystal (see Figure 7.3(d)), but the part with the single-photon emitter is not affected. Intermediate microscope images after each step show that the cracks are not caused by the polymers, but rather occur during peeling off the polymer carpet from the initial substrate. Repeated experiments proved that this happens only where the host crystal already has cracks prior to the transfer process (see Figure 7.3(a)). Defects that are close to such cracks are therefore not suitable for this transfer method. The ZPL is slightly blue-shifted to 567.39(13) nm with the linewidth unchanged, as shown in Figure 7.3(e). The defect's ZPL peak brightness is only 53.47 % of the brightness before the transfer, with the phonon sideband approximately equally strong compared to prior to the transfer. This results in 13.0 % of the light being emitted into the ZPL, which was 24.9 % prior to the transfer. Narrow filtering of the ZPL nevertheless allowed measurement of the excited state lifetime, which is shortened to 375(15) ps with $g^{(2)}(0)$ increased to 0.433(57). The shortening of the lifetime might be due to small alterations of the host crystal structure (meaning the defect's environment) during the plasma cleaning. The same might apply for the reduction of emission into the ZPL. Further optimization of the transfer process might increase the overall performance of the transfer cycle, especially in reference to the loss in brightness of the ZPL. However, so far every transfer cycle was successful. A full process cycle starting with the bulk hBN to the chemical transfer process is shown in Figure 7.4.

7.7 Conclusion

The fabrication techniques reported here demonstrate how oxygen plasma etching can create color centers in exfoliated multilayer hexagonal boron nitride that form, after optical activation through thermal annealing, stable single-photon emitters. The emitters show excellent optical properties in terms of narrow linewidths and lifetimes as short as 294 ps, which are 1 order of magnitude shorter than reported so far, allowing for a high operational bandwidth of the single-photon source. Extended statistics show that many emitters with these photophysical properties are created, almost all of which have a lower time-bandwidth product at room temperature than previously reported. The emitters are also very robust, maintaining their single-photon emission capabilities over the time frame of this experimental work, which is currently 8 months. However, due to the substantial variation of even basic optical properties such as ZPL position in the spectrum or excitonic lifetime even from emitter to emitter hosted by the same flake, the exact nature of the defect remains obscure. This indicates that different defects are present, which is additionally emphasized by the fact that we did not find a correlation between single-photon emission properties and the fabrication parameters or geometrical features of the host crystals. Finally, we have also demonstrated that these quantum emitters can be transferred reliably, while preserving their single-photon emission capabilities. This technique allows the integration of the single-photon sources into photonic circuits

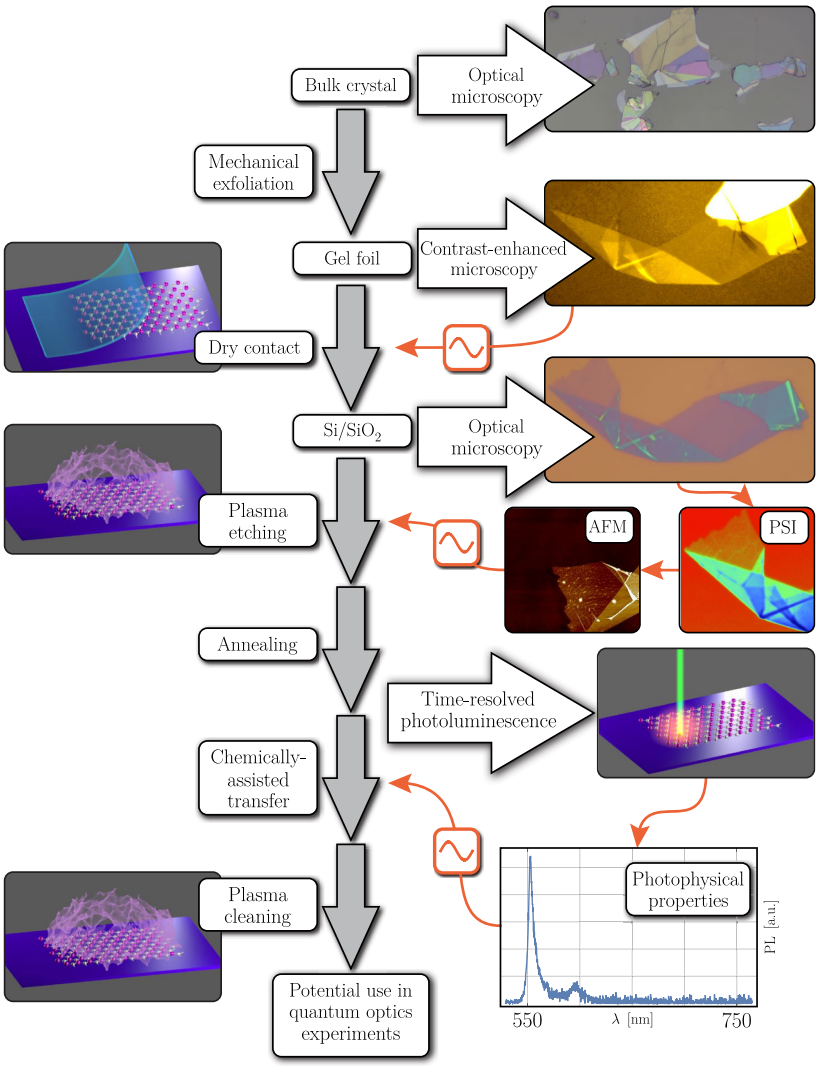

Figure 7.4: Full process cycle for hBN quantum emitter fabrication. The left column shows the processes introduced, and the right column shows the characterization and selection of samples. The central column shows the development of the sample. hBN flakes are initially exfoliated from the bulk crystal. The flakes are first optically identified using contrast-enhanced microscopy. Appropriate flakes are selected for a dry contact transfer to Si/SiO_2 substrates. The transferred flakes are again selected for flake thickness measurement using phase-shift interferometry (PSI). Depending on the optical path length value, the exact physical thickness is measured using atomic force microscopy (AFM). Crystals with thicknesses in the suitable range undergo oxygen plasma etching and thermal annealing, after which they are fully optically characterized in a time-resolved photoluminescence (TRPL) setup. Flakes with good photophysical properties could be transferred onto waveguides or fibers, where the single-photon sources could be used in a potential quantum optics experiment.

and networks, such as fibers and waveguide platforms. Thus, this provides a building block for next-generation quantum information processing. Only commonly available nanofrabrication processes have been used, making the fabrication easy and repeatable.

Note added: While under review we became aware of a recent related work[33].

7.8 Methods

Sample fabrication

The bulk crystal was acquired from HQGraphene, exfoliated to Gel-Pak WF-40-X4, and transferred by dry contact to Si/SiO_2 substrates (280 nm thermally grown). After thickness measurements using PSI or AFM the samples were treated with microwave plasmas of different powers and lengths. The pressure for all plasmas was set to 0.3 mbar at an oxygen gas flow rate of 300 cm^3/min at room temperature. Subsequent annealing at different temperatures for a few minutes under an argon atmosphere took place in a rapid thermal annealer. After multiple evacuations of any residual gases the Ar flow was set to 500 cm^3/min. After the annealing the samples cooled at their natural cooling rate, without keeping the cooling rate at a maximal value.

Optical characterization

The home-built micro-photoluminescence setup used an ultrashort pulsed frequency-doubled 1044 nm laser (High Q Laser URDM) focused down to the diffraction limit by an Olympus 100×/NA = 0.9 dry objective. The samples were mounted on Newport piezoscanning stages with 0.2 μm resolution. The emission, collected through the same objective, was frequency-filtered (Semrock RazorEdge ultrasteep long-pass edge filter) to dump the excitation light and guided to a spectrometer (Princeton Instruments SpectraPro). The pulse length of the laser was 300 fs at a repetition rate of 20.8 MHz. The laser pulses were split into trigger and excitation beams and a single-photon counter (Micro Photon Devices) detected the emitted photons after the trigger signal. The temporal correlation between trigger time and single-photon arrival time was given by a PicoHarp 300. The second-order correlation function was measured in a different setup using a 512 nm diode laser. This setup was equipped with a nanopositioning stage and a spectrometer as well. The single-photon counters used in this setup are PerkinElmer SPCM-AQR-16, which are ultralow dark count single-photon counting module with dark count rates as low as 20 s^{-1}.

Transfer process

The method was developed in ref [31], but the polymer concentrations for hBN have been adjusted. The target substrates were initially plasma cleaned. The samples were pre-baked at 80°C for $1-2$ min and subsequently spin coated at 2000 rpm for 50 s with a PVP/NVP solution (1.7 g of PVP + 1.5 mL of NVP + 0.75 mL of H_2O + 7 mL of ethanol, dissolved at 40°C and filtered) and then post-baked for $1-2$ min. This was repeated with a 9 % PVA solution (molecular weight in DI water). The resulting polymer was peeled off at the edges using a scalpel and then pressed onto a new gel foil (Gel-Pak WF-40-X4) and the polymer carpet remains on the foil. Next, the crystal was transferred to a new sample by standard means. After baking the new substrate with the gel foil attached at 120°C for $3-5$ min, the polymer remained on the new substrate and was dissolved in DI water for 1 h and rinsed with IPA. A final plasma cleaning step removed remaining polymer chains.

Acknowledgments

This work was funded by the Australian Research Council (CE110001027, FL150100019, and DE140100805). We thank the ACT Node of the Australian National Fabrication Facility for access to their nano- and microfabrication facilities, particularly Kaushal Vora for technical support with the RTA and Fouad Karouta for technical support with the plasma system. We also thank Hark Hoe Tan for access to the TRPL system.

Supplementary information

The supplementary information is available free of charge on the ACS Publications website at https://doi.org/10.1021/acsphotonics.8b00127 or in the Appendix A.2.

References

[1] K. S. Novoselov, A. K. Geim, S. V. Morozov, D. Jiang, Y. Zhang, S. V. Dubonos, I. V. Grigorieva, and A. A. Firsov, *Electric Field Effect in Atomically Thin Carbon Films*, Science, **306** 666–669, 2004.

[2] Z. Lin, A. McCreary, N. Briggs, S. Subramanian, K. Zhang, Y. Sun, X. Li, N. J. Borys, H. Yuan, S. K. Fullerton-Shirey, A. Chernikov, H. Zhao, S. McDonnell, A. M. Lindenberg, K. Xiao, B. J. LeRoy, M. Drndić, J. C. M. Hwang, J. Park, M. Chhowalla, R. E. Schaak, A. Javey, M. C. Hersam, J. Robinson, and M. Terrones, *2D materials advances: from large scale synthesis and controlled heterostructures to improved characterization techniques, defects and applications*, 2D Mater., **3** 042001, 2016.

[3] S. Manzeli, D. Ovchinnikov, D. Pasquier, O. V. Yazyev, and A. Kis, *2D transition metal dichalcogenides*, Nat. Rev. Mats., **2** 17033, 2017.

[4] S. Wachter, D. K. Polyushkin, O. Bethge, and T. Mueller, *A microprocessor based on a two-dimensional semiconductor*, Nat. Commun., **8** 14948, 2017.

[5] J. S. Ponraj, Z.-Q. Xu, S. C. Dhanabalan, H. Mu, Y. Wang, J. Yuan, P. Li, S. Thakur, M. Ashrafi, K. Mccoubrey, Y. Zhang, S. Li, H. Zhang, and Q. Bao, *Photonics and optoelectronics of two-dimensional materials beyond graphene*, Nanotechnology, **27** 462001, 2016.

[6] S. Yang, C. Jiang, and S.-H. Wei, *Gas sensing in 2D materials*, Appl. Phys. Rev., **4** 021304, 2017.

[7] S. Thomas, A. C. Rajan, M. R. Rezapour, and K. S. Kim, *In Search of a Two-Dimensional Material for DNA Sequencing*, J. Phys. Chem. C, **118** 10855–10858, 2014.

[8] T. T. Tran, K. Bray, M. J. Ford, M. Toth, and I. Aharonovich, *Quantum emission from hexagonal boron nitride monolayers*, Nat. Nanotechnol., **11** 37–41, 2016.

[9] T. Vogl, Y. Lu, and P. K. Lam, *Room temperature single photon source using fiber-integrated hexagonal boron nitride*, J. Phys. D: Appl. Phys., **50** 295101, 2017.

[10] M. Gould, E. R. Schmidgall, S. Dadgostar, F. Hatami, and K.-M. C. Fu, *Efficient Extraction of Zero-Phonon-Line Photons from Single Nitrogen-Vacancy Centers in an Integrated GaP-on-Diamond Platform*, Phys. Rev. Applied, **6** 011001, Jul 2016.

[11] S. A. Tawfik, S. Ali, M. Fronzi, M. Kianinia, T. T. Tran, C. Stampfl, I. Aharonovich, M. Toth, and M. J. Ford, *First-principles investigation of quantum emission from hBN defects*, Nanoscale, **9** 13575–13582, 2017.

[12] M. Abdi, J.-P. Chou, A. Gali, and M. B. Plenio, *Color centers in hexagonal boron nitride monolayers: A group theory and ab initio analysis*, arXiv:1709.05414, 2017.

[13] T. T. Tran, C. Elbadawi, D. Totonjian, C. J. Lobo, G. Grosso, H. Moon, D. R. Englund, M. J. Ford, I. Aharonovich, and M. Toth, *Robust Multicolor Single Photon Emission from Point Defects in Hexagonal Boron Nitride*, ACS Nano, **10** 7331–7338, 2016.

[14] R. Bourrellier, S. Meuret, A. Tararan, O. Stéphan, M. Kociak, L. H. G. Tizei, and A. Zobelli, *Bright UV Single Photon Emission at Point Defects in h-BN*, Nano Lett., **16** 4317–4321, 2016.

[15] N. Gisin, G. Ribordy, W. Tittel, and H. Zbinden, *Quantum cryptography*, Rev. Mod. Phys., **74** 145–195, 2002.

[16] P. Kok, W. J. Munro, K. Nemoto, T. C. Ralph, J. P. Dowling, and G. J. Milburn, *Linear optical quantum computing with photonic qubits*, Rev. Mod. Phys., **79** 135–174, 2007.

[17] A. C. Elitzur and L. Vaidman, *Quantum mechanical interaction-free measurements*, Found. Phys., **23** 987, 1993.

[18] A. W. Schell, H. Takashima, T. T. Tran, I. Aharonovich, and S. Takeuchi, *Coupling Quantum Emitters in 2D Materials with Tapered Fibers*, ACS Photonics, **4** 761–767, 2017.

[19] T. T. Tran, M. Kianinia, M. Nguyen, S. Kim, Z.-Q. Xu, A. Kubanek, M. Toth, and I. Aharonovich, *Resonant Excitation of Quantum Emitters in Hexagonal Boron Nitride*, ACS Photonics, **5** 295–300, 2018.

[20] B. Sontheimer, M. Braun, N. Nikolay, N. Sadzak, I. Aharonovich, and O. Benson, *Photodynamics of quantum emitters in hexagonal boron nitride revealed by low-temperature spectroscopy*, Phys. Rev. B, **96** 121202, 2017.

[21] S. Choi, T. T. Tran, C. Elbadawi, C. Lobo, X. Wang, S. Juodkazis, G. Seniutinas, M. Toth, and I. Aharonovich, *Engineering and Localization of Quantum Emitters in Large Hexagonal Boron Nitride Layers*, ACS Appl. Mater. Interfaces, **8** 29642–29648, 2016.

[22] N. Chejanovsky, M. Rezai, F. Paolucci, Y. Kim, T. Rendler, W. Rouabeh, F. Fávaro de Oliveira, P. Herlinger, A. Denisenko, S. Yang, I. Gerhardt, A. Finkler, J. H. Smet, and J. Wrachtrup, *Structural Attributes and Photodynamics of Visible Spectrum Quantum Emitters in Hexagonal Boron Nitride*, Nano Lett., **16** 7037–7045, 2016.

[23] A. Castellanos-Gomez, M. Buscema, R. Molenaar, V. Singh, L. Janssen, H. S. J. van der Zant, and G. A. Steele, *Deterministic transfer of two-dimensional materials by all-dry viscoelastic stamping*, 2D Mater., **1** 011002, 2014.

[24] J. Yang, Z. Wang, F. Wang, R. Xu, J. Tao, S. Zhang, Q. Qin, B. Luther-Davies, C. Jagadisch, and Y. Lu, *Atomically thin optical lenses and gratings*, Light Sci. Appl., **5** e16046, 2002.

[25] M. Schubert, B. Rheinländer, E. Franke, H. Neumann, J. Hahn, M. Röder, and F. Richter, *Anisotropy of boron nitride thin-film reflectivity spectra by generalized ellipsometry*, Appl. Phys. Lett., **70** 1819–1821, 1997.

[26] G. Cassabois, P. Valvin, and B.Gil, *Hexagonal boron nitride is an indirect bandgap semiconductor*, Nat. Photon., **10** 262–266, 2016.

[27] A. Dietrich, M. Bürk, E. S. Steiger, L. Antoniuk, T. T. Tran, M. Nguyen, I. Aharanovich, F. Jelezko, and A. Kubanek, *Narrowband quantum emitters over large spectral range with Fourier-limited linewidth in hexagonal boron nitride*, arXiv:1712.06938, 2017.

[28] Y. Miyauchi, M. Iwamura, S. Mouri, T. Kawazoe, M. Ohtsu, and K. Matsuda, *Brightening of excitons in carbon nanotubes on dimensionality modification*, Nat. Photon., **7** 715–719, 2013.

[29] T. T. Tran, D. Wang, Z.-Q. Xu, A. Yang, M. Toth, T. W. Odom, and I. Aharonovich, *Deterministic Coupling of Quantum Emitters in 2D Materials to Plasmonic Nanocavity Arrays*, Nano Lett., **17** 2634–2639, 2017.

[30] C. Palacios-Berraquero, D. M. Kara, A. R.-P. Montblanch, M. Barbone, P. Latawiec, D. Yoon, A. K. Ott, M. Loncar, A. C. Ferrari, and M. Atatüre, *Large-scale quantum emitter arrays in atomically thin semiconductors*, Nat. Commun., **8** 15093, 2017.

[31] Z. Lu, L. Sun, G. Xu, J. Zheng, Q. Zhang, J. Wang, and L. Jiao, *Universal Transfer and Stacking of Chemical Vapor Deposition Grown Two-Dimensional Atomic Layers with Water-Soluble Polymer Mediator*, ACS Nano, **10** 5237–5242, 2016.

[32] F. Pizzocchero, L. Gammelgaard, B. S. Jessen, J. M. Caridad, L. Wang, J. Hone, P. Boggild, and T. J. Booth, *The hot pick-up technique for batch assembly of van der Waals heterostructures*, Nat. Commun., **7** 11894, 2016.

[33] Z.-Q. Xu, C. Elbadawi, T. T. Tran, M. Kianinia, X. Li, D. Liu, T. B. Hoffman, M. Nguyen, S. Kim, J. H. Edgar, X. Wu, L. Song, M. Ford, M. Toth, and I. Aharonovich, *Single Photon Emission from Plasma Treated 2D Hexagonal Boron Nitride*, arXiv:1710.07010, 2017.

Chapter 8

Radiation tolerance of two-dimensional material-based devices for space applications

8.1 Foreword

The previous chapter presented the improvement of the quantum emitter fabrication cycle. The key element of this process was an oxygen plasma etching step, creating high-quality quantum emitters in 2D hBN.[1] The single-photon purity, as well as spectral purity was now sufficient to provide a path for implementations for quantum information processing. As already mentioned, the application which most requires single-photon sources is quantum key distribution. Also, improving the source's performance to be sufficient for this application is easy compared with the requirements for photonic quantum computing.

In the experiments so far, the emission lines were covering a wide range of frequencies in the visible spectrum, but so far no emitter with a transition at telecom wavelengths has been discovered or reported elsewhere. In general, a different setup is necessary for telecom wavelengths, as near-infrared optics and detectors are required as well as a different excitation laser. Thus, the lack of reports of such emitters is not surprising. It is also possible that the electronic band structure of defects in hBN simply does not allow near-infrared emitters, but it is likely that at least some other 2D material would allow these.

The large loss coefficients in fibers for visible light renders efficient fiber-based quantum key distribution out-of-reach, at least for now. For free space channels, however, the attenuation at long distances is dominated by diffraction and atmospheric molecular scattering. The Rayleigh length (the distance at which a Gaussian beam diameter increases by a factor of $\sqrt{2}$) is inversely proportional to the wavelength. Therefore, systems working at shorter wavelengths suffer less from beam spread and consequently manage to operate with smaller telescopes. Furthermore, if linked via a satellite, space-to-ground channels allow much higher transmission efficiencies than that of any fiber system. The Micius satellite demonstrated 200 dB advantage over a telecom fiber at 1200 km distance[45].

The performance of Micius can be enhanced by using a true single-photon source. The requirements to any space-based system, however, are stricter compared to any terrestrial system. Size, weight and power (SWaP) are limited on satellites, but that is precisely where quantum emitters in hBN excel. One essential requirement for the use on satellites

[1] The term "high-quality" here refers to in comparison with other typical quantum emitters hosted by hBN.

is the certification for the harsh conditions of space. Space qualification studies usually include thermal and vacuum cycling, vibration and shock tests as well as exposure to high-energy radiation. Vibration and shock will not pose a threat for 2D materials (this is relevant for the complete satellite structure), and vacuum and thermal cycling is routinely done in experiments. The remaining radiation tolerance is of particular interest, since weight restrictions on satellites limit shielding options.

In this chapter, radiation effects in Earth's atmosphere on various devices based on 2D materials are comprehensively investigated. This includes not only the hBN-based single-photon sources, but also atomically thin field-effect transistors as well as monolayered 2D materials in their native state. These other materials are believed to be basic building blocks for future electronics and optoelectronics. Beyond quantum light sources for long-distance quantum cryptography, applications for 2D materials on satellites include photovoltaics, batteries, electronics, and sensors. The study suggests robust suitability for space instrumentation of 2D materials. This work has been published in and is here reprinted (adapted) with permission from Nature Communications **10**, 1202 (2019) under the terms of the Creative Commons Attribution 4.0 International License (CC BY 4.0), http://creativecommons.org/licenses/by/4.0. All graphics have been recreated to match the style of this thesis.

The paper has been featured as Nature Communication's condensed matter physics highlight of the month (March 2019).[2]

[2] https://www.nature.com/ncomms/editorshighlights

Radiation tolerance of two-dimensional material-based devices for space applications

Tobias Vogl[1], Kabilan Sripathy[1], Ankur Sharma[2], Prithvi Reddy[3], James Sullivan [4], Joshua R. Machacek[4], Linglong Zhang[2], Fouad Karouta[5], Ben C. Buchler[1], Marcus W. Doherty[3], Yuerui Lu[2], and Ping Koy Lam[1]

[1] *Centre for Quantum Computation and Communication Technology, Department of Quantum Science, Research School of Physics and Engineering, The Australian National University, Acton ACT 2601, Australia*

[2] *Research School of Engineering, The Australian National University, Acton ACT 2601, Australia*

[3] *Laser Physics Centre, Research School of Physics and Engineering, The Australian National University, Acton ACT 2601, Australia*

[4] *Plasma Research Laboratory, Research School of Physics and Engineering, The Australian National University, Acton ACT 2601, Australia*

[5] *Australian National Fabrication Facility, Research School of Physics and Engineering, The Australian National University, Acton ACT 2601, Australia*

Abstract

Characteristic for devices based on two-dimensional materials are their low size, weight and power requirements. This makes them advantageous for use in space instrumentation, including photovoltaics, batteries, electronics, sensors and light sources for long-distance quantum communication. Here we present a comprehensive study on combined radiation effects in Earth's atmosphere on various devices based on these nanomaterials. Using theoretical modeling packages, we estimate relevant radiation levels and then expose field-effect transistors, single-photon sources and monolayers as building blocks for future electronics to γ-rays, protons and electrons. The devices show negligible change in performance after the irradiation, suggesting robust suitability for space use. Under excessive γ-radiation, however, monolayer WS_2 shows decreased defect densities, identified by an increase in photoluminescence, carrier lifetime and a change in doping ratio proportional to the photon flux. The underlying mechanism is traced back to radiation-induced defect healing, wherein dissociated oxygen passivates sulfur vacancies.

8.2 Introduction

In the near future, quantum tunneling will set a hard limit to further miniaturization of silicon-based electronics. Research on alternative materials, however, demonstrated fabrication beyond this limit[1, 2]. Of particular interest are monolayered two-dimensional (2D) materials such as graphene[3] and transition metal dichalcogenides (TMDs) of the form of MX_2 (M = Mo, W and X = S, Se)[4]. Record electron mobility in 2D materials has enabled multiple technology demonstrations of atomically-thin field-effect transistors (FETs)[5–9]. Furthermore, due to their semiconducting band structure, TMDs have applications in optoelectronics and photonics[10]. Their intrinsically low size, weight and

power (SWaP) requirements and chemical stability make 2D material-based devices a promising candidate for space instrumentation. Beyond integrated electronics, 2D materials in space technology can be utilized for solar cells[11], batteries[12], sensors as well as non-classical light sources for long-distance quantum communication[13]. The quantum emission from point defects in 2D materials have desirable properties for single-photon sources, as they can be easily integrated with photonic networks, have an intrinsic outcoupling efficiency of unity and offer long-term stable, high luminosity single-photons at room temperature[13–17]. An ideal single-photon source can enhance the data communication rates of satellite-based quantum key distribution[18].

While 2D materials offer great opportunities for space missions, their current low technological readiness level (TRL) restricts deployment (current state-of-the-art is TRL 3-4). In addition to further device development, 2D materials need to be certified for the harsh conditions of space. Space qualification studies usually consist of vacuum and thermal cycling, vibration and shock tests as well as exposure to radiation[19]. Vibration or shock will not pose a threat for nanomaterials and vacuum and thermal cycling is routinely done in experiments[20–22]. Of particular interest, however, is the effect of radiation on 2D materials. While radiation effects on the electrical properties of graphene have been studied extensively[23–28], less is known about these effects on TMDs and other 2D materials[29–33]. In particular, no study investigates the effect of radiation on optical characteristics of 2D materials. Moreover, there exists no comprehensive study on the effects of combined radiation types on properties of various devices in the context of space certification. The damage caused by high-energy particles and γ-rays is of major concern for all spacecraft, especially as weight restrictions limit shielding options. While testing directly in a space environment as planned for graphene is possible[34], a more practical way is to replicate space environments on Earth.

As already mentioned, single-photon sources based e.g. on defects in hexagonal boron nitride (hBN) and FETs based on monolayers are useful for space applications. These devices are influenced by their electrical and/or optical properties (quantum emitters in hBN are dependent on the piezoelectric environment of hBN[35]). It is possible that low-energy radiation on the order of the band gap ($\sim 1 - 10\,\mathrm{eV}$) could change the charge state of defects, causing them to enter a dark state, usually for a finite time. High-energy radiation, on the other hand, could create new defects in the crystal lattice. If close to the quantum emitter, the new defects could either change the charge state permanently or create a second independent emitter nearby. In any of these scenarios, the single-photon source would become unusable. With respect to the FETs, the radiation could change the carrier density, which alters their performance.

Here we present a comprehensive study on the effects of radiation in the atmosphere on various devices based on 2D materials. We start with modeling radiation levels in the thermosphere using the SPace ENVironment Information System (SPENVIS), software provided by the European Space Agency[36]. With the knowledge from the simulations, we expose our devices to the most common radiation types in orbit: Gamma-rays as well as energetic protons and electrons. We look at isolated effects and combined effects by exposing devices to all three types of radiation. For each test we fully characterize all devices back-to-back, shortly before and after the exposure. At radiation levels common for satellite altitudes up to geostationary orbit, no changes in the characteristics of the 2D materials are observed. However, under excessive γ-irradiation, WS_2 monolayers exhibit significant change in its optical emission. By studying the effects of oxygen plasmas and γ-irradiation in different atmospheres, the mechanism is traced back to oxygen-related

vacancy healing. Additional density functional theory calculations show that charge trapping states disappear after the healing, thus explaining the change in optical emission.

8.3 Results

8.3.1 Radiation levels in orbit

The Earth is protected from solar wind and cosmic particles by its magnetic field. As a result, high-energy protons and electrons are trapped on trajectories oscillating between both magnetic poles in the so-called Van Allen belts. While essential for life on Earth, the trapped particle belts pose great threat to any spacecraft orbiting through these particle belts. Near the magnetic poles the inner belt can extend down to altitudes of 200 km. Due to misalignment of the magnetic dipole and rotation axis of the Earth, this appears as the South Atlantic Anomaly (SAA, see Figure 8.1(a, b)). Because of this inhomogeneity, the total radiation dosage is strongly dependent on the orbital inclination. Thus, we calculated the particle spectra for different spacecraft trajectories with inclinations of 20° (here defined as equatorial orbit), 51.6° (orbit of the International Space Station, ISS) and 98° (here defined as polar orbit) for 500 km altitude and average over the full orbit. In general, the energy spectrum for protons in low Earth orbit (LEO) ranges from 100 keV to 400 MeV, while for electrons it ranges from 40 keV to 7 MeV. Low-energy particles are typically absorbed by the walls of the spacecraft, which acts as a non-ideal high-pass filter. High-energy ions, however, loose energy during their interaction with the shielding material and thus, the lower ends of the spectra are always finite unless every charge carrier is stopped (e.g. for thick shielding). The shielded flux spectra for protons and electrons after 1.85 mm of Al shielding and integrated over a one year mission is shown in Figure 8.1(c, d). Surprisingly, the polar orbit does not have the highest fluence, as spacecrafts with 51.6° inclination spend more time in the SAA than spacecrafts with 98° inclination, similarly for protons and electrons. A spectral distribution with an absence of low-energy protons, as shown in Figure 8.1(c), is advantageous, because only low-energy particles can deposit significant amounts of energy into the payload. It should be mentioned, that the electrons in Figure 8.1(d) do not originate from trapped electrons in the Van Allen belt, but rather are secondary electrons produced via ionizing interactions of high-energy protons with the Al atoms in the shielding material.

While the particle fluence spectra are directly accessible through SPENVIS, similar tools for γ-rays do not exist. Gamma-rays mostly originate either directly from the sun or radioactive decay of trapped particles. For our study we use data from the CORONAS-I

Table 8.1: Summary of total measured gamma-ray flux from the CORONAS-I satellite at 500 km altitude. Full data available in Ref. [38].

Location	γ-ray energy [MeV]	Flux [$cm^{-2}s^{-1}sr^{-1}MeV^{-1}$]
Equator	0.32 - 1	0.079(59)
Equator	1 - 3	0.022(14)
Polar cap	0.32 - 1	0.174(59)
Polar cap	1 - 3	0.095(14)

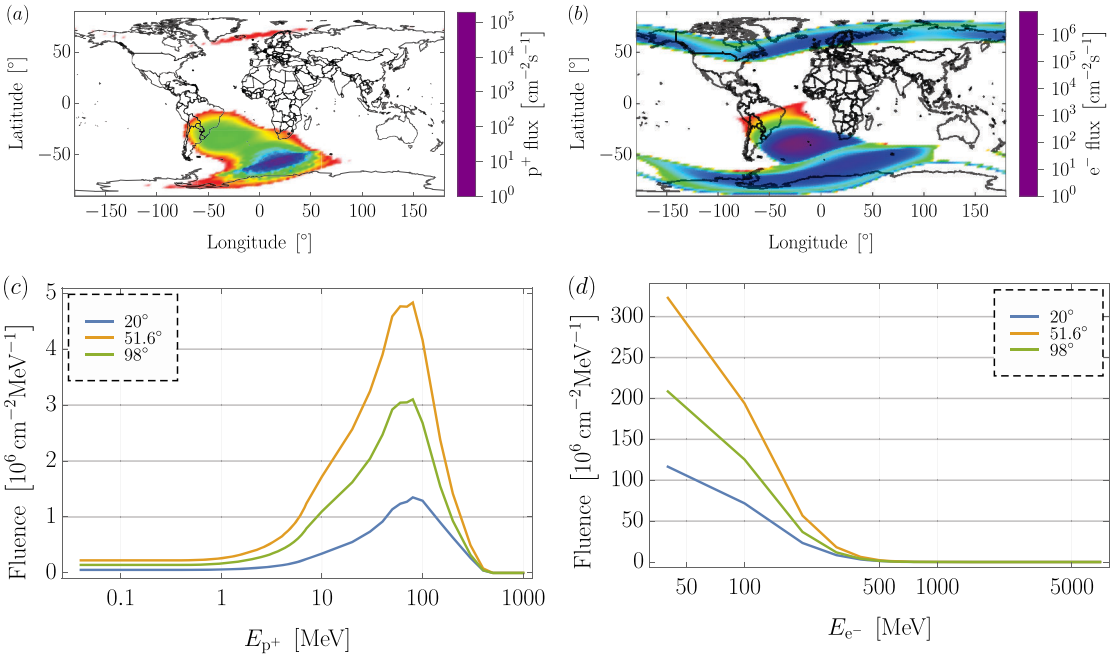

Figure 8.1: Space environment. Geographical distribution of the trapped (a) proton and (b) electron flux at 500 km altitude, calculated with the AP-8 MAX and AE-8 MAX models in SPENVIS, respectively. Integrated annual (c) proton and (d) electron fluence after 1.85 mm of Al shielding for typical orbital inclinations.

satellite[37,38], which mapped the γ-ray flux above the Earth at 500 km altitude (see Table 8.1).

8.3.2 Device fabrication and characterization

Exfoliated hBN flakes have been treated with an oxygen plasma and successively rapidly thermally annealed[14]. The oxygen plasma creates point defects in the crystal lattice, which act as trapping sites for localized excitons. The single-photon emitters formed in this way were located and characterized using a confocal microphotoluminescence (μPL) system equipped with an ultrashort-pulsed laser for time-resolved measurements (see Methods). The emitters are excited off-resonantly at 522 nm, less than half of the band gap of hBN (E_g = 6 eV[39]), preventing two-photon absorption. For the quantum emitters we measured the spectrum, excited state lifetime and second-order correlation function (see Methods).

The atomically-thin FET devices (see Figure 8.2(a)) were characterized by their device ON/OFF performance using the standard back gate sweep from −60 to +60 V at different biases between source and drain. Also, the conventional performance I-V curves of the device were recorded at various back gate voltages in the ON regime of the functional FET device.

Since 2D materials have often been proposed as candidates for the post-silicon age, we also tested monolayer TMDs in their native state as basic building blocks for future electronics and optoelectronics. After transfer to a Si/SiO_2 substrate (see Figure 8.2(b)), the monolayer thickness is confirmed by phase-shift interferometry (PSI), with the corresponding PSI image shown in Figure 8.2(c). In this case, the WS_2 crystal has an optical path length difference (OPD) of 17.7 nm. With rigorous coupled-wave analysis (RCWA)

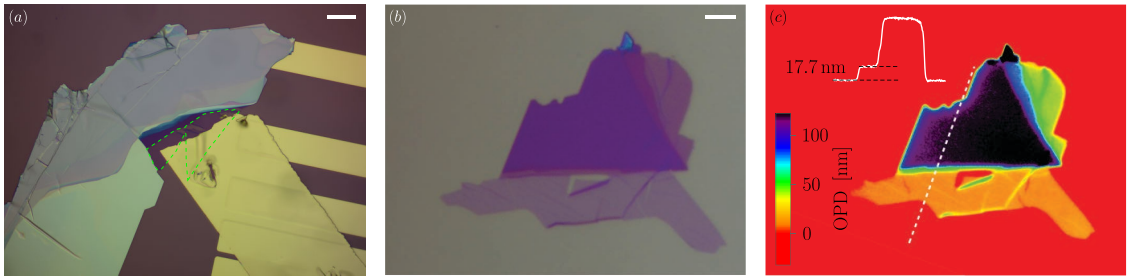

Figure 8.2: Fabrication. (a) Microscope image of a MoS_2 FET device under 500× magnification. The monolayer is framed within the green dashed line. (b, c) Microscope and PSI images of the WS_2 monolayer presented in the main text. The inset in (c) shows the OPD along the white dashed line. The monolayer has an OPD of 17.7 nm, which corresponds to a physical thickness of 0.66 nm. The scale bars in (a, b) are 20 and 5 μm, respectively.

simulations[40], the OPD can be converted to a physical thickness of 0.66 nm, matching well atomic force microscope (AFM) measurements[41]. We characterized each flake optically with the μPL setup in terms of emission spectrum (averaged over the full monolayer), carrier lifetime and power saturation. The carrier lifetime data, deconvoluted from the system response, is fitted with a bi-exponential from which radiative and non-radiative decay time τ_r and τ_{nr} can be extracted. Every flake is scanned with a 1 μm grid and a spectrum is recorded at each point. To gather enough statistics, a total of 49 monolayer flakes with areas ranging from 60 to 1290 μm^2 have been characterized. Unless stated otherwise, all optical and electrical measurements have been carried out at room temperature (RT). More than 80 devices were investigated throughout this study; herein we only show exemplary results and average over the full data set (see Supplementary Note 2, 5, and 6).

8.3.3 Gamma-ray tests

The γ-ray source predominantly used for space qualification is the radioactive isotope $^{60}_{27}$Co, which emits photons with energies of 1.17 and 1.33 MeV as it decays. Due to availability, we used the isotope $^{22}_{11}$Na instead, which decays into $^{22}_{10}$Ne via the emission of a 1.28 MeV photon[42], similar to the γ-ray energy from the Co isotope. From its initial nominal activity of 1.04 GBq, a total photon flux of 10.3 MBq cm^{-2}sr^{-1}MeV^{-1} is emitted into the output mode of the Tungsten container in which the source was kept. We placed the samples at distances of d = 10.0(1), 13.0(1), 18.0(1) and 40.0(1) cm to the source output, thus simulating various altitudes and times in orbit (see Supplementary Figure 1). All samples were irradiated for 2:27 hrs, meaning that the maximal fluence at the closest distance to the source was $F_\gamma = 18.41 \times 10^9$ cm^{-2}sr^{-1}MeV^{-1}. Unless stated otherwise, the crystals presented in this section were irradiated with the highest photon flux. Unexposed control samples ensured that any potential changes are solely due to irradiation.

The performance of the single-photon emitters in hBN and the FET devices remained invariant when comparing samples before and after the γ-ray exposure. The zero phonon line (ZPL) of a sample quantum emitter as shown in Figure 8.3(a) peaked initially at 563.78(8) nm with a linewidth of 4.29(13) nm (extracted from fit). Unless stated otherwise, all uncertainties are 95% confidence intervals. After the crystal was irradiated, the ZPL peaked at 563.79(13) nm with a linewidth of 4.73(19) nm. Similarly, its $g^{(2)}(0)$ did not change (see Figure 8.3(b)) with $g_i^{(2)}(0) = 0.185(23)$ and $g_f^{(2)}(0) = 0.188(25)$, where index i and f stand for before and after the exposure, respectively. While the quantum emitters

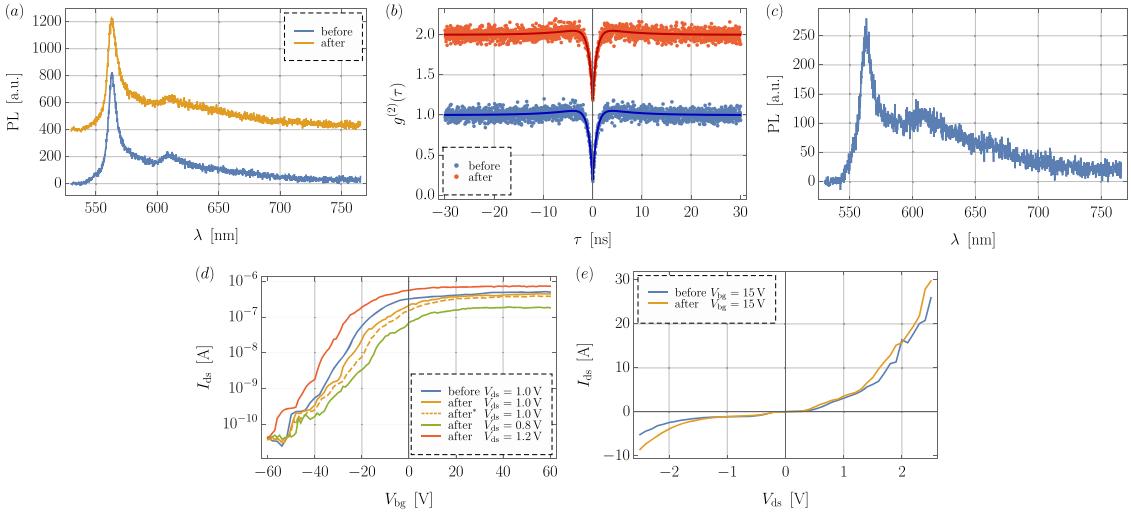

Figure 8.3: γ-ray tests of 2D material-based devices. (a) PL spectra of an hBN quantum emitter before and after the γ-ray tests show no changes (vertically offset for clarity). (b) Second-order correlation function dipping at zero time delay to 0.185(23) before and to 0.188(25) after the irradiation. The values were obtained from fitting a three-level system (vertically offset for clarity). (c) Spectrum of a newly created quantum emitter after the γ-ray test. As the emitter was not annealed following the irradiation, its brightness and stability was lacking behind plasma-etched and annealed emitters. (d) Back gate sweeps before and after the irradiation with different drain-source biases V_{ds}. The orange dashed line was recorded 5 hrs past the orange solid line to check for temporal variations. In terms of current ON/OFF ratio the temporal variations are larger than the variations caused by the γ-rays. Tuning the V_{ds} can restore the initial performance (see area between green and red lines). (e) The I-V curve at a fixed $V_{bg} = 15$ V shows only slight alteration after irradiation. The shift of the threshold voltage is < 0.1 V.

already present in the hBN crystal did not change with respect to their optical emission properties, the γ-rays were able to create five new emitters on $\approx 40000\,\mu m^2$ of crystal area. Thus, the probability of creating a second emitter directly adjacent to another is very low. Figure 8.3(c) shows the spectrum of one of the newly created emitters. As the crystal was not subsequently annealed, its brightness as well as stability was not as good as for other emitters[14].

Comparably, the FETs were also only marginally affected by the γ-rays. Figure 8.3(d) shows back gate sweeps for a MoS_2 transistor. The current ON/OFF ratio β was reduced from $\beta_i = 21213$ to $\beta_f = 14863$ at a drain-source bias of $V_{ds} = 1$ V. While this is a significant change in the ON/OFF ratio, we measured the ON/OFF ratio 5 hrs later and saw β further reduced to 11781 (dashed line in Figure 8.3(d)). In fact, the standard deviation of the variations on control samples as well as variations before and after irradiation were roughly 4000. Hence, we attribute these changes in the ON/OFF ratio to temporal variations only. The FETs in general are sensitive to surface adsorption which causes these temporal variations. In addition, I-V characteristics are highly dependent on the Schottky or contact resistance which varies across different measurements. However, by varying the drain-source bias from $0.8 - 1.2$ V, the initial performance could be restored (see Figure 8.3(d)). Another characteristic of transistors is the I-V curve measured at fixed back gate voltages V_{bg}. For $V_{bg} = 15$ V this is shown in Figure 8.3(e) and for other V_{bg} in Supplementary Figure 2. The I-V curves show no change due to the irradiation. The FETs, while conducting at a particular back gate bias, show no threshold voltage

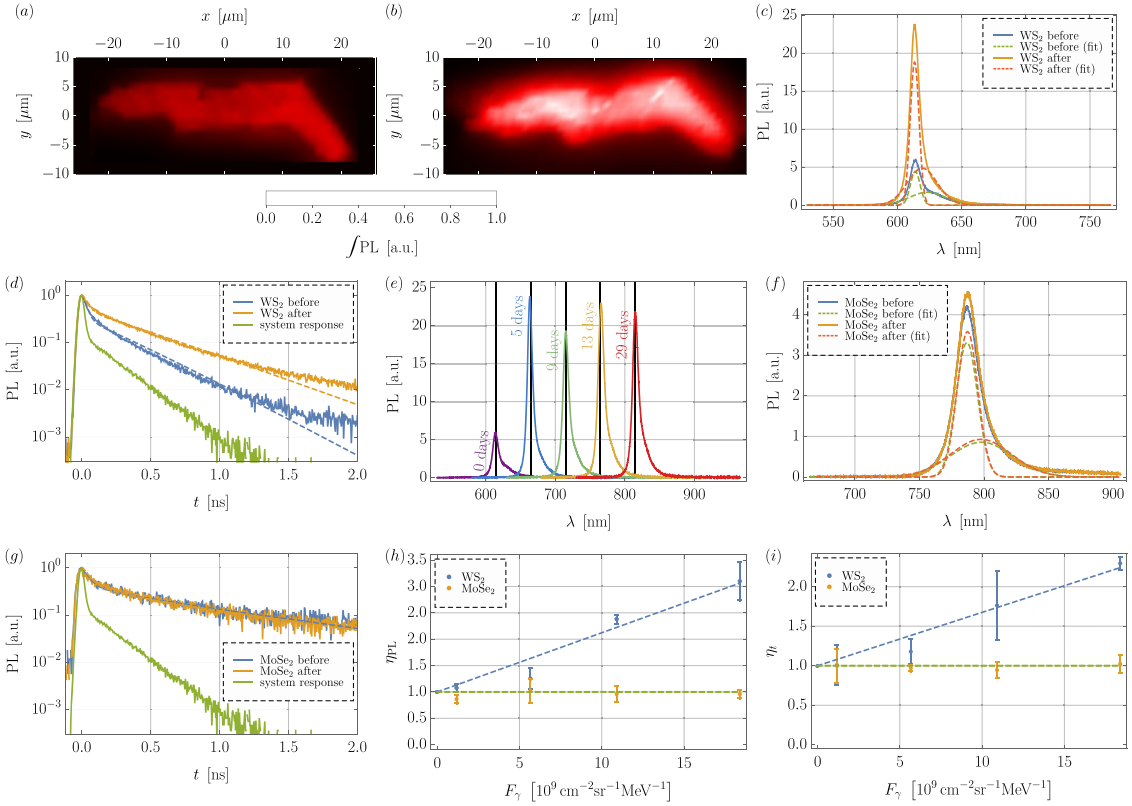

Figure 8.4: γ-ray tests of TMD monolayers. (a-e) Optical characterization of a WS_2 monolayer before and after the γ-ray exposure. (a, b) The PL intensity maps scanned with 1 μm resolution integrated over the full spectrum show a strong increase in brightness after the irradiation. (c) In addition to the brightness increase of 2.99, the PL spectrum shows that the exciton/trion ratio also changed from 0.706(11) to 1.138(19). This was extracted from fitting two Gaussian distributions. (d) Similarly, the radiative carrier lifetime increased from 336(3) to 678(5) ps. The fit routine deconvolutes the data from the system response. (e) Long-term stability of the PL spectrum measured at different days. The irradiation took place at day 2. For clarity each subsequent spectra is shifted by 50 nm. The peak wavelength remained invariant with its mean at 614.65 nm. The mean peak wavelength is visualized with the black guidelines. (f, g) PL emission spectrum and carrier lifetime for monolayer $MoSe_2$. This material remains predominantly unaffected by the gamma-rays, with the overall brightness increased by less than 5% and the radiative lifetimes before and after the irradiation being 1086(41) and 1071(47) ps, respectively. Both sample monolayers experienced the same photon fluence. (h, i) Relative brightness and carrier lifetime increase as a function of γ-ray fluence averaged over all samples for WS_2 and $MoSe_2$. While there is little to no change for $MoSe_2$, for WS_2 the relative changes are linearly proportional to the radiation fluence. The data point at zero is the control sample. The green dashed line indicates $\eta = 1$ (no change). The error bars are the standard deviation of the average.

shift with $\Delta V_{\mathrm{th}} < 0.1\,\mathrm{V}$.

While the 2D material-based devices showed no change after the γ-ray tests, the optical signature of monolayer WS_2 changed remarkably: the monolayer shown in Figure 8.2(b) showed a significant increase in photoluminescence. Moreover, the brightness increased by a factor of 2.99 after being exposed to the γ-rays (see Figure 8.4(a, b)). Furthermore, from the averaged photoluminescence (PL) spectrum of the monolayer (see Figure 8.4(c), for details of the averaging algorithm see Supplementary Note 1), we extract that the

exciton/trion ratio α changed from 0.706(11) to 1.138(19). Both, the exciton and trion emission were enhanced, however, the exciton emission was enhanced more strongly as the change from $\alpha < 1$ to $\alpha > 1$ shows. This also indicates a change in doping ratio. Given the initial linewidths of 3.80(3) for excitons and 14.07(13) nm for trions, there was no change in center wavelength of the exciton emission (613.89(3) to 613.41(2) nm) and only a slight change of the trion emission (623.45(19) to 619.28(19) nm). However, the linewidths changed to 3.45(2) for excitons and 11.73(13) nm for trions. In addition, the radiative carrier lifetime (see Figure 8.4(d)) had also increased from 336(3) to 678(5) ps (for more data see Supplementary Note 2 and Supplementary Figures 4 through 8). The increase in PL and lifetime was persistent over months (see Figure 8.4(e)). Only one month is shown, as the samples were subsequently irradiated with protons, but the samples kept their increased PL during these following tests. The small variations in the peak maxima are most likely due to laser defocusing, owing to the small Rayleigh length of the laser with the high numerical aperture objective (see Methods). Nevertheless, quantities independent of this, such as the exciton/trion ratio as well as carrier lifetime, remained fully stable at all measurement days. Moreover, other samples (see Supplementary Figure 9) were less affected by laser defocusing during the long-term stability tests.

Since free excitons easily scatter and recombine at trapped charge carriers at defect sites, a change in doping ratio as well as longer carrier lifetime and increased PL intensity likely indicates a reduction in defect density. By averaging over the full data set of samples at the corresponding distance to the source, it can be seen that the effect of an increased PL and lifetime is linearly proportional to the γ-ray flux (see Figure 8.4(h, i), respectively). Interestingly, this effect was not observed for $MoSe_2$ monolayers, (see Figure 8.4(f, i)). Moreover, under the same exposure conditions, the PL had only increased marginally by 1.05 compared to the 2.99 from the WS_2 sample presented previously. In addition, the exciton/trion ratio was stable with $\alpha_i = 1.328(36)$ and $\alpha_f = 1.317(36)$ as well as was the carrier lifetime with $\tau_r^i = 1086(41)$ and $\tau_r^f = 1071(47)$ (see Figure 8.4(f, g)). It should be mentioned that $MoSe_2$ and WS_2 have intrinsically different exciton/trion ratios, since our $MoSe_2$ is a p-type and WS_2 is an n-type semiconductor. By averaging over all samples we found $\alpha_{MoSe2} = 1.252(86)$ and $\alpha_{WS2} = 0.715(117)$ (the uncertainty is the standard deviation).

During the data analysis we noted that the γ-radiation dose was higher than intended due to a calculation error. The resulting highest γ-ray fluence is equivalent to 2170 years at 500 km above the polar caps. However, in terms of space certification this is not an issue. If anything, this further confirms radiation resistance. This proves that 2D materials can withstand even harsher radiation environments than LEO, such as during solar flares or near nuclear reactors. For the WS_2 monolayer we extrapolate the effect of increased photoluminescence and carrier lifetime after 4 years in orbit to be less than 0.15% and 0.10%, respectively.

8.3.4 Backtracing of the healing mechanism

An increase in photoluminescence and carrier lifetime is very surprising: initially it was expected that radiation could lead to the formation of new defects, but not to defect healing. We note that low-energy X-ray irradiation of graphene in oxygen environments can lead to the formation of oxygen-related defects[43–45]. Although radiation-induced healing of nanomaterials has been reported[46], such an effect has not been observed with γ-rays, specifically not with such remarkable consequences. It is known that the most

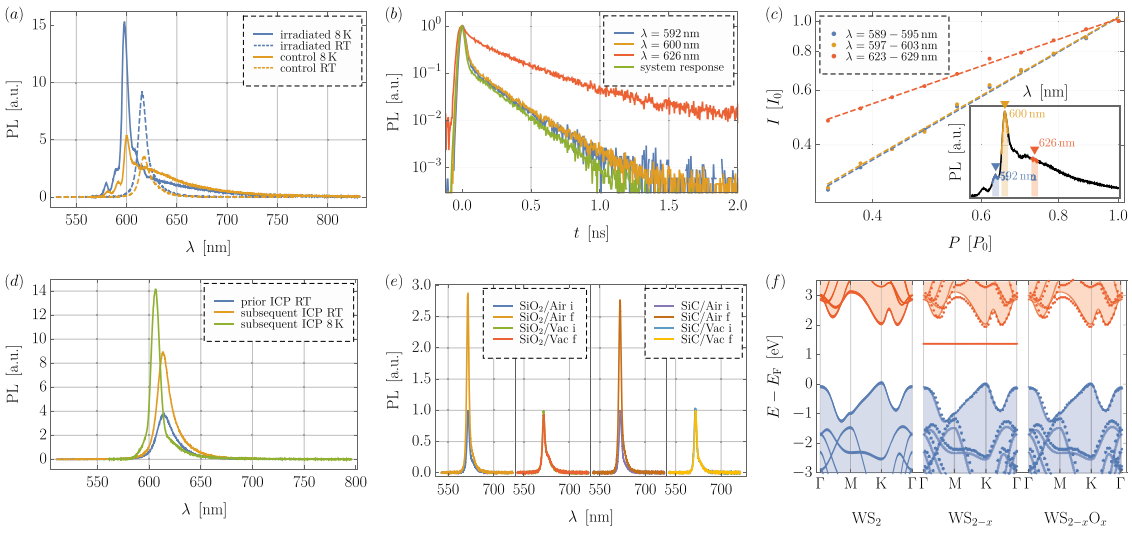

Figure 8.5: Identification of the γ-ray induced healing mechanism. (a) PL spectrum of γ-irradiated and control sample at 8 K and RT. The control sample shows strong defect emission in the red sideband. (b) Spectrally- and time-resolved PL reveals carrier lifetimes close to the system response at $\lambda = 592, 600$ nm and 361(3) ps at 626 nm, confirming excitonic and defect nature of the emission. Unlike for defects, the radiative lifetime for excitons/trions is proportional to temperature. The spectral positions at which the lifetimes were measured are marked with correspondingly colored triangles in **c** (small inset). (c) Spectrally-resolved power dependence on a log-log-plot reveals a slope close to 1 at $\lambda = 592, 600$ nm, indicating excitonic emission, while the slope < 1 at 626 nm means the emission originates from defects. The inset shows the positions in the spectrum (marked with the corresponding colors) at which the power dependence is measured. (d) PL emission prior and subsequent to the ICP treatment shows a similar increase in PL brightness compared to the γ-irradiated samples. In addition, at low temperature no defect emission becomes visible, confirming that oxygen can passivate vacancies. (e) Repetition of the γ-irradiation on SiO_2 and SiC substrates as well as in air and vacuum show that the atmosphere must be the source of oxygen used for the defect healing, most likely through adsorbed oxygen onto the surface. (f) DFT calculations of the band structure of pristine WS_2 (left), WS_{2-x} (middle), $WS_{2-x}O_x$ (right) show that unlike the V_S defect, the S_O defect has no unoccupied deep mid-band gap state. The middle and right band structure show the conduction and valence band from the primitive pristine unit cell (solid lines) overlayed with the conduction and valence band from the supercell calculations (dotted lines).

common defects in exfoliated TMD materials are chalcogen vacancies[47]. Simulations do also predict that these vacancies can chemically react with oxygen[48], because oxygen itself is a chalcogen. Thus, we propose this healing is due to the chemadsorption of atmospheric oxygen, catalyzed by γ-irradiation. A similar mechanism was proposed in a study involving laser-induced defect healing of WSe_2[49]. The γ-ray induced healing observed in our study could happen via several different pathways. One possibility involves the formation of oxygen radicals due to the presence of free electrons from primary reactions like Compton scattering.

To support this, we conducted low temperature PL measurements of irradiated and control samples at 8 K. The low temperature environment reduces thermal broadening which allows the individual emission signature to be resolved. We discovered multiple blue-shifted peaks compared to the RT measurements (see Figure 8.5(a)), most of which are attributed to negatively charged trions. Consistent with standard semiconductor models

and experiments[50], the exciton emission decreases with temperature as the trion emission increases. While both samples exhibit these low temperature excitonic features, the control sample showed additional PL emission in the red sideband. In contrast, the irradiated sample shows only weak emission in the red sideband. This becomes more evident by comparing the fraction of PL from trions and defects, which is 2.08:1 and 0.35:1 for irradiated and control sample, respectively. Therefore, the defect density had decreased 6-fold after the sample was exposed to the γ-radiation. We confirm this by measuring the spectrally- and time-resolved photoluminescence (TRPL): The PL emission is coupled to the single-photon counting module via a grating which makes the TRPL wavelength-selective. Figure 8.5(b) shows the lifetime measurements for three wavelengths, with the positions marked with correspondingly-colored triangles in the spectrum (see Figure 8.5(c) inset). Unlike for defect states, the radiative lifetime of excitons and trions is directly proportional to the temperature[20]. With the lifetime of the control sample at room temperature being 286(4) ps, we expect the lifetime of any excitonic emission at 8 K to be around 7 ps. In fact, at $\lambda = 592$ and 600 nm we measured a lifetime just above our system response time (which is ≈ 3 ps), much shorter than the room temperature measurements. However, at 626 nm the radiative lifetime was 361(3) ps, thus indicating defect emission. Furthermore, we also measured the spectrally-resolved power dependence (see Figure 8.5(c)) at the same wavelengths at which the TRPL was measured. While the slope of the bands around 592 and 600 nm are close to 1 if plotted on a log-log-scale, which means it originates from free excitons or trions, the slope at 626 nm is < 1, which indicates defect emission[51].

In the next phase of this study, we confirm that the defect healing is oxygen-related. We replicate the optical signature of the γ-ray exposed samples by treating freshly prepared monolayers with an O_2 inductively coupled plasma (ICP) and optimizing the plasma parameters (see Methods). Figure 8.5(d) shows the PL spectrum prior and subsequent to the ICP treatment at RT and 8 K. Much like the irradiated samples, also the monolayers treated with the oxygen plasma show a strong increase in brightness and no defect emission at low temperature as well as a longer carrier lifetime.[3] Similar PL enhancement through defect engineering and oxygen bonding using mild oxygen plasma treatment of monolayer MoS_2 has been reported previously[52]. While these results uphold the conjecture of oxygen-related defect healing, the oxygen in the γ-ray experiments could either be supplied by atmospheric oxygen or oxygen from the SiO_2 layer. Therefore, we repeated the irradiation with samples on both, Si/SiO_2 and SiC substrates in air and under vacuum at 10^{-4} atm. This will also strongly reduce the amount of surface adsorbed oxygen. The in-air irradiated samples showed the characteristic increase in brightness and carrier lifetime, while the under vacuum irradiated samples remained unaffected (see Figure 8.5(e)). We found no dependency on the substrate material. In the context of space certification, this means that WS_2 monolayers in evacuated spacecrafts are also not affected even by excessive γ-radiation. In addition to the WS_2 crystals, we also exposed MoS_2 and WSe_2 monolayers to gamma-rays (in air). We observed a slight increase in PL intensity and carrier lifetime after the irradiation for WSe_2 (see Supplementary Figure 8) and no change for MoS_2. It should be mentioned that the PL emission from monolayer MoS_2 in general is much weaker than for other TMDs, so any change is harder to observe. Furthermore, the change in PL and lifetime for the WSe_2 was much weaker than for WS_2, even though

[3] In a follow-up experiment, we demonstrated that such optical emission signature could not be replicated with an H_2 ICP. This essentially rules out hydrogen passivation of the sulfur vacancies as cause for the change in PL. This information was not contained in the original paper, but is further evidence supporting the proposed oxygen-related defect healing mechanism.

both samples experienced the same γ-ray fluence.

We now turn to a theoretical analysis of the electronic structure of the proposed defect using density functional theory (DFT). We calculate the electronic band structure (see Methods) for pristine WS_2, WS_{2-x} (with a sulfur vacancy: V_S), and $WS_{2-x}O_x$ (with an oxygen-substituted sulfur atom: S_O). The V_S defect has a deep unoccupied state in the band gap (see Figure 8.5(f), middle). This is consistent with our experimental observations: The sub-state is an acceptor state trapping electrons, which changes the doping ratio in the crystal. This means more charge carriers are available for charged excitons and thus the trion emission is enhanced. In turn, excitons recombine easily at defects leading to a shorter exciton lifetime. The S_O defect shows no such deep defect state (see Figure 8.5(f), right), meaning as soon as the vacancy is passivated with oxygen, the electronic configuration is similar to the pristine crystal. The crystal structures of the proposed defects are shown in the Supplementary Note 3 and Supplementary Figure 10.

The V_{Se} and Se_O defects in $MoSe_2$, however, show a very similar electronic structure (see Supplementary Figure 11), thus our DFT calculations alone cannot explain why the γ-ray induced defect healing only happens for WS_2. Selenide TMDs are known to have less chalcogen vacancies than sulfide TMDs. In fact, in our experiment we see this by the averaged longer carrier lifetime in $MoSe_2$ of 1264 ps, revealing an inherently much smaller presence of defect sites. As already mentioned, scattering and recombination of excitons at defect sites leads to a reduced lifetime. This means intrinsically less defect healing can occur for $MoSe_2$.

8.3.5 Proton and electron irradiation

After the γ-ray tests, the samples were irradiated with high-energy charged particles, starting with protons and then electrons. In addition to the γ-irradiated samples, after each radiation test fresh samples were added to study both, combined and isolated radiation damage effects. The samples were irradiated with protons from a 1.7 MV tandem accelerator. Due to the maximally available proton energy of 3.4 MeV, the annual fluence spectra shown in Figure 8.1(c) cannot directly be replicated. Instead, we integrate the annual fluence spectrum over the full energy range for each orbital inclination, which yields 241.820, 721.318 and $464.770 \times 10^6\,\mathrm{cm}^{-2}$ for 20°, 51.6° and 98°, respectively. Unfortunately, these fluence values are below the range of the used charge carrier counter, which is why we tested the samples at $F_{p^+} = 10^{10}\,\mathrm{cm}^{-2}$. However, at the lower proton energies (200, 500, 1000 and 2500 keV) we used, the potential displacement damage caused by the protons[53] is higher due to the higher stopping power of the 2D materials at lower energies (see Supplementary Note 4 and Supplementary Figures 12 through 14). As our fluence is anyway higher than required for 500 km altitude, we cannot scale the fluence down according to the used proton energies. For all proton energies, we did not observe any changes in the device performances, PL spectra or carrier lifetimes (see Supplementary Note 5 and Supplementary Figures 15 through 17). Even after increasing the proton flux 100-fold, there were still no changes. This result is also consistent with previous work[54]. Furthermore, Kim et al. found the onset of degradation at a fluence of $10^{13}\,\mathrm{cm}^{-2}$, with strong degradation at $10^{14}\,\mathrm{cm}^{-2}$,[54] while Shi et al. found the damage threshold of WSe_2/SiC heterostructures at $10^{16}\,\mathrm{cm}^{-2}$ proton fluence[32]. In our case, the proton fluence of $10^{12}\,\mathrm{cm}^{-2}$ corresponds to 1386 years in orbit (at 51.6° inclination and 500 km altitude). The scaling is based on the number of protons. Hence, we conclude that proton irradiation is no concern for 2D materials and devices in LEO.

Finally, we exposed the samples to electrons using a scanning electron microscope (SEM). The damage to 2D materials caused by electrons is mostly displacement and sputtering[33]. Similar to the proton accelerator, both the energy range as well as the integrated flux are beyond the capabilities of the SEM. The tested energies were 5, 10, 20 and 30 keV while the fluence varied from 10^{10} to 10^{15} cm^{-2}. At 500 km altitude, the integrated fluences are 12.35, 32.06 and 20.73×10^{6} cm^{-2} for equatorial, ISS and polar orbit, respectively. At the lowest accessible fluence, which is still three orders of magnitude above what is expected in LEO, the crystals were mostly unaffected by the electron irradiation (see Supplementary Note 6 and Supplementary Figures 18 through 20). Extrapolating the fluence to LEO levels predict that electrons will not have any impact on 2D materials. Higher electron fluences result in permanent loss of photoluminescence for TMDs. We propose that this is due to the creation of chalcogen vacancies by knock-on damage, which, as previously mentioned, cause recombination, thereby quenching the PL[55]. However, if the electron energy is increased from 5 to 30 keV, even at the highest fluence such damage was mitigated. This is because higher energy electrons have a smaller interaction cross section (see Supplementary Figure 12). The single-photon emitters remain unaffected by the electron irradiation, however, at extremely high fluences, the emitter density can be increased significantly[17,56]. In our case this happened while focusing the SEM on a small crystal part before exposing the full crystals to the electrons. The experienced electron fluence at these positions was up to 10^{18} cm^{-2} (see Supplementary Figure 21).

All radiation tests so far indicate that 2D materials tolerate significant amounts of ionizing radiation, far beyond the requirements for LEO. The question arises, if the radiation resilience is also sufficient for higher altitudes. Using SPENVIS we calculate the integrated annual particle fluence (integrated over the full energy range) as a function of altitude (see Supplementary Figure 22). While the proton fluence always remains nearly two orders of magnitude below the damage onset threshold, the electron fluence exceeds the observed damage onset at altitudes > 1000 km. It should be mentioned that these calculations assume the same 1.85 mm of Al shielding as above. The shielding also explains the leap in electron fluence at 2000 km: The electron energy increases with altitude and thus actually trapped electrons can penetrate the shielding. As already mentioned, at lower altitudes the electrons are secondary electrons produced via ionizing interactions of high-energy protons with the shielding. Nevertheless, by using an appropriate shield (5.8 mm graded Al/Ta with a Ta to Al mass ratio of 35%), the electron fluence can be kept below the damage threshold. Shielding meeting this requirement is common for higher orbits such as in geostationary satellites. Furthermore, this means that 2D materials also can operate in other environments with heavy irradiation, such as during solar flares or near nuclear reactors.

8.4 Discussion

We presented a comprehensive study on the effects of radiation on 2D materials in vision of space certification. Moreover, this study covered the effects of γ-, proton and electron irradiation on TMD-based FETs and single-photon sources in hBN as well as their interaction with blank TMD monolayers. These nanomaterials were investigated back-to-back, shortly before and after irradiation. While all crystals remained effectively invariant under irradiation relevant for space environments, after excessive γ-radiation monolayer WS_2 exhibit significant increase in photoluminescence and carrier lifetime proportionally to the photon flux. This is attributed to the healing of sulfur vacancies induced by γ-radiation.

We propose that the γ-rays, through a process like Compton scattering, dissociate atmospheric oxygen, which then chemically reacts with the vacancies. This mechanism was confirmed by low temperature measurements showing that defect emission was weakened upon γ-irradiation. Furthermore, band structure modeling of this reaction shows disappearing trapping sites, thus explaining the observed changes.

A potential application of this effect could be a compact radiation dosimeter or radiation detector. In addition to the radiation tests, the low temperature measurements also confirm that 2D materials survive vacuum and thermal cycling. The tested radiation fluences were much higher than required for LEO. Hence, 2D materials and devices based on them have been proven to withstand the harsh space radiation. Moreover, 2D materials can even operate in environments with heavy irradiation, such as during solar flares or near nuclear reactors. In addition, if the spacecraft shielding is adapted appropriately, we predict that 2D materials can even be used in any orbit. Our results pave the way towards establishing the robustness and reliability of 2D material-based devices for space instrumentation. This combines the fields of space science and nanomaterials, thus opening new possibilities for future space missions.

8.5 Methods

Device Fabrication

The bulk crystals were acquired from HQGraphene and used as received. After mechanical exfoliation onto Gel-Pak WF-40-X4, monolayer TMD and multilayer hBN crystals were optically identified by contrast and transferred via dry contact to Si/SiO_2 substrates (262 nm thermally grown) or 4H-SiC substrates supplied by SiCrystal. The crystal thickness was confirmed using PSI measurements. The hBN crystals were exposed to an oxygen plasma generated from a microwave field at 200 W for 1 min and a pressure of 0.3 mbar at a gas flow rate of $300\,cm^3\,min^{-1}$ at room temperature. The subsequent rapid thermal annealing was done under an Argon atmosphere at 850°C at a gas flow of $500\,cm^3\,min^{-1}$. The substrates for the FETs have been pre-patterned with gold electrodes using photolithography: After spin coating AZ MiR 701, the positive photoresist is exposed to UV light through a mask and developed. Using electron-beam thermal evaporation, 100 nm of gold is deposited and then LOR 3A was used for lift-off. The monolayer crystals were mechanically transferred between the two electrodes with an approximate gap of 10 μm, with an attached multilayer crystal touching the electrode completing the electrical connection. The two electrodes served as top gates (source and drain), while the heavily n^+-doped silicon substrate served as the back gate.

Optical Characterization

The home-built μPL setup utilized second harmonic generation to generate 522 nm ultrashort laser pulses (High Q Laser URDM). The linearly polarized laser is focused down to the diffraction limit by an Olympus 100×/0.9 dry objective. For confocal PL mapping, the samples were moved on Newport precision stages with up to 0.2 μm resolution. The in-reflection collected emission is wavelength filtered (Semrock RazorEdge ultrasteep long-pass edge filter), fully suppressing the pump light, while still collecting the full emission spectrum. This spectrum is recorded using a grating-based spectrometer (Princeton Instruments SpectraPro). The laser pulse length for time-resolved measurements is 300 fs

length at a repetition rate of 20.8 MHz. The pulses were split into trigger signal and excitation pulse. The emitted photons were detected by a single-photon counter (Micro Photon Devices) after the grating, so that the time-resolved photoluminescence is also spectrally resolved. Both, trigger and single-photon signal were correlated by a PicoHarp 300. For low temperature measurements, a cryogenic chamber was added to the setup and the samples were cooled down to 8 K with liquid He, at a pressure of 13 μTorr to prevent the formation of ice on the window. The objective was replaced with a Nikon S Plan Fluor 60×/0.7 objective with adjustable correction ring. The second-order correlation function was measured using a Hanbury Brown and Twiss (HBT)-type interferometer in a different confocal setup with a 512 nm diode laser, equipped with a spectrometer and nano-positioning stage, ensuring that the defects can be localized. The correlation function data is fitted to a three-level system with ground and excited states as well as a meta-stable shelving state:

$$g^{(2)}(\tau) = 1 - Ae^{-|\tau-\mu|/t_1} + Be^{-|\tau-\mu|/t_2} \tag{8.1}$$

where t_1 and t_2 are the excited and meta-stable state lifetimes respectively, μ accounts for different electrical and optical path lengths in the HBT interferometer and A and B are the anti-bunching and bunching amplitudes. The experimental data has been normalized such that for very long time delays $g^{(2)}(\tau \to \infty) = 1$.

Electrical Characterization

The FETs were characterized with a Kiethley 4200 Semiconductor Analyzer. One of the the gold electrodes is grounded, while the n^+-doped Si substrate functions as a back gate, providing uniform electrostatic doping in the monolayer. Back gate sweeps at different biases between source and drain were measured as well as I-V curves at various back gate voltages. All electrical measurements were carried out at room temperature.

Irradiation

The radioactive isotope $^{22}_{11}$Na was used as a γ-ray source and was kept in a sealed Tungsten container, which was opened for the duration of the exposure. For every disintegration, a 1.275 MeV photon is emitted into 4π. With a branching ratio of approximately 9:1 the decay either happens via a β^+ transition or electron capture, respectively, resulting in a 90 % probability that a positron is emitted. The positrons are shielded by Al foil, where they recombine with electrons to create two γ-rays with energies of 511 keV in opposite directions. The nominal activity was $A = 1.04$ GBq (number of decays), which together with the container geometry leads to a total photon flux of 10.3 MBq cm^{-2}sr^{-1}MeV^{-1} at the output of the container. The differential flux was calculated with

$$F_\gamma = \sum_E \frac{A\eta_E}{G_E E} \tag{8.2}$$

with branching ratio η_E, photon energy E and geometrical form factor of the container G_E (which is energy-dependent due to the position of the Al foil). The samples were placed at different distances to the source, simulating different altitudes/times in orbit, with a placement accuracy of 1 mm. All samples were mounted facing towards the γ-ray source. The second γ-ray experiment took place 117 days later, after which the source activity decreased to 91.8% ($\tau_{1/2} = 2.603$ years). We accounted for this by adjusting the

distance to the source. We exposed samples in air and in a vacuum chamber at 10^{-4} atm. The γ-rays were attenuated by the glass window ports of the vacuum chamber by only 5%. This attenuation does not account for the complete disappearance of the healing effect on the samples in the chamber. For the proton irradiation a high-energy implanter featuring a 1.7 MV tandem Pelletron accelerator was used. TiH was used as target for the ion sputter source and Ti ions were filtered by a 90° magnet. The tandem accelerator can double the maximal proton energy, however, due to the used configuration the proton energy was limited from 200 keV to 2.5 MeV. The ion energy is typically well defined within ±5 keV and the error on the fluence is less than ±10%. The irradiation took place under pressures of 10^{-7} Torr at room temperature. For the electron irradiation the SEM from an FEI Helios 600 NanoLab was used, allowing for electron energies ranging from 1 to 30 keV at 2.2 mPa and room temperature. The current was varied from 0.17 to 0.69 nA. The electron fluence F_e is given by $F_e = \frac{I \cdot t}{e \cdot A}$ where I is the electron current, t the frame time, e the electron charge and A the frame area. The crystal flakes were located at a very low electron flux and then the SEM was aligned using another flake nearby, so that the crystal flake under investigation is targeted with a focused electron beam.

Plasma etching

We used the commercial ICP-RIE (reactive ion etching) system Samco RIE-400iP and varied all process parameters. We found the optimal process parameters to be 75 W ICP power, 0 W RF power, 3 min plasma interaction time as well as a gas pressure of 6.6 Pa at an oxygen gas flow rate of 30 $\mathrm{cm^3\,min^{-1}}$. The RF power is chosen zero to avoid any ion bombardment during the plasma exposure, thus ensuring the process is chemical and not physical (this results in crystal etching or thinning). All ICP processes were carried out at room temperature.

Computational Methods

The space environment calculations were performed using the SPENVIS web interface. The proton and electron flux spectra were calculated using the AP-8 MAX and AE-8 MAX models. The shielded fluence spectra for 1.853 mm Al shielding were obtained using the MFLUX package. The interactions between charge carriers and matter are calculated using Monte Carlo simulations (see Supplementary Note 4)[57–59]. These simulations take electromagnetic scattering processes and hadronic nuclear interactions into account. Due to the more complicated nature of the interactions of electrons with the shielding material, the electron fluence spectra are less accurate. The DFT calculations have been performed using the ab-initio total-energy and molecular-dynamics program VASP (Vienna Ab initio Simulation Package) developed at the Fakultät für Physik of the Universität Wien[60,61]. First, the geometry of the pristine conventional cell was optimized using a $15 \times 15 \times 1$ Monkhorst-Pack reciprocal space grid such that all forces were less than 0.001 $\mathrm{eV\,Å^{-1}}$. We used a plane-wave energy cutoff of 450 eV and norm-conserving pseudopotentials with nonlinear core-correction to describe the core electrons. We also used the Perdew-Burke-Ernzerhof (PBE) functional in the generalized gradient approximation to describe the exchange-correlation energy[62]. The monolayer was constructed using a $7 \times 7 \times 1$ supercell of the optimized primitive unit cell. The ionic positions were then relaxed again, while keeping the cell size fixed. We chose the vacuum distance between each layer, described by the lattice parameter c, such that the band structure is flat in Γ to A direction of the Brillouin zone. This indicates that there is no inter-layer interaction. We used the same

method to obtain the band structure of the oxygen and vacancy centers in both, WS_2 and $MoSe_2$. These calculations show flat bands in each high symmetry direction, which indicates that there is minimal defect-defect interaction between neighboring supercells. The effective band structures shown here were unfolded using the PyVaspwfc package[63, 64].

When analyzing these calculations, it is important to remember that PBE DFT systematically underestimates the quasiparticle band gap[65]. Further, verifying the DFT band gap against the experimental optical band gap requires consideration of the exciton binding energy, which is significant in 2D TMDs (~ 1 eV)[66]. Noting these problems, we only consider our calculations as accurate enough to qualitatively predict the presence and relative ordering of unoccupied defect levels in the band gap. To confirm our conclusions, future calculations should apply GW corrections.

Code availability

The custom-code used for analyzing the data of the confocal PL mapping of monolayer 2D materials (averaging algorithm, see also Supplementary Note 1) is freely available and archived at https://doi.org/10.5281/zenodo.2584405.

Data availability

The data that supports the findings of this study are available from the corresponding author upon reasonable request.

Acknowledgments

This work was funded by the Australian Research Council (CE170100012, FL150100019, DE140100805, DE170100169, DE160100098 and DP180103238). We acknowledge financial support from ANU PhD scholarships, the China Scholarship Council and the ANU Major Equipment Committee fund (No. 14MEC34). We thank the ACT Node of the Australian National Fabrication Facility for access to their nano- and microfabrication facilities. This research was undertaken with the assistance of resources and services from the National Computational Infrastructure (NCI). We also thank Hark Hoe Tan for access to the TRPL system. We acknowledge access to NCRIS facilities (ANFF and the Heavy Ion Accelerator Capability) at the Australian National University, in particular we thank Rob Elliman and Tom Ratcliff for assistance with the implanter.

Supplementary information

Supplementary information accompanies this paper at https://doi.org/10.1038/s41467-019-09219-5 or in the Appendix A.3.

References

[1] G. Cheng, P. F. Siles, F. Bi, C. Cen, D. F. Bogorin, C. W. Bark, C. M. Folkman, J.-W. Park, C.-B. Eom, G. Medeiros-Ribeiro, and J. Levy, *Sketched oxide single-electron transistor*, Nat. Nanotechnol., **6** 343–347, 2011.

[2] M. Fuechsle, J. A. Miwa, S. Mahapatra, H. Ryu, S. Lee, O. Warschkow, L. C. L. Hollenberg, G. Klimeck, and M. Y. Simmons, *A single-atom transistor*, Nat. Nanotechnol., **7** 242–246, 2012.

[3] K. S. Novoselov, A. K. Geim, S. V. Morozov, D. Jiang, Y. Zhang, S. V. Dubonos, I. V. Grigorieva, and A. A. Firsov, *Electric Field Effect in Atomically Thin Carbon Films*, Science, **306** 666–669, 2004.

[4] K. F. Mak, C. Lee, J. Hone, J. Shan, and T. F. Heinz, *Atomically Thin MoS_2: A New Direct-Gap Semiconductor*, Phys. Rev. Lett., **105** 136805, 2010.

[5] F. Schwierz, *Graphene transistors*, Nat. Nanotechnol., **5** 487–496, 2010.

[6] B. Radisavljevic, A. Radenovic, J. Brivio, V. Giacometti, and A. Kis, *Single-layer MoS_2 transistors*, Nat. Nanotechnol., **6** 147–150, 2011.

[7] T. Roy, M. Tosun, J. S. Kang, A. B. Sachid, S. B. Desai, M. Hettick, C. C. Hu, and A. Javey, *Field-Effect Transistors Built from All Two-Dimensional Material Components*, ACS Nano, **8** 6259–6264, 2014.

[8] M. Zhao, Y. Ye, Y. Han, Y. Xia, H. Zhu, S. Wang, Y. Wang, D. A. Muller, and X. Zhang, *Large-scale chemical assembly of atomically thin transistors and circuits*, Nat. Nanotechnol., **11** 954–959, 2016.

[9] S. B. Desai, S. R. Madhvapathy, A. B. Sachid, J. P. Llinas, Q. Wang, G. H. Ahn, G. Pitner, M. J. Kim, J. Bokor, C. Hu, H.-S. P. Wong, and A. Javey, *MoS_2 transistors with 1-nanometer gate lengths*, Science, **354** 99–102, 2016.

[10] N. Huo, Y. Yang, and J. Li, *Optoelectronics based on 2D TMDs and heterostructures*, J. Semicond., **38** 031002, 2017.

[11] M. M. Furchi, F. Höller, L. Dobusch, D. K. Polyushkin, S. Schuler, and T. Mueller, *Device physics of van der Waals heterojunction solar cells*, npj 2D Mater. Appl., **2** 3, 2018.

[12] L. Shi and T. Zhao, *Recent advances in inorganic 2D materials and their applications in lithium and sodium batteries*, J. Mater. Chem. A, **5** 3735–3758, 2017.

[13] T. T. Tran, K. Bray, M. J. Ford, M. Toth, and I. Aharonovich, *Quantum emission from hexagonal boron nitride monolayers*, Nat. Nanotechnol., **11** 37–41, 2016.

[14] T. Vogl, G. Campbell, B. C. Buchler, Y. Lu, and P. K. Lam, *Fabrication and Deterministic Transfer of High-Quality Quantum Emitters in Hexagonal Boron Nitride*, ACS Photonics, **5** 2305–2312, 2018.

[15] T. Vogl, Y. Lu, and P. K. Lam, *Room temperature single photon source using fiber-integrated hexagonal boron nitride*, J. Phys. D: Appl. Phys., **50** 295101, 2017.

[16] T. T. Tran, C. Elbadawi, D. Totonjian, C. J. Lobo, G. Grosso, H. Moon, D. R. Englund, M. J. Ford, I. Aharonovich, and M. Toth, *Robust Multicolor Single Photon Emission from Point Defects in Hexagonal Boron Nitride*, ACS Nano, **10** 7331–7338, 2016.

[17] S. Choi, T. T. Tran, C. Elbadawi, C. Lobo, X. Wang, S. Juodkazis, G. Seniutinas, M. Toth, and I. Aharonovich, *Engineering and Localization of Quantum Emitters in Large Hexagonal Boron Nitride Layers*, ACS Appl. Mater. Interfaces, **8** 29642–29648, 2016.

[18] S.-K. Liao, W.-Q. Cai, W.-Y. Liu, L. Zhang, Y. Li, J.-G. Ren, J. Yin, Q. Shen, Y. Cao, Z.-P. Li, F.-Z. Li, X.-W. Chen, L.-H. Sun, J.-J. Jia, J.-C. Wu, X.-J. Jiang, J.-F. Wang, Y.-M. Huang, Q. Wang, Y.-L. Zhou, L. Deng, T. Xi, L. Ma, T. Hu, Q. Zhang, Y.-A. Chen, N.-L. Liu, X.-B. Wang, Z.-C. Zhu, C.-Y. Lu, R. Shu, C.-Z. Peng, J.-Y. Wang, and J.-W. Pan, *Satellite-to-ground quantum key distribution*, Nature, **549** 43–47, 2017.

[19] NASA. *General Environmental Verification Standard GSFC-STD-7000*, https://standards.nasa.gov/standard/gsfc/gsfc-std-7000, 2013.

[20] C. Robert, D. Lagarde, F. Cadiz, G. Wang, B. Lassagne, T. Amand, A. Balocchi, P. Renucci, S. Tongay, B. Urbaszek, and X. Marie, *Exciton radiative lifetime in transition metal dichalcogenide monolayers*, Phys. Rev. B, **93** 205423, 2016.

[21] M. Kianinia, B. Regan, S. A. Tawfik, T. T. Tran, M. J. Ford, I. Aharonovich, and M. Toth, *Robust Solid-State Quantum System Operating at 800 K*, ACS Photonics, **4** 768–773, 2017.

[22] A. Dietrich, M. Bürk, E. S. Steiger, L. Antoniuk, T. T. Tran, M. Nguyen, I. Aharonovich, F. Jelezko, and A. Kubanek, *Observation of Fourier transform limited lines in hexagonal boron nitride*, Phys. Rev. B, **98** 081414, 2018.

[23] I. Childres, L. A. Jauregui, M. Foxe, J. Tian, R. Jalilian, I. Jovanovic, and Y. P. Chen, *Effect of electron-beam irradiation on graphene field effect devices*, Appl. Phys. Lett., **97** 173109, 2010.

[24] H. Mai-Xing, J. Zhuo-Yu, S. Li-Wei, C. Ying-Ping, W. Hong, L. Xin, L. Dong-Mei, and L. Ming, *γ radiation caused graphene defects and increased carrier density*, Chinese Phys. B, **20** 086102, 2011.

[25] M. Foxe, G. Lopez, I. Childres, R. Jalilian, A. Patil, C. Roecker, J. Boguski, I. Jovanovic, and Y. P. Chen, *Graphene Field-Effect Transistors on Undoped Semiconductor Substrates for Radiation Detection*, IEEE Trans. Nanotechnol., **11** 581–587, 2012.

[26] C. X. Zhang, B. Wang, G. X. Duan, E. X. Zhang, D. M. Fleetwood, M. L. Alles, R. D. Schrimpf, A. P. Rooney, E. Khestanova, G. Auton, R. V. Gorbachev, S. J. Haigh, and S. T. Pantelides, *Total Ionizing Dose Effects on hBN Encapsulated Graphene Devices*, IEEE Trans. Nucl. Sci., **61** 2868–2873, 2014.

[27] K. Alexandrou, A. Masurkar, H. Edrees, J. F. Wishart, Y. Hao, N. Petrone, J. Hone, and I. Kymissis, *Improving the radiation hardness of graphene field effect transistors*, Appl. Phys. Lett., **109** 153108, 2016.

[28] E. Cazalas, B. K. Sarker, I. Childres, Y. P. Chen, and I. Jovanovic, *Modulation of graphene field effect by heavy charged particle irradiation*, Appl. Phys. Lett., **109** 253501, 2016.

[29] C. X. Zhang, A. K. M. Newaz, B. Wang, E. X. Zhang, G. X. Duan, D. M. Fleetwood, M. L. Alles, R. D. Schrimpf, K. I. Bolotin, and S. T. Pantelides, *Electrical Stress and Total Ionizing Dose Effects on MoS_2 Transistors*, IEEE Trans. Nucl. Sci., **61** 2862–2867, 2014.

[30] G. R. Bhimanapati, M. Wetherington, S. Mahabir, and J. A. Robinson, *Synthesis and radiation response of BCON: a graphene oxide and hexagonal boron nitride hybrid*, 2D Mater., **3** 025028, 2016.

[31] C. Liang, Y. Su, E. X. Zhang, K. Ni, M. L. Alles, R. D. Schrimpf, D. M. Fleetwood, and S. J. Koester, *Total Ionizing Dose Effects on HfO2-Passivated Black Phosphorus Transistors*, IEEE Trans. Nucl. Sci., **64** 170–175, 2017.

[32] T. Shi, R. C. Walker, I. Jovanovic, and J. A. Robinson, *Effects of energetic ion irradiation on WSe2/SiC heterostructures*, Sci. Rep., **7** 4151, 2017.

[33] R. C. Walker, T. Shi, E. C. Silva, I. Jovanovic, and J. A. Robinson, *Radiation effects on two-dimensional materials*, Phys. Status Solidi A, **213** 3268–3268, 2016.

[34] R. Milliron. *Interorbital Preps for NEPTUNE Test Launch - and eleven smallsats will go along for the ride.*, http://www.satmagazine.com/story.php?number=1600200139, 2017.

[35] N. V. Proscia, Z. Shotan, H. Jayakumar, P. Reddy, C. Cohen, M. Dollar, A. Alkauskas, M. Doherty, C. A. Meriles, and V. M. Menon, *Near-deterministic activation of room-temperature quantum emitters in hexagonal boron nitride*, Optica, **5** 1128–1134, 2018.

[36] European Space Agency. *The Space Environment Information System*, http://www.spenvis.oma.be, 2018.

[37] R. Bučík, K. Kudela, A. Bogomolov, I. Myagkova, S. Kuznetsov, and S. Ryumin, *Distribution of gamma ray fluxes at altitude 500 km: CORONAS-I data*, Acta Phys. Slovaca, **50** 267, 2000.

[38] R. Bučík, A. Dmitriev, K. Kudela, and S. Ryumin, *Gamma-Radiation of the Earth's Atmosphere from the CORONAS-I Data*, Proc. 26 ICRC, **7** 433–436, 1999.

[39] G. Cassabois, P. Valvin, and B.Gil, *Hexagonal boron nitride is an indirect bandgap semiconductor*, Nat. Photon., **10** 262–266, 2016.

[40] J. Yang, Z. Wang, F. Wang, R. Xu, J. Tao, S. Zhang, Q. Qin, B. Luther-Davies, C. Jagadisch, and Y. Lu, *Atomically thin optical lenses and gratings*, Light Sci. Appl., **5** e16046, 2002.

[41] H. R. Gutiérrez, N. Perea-López, A. L. Elías, A. Berkdemir, B. Wang, R. Lv, F. López-Urías, V. H. Crespi, H. Terrones, and M. Terrones, *Extraordinary Room-Temperature Photoluminescence in Triangular WS_2 Monolayers*, Nano Lett., **13** 3447–3454, 2013.

[42] S. Y. F. Chu, L. P. Ekström, and R. B. Firestone. *WWW Table of Radioactive Isotopes*, http://nucleardata.nuclear.lu.se/nucleardata/toi/, 1999.

[43] E. X. Zhang, A. K. M. Newaz, B. Wang, S. Bhandaru, C. X. Zhang, D. M. Fleetwood, K. I. Bolotin, S. T. Pantelides, M. L. Alles, R. D. Schrimpf, S. M. Weiss, R. A. Reed,

and R. A. Weller, *Low-Energy X-ray and Ozone-Exposure Induced Defect Formation in Graphene Materials and Devices*, IEEE Trans. Nucl. Sci., **58** 2961–2967, 2011.

[44] Y. S. Puzyrev, B. Wang, E. X. Zhang, C. X. Zhang, A. K. M. Newaz, K. I. Bolotin, D. M. Fleetwood, R. D. Schrimpf, and S. T. Pantelides, *Surface Reactions and Defect Formation in Irradiated Graphene Devices*, IEEE Trans. Nucl. Sci., **59** 3039–3044, 2012.

[45] S. A. Francis, J. C. Petrosky, J. W. McClory, and C. D. Cress, *Effects of Proton and X-ray Irradiation on Graphene Field-Effect Transistors with Thin Gate Dielectrics*, IEEE Trans. Nucl. Sci., **61** 3010–3017, 2014.

[46] V. V. Anikeyev, B. V. Kovalchuk, V. M. Lazorenko, G. Y. Mikhaylova, M. M. Nishchenko, V. N. Pimenov, G. P. Prikhodko, S. I. O. Sadykhov, and V. I. Tovtin, *Effect of electron irradiation on the formation and healing of defects in carbon nanotubes*, Inorganic Mater: Appl. Research, **7** 204–209, 2016.

[47] J. Hong, Z. Hu, M. Probert, K. Li, D. Lv, X. Yang, L. Gu, N. Mao, Q. Feng, L. Xie, J. Zhang, D. Wu, Z. Zhang, C. Jin, W. Ji, X. Zhang, J. Yuan, and Z. Zhang, *Exploring atomic defects in molybdenum disulphide monolayers*, Nat. Commun., **6** 6293, 2015.

[48] Y. Liu, P. Stradins, and S.-H. Wei, *Air Passivation of Chalcogen Vacancies in Two-Dimensional Semiconductors*, Angew. Chem. Int. Ed., **55** 965–968.

[49] J. Lu, A. Carvalho, X. K. Chan, H. Liu, B. Liu, E. S. Tok, K. P. Loh, A. H. Castro Neto, and C. H. Sow, *Atomic Healing of Defects in Transition Metal Dichalcogenides*, Nano Lett., **15** 3524–3532, 2015.

[50] K. Wei, Y. Liu, H. Yang, X. Cheng, and T. Jiang, *Large range modification of exciton species in monolayer WS_2*, Appl. Opt., **55** 6251–6255, 2016.

[51] Y. Miyauchi, M. Iwamura, S. Mouri, T. Kawazoe, M. Ohtsu, and K. Matsuda, *Brightening of excitons in carbon nanotubes on dimensionality modification*, Nat. Photon., **7** 715–719, 2013.

[52] H. Nan, Z. Wang, W. Wang, Z. Liang, Y. Lu, Q. Chen, D. He, P. Tan, F. Miao, X. Wang, J. Wang, and Z. Ni, *Strong Photoluminescence Enhancement of MoS_2 through Defect Engineering and Oxygen Bonding*, ACS Nano, **8** 5738–5745, 2014.

[53] S. Mathew, T. Chan, D. Zhan, K. Gopinadhan, A.-R. Barman, M. Breese, S. Dhar, Z. Shen, T. Venkatesan, and J. T. Thong, *The effect of layer number and substrate on the stability of graphene under MeV proton beam irradiation*, Carbon, **49** 1720–1726, 2011.

[54] T.-Y. Kim, K. Cho, W. Park, J. Park, Y. Song, S. Hong, W.-K. Hong, and T. Lee, *Irradiation Effects of High-Energy Proton Beams on MoS_2 Field Effect Transistors*, ACS Nano, **8** 2774–2781, 2014.

[55] H.-P. Komsa, J. Kotakoski, S. Kurasch, O. Lehtinen, U. Kaiser, and A. V. Krasheninnikov, *Two-Dimensional Transition Metal Dichalcogenides under Electron Irradiation: Defect Production and Doping*, Phys. Rev. Lett., **109** 035503, 2012.

[56] H. Ngoc My Duong, M. A. P. Nguyen, M. Kianinia, T. Ohshima, H. Abe, K. Watanabe, T. Taniguchi, J. H. Edgar, I. Aharonovich, and M. Toth, *Effects of High-Energy Electron Irradiation on Quantum Emitters in Hexagonal Boron Nitride*, ACS Appl. Mater. Interfaces, **10** 24886–24891, 2018.

[57] J. F. Ziegler, M. Ziegler, and J. Biersack, *SRIM - The stopping and range of ions in matter*, Nucl. Instr. Meth. Phys. Res. B, **268** 1818–1823, 2010.

[58] M. Berger, J. Coursey, M. Zucker, and J. Chang. *ESTAR, PSTAR, and ASTAR: Computer Programs for Calculating Stopping-Power and Range Tables for Electrons, Protons, and Helium Ions*, http://physics.nist.gov/Star (National Institute of Standards and Technology, Gaithersburg, MD), 2005.

[59] D. Drouin, A. R. Couture, D. Joly, X. Tastet, V. Aimez, and R. Gauvin, *CASINO V2.42 - A Fast and Easy-to-use Modeling Tool for Scanning Electron Microscopy and Microanalysis Users*, Scanning, **29** 92–101, 2007.

[60] G. Kresse and J. Furthmüller, *Efficient iterative schemes for ab initio total-energy calculations using a plane-wave basis set*, Phys. Rev. B, **54** 11169–11186, 1996.

[61] G. Kresse and D. Joubert, *From ultrasoft pseudopotentials to the projector augmented-wave method*, Phys. Rev. B, **59** 1758–1775, 1999.

[62] J. P. Perdew, K. Burke, and M. Ernzerhof, *Generalized Gradient Approximation Made Simple [Phys. Rev. Lett. 77, 3865 (1996)]*, Phys. Rev. Lett., **78** 1396–1396, 1997.

[63] V. Popescu and A. Zunger, *Extracting E versus k effective band structure from supercell calculations on alloys and impurities*, Phys. Rev. B, **85** 085201, 2012.

[64] Q. Zheng. *VASP Band Unfolding*. https://github.com/QijingZheng/VaspBandUnfolding, 2018.

[65] J. P. Perdew and M. Levy, *Physical Content of the Exact Kohn-Sham Orbital Energies: Band Gaps and Derivative Discontinuities*, Phys. Rev. Lett., **51** 1884–1887, 1983.

[66] C. Zhang, C. Gong, Y. Nie, K.-A. Min, C. Liang, Y. J. Oh, H. Zhang, W. Wang, S. Hong, L. Colombo, R. M. Wallace, and K. Cho, *Systematic study of electronic structure and band alignment of monolayer transition metal dichalcogenides in Van der Waals heterostructures*, 2D Mater., **4** 015026, 2017.

Chapter 9

Space-compatible cavity-enhanced single-photon generation with hexagonal boron nitride

9.1 Foreword

The previous chapter presented the space qualification of 2D material based devices, which included the single-photon emitters hosted by hexagonal boron nitride. The quantum emitters are projected to survive the harsh radiation environments in space, without any modification in photophysics. For satellite-based single-photon quantum key distribution, however, this certification is only a necessary, but not sufficient condition. Even with the plasma treated hBN, the single-photon source performance is still far from the requirements of quantum information processing, let alone for quantum cryptography or quantum computing.

A straightforward path for enhancing a spontaneous emission process is by coupling the emitter to an optical resonator, known as the Purcell effect. The resonator reduces the photonic density of states, so emission into the resonant modes is enhanced. This cleans the emission spectrum, as any off-resonant noise is suppressed. As the emission is predominantly into the resonator modes, the collection efficiency is enhanced. Moreover, as any non-radiative decay path remains unaffected, but radiative decay is enhanced by the Purcell factor, the quantum efficiency is ultimately increased. The increase in radiative decay also shortens the excited state lifetime, which is important for efficient post-selection and the single-photon repetition rate. A cavity linewidth that is narrower than the emitter linewidth can also increase the indistinguishability of consecutively emitted single-photons. This allows one to use even strongly dephasing emitters for photonic quantum computing.

In order to achieve a strong Purcell enhancement, the cavity mode volume must be small, and the cavity quality factor high. A small mode volume can be achieved by utilizing nanofabrication techniques, while for a high quality factor, highly reflecting coatings are required. This chapter presents the results of such a cavity-enhanced emitter. The cavity was fully fabricated at the Australian National Fabrication Facility node at the Australian National University. While the achieved dielectric high-reflection coatings are lagging behind state-of-the-art commercial coatings, having the entire fabrication cycle local allows for fast turn-around times in the device fabrication. The complete single-photon source was implemented on a pico-class satellite platform, including excitation laser, driving electronics, and control units. Thus, this work tests if such a single-photon source can be enhanced

such that the performance is sufficient for quantum key distribution, while at the same time being compact enough to fulfill the strict size, weight and power requirements on satellites. This could lead to low-cost satellite-based long-distance quantum networks. The work has been published as an as soon as publishable article in ACS Photonics and is here reprinted (adapted) with permission from https://pubs.acs.org/doi/10.1021/acsphotonics.9b00314. All graphics have been recreated to match the style of this thesis. A preprint is available at arXiv:1902.03019 (2019).

Space-compatible cavity-enhanced single-photon generation with hexagonal boron nitride

Tobias Vogl[1], Ruvi Lecamwasam[1], Ben C. Buchler[1], Yuerui Lu[2], and Ping Koy Lam[1]

[1] *Centre for Quantum Computation and Communication Technology, Department of Quantum Science, Research School of Physics and Engineering, The Australian National University, Acton ACT 2601, Australia*

[2] *Centre for Quantum Computation and Communication Technology, Research School of Electrical, Energy and Materials Engineering, The Australian National University, Acton ACT 2601, Australia*

Abstract

Sources of pure and indistinguishable single-photons are critical for near-future optical quantum technologies. Recently, color centers hosted by two-dimensional hexagonal boron nitride (hBN) have emerged as a promising platform for high luminosity room temperature single-photon sources. Despite the brightness of the emitters, the spectrum is rather broad and the single-photon purity is not sufficient for practical quantum information processing. Here, we report integration of such a quantum emitter hosted by hBN into a tunable optical microcavity. A small mode volume of the order of λ^3 allows us to Purcell enhance the fluorescence, with the observed excited state lifetime shortening. The cavity significantly narrows the spectrum and improves the single-photon purity by suppression of off-resonant noise. We explore practical applications by evaluating the performance of our single-photon source for quantum key distribution and quantum computing. The complete device is compact and implemented on a picoclass satellite platform, enabling future low-cost satellite-based long-distance quantum networks.

9.2 Introduction

Near-future optical quantum information processing[1] relies on sources of pure and indistinguishable single-photons. Promising candidates include quantum dots[2], trapped ions[3], color centers in solids[4] and single-photon sources (SPSs) based on heralded spontaneous parametric down-conversion[5]. The recent discovery of fluorescent defects in two-dimensional (2D) materials has added yet another class of quantum emitters to the solid-state color centers. Stable quantum emitters have been reported in the transition metal dichalcogenides WSe_2[6–10], WS_2[11], $MoSe_2$[12] and MoS_2[13]. The optical transition energies for these emitters, however, are located in close vicinity to the electronic band gap. Thus, cryogenic cooling below 15 K is required to resolve the zero phonon lines (ZPLs). For room temperature quantum emission, defects hosted by large band gap materials are ideal, as has been demonstrated in 2D hexagonal boron nitride (hBN)[14–16]. In this case, the energy levels introduced by the defects into the band structure are well isolated. The large band gap of 6 eV[17] also prevents non-radiative decay, which in turn allows for high quantum efficiencies. Unlike solid-state quantum emitters in 3D systems, the 2D crystal lattice of hBN allows for an intrinsically high extraction efficiency. More precisely, the single-photon emitters have an in-plane dipole resulting in out-of-plane emission, where the emitters are not surrounded by high refractive index materials. Hence,

total internal or Frensel reflection does not affect the collection of the single-photons. Furthermore, 2D crystals can be easily attached by Van der Waals forces to components such as fibers or waveguides, making them suitable for integration with photonic networks[18, 19]. The exceptionally high thermal and chemical robustness of hBN benefits the durability of the quantum emitters, achieving long-term stable operation[20] over a huge temperature range[21]. Moreover, the quantum emitters (and 2D materials in general) have a high tolerance to ionizing radiation, allowing for use in space applications[22].

In spite of large experimental research efforts and theoretical calculations[23, 24], the exact nature of the defects yet has to be determined. Furthermore, the identification is hampered by the large variations of the lifetime and ZPL wavelength from defect to defect. Lifetimes ranging from 0.3 up to 20 ns[18, 20] and ZPLs in the UV[25] and the full visible spectrum[15, 26] have been reported. In addition to naturally occurring defects[14], the emitters can also be created artificially using diverse methods, including chemical etching[27], plasma etching[20, 28], ion[29] and electron irradiation[29, 30] as well as near-deterministic stress-induced activation[31]. Although most researchers agree that quantum emitters in hBN provide a number of unique opportunities, the performance still lags behind state-of-the-art SPSs. Moreover, the reported quality of single-photons from hBN is not sufficient for practical quantum information processing like quantum key distribution (QKD)[32] or photonic quantum computing[33].

A straightforward path for improving the performance of a spontaneous emission process is to use the Purcell effect by coupling the emitter to an optical resonator[34]. The optical resonator reduces the number of modes the emitter can couple to, thereby enhancing emission into the resonant modes. This even works in the "bad-emitter" regime, when the emitter linewidth is larger than the cavity linewidth[35]. Work on cavity-integration of emitters in 2D materials has been reported, with quantum emitters hosted by WSe_2 coupled to plasmonic nanocavities[36, 37] and microcavities[38]. Quantum emitters hosted by hBN have been coupled to plasmonic nanocavities[39]. Hexagonal boron nitride can also be used to fabricate photonic crystal cavities, however, this makes the required spectral matching between optical cavity mode and emitter difficult[40]. Yet, the performance is still not sufficient for use in quantum information experiments.

In this article, we report room temperature single-photon emission from multilayer hBN flakes coupled with a microcavity. The plano-concave cavity fully suppresses the phonon sideband (PSB) and other off-resonant noise, while at the same time greatly enhances directionality and the spontaneous emission rate. The hemisphere is fabricated using focused ion beam (FIB) milling, allowing for a small radius of the accurate and precise curvature. This leads to an ultra-small mode volume on the order of λ^3. We fully characterize the SPS and assess its feasibility for QKD and quantum computing. Moreover, the single-photon source in its current configuration is fully self-contained and compact enough for integration on a pico-class satellite, making it interesting for satellite-based quantum communication[41].

9.3 Design and fabrication

The confocal microcavity consists of a hemispherical and a flat mirror, with the hBN flake hosting the quantum emitter transferred to the focal point of the cavity (see Figure 9.1(a)). The hemisphere spatially confines the cavity mode to the location of the emitter and is fabricated using I_2-enhanced focused ion beam milling[42, 43]. We fabricated arrays of 64 hemispheres per substrate with varying geometrical parameters. The surface roughness

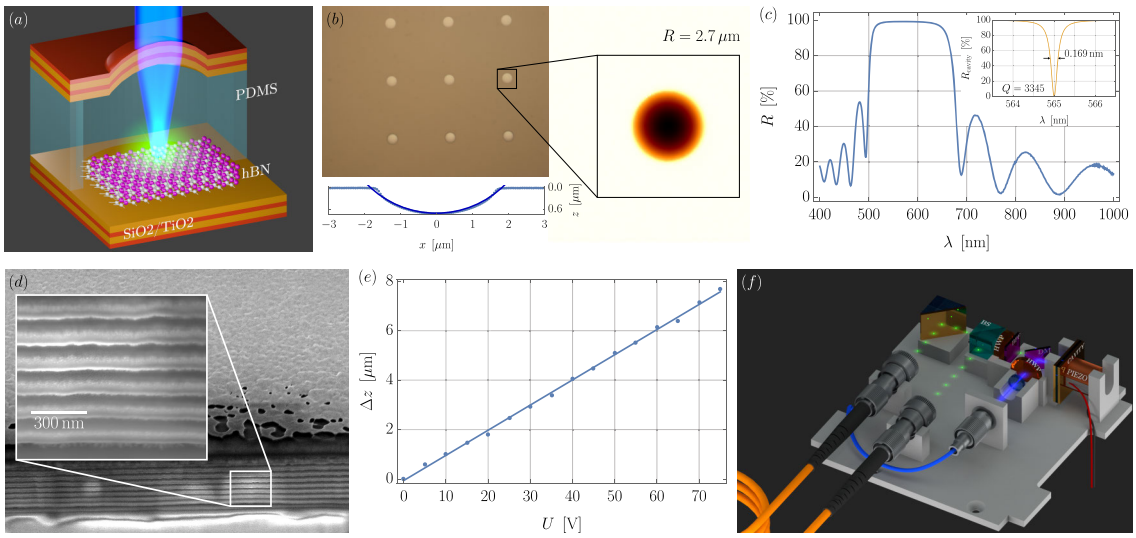

Figure 9.1: Design and fabrication. (a) The microcavity consists of a hemispherical and flat mirror (only two stacks shown on either sides). The quantum emitter hosted by hBN emits confocally with the excitation laser. A PDMS spacer sets the cavity length. To prevent influence of the polymer on the emitter, the PDMS is etched in the middle. (b) Microscope image of the array of hemispheres (not all 64 shown). The surface profile of the hemisphere actually used for the cavity is shown in the right inset. The bottom inset shows the height profile through an arbitrarily chosen axis. The solid blue line shows an ideal cross section of a hemisphere with radius 2.7 μm. (c) Reflectivity of the coating measured by spectrophotometry, with $R = 99.2\%$ at the target wavelength $\lambda = 565\,\text{nm}$. The inset shows the calculated cavity reflectivity based on the coating. (d) SEM image (immersion mode) of the mirror stacks, coated with a layer of gold. The sample is tilted by 52°, so the image is skewed in the vertical direction. The lighter areas in the cross section are regions which have been imaged with a magnification of 125000× (see inset). The intense electron beam makes the surface reactive, and carbon-contaminations by residual organic materials in the SEM chamber are bonded at these areas. (e) Thickness change of a PDMS film with driving voltage reveals linear tuning with $102\,\text{nm}\cdot\text{V}^{-1}$. (f) Design of the CubeSat platform (all components to scale). A polarization maintaining fiber (blue) guides the excitation laser from the diode below the platform. The laser is focused to the diffraction limit into the cavity onto the defect. The single-photons transmit through the dicroic mirror and are additionally band-pass filtered. Next, they are split by a 50:50 beam splitter and fiber-coupled into multimode fibers.

could be minimized by adding I_2-gas during the milling process. With the FIB we can achieve radii of curvature down to $< 3\,\mu$m (see Figure 9.1(b)). We initially characterized the hemispheres using an atomic force microscope (AFM) and phase-shift interferometry (PSI). The characteristic parameters extracted with both methods agree well, which allows us to use the much faster PSI for the characterizations. The hemisphere profile shown in Figure 9.1(b) has a radius of 2.7 μm and root mean square deviations $< 1\,\text{nm}$ from an ideal hemisphere (see Supplementary Information S1). Note that we did not fabricate full hemispheres and the shapes deviate at the edges (which is due to a conductive coating to prevent charging effects during the milling). Both the flat and concave substrate are coated with 9 pairs of alternating dielectric quarter wave stacks (SiO_2/TiO_2), deposited using plasma sputtering. We measured a reflectivity of 99.2% at a wavelength of 565 nm (see Figure 9.1(c)). The calculated resulting cavity reflectivity (see Figure 9.1(c), small inset) has a FWHM of 0.169 nm, corresponding to a quality factor of $Q = 3345$. The stop-

band of the cavity requires the single-photon excitation laser to be shorter than 504 nm, otherwise the cavity has to be resonant at both the ZPL and excitation wavelength. By cutting through one of the stacks with a FIB and imaging with a scanning electron microscope (SEM) in immersion mode (see Figure 9.1(d)), we see that stacking defects occur, as expected predominantly in higher layers. This is not an issue, however, as they are still $\ll \lambda$. The reflectivity is most likely limited by incorporated residual nitrogen, leading to scattering losses. It should also be noted that at a high magnification (see inset) the stacks show a spotted pattern. This is actually re-deposition of atoms during the milling with the FIB. The backsides of the substrates were coated with anti-reflective coatings, consisting of a single quarter wave layer MgF_2. This reduces the reflection losses at the glass-air interface from 4.33% to 2.97%.

Multilayer hBN flakes have been placed onto the flat mirror via clean polymer transfer (see Methods). The more common direct dry transfer was not used as this usually also transfers residues. The hBN crystals were treated using an oxygen plasma followed by rapid thermal annealing under an Ar atmosphere[20]. Using plasma etching, defects with their ZPL primarily around 560 nm form, well within the stopband of the coating. Finally, a tuneable polymer spacer is deposited onto the concave mirror. A piezoelectric actuator provides the tuning force and compresses the polymer. In contrast to monolithic cavities[44–46], this approach allows for *in-situ* tuning of the cavity length. The tuning capability is essential, since the exact position of the ZPL cannot yet be controlled and the optical cavity mode has to be artificially matched to the spectrum of the emitter[40]. Due to a suitable Young's modulus and the ability to deform reversibly, we selected PDMS (polydimethylsiloxane) from a range of polymers (see Supplementary Information S2). Figure 9.1(e) shows that the compression of the PDMS film is linear with the driving voltage at the actuator, with a tuning of $102\,\mathrm{nm{\cdot}V^{-1}}$. This allows us to easily lock the cavity to any arbitrary wavelength. To prevent influence of the PDMS on the emitter, the PDMS was deposited on the opposing mirror and etched around the array prior to contacting with the other mirror.

The cavity mirrors, together with all in- and out-coupling optics, were aligned and glued to a monolithic platform (see Figure 9.1(f) and see Supplementary Information S3). Prior to the gluing each component, held with vacuum tweezers, has been aligned with a motorized 6-axis translation stage. This greatly reduces the size of the complete SPS, at the cost of limiting the tuneability to only cavity length. Changing the radius of curvature of the cavity as demonstrated in a similar experiment is thus not possible[38]. Nevertheless, the compact size of optics, as well as choice of electronics and excitation laser, allow us to reduce the size of the full experiment to $10 \times 10 \times 10\,\mathrm{cm}^3$. This is the size requirement of the 1U CubeSat standard, a miniature pico-class satellite. This makes the single-photon source portable and a promising candidate for low cost CubeSat-based single-photon QKD, especially as the quantum ermitters in hBN are space-certified[22]. In addition, the form factor is a standard size in the space industry, making the launch comparably cheap compared to previous, still larger, compact photoluminescence (PL) setups[47].

9.4 Performance of the single-photon source

Prior to the cavity experiments we performed a free space characterization of the quantum emitter on the mirror. All measurements were carried out at room temperature. The defects were located using confocal photoluminescence (PL) mapping under off-resonant

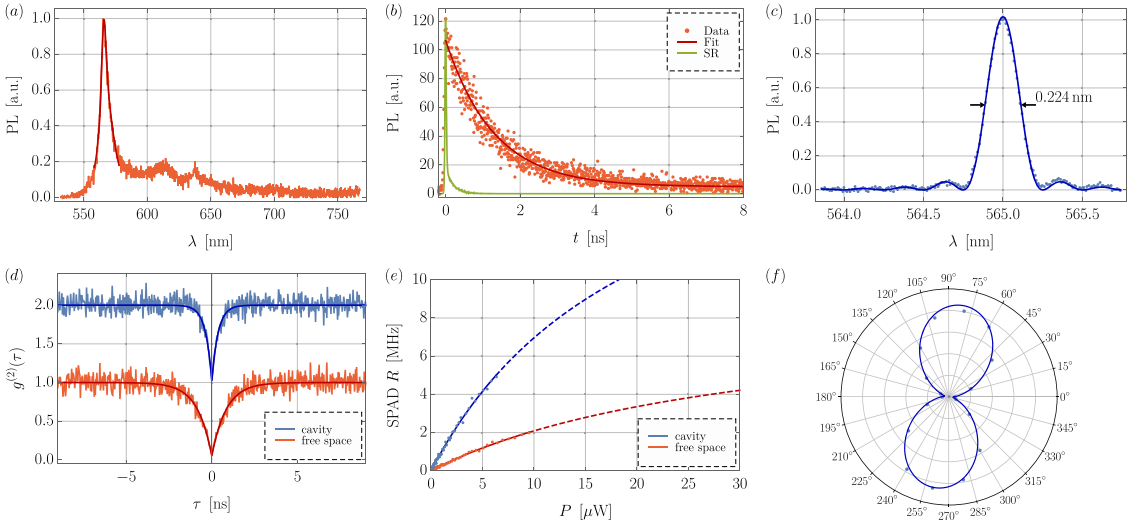

Figure 9.2: Performance of the single-photon source. (a) free space spectrum after off-resonant excitation measured in-reflection and coupled to a grating-based spectrometer. From a Lorentzian fit we extract the ZPL at 565.85(5) nm and a linewidth (FWHM) of 5.76(34) nm. (b) Time-resolved photoluminescence reveals an excited state lifetime of $\tau = 897(8)$ ps. The exponential fit function is convoluted with the system response (SR). (c) The cavity narrows the spectrum down to 0.224 nm (FWHM). The spectrum has been recorded using a high-resolution Fourier-transform spectrometer. The finite scan range result in the spectrum being convoluted with the system response function (of the form of a $\mathrm{sinc}^2(x)$), which in turn leads to the side lobes. (d) When comparing free space with cavity-coupled emission, the second-order correlation function measurements show a decrease of g_0^2 from 0.051(23) or -12.9 dB to 0.018(36) to -17.4 dB and shortening of the lifetime from 837(30) to 366(19) ps due to the Purcell effect. The cavity data is vertically offset for clarity. (e) The cavity increases the single-photon count rate, even at lower excitation power. This is because of the shortening of the lifetime due to the Purcell effect, but also due to an enhanced collection efficiency with the cavity. (f) The emission is dipole-like, as the projections on different polarization directions show. The solid line is obtained by fitting a $\cos^2(\theta)$ function.

excitation at 522 nm. As hBN itself is optically inactive in the visible spectrum, all emission originates from the defects or surface contaminants. Each crystal is scanned with a resolution of 0.5 μm. For the cavity, we selected a suitable defect with a ZPL at 565.85(5) nm and a Lorentzian linewidth (FWHM) of 5.76(34) nm (see Figure 9.2(a)). The PL spectrum shows the typical asymmetric lineshape. Note that this is not a result of partial suppression of the long pass filter used to block the pump laser (see Methods), but rather the PSB being adjacent to the ZPL. The defect emits 63.2% into its ZPL. We note that the emission > 580 nm originates from surface contaminants activated during the annealing and is usually filtered out (see Methods). Alternatively, annealing in a reactive environment can burn off these contaminants. Time-resolved PL (TRPL) reveals a single-exponential decay with a lifetime of 897(8) ps (see Figure 9.2(b)). The fit function is convoluted with the system response (also shown in Figure 9.2(b)) in order to reproduce the observed data.

For the cavity experiments we used a custom-built high-resolution Fourier-transform spectrometer (FTS), instead of the grating-based spectrometer. After aligning the concave to the flat mirror and coupling the emitter with the cavity mode, we saw an improved spectral purity (see Figure 9.2(c)), with the single-photon linewidth narrowing down to 0.224 nm (FWHM), corresponding to a cavity quality factor of 2522. In frequency space

this corresponds to 210.6 GHz. The spectrum, however, shows side lobes, which do not originate from higher-order transverse cavity modes. The transverse mode spacing is much larger than the difference in observed peak positions (see Supplementary Information S4). These peaks are artifacts from the finite scan range of the FTS which results in a truncated Fourier-transform. Convoluting this response (which is of the form of $\mathrm{sinc}^2(x)$) with a Lorentzian reproduces the observed data.

The lifetime cannot be measured directly using time-resolved PL, as the wavelength of the ultra-short pulsed laser is within the stopband of the cavity. For a single-photon emitter, however, it is possible to extract the lifetime directly from the second-order correlation function, which we measure using a Hanbury Brown and Twiss (HBT)-type interferometer.[1] For the emitter in the cavity, we measure $g_0^2 \equiv g^{(2)}(\tau = 0) = 0.018(36)$ (see Figure 9.2(d)) and from the fit we extract a lifetime of 366(19) ps (see Methods). For a fair comparison of free space and cavity-enhanced lifetimes we compare the correlation function measurements in free space and with the cavity. The $g^{(2)}(\tau)$ for the uncoupled emitter dips only to 0.051(23) and has a lifetime of 837(30) ps. The lifetimes measured with time-resolved PL and extracted from the $g^{(2)}(\tau)$ measurements agree reasonably well, even though we note that the 897(8) ps from the TRPL measurement is likely more accurate. While $g_0^2 = 0$ is within the error margin for the cavity-coupled emitter, more accurate measurements are required to reduce the error margin to extract the true value of g_0^2. Knowing this is crucial for QKD applications (see below). A small error margin on correlation function measurements can typically be achieved with ultra-short pulsed excitation[48, 49]. We also calculated the background correction term[50] and found that it is smaller than the significant digits of our measurement result ($< 5 \times 10^{-5}$), so we conclude that any deviation from 0 is not due to detector dark counts, but rather other noise sources excited through the laser. If we directly compare g_0^2 of the uncoupled and cavity-enhanced emitter, however, we see a reduction of a factor of 2.83. Such reduction can typically be achieved in the "bad-emitter" regime and means that off-resonant noise sources are successfully suppressed. A narrower cavity linewidth could thus further reduce g_0^2. It is worth noting that many applications require the generation of single-photons on-demand, which can be achieved by pulsed excitation of the emitter. As already mentioned, our pulsed laser is within the stopband of the cavity, making it impossible to match excitation and emission wavelength for this laser due to the large free spectral range. The values for the second-order correlation function, however, can be equal for both continuous and pulsed excitation schemes[51], allowing for simply replacing the continuous excitation laser in our experiment with a suitable pulsed laser for potential quantum information experiments (see below). The ratio of free space (or rather half-sided cavity) to cavity-coupled lifetime is $f = 2.29$. The effective Purcell enhancement is given by

$$F_p^{\mathrm{eff}} = \frac{3}{4\pi^2}\lambda^3 \frac{Q^{\mathrm{eff}}}{V} \tag{9.1}$$

[1] In general, the anti-bunching time constant is power-dependent. Thus, the correct way to extract it, is to perform a power-resolved measurement and extrapolate to zero excitation power. In this case, however, the excitation power was already very low, only a few μW. Previous experiments showed extrapolating from this power does not change the result beyond the error margins.

with Q^{eff} being the effective quality factor and V being the cavity mode volume. This can be calculated by integrating over the Gaussian fundamental mode in a resonator:

$$V = \int_0^{2\pi} \int_0^{\infty} \int_0^{L'} d\phi dr dz \sin^2\left(\frac{2\pi z}{\lambda}\right) r \exp^{-\frac{2r^2}{w_0^2}} = \frac{\pi}{4} L' w_0^2 \tag{9.2}$$

where L' is the effective cavity length (see below for the calculation) and $w_0^2 = \frac{\lambda}{\pi}\sqrt{L'r - r^2}$ is the cavity waist, determined by the effective cavity length and r, the radius of the hemisphere. We calculate the mode volume to be $1.76\lambda^3$. In the "bad-emitter" regime the effective quality factor $Q^{\text{eff}} = \frac{\lambda}{\Delta\lambda_{\text{cav}} + \Delta\lambda_{\text{em}}}$ has to be used, which is dominated by the emitter dynamics. It should be mentioned that this is only an approximation and it is more accurate to calculate the overlap integral of the photonic density of states of the cavity and electronic density of states of the emitter. In addition, this effective Purcell factor is different from the ratio f, because the dielectric environment of the mirror is modifying the available density of states, whereas the Purcell factor is the ratio of vacuum (or true free space) to cavity lifetime. We calculate the effective Purcell factor to be 4.07. This also allows for the direct calculation of the quantum efficiency[38], given by

$$\eta = \frac{f - 1}{f + F_p^{\text{eff}} - \varepsilon f} \tag{9.3}$$

where ε is the Purcell factor caused by the mirror and is determined by finite-difference time-domain (FDTD) simulations. For our mirror we find $\varepsilon = 1.68$ (see Supplementary Information S5) and thus the quantum efficiency is 51.3%.

The cavity also modifies the power saturation behavior (see Figure 9.2(e)), with an increased single-photon count rate even at lower excitation power. This is a result of the Purcell enhancement, which makes the emitter brighter, but also from the increased collection efficiency of the cavity, as the emitter predominantly emits into the cavity mode. The low excitation power also assists the single-photon count rate stability, because at low excitation power the emitters show no blinking or photobleaching. This is particular important as the photobleaching increases with decreasing wavelength[26] and due to the stopband of the cavity our excitation laser is at 450 nm. Note that the count rates at the single-photon avalanche diodes (SPADs) shown in Figure 9.2(e) are the raw count rates, not corrected for transmission loss or detector efficiency. The quantum emitter also emits linearly polarized light (see Figure 9.2(f)) with a degree of polarization (DOP) of 90.4%. The fit is obtained using a $\cos^2(\theta)$ function. A high polarization contrast is crucial for QKD applications which use polarization encoding. Increasing the DOP of not fully polarized light is always accompanied by loss, and so it sets an upper bound on the efficiency of the SPS.

Since the cavity length is tuneable, the single-photon wavelength can also be tuned. Effectively, the tuning range is the linewidth of the free space emission. The cavity is only sampling the free space emission spectrum, however, so the actual single-photon count rate is the spectral overlap integral of optical cavity mode and emitter. This results in the emission rate decreasing with increasing cavity detuning.

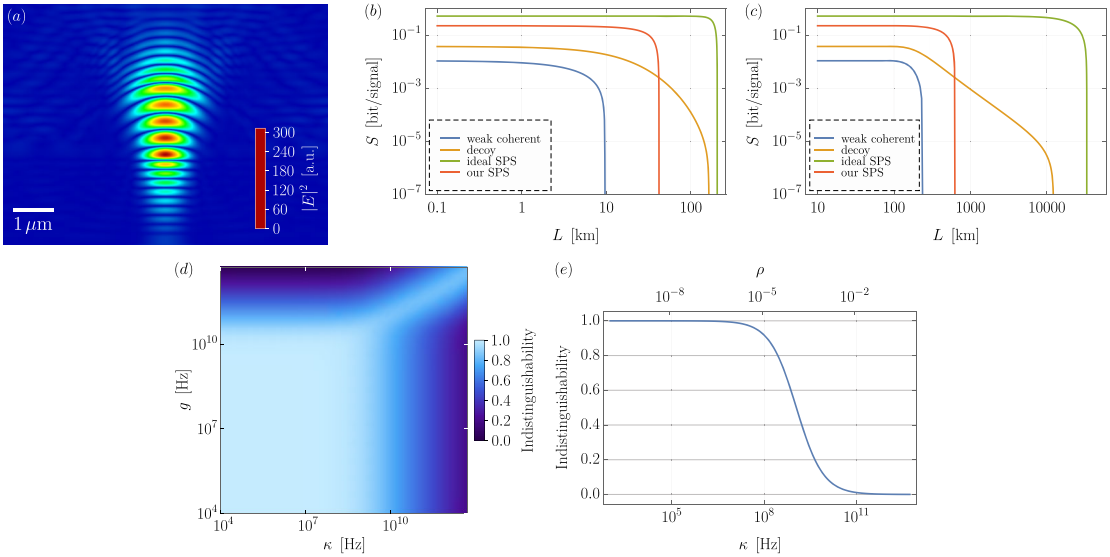

Figure 9.3: Theoretical modeling. (a) Electric field mode profile of a dipole emitter in the cavity obtained using FDTD simulations. (b) QKD for different photon sources for a fiber channel with 0.21 dB/km loss. Our SPS outperforms weak coherent states at all distances and decoy state at short to medium distances up to 42 km. (c) QKD for different photon sources for a free space satellite-to-ground link. The satellite assumes a 5 cm telescope, the ground station a 60 cm telescope. Our SPS outperforms decoy states at distances up to 630 km and weak coherent states at all distances. For both channels, our single-photon source assumes $g_0^2 = 0.018$ and a quantum efficiency of 51.3% (see Supplementary Information S6). (d) Indistinguishability in the weak coupling limit as a function of cavity coupling rate g and cavity linewidth κ. The simulations assume the photophysics of our actual emitter in the cavity. A high indistinguishability can be achieved for $g, \kappa < 10^9$ Hz. (e) Indistinguishability in the limit $g \ll 10^8$ Hz. $I > 0.9$ requires $\kappa < 124$ MHz.

9.5 Theoretical modeling

9.5.1 Numerical modeling

We can use FDTD simulations to calculate the electric field distribution of the dipole emitter in the cavity. The electric field intensity ($|E|^2$) is shown in Figure 9.3(a). The simulations also show that resonance does not occur at a physical mirror separation L' which is a multiple of $\lambda/2$. This is due to the finite penetration depth of the electric field into the dielectric mirror stacks, leading to an effective cavity length. The penetration depth ξ thereby is given by

$$\xi = \frac{q\lambda/2 - L'}{2} \tag{9.4}$$

The physical mirror separation L' is determined by maximizing the intracavity electric field (see Supplementary Information S5). Our simulations yield $\xi = 122$ nm. When designing the thickness of the PDMS spacer, this has to be taken into account. To reduce the computational time we simulated the longitudinal mode $q = 5$ instead of the experimentally realized $q = 8$. Nevertheless, the parameter ξ is not affected by this beyond the numerical precision of the simulation.

9.5.2 Applications in quantum technologies

We now turn to an evaluation of the SPS for the two most common quantum information applications: quantum key distribution and quantum computing. Due to the lack of suitable SPSs the vast majority of QKD implementations use weak coherent states (WCSs). These are characterized by a low mean photon number (resulting in a low efficiency of the protocol) and a non-zero probability of emitting two or more photons at the same time. The multi-photon pulses contain information leaking to a potential eavesdropper. This can be reduced at the expense of sacrificing parts of the exchanged key. In comparison, an ideal single-photon source has an efficiency of unity and no multi-photon emission, so it always performs better than any protocol based on WCSs. We assess the performance of our single-photon source for the BB84 protocol[32] over a fiber channel with a loss of 0.21 dB/km and realistic parameters from the experiment by Gobby, Yuan and Shields (GYS)[52]. It should be mentioned that such loss can only be achieved at telecom wavelengths, where single-photon emission from hBN has yet to be demonstrated, but for simplicity we still use all GYS parameters. The relevant metric is the extractable secret bit per sent signal (see Supplementary Information S6). Moreover, we compare the results with an ideal SPS and the most common conventional QKD protocols: weak coherent and decoy states[53]. The latter is the most efficient protocol that is publicly known. The simulations for weak coherent and decoy states assume a fixed mean photon number per pulse μ, however, there is an optimal choice of μ for every distance.

At short and medium distances below 42 km, our SPS outperforms both weak coherent and decoy states, while at long distances decoy states become more efficient (see Figure 9.3(b)). This is due to the fact that at long distances (i.e. high losses), multi-photon pulses harm the extractable secret bit disproportionately. Nevertheless, our SPS performs better than weak coherent states in each instance. Decoy state protocols can still achieve a finite secret key rate at large distances, because they can extract information from multi-photon states while at the same time defeating the photon-number splitting attack (multi-photon states dominate at long distances with high losses). A communication distance of < 42 km would be typical for metropolitan networks. The ideal SPS of course outperforms all protocols and also our source at all distances. For space-to-ground links the loss is dominated by diffraction and atmospheric attenuation plays a role only in the lowest 10 km. The simulations (see Figure 9.3(c)) show that our source outperforms the decoy state protocol on distances up to 630 km. For a comparison: the Micius satellite, which performed the first satellite-to-ground quantum key exchange, orbits at around 500 km[41]. Thus, our single-photon source could enhance the key generation rate even with its current performance for such a satellite. We note that the free space loss channel assumes only diffraction losses and no other noise sources such as pointing errors, atmospheric loss and losses in the transmitter or receiver, which would change the result only marginally. The crossing point where our SPS and the decoy state protocol perform equally efficient for both channels is at a loss of 8.82 dB.

Quantum emitters hosted by hBN can open unique opportunities for single-photon QKD applications, due to the large spread of optical transition lines. It is possible to choose a particular defect with a ZPL coinciding with one of the Fraunhofer lines (e.g. Hα) in the solar spectrum. Narrow filtering around this line allows one to operate the QKD system at daylight, as the background from sunlight at that particular wavelength is suppressed[54]. Other color centers in solids have their ZPL fixed, so these cannot be used in this way. In addition, the intrinsically ideal out-coupling efficiency of 2D materials,

large single-photon luminosity and quantum efficiency, and low excitation power benefit satellite-based QKD applications. Furthermore, while there is *a priori* no reason to believe other color centers in solid-state crystals would not withstand space radiation, this has been certified only for color centers in hBN so far[22]. While the hBN system is not exclusive for space applications (and other room temperature color centers in diamond or SiC might be suitable as well), it is nonetheless a system featuring many desirable properties.

Notably, QKD only requires maximal entropy on all degrees of freedom which are not used for qubit encoding. Other quantum information protocols, however, do require truly indistinguishable single-photons. An example are entangling gates for single-photons for use in one-way quantum computing[55]. A measure of how indistinguishable consecutively emitted single-photons are is the interference contrast I in a Hong-Ou-Mandel experiment[56]. Unfortunately, as our cavity is pumped continuously, we cannot directly measure I. Nevertheless, we can at least theoretically calculate the expected indistinguishability. The indistinguishability of a quantum emitter with pure dephasing is given by

$$I = \frac{\gamma}{\gamma + \gamma^*} \tag{9.5}$$

where γ is the emission rate and γ^* is the pure dephasing rate. At room temperature we find $I = 2 \times 10^{-4}$, meaning only 1 in 5000 photons would interfere in a Hong-Ou-Mandel experiment. Even such a strongly dephasing emitter, however, can reach a regime of high indistinguishability, when coupled with a high-Q cavity. In the limit of weak coupling I modifies to

$$I = \frac{\gamma + \kappa R/(\kappa + R)}{\gamma + \kappa + 2R} \tag{9.6}$$

where the parameter $R = \frac{4g^2}{\kappa+\gamma+\gamma^*}$ is the effective transfer rate between the emitter and the cavity, κ is the cavity linewidth and g is the cavity coupling strength[57]. For our cavity parameters we find $I = 5.3 \times 10^{-3}$. While this is an improvement by a factor of 26, it is still far beyond being useful for fault-tolerant quantum computing. The indistinguishability for generalized cavity linewidth and coupling strength is shown in Figure 9.3(d). Note that in the limit of strong coupling it is also possible to achieve a high indistinguishability. With the coupling strength typically $\ll 1\,\mathrm{GHz}$, a narrow cavity linewidth is required to maximize I. Figure 9.3(e) shows that $I > 90\%$ requires a cavity linewidth less than 124 MHz. At a reflectivity of 99.95%[38], this linewidth limits the free spectral range (FSR) to 779 GHz. Compared with the free space emission linewidth (5.41 THz) this means that the spectral profile of the cavity would be comb-shaped, with the cavity sampling the emitter spectrum at multiples of the FSR. Single-photons originating from different comb peaks are of course distinguishable, so a high indistinguishability requires filtering out only one peak (for example with another cavity). This, however, is balanced by a loss in efficiency. To overcome this, the natural linewidth of the emitter into free space must be narrowed. Cryogenic cooling is one option to narrow the linewidth sufficiently[58].

9.6 Conclusion

We have demonstrated coupling of a quantum emitter hosted by multilayer hBN to a confocal microcavity. The hemispherical geometries have been fabricated using FIB milling

with sub-nm precision. The cavity mode volume is of the order of λ^3. The cavity improves the spectral purity of the emitter substantially, with the FWHM decreasing from 5.76 to 0.224 nm. Moreover, the cavity suppresses off-resonant noise, which allows us to improve its single-photon purity. The excited state lifetime of the emitter is also shortened by the Purcell effect by a factor of 2.3. The emission of the cavity is linearly polarized and stable over long timeframes, with no signs of photobleaching or blinking. The cavity also features a linearly tunable PDMS spacer between both mirrors, which allows *in-situ* tuning of the single-photon line over the full free space ZPL of the quantum emitter. This would allow us to fabricate multiple identical single-photon sources, by locking all to the same emission wavelength, making this approach fully scalable. Furthermore, the complete SPS is portable and fully self-contained within $10 \times 10 \times 10\,\mathrm{cm}^3$, the size of a 1U CubeSat. This makes the single-photon source a promising candidate for low cost satellite-based long-distance QKD, especially as the quantum emitters in hBN are space-certified. Despite the source's performance being not yet sufficient for one-way quantum computing, using the single-photon source for QKD even now enhances the quantum key generation rate on useful distances. The microcavity platform can also be easily adapted to other quantum emitters in 2D materials and offers a promising path towards scalable quantum information processing.

9.7 Methods

FIB milling

Borosilicate glass substrates with a size of $18 \times 18\,\mathrm{mm}^2 \times 160\,\mu\mathrm{m}$ have been coated with 100 nm gold using electron-beam thermal evaporation to prevent substrate charging effects. The ion accelerating voltage in the FIB (FEI Helios 600 NanoLab) is 30 kV with currents ≤ 0.28 nA. The dose rate is encoded in the RGB color of a hemispherical pixel map. The dose rate to RGB value was carefully calibrated using AFM measurements. During the milling process we add I_2-gas, which ensures a smooth surface. Finally, the gold film is chemically etched using a custom-made potassium iodide ($KI:I_2:H_2O$ with ratio 4:1:40 by weight) solution. Surface characterizations before and after the KI-etching show no difference in radius or roughness. We also tried hydrofluoric acid to etch the hemispheres, but for the feature sizes required for the cavity we could not achieve a smooth surface.

Plasma sputtering

We calibrated the deposition rate of the sputter coater (AJA) using variable angle spectroscopic ellipsometry (JA Woollam M-2000D), which measures film thickness and refractive index. At 565 nm we found $n_{SiO2} = 1.521$, $n_{TiO2} = 2.135$ and $n_{MgF2} = 1.390$. The deposition was done at room temperature. For the highly reflective coating we deposit alternating layers of SiO_2/TiO_2 with thickness of $\lambda/4n$ and the SiO_2 terminating the mirror. Due to the refractive index of MgF_2 being roughly in the middle between glass and air, the backsides of the substrates are coated with one quarter wave layer of MgF_2, serving as an anti-reflective coating. To maximize the escape efficiency into one particular direction it is common to make one of the stacks thicker (e.g. 10:9), so the photons couple primarily into a single direction. For simplicity, we used 9:9 stacks, which thus introduces 50% loss.

Quantum emitter fabrication

The flat mirrors have been coated with 300 nm 950 PMMA A4. Multilayer hBN flakes have been exfoliated from bulk (HQGraphene) and transferred onto the PMMA layer by dry contact. Oxygen plasma etching (500 W for 2 min generated from a microwave field at a gas flow of 300 ccm^3/min) removes the PMMA around the flake as well as creates the quantum emitters. The PMMA below the flake is decomposed during the annealing, which also stabilizes the optical emission properties (more details have been published previously[20]).

Optical characterization

Each flake has been scanned using a custom-built confocal micro-photoluminescence setup with a resolution of 0.5 μm and a spectrum has been recorded at each scanning position. The excitation laser with a wavelength of 522 nm is non-resonant with the optical transition energy of the defect. The laser light is blocked with a Semrock RazorEdge ultrasteep long-pass edge filter. With a laser pulse length of 300 fs at a repetition rate of 20.8 MHz, the setup also allows us to measure the excited state lifetime. The pulses are split into trigger and excitation pulses, and the photoluminescence is detected by a SPAD (Micro Photon Devices). The time correlation between trigger pulse and arrival time of the photoluminescence is given by a time-to-digital converter (PicoQuant PicoHarp 300). The photoluminescence is coupled via a grating to the SPAD, which makes the TRPL wavelength-sensitive. This allows us to measure the lifetime of the ZPL only. The second-order correlation function measurements have been performed using two SPADs in the exit ports of a beam splitter and under continuous excitation. We fit the function

$$g^{(2)}(\tau) = 1 - Ae^{-|\tau|/t_1} + Be^{-|\tau|/t_2} \tag{9.7}$$

with the anti- and bunching amplitudes A and B, and the decay times t_1 and t_2. The experimental data is normalized such that $g^{(2)}(\tau \to \infty) = 1$. The background corrected $g_{\mathrm{c}}^{(2)}$ is given by

$$g_{\mathrm{c}}^{(2)} = \frac{g^{(2)} - (1-\rho^2)}{\rho^2} \tag{9.8}$$

with $\rho = \mathrm{SNR}/(\mathrm{SNR}+1)$ where SNR is the signal-to-noise ratio. In addition to the long-pass filter, the photoluminescence for correlation function measurements is band-pass filtered around the ZPL. We utilize linear variable filters (Delta Optical Thin Film 3G LVLWP and 3G LVSWP) to tune center and bandwidth of the band-pass filtering system.

Cavity alignment

The emitter on the mirror has been located and characterized in free-space. The hBN flake capable of hosting a defect (determined by flake thickness) was centered onto the mirror, making it easy to locate on the mirror. Nearby crystal flakes serve as markers for localizing the flake with the pre-characterized defect. For aligning the crystal long working distance objectives in a custom-built microscope have been used, illuminated with a near infrared LED where all coatings are transparent. Each component, held and aligned with vacuum tweezers on a motorized 6-axis nanopositioning stage, is glued one after another.

The adhesive used was UHU Plus Endfest 300, a two component epoxy glue and was cured for 24 hours at room temperature. Where required a second layer of glue was added and cured for another 24 hours. Diagnostics were used to provide feedback for a good alignment, e.g. single-photon detection rate when aligning the cavity, combined with the spectrometer to check the cavity mode profile.

Acknowledgments

This work was funded by the Australian Research Council (CE110001027, FL150100019, DE140100805, DP180103238). We thank the ACT Node of the Australian National Fabrication Facility for access to their nano- and microfabrication facilities. We also thank Hark Hoe Tan for access to the TRPL system. R.L. acknowledges support by an Australian Government Research Training Program (RTP) Scholarship.

Supplementary information

The supplementary information is available free of charge on the ACS Publications website at https://pubs.acs.org/doi/10.1021/acsphotonics.9b00314 or in the Appendix A.4.

References

[1] J. L. O'Brien, A. Furusawa, and J. Vučković, *Photonic quantum technologies*, Nat. Photon., **3** 687–695, 2009.

[2] P. Senellart, G. Solomon, and A. White, *High-performance semiconductor quantum-dot single-photon sources*, Nat. Nanotechnol., **12** 1026–1039, 2017.

[3] H. G. Barros, A. Stute, T. E. Northup, C. Russo, P. O. Schmidt, and R. Blatt, *Deterministic single-photon source from a single ion*, New J. of Phys., **11** 103004, 2009.

[4] I. Aharonovich, D. Englund, and M. Toth, *Solid-state single-photon emitters*, Nat. Photon., **10** 631–641, 2016.

[5] M. Bock, A. Lenhard, C. Chunnilall, and C. Becher, *Highly efficient heralded single-photon source for telecom wavelengths based on a PPLN waveguide*, Opt. Express, **24** 23992–24001, 2016.

[6] P. Tonndorf, R. Schmidt, R. Schneider, J. Kern, M. Buscema, G. A. Steele, A. Castellanos-Gomez, H. S. J. van der Zant, S. M. de Vasconcellos, and R. Bratschitsch, *Single-photon emission from localized excitons in an atomically thin semiconductor*, Optica, **2** 347–352, 2015.

[7] A. Srivastava, M. Sidler, A. V. Allain, D. S. Lembke, A. Kis, and A. Imamoğlu, *Optically active quantum dots in monolayer WSe2*, Nat. Nanotechnol., **10** 491–496, 2015.

[8] M. Koperski, K. Nogajewski, A. Arora, V. Cherkez, P. Mallet, J.-Y. Veuillen, J. Marcus, P. Kossacki, and M. Potemski, *Single photon emitters in exfoliated WSe2 structures*, Nat. Nanotechnol., **10** 503–506, 2015.

[9] Y.-M. He, G. Clark, J. R. Schaibley, Y. He, M.-C. Chen, Y.-J. Wei, X. Ding, Q. Zhang, W. Yao, X. Xu, C.-Y. Lu, and J.-W. Pan, *Single quantum emitters in monolayer semiconductors*, Nat. Nanotechnol., **10** 497–502, 2015.

[10] C. Chakraborty, L. Kinnischtzke, K. M. Goodfellow, R. Beams, and A. N. Vamivakas, *Voltage-controlled quantum light from an atomically thin semiconductor*, Nat. Nanotechnol., **10** 507–511, 2015.

[11] C. Palacios-Berraquero, M. Barbone, D. M. Kara, X. Chen, I. Goykhman, D. Yoon, A. K. Ott, J. Beitner, K. Watanabe, T. Taniguchi, A. C. Ferrari, and M. Atatüre, *Atomically thin quantum light-emitting diodes*, Nat. Commun., **7** 12978, 2016.

[12] A. Branny, G. Wang, S. Kumar, C. Robert, B. Lassagne, X. Marie, B. D. Gerardot, and B. Urbaszek, *Discrete quantum dot like emitters in monolayer MoSe2: Spatial mapping, magneto-optics, and charge tuning*, Appl. Phys. Lett., **108** 142101, 2016.

[13] J. Klein, M. Lorke, M. Florian, F. Sigger, J. Wierzbowski, J. Cerne, K. Müller, T. Taniguchi, K. Watanabe, U. Wurstbauer, M. Kaniber, M. Knap, R. Schmidt, J. J. Finley, and A. W. Holleitner, *Atomistic defect states as quantum emitters in monolayer MoS_2*, arXiv:1901.01042, 2019.

[14] T. T. Tran, K. Bray, M. J. Ford, M. Toth, and I. Aharonovich, *Quantum emission from hexagonal boron nitride monolayers*, Nat. Nanotechnol., **11** 37–41, 2016.

[15] T. T. Tran, C. Elbadawi, D. Totonjian, C. J. Lobo, G. Grosso, H. Moon, D. R. Englund, M. J. Ford, I. Aharonovich, and M. Toth, *Robust Multicolor Single Photon Emission from Point Defects in Hexagonal Boron Nitride*, ACS Nano, **10** 7331–7338, 2016.

[16] T. T. Tran, C. Zachreson, A. M. Berhane, K. Bray, R. G. Sandstrom, L. H. Li, T. Taniguchi, K. Watanabe, I. Aharonovich, and M. Toth, *Quantum Emission from Defects in Single-Crystalline Hexagonal Boron Nitride*, Phys. Rev. Applied, **5** 034005, 2016.

[17] G. Cassabois, P. Valvin, and B.Gil, *Hexagonal boron nitride is an indirect bandgap semiconductor*, Nat. Photon., **10** 262–266, 2016.

[18] A. W. Schell, H. Takashima, T. T. Tran, I. Aharonovich, and S. Takeuchi, *Coupling Quantum Emitters in 2D Materials with Tapered Fibers*, ACS Photonics, **4** 761–767, 2017.

[19] T. Vogl, Y. Lu, and P. K. Lam, *Room temperature single photon source using fiber-integrated hexagonal boron nitride*, J. Phys. D: Appl. Phys., **50** 295101, 2017.

[20] T. Vogl, G. Campbell, B. C. Buchler, Y. Lu, and P. K. Lam, *Fabrication and Deterministic Transfer of High-Quality Quantum Emitters in Hexagonal Boron Nitride*, ACS Photonics, **5** 2305–2312, 2018.

[21] M. Kianinia, B. Regan, S. A. Tawfik, T. T. Tran, M. J. Ford, I. Aharonovich, and M. Toth, *Robust Solid-State Quantum System Operating at 800 K*, ACS Photonics, **4** 768–773, 2017.

[22] T. Vogl, K. Sripathy, A. Sharma, P. Reddy, J. Sullivan, J. R. Machacek, L. Zhang, F. Karouta, B. C. Buchler, M. W. Doherty, Y. Lu, and P. K. Lam, *Radiation tolerance of two-dimensional material-based devices for space applications*, Nat. Commun., **10** 1202, 2019.

[23] S. A. Tawfik, S. Ali, M. Fronzi, M. Kianinia, T. T. Tran, C. Stampfl, I. Aharonovich, M. Toth, and M. J. Ford, *First-principles investigation of quantum emission from hBN defects*, Nanoscale, **9** 13575–13582, 2017.

[24] M. Abdi, J.-P. Chou, A. Gali, and M. B. Plenio, *Color Centers in Hexagonal Boron Nitride Monolayers: A Group Theory and Ab Initio Analysis*, ACS Photonics, **5** 1967–1976, 2018.

[25] R. Bourrellier, S. Meuret, A. Tararan, O. Stéphan, M. Kociak, L. H. G. Tizei, and A. Zobelli, *Bright UV Single Photon Emission at Point Defects in h-BN*, Nano Lett., **16** 4317–4321, 2016.

[26] Z. Shotan, H. Jayakumar, C. R. Considine, M. Mackoit, H. Fedder, J. Wrachtrup, A. Alkauskas, M. W. Doherty, V. M. Menon, and C. A. Meriles, *Photoinduced Modification of Single-Photon Emitters in Hexagonal Boron Nitride*, ACS Photonics, **3** 2490–2496, 2016.

[27] N. Chejanovsky, M. Rezai, F. Paolucci, Y. Kim, T. Rendler, W. Rouabeh, F. Fávaro de Oliveira, P. Herlinger, A. Denisenko, S. Yang, I. Gerhardt, A. Finkler, J. H. Smet, and J. Wrachtrup, *Structural Attributes and Photodynamics of Visible Spectrum Quantum Emitters in Hexagonal Boron Nitride*, Nano Lett., **16** 7037–7045, 2016.

[28] Z.-Q. Xu, C. Elbadawi, T. T. Tran, M. Kianinia, X. Li, D. Liu, T. B. Hoffman, M. Nguyen, S. Kim, J. H. Edgar, X. Wu, L. Song, S. Ali, M. Ford, M. Toth, and I. Aharonovich, *Single photon emission from plasma treated 2D hexagonal boron nitride*, Nanoscale, **10** 7957–7965, 2018.

[29] S. Choi, T. T. Tran, C. Elbadawi, C. Lobo, X. Wang, S. Juodkazis, G. Seniutinas, M. Toth, and I. Aharonovich, *Engineering and Localization of Quantum Emitters in Large Hexagonal Boron Nitride Layers*, ACS Appl. Mater. Interfaces, **8** 29642–29648, 2016.

[30] H. Ngoc My Duong, M. A. P. Nguyen, M. Kianinia, T. Ohshima, H. Abe, K. Watanabe, T. Taniguchi, J. H. Edgar, I. Aharonovich, and M. Toth, *Effects of High-Energy Electron Irradiation on Quantum Emitters in Hexagonal Boron Nitride*, ACS Appl. Mater. Interfaces, **10** 24886–24891, 2018.

[31] N. V. Proscia, Z. Shotan, H. Jayakumar, P. Reddy, C. Cohen, M. Dollar, A. Alkauskas, M. Doherty, C. A. Meriles, and V. M. Menon, *Near-deterministic activation of room-temperature quantum emitters in hexagonal boron nitride*, Optica, **5** 1128–1134, 2018.

[32] N. Gisin, G. Ribordy, W. Tittel, and H. Zbinden, *Quantum cryptography*, Rev. Mod. Phys., **74** 145–195, 2002.

[33] P. Kok, W. J. Munro, K. Nemoto, T. C. Ralph, J. P. Dowling, and G. J. Milburn, *Linear optical quantum computing with photonic qubits*, Rev. Mod. Phys., **79** 135–174, 2007.

[34] K. J. Vahala, *Optical microcavities*, Nature, **424** 839–846, 2003.

[35] H. Kaupp, C. Deutsch, H.-C. Chang, J. Reichel, T. W. Hänsch, and D. Hunger, *Scaling laws of the cavity enhancement for nitrogen-vacancy centers in diamond*, Phys. Rev. A, **88** 053812, 2013.

[36] O. Iff, N. Lundt, S. Betzold, L. N. Tripathi, M. Emmerling, S. Tongay, Y. J. Lee, S.-H. Kwon, S. Höfling, and C. Schneider, *Deterministic coupling of quantum emitters in WSe2 monolayers to plasmonic nanocavities*, Opt. Express, **26** 25944–25951, 2018.

[37] Y. Luo, G. D. Shepard, J. V. Ardelean, D. A. Rhodes, B. Kim, K. Barmak, J. C. Hone, and S. Strauf, *Deterministic coupling of site-controlled quantum emitters in monolayer WSe2 to plasmonic nanocavities*, Nat. Nanotechnol., **13** 1137–1142, 2018.

[38] L. C. Flatten, L. Weng, A. Branny, S. Johnson, P. R. Dolan, A. A. P. Trichet, B. D. Gerardot, and J. M. Smith, *Microcavity enhanced single photon emission from two-dimensional WSe2*, Appl. Phys. Lett., **112** 191105, 2018.

[39] T. T. Tran, D. Wang, Z.-Q. Xu, A. Yang, M. Toth, T. W. Odom, and I. Aharonovich, *Deterministic Coupling of Quantum Emitters in 2D Materials to Plasmonic Nanocavity Arrays*, Nano Lett., **17** 2634–2639, 2017.

[40] S. Kim, J. E. Fröch, J. Christian, M. Straw, J. Bishop, D. Totonjian, K. Watanabe, T. Taniguchi, M. Toth, and I. Aharonovich, *Photonic crystal cavities from hexagonal boron nitride*, Nat. Commun., **9** 2623, 2018.

[41] S.-K. Liao, W.-Q. Cai, W.-Y. Liu, L. Zhang, Y. Li, J.-G. Ren, J. Yin, Q. Shen, Y. Cao, Z.-P. Li, F.-Z. Li, X.-W. Chen, L.-H. Sun, J.-J. Jia, J.-C. Wu, X.-J. Jiang, J.-F. Wang, Y.-M. Huang, Q. Wang, Y.-L. Zhou, L. Deng, T. Xi, L. Ma, T. Hu, Q. Zhang, Y.-A. Chen, N.-L. Liu, X.-B. Wang, Z.-C. Zhu, C.-Y. Lu, R. Shu, C.-Z. Peng, J.-Y. Wang, and J.-W. Pan, *Satellite-to-ground quantum key distribution*, Nature, **549** 43–47, 2017.

[42] P. R. Dolan, G. M. Hughes, F. Grazioso, B. R. Patton, and J. M. Smith, *Femtoliter tunable optical cavity arrays*, Opt. Lett., **35** 3556–3558, 2010.

[43] A. A. P. Trichet, P. R. Dolan, D. M. Coles, G. M. Hughes, and J. M. Smith, *Topographic control of open-access microcavities at the nanometer scale*, Opt. Express, **23** 17205–17216, 2015.

[44] X. Liu, T. Galfsky, Z. Sun, F. Xia, E.-c. Lin, Y.-H. Lee, S. Kéna-Cohen, and V. M. Menon, *Strong light-matter coupling in two-dimensional atomic crystals*, Nat. Photon., **9** 30–34, 2014.

[45] N. Lundt, S. Klembt, E. Cherotchenko, S. Betzold, O. Iff, A. V. Nalitov, M. Klaas, C. P. Dietrich, A. V. Kavokin, S. Höfling, and C. Schneider, *Room-temperature Tamm-plasmon exciton-polaritons with a WSe2 monolayer*, Nat. Commun., **7** 13328, 2016.

[46] H. Knopf, N. Lundt, T. Bucher, S. Höfling, S. Tongay, T. Taniguchi, K. Watanabe, I. Staude, U. Schulz, C. Schneider, and F. Eilenberger, *Integration of atomically thin layers of transition metal dichalcogenides into high-Q, monolithic Bragg-cavities: an experimental platform for the enhancement of the optical interaction in 2D-materials*, Opt. Mater. Express, **9** 598–610, 2019.

[47] M. Leifgen, T. Schröder, F. Gädeke, R. Riemann, V. Métillo , E. Neu, C. Hepp, C. Arend, C. Becher, K. Lauritsen, and O. Benson, *Evaluation of nitrogen- and silicon-vacancy defect centres as single photon sources in quantum key distribution*, New J. Phys., **16** 023021, 2014.

[48] L. Hanschke, K. A. Fischer, S. Appel, D. Lukin, J. Wierzbowski, S. Sun, R. Trivedi, J. Vučković, J. J. Finley, and K. Müller, *Quantum dot single-photon sources with ultra-low multi-photon probability*, npj Quantum Inf., **4** 43, 2018.

[49] L. Schweickert, K. D. Jöns, K. D. Zeuner, S. F. Covre da Silva, H. Huang, T. Lettner, M. Reindl, J. Zichi, R. Trotta, A. Rastelli, and V. Zwiller, *On-demand generation of background-free single photons from a solid-state source*, Appl. Phys. Lett., **112** 093106, 2018.

[50] A. Beveratos, R. Brouri, T. Gacoin, J.-P. Poizat, and P. Grangier, *Nonclassical radiation from diamond nanocrystals*, Phys. Rev. A, **64** 061802, 2001.

[51] B. C. Pursley, S. G. Carter, M. K. Yakes, A. S. Braker, D. Gammon, *Picosecond pulse shaping of single photons using quantum dots*, Nat. Commun., **9** 115, 2018.

[52] C. Gobby, Z. L. Yuan, and A. J. Shields, *Quantum key distribution over 122 km of standard telecom fiber*, Appl. Phys. Lett., **84** 3762–3764, 2004.

[53] H.-K. Lo, X. Ma, and K. Chen, *Decoy State Quantum Key Distribution*, Phys. Rev. Lett., **94** 230504, 2005.

[54] D. J. Rogers, J. C. Bienfang, A. Mink, B. J. Hershman, A. Nakassis, X. Tang, L. Ma, D. H. Su, C. J. Williams, and C. W. Clark, *Free-space quantum cryptography in the H-alpha Fraunhofer window*, Proc. SPIE, **6304** 630417, 2006.

[55] R. Raussendorf and H. J. Briegel, *A One-Way Quantum Computer*, Phys. Rev. Lett., **86** 5188–5191, 2001.

[56] C. K. Hong, Z. Y. Ou, and L. Mandel, *Measurement of subpicosecond time intervals between two photons by interference*, Phys. Rev. Lett., **59** 2044–2046, 1987.

[57] T. Grange, G. Hornecker, D. Hunger, J.-P. Poizat, J.-M. Gérard, P. Senellart, and A. Auffèves, *Cavity-Funneled Generation of Indistinguishable Single Photons from Strongly Dissipative Quantum Emitters*, Phys. Rev. Lett., **114** 193601, 2015.

[58] A. Dietrich, M. Bürk, E. S. Steiger, L. Antoniuk, T. T. Tran, M. Nguyen, I. Aharonovich, F. Jelezko, and A. Kubanek, *Observation of Fourier transform limited lines in hexagonal boron nitride*, Phys. Rev. B, **98** 081414, 2018.

Chapter 10

Atomic localization of quantum emitters in multilayer hexagonal boron nitride

10.1 Foreword

The previous chapter presented a space-compatible cavity-enhanced single-photon source based on hexagonal boron nitride. The device's performance was not only sufficient to beat state-of-the-art decoy state quantum key distribution protocols on typical metropolitan fiber network distances, but also for low Earth orbit satellite distances, most notably on the altitude at which the Micius satellite orbits and performed the first space-to-ground quantum key exchange. Furthermore, the complete single-photon source was fully self-contained on a satellite platform, a 1U CubeSat with 10 cm edge length. Future experiments will have to prove the source is capable of beating decoy state protocols in terms of secret key rate, the ultimate metric for any QKD experiment. Given that, the single-photon source could be mass-produced and employed on a constellation of satellites, providing the backbone for a future quantum internet.

To make hexagonal boron nitride an even better single-photon source, it is important to understand the nature of the defect, as the origin of the emission is still unknown. This allows one to model the dynamics and to predict further improvements, especially tuning the emitter. Polarization-resolved photoluminescence measurements show the defects emit in a dipole-like pattern, which indicates that a low symmetry in-plane defect is involved, potentially comprised of vacancies and impurities. Among the candidates for impurities are carbon and oxygen complexes. The fact is, power saturation measurements show clear defect-like behavior. The large spread in photophysics between different emitters make it difficult to assign the responsible complex, especially since density functional theory predicts many of the studied point-like defects have multiple transition energies matching those experimentally observed.

To overcome this issue of defect misassignments, more experimental studies are required. The results can either point toward a direct identification, or can at least rule out specific point-like complexes, so that theoretical calculations can be refined. This chapter presents the localization of the quantum emitters with atomic precision. The study finds that the position where the defects form or are activated correlates with the fabrication method. This in turn allows one to engineer the emitters to be close to the surface, where high-resolution electron imaging techniques might have a chance of at least confirming

whether a vacancy is involved or not.[1] The difference in distance of emitter location to the crystal surface also explains the spread in emitter lifetime that is experimentally observed. This work has been published in and is here reproduced from Nanoscale **11**, 14362-14371 (2019) with permission from the Royal Society of Chemistry. All graphics have been recreated to match the style of this thesis.

[1] To identify an impurity, the substitutional atom would need to have a vastly different van der Waals radius.

Atomic localization of quantum emitters in multilayer hexagonal boron nitride

Tobias Vogl[1], Marcus W. Doherty[2], Ben C. Buchler[1], Yuerui Lu[3], and Ping Koy Lam[1]

[1] *Centre for Quantum Computation and Communication Technology, Department of Quantum Science, Research School of Physics and Engineering, The Australian National University, Acton ACT 2601, Australia*

[2] *Laser Physics Centre, Research School of Physics and Engineering, The Australian National University, Acton ACT 2601, Australia*

[3] *Centre for Quantum Computation and Communication Technology, Research School of Electrical, Energy and Materials Engineering, The Australian National University, Acton ACT 2601, Australia*

Abstract

The recent discovery of single-photon emitting defects hosted by the two-dimensional wide band gap semiconductor hexagonal boron nitride (hBN) has inspired a great number of experiments. Key characteristics of these quantum emitters are their capability to operate at room temperature with a high luminosity. In spite of large theoretical and experimental research efforts, the exact nature of the emission remains unresolved. In this work we utilize layer-by-layer etching of multilayer hBN to localize the quantum emitters with atomic precision. Our results suggest the position of the emitters correlates with the fabrication method: emitters formed under plasma treatment are always in close proximity to the crystal surface, while emitters created under electron irradiation are distributed randomly throughout the entire crystal. This disparity could be traced back to the lower kinetic energy of the ions in the plasma compared to the kinetic energy of the electrons in the particle accelerator. The emitter distance to the surface also correlates with the excited state lifetime: near-surface emitters have a shorter compared to emitters deep within the crystal. Finite-difference time-domain and density functional theory simulations show that optical and electronic effects are not responsible for this difference, indicating effects such as coupling to surface defects or phonons might cause the reduced lifetime. Our results pave a way toward identification of the defect, as well as engineering the emitter properties.

Reproduced from Nanoscale **11**, 14362-14371 (2019) with permission from the Royal Society of Chemistry.

10.2 Introduction

The recent discovery of quantum emitters in two-dimensional (2D) materials attracted considerable attention, due to their applications in photonic quantum technologies[1]. These include unconditionally secure communication[2], quantum simulators[3] and quantum computing[4], which fueled the development of single-photon sources (SPSs). In contrast to their counterparts in 3D, quantum emitters hosted by 2D lattices are not surrounded by any high refractive index medium. This eliminates total internal and Fresnel reflection of emitted single-photons, making it possible to have intrinsically near-ideal extraction efficiency. Quantum emission has been reported from a diversity of materials, in semiconducting transition metal dichalcogenides (TMDs)[5–12] and insulating hexagonal boron nitride (hBN)[13]. The large band gap of the latter even allows one to resolve the zero phonon line (ZPL) at room temperature and thwarts non-radiative recombination of the localized

exciton. Thus, single-photon emitters in hBN have an intrinsically high quantum efficiency which leads to significantly brighter emission[13, 14]. In addition, single-photon sources based on hBN are suitable for many practical field applications due to their resistance to ionizing radiation[15], temperature stability over a huge range spanning 800 K[16, 17], long-term operation[18] and capabilities for integration with photonic networks[19, 20], as well as easy handling. While these emitters can occur naturally[13], it is common to enhance the defect formation synthetically through chemical[21] or plasma etching[18, 22], γ-ray[15], ion[23] and electron irradiation[23, 24] or near-deterministic stress-induced activation[25].

The generally accepted model for the single-photon emission is based on a localized exciton. These fluorescent point-like defects introduce trap states into the electronic band gap, acting thus as an effective two-level system. In defiance of several attempts to identify the origin of the fluorescence using group theory and *ab initio* density functional theory (DFT) calculations[26–28], the exact nature of the defects remains controversial. Possible defect candidates include the C_BV_N, V_BC_N, V_NN_B and V_B defects (C_BV_N: a carbon atom replaces a boron atom with an adjacent nitrogen vacancy; V_BC_N: a carbon atom substitutes for a nitrogen atom with an adjacent boron vacancy; V_NN_B: a nitrogen occupying the lattice site of a boron atom with an adjacent nitrogen vacancy; V_B: single boron vacancy). It was recently noted, however, that widely used generalized gradient functionals can perform poorly and lead to misassignment of the defect states, hence, hybrid or long-range corrected functionals should be applied[29]. Moreover, DFT calculations often assume monolayered supercells due to the exponential scaling with the number of atoms and limited computational resources, while most experimental works involve multilayer hBN. For yet not fully understood reasons, the optical emission signatures of quantum emitters hosted by mono- and multilayer hBN differ substantially[13].

On the experimental side, research efforts toward the identification[30, 31] are hampered by the strongly varying optical emission properties. These vary not only from defect to defect on different hBN crystals, but also for defects on the same host crystal. ZPLs have been reported in the UV[32] and in the the visible spectrum from 550 to 800 nm[16, 18, 33, 34] and the excited state lifetimes vary from 20 ns down to 0.3 ns[18, 19]. A conclusive explanation for this requires additional experimental analysis. What is definitely known is the power saturation behavior is that of an idealized two- or multi-level system and the emitters exhibit an in-plane dipole. This indicates a low symmetry in-plane defect that is potentially comprised of vacancies and impurities.

The variations in ZPL position cannot be explained alone by local strain in the crystal environment. The shifts caused by strain are too small to account for the variety of ZPLs[35]. Of particular note is that the ZPLs seem to bunch in groups around 560 nm[18], 580 nm[36], 640 nm[13, 33] and 714 nm[33]. We define these as groups 1 through 4, respectively. It is believed that a different point-like defect is responsible for each group with the crystal lattice locally strained or changed otherwise, thus explaining the spread around these wavelengths. Shifts of the transition line caused by different isotopes would be much smaller than the emission linewidth. The vibronic bandshape of most defects is very similar, indicating that they have the same symmetry group. We note that there are occasional ZPLs falling into neither of these categories. It is likely that these originate from surface contaminants. Moreover, the bandshape of these differ from the bandshape typical for other emitters in the four groups, which supports this conjecture.

Using super-resolution techniques, these defects have been localized in 2D with sub-diffraction resolution[37]. The direct imaging on the atomic scale using high-resolution

scanning transmission electron microscopy (STEM) is limited to a few layers, as the images contain information from all layers (essentially being a projection of all layers onto 2D). One way around this is to use a more advanced method like high-angle annular dark-field imaging (HAADF), with which it is possible to detect the presence of a vacancy within a few layers (maybe up to 3-5 layers). A vacancy would change the detected intensity by changing the scattering probability locally, and thus this would reveal such a defect with the exact location in the XY plane. However, this still does not contain any information about the Z direction. Recently, a method to correlate optical and electron characterizations of quantum emitters in very thin hBN was demonstrated[31]. This method, however, also yields no information about the Z direction. In addition, detecting the presence of a vacancy using HAADF cannot be used on thicker crystals, because the intensity contrast would be too low.

In this work, we localize the quantum emitters hosted by multilayer hBN in the third dimension with atomic precision. We develop deterministic layer-by-layer plasma etching of hBN. This way we can remove a single hBN monolayer at a time and check *ex-situ* when the defect disappears. We thereby measure the precise distance of the emitter from the surface of the host crystal. While this is a destructive technique, it allows us to extract the exact number of layers in which the defect was located. Repeating our experiment for many defects allows us to generate sufficient statistics. We also model photophysical properties theoretically with finite-difference time-domain simulations and density functional theory.

10.3 Results and discussion

10.3.1 Layer-by-layer etching of hBN

Our approach to extract the location of the defects in the Z direction is to selectively remove one hBN monolayer at a time and check after each step, if the defect is still present. We first developed the layer-by-layer etching of hBN using an oxygen plasma. We note that similar etching of hBN on the atomic scale was reported recently using an argon plasma[38]. While this is an important milestone, however, Park *et al.* etched ~ 20 layers at a time and scaled this down to monolayer etching[38]. Nevertheless, with this technique as well as our method (see below), it is possible to fabricate large hBN monolayers. These are very difficult to obtain using mechanical exfoliation alone, due to the poor optical contrast of hBN, which has a zero-crossing in the visible spectrum[39].

We mechanically exfoliated hexagonal boron nitride from bulk crystal onto a viscoelastic polymer. Thin, but still several nm thick hBN flakes were selected by optical contrast for dry transfer to a Si substrate terminated with a layer of thermally grown SiO_2 (262 nm). For the etching we used an oxygen plasma generated from a microwave field and empirically optimized the plasma parameters (see Methods). The crystal thickness after each successive etching step is measured with a phase-shift interferometer (PSI), which is a much faster method than using an atomic force microscope (AFM) at the cost of a lower lateral resolution. Figure 10.1(a) shows the PSI image prior to any plasma treatment and after 2 min of etching time, where the crystal thickness decreased. The top flake consists of 9 and 7 atomic layers, respectively. The optical path length (OPL) difference between the substrate and the crystal (measured along the white dashed lines in Figure 10.1(a)) at a PSI wavelength of $\lambda = 532\,\text{nm}$ after each cumulative etching step is shown in Figure 10.1(b). It can be seen that the etched thickness is linear with time. The OPL

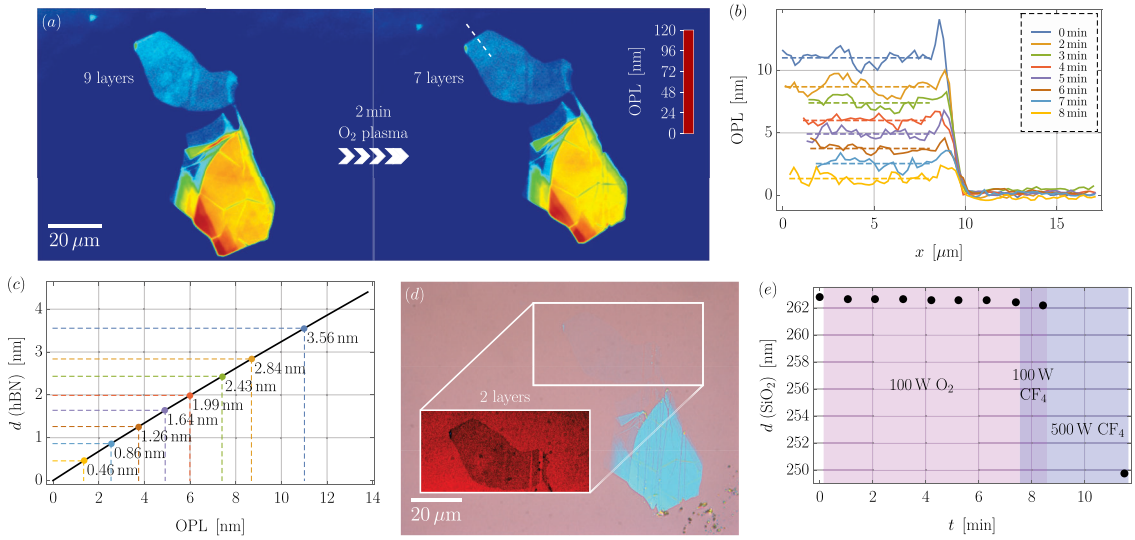

Figure 10.1: Layer-by-layer etching of hBN. (a) PSI image of an hBN flake prior to any plasma treatment (left) and after 2 min at 100 W of oxygen plasma treatment (right). The thickness of the thin flake at the top is reduced from 9 to 7 atomic layers. The white dashed lines show the direction at which the traces in (b) are measured. (b) Optical path length difference along the white lines in (a) measured *ex-situ* after each plasma etching step. The dashed lines denote the average. The start point of each is not equal. (c) RCWA simulation of the OPL difference for hBN on 262 nm SiO_2 on Si (black line). The points visualize how the measured OPL can be converted into physical thickness of the flake. The physical thickness for each measured OPL is displayed in black next to the corresponding data point. (d) Microscope image (1000× magnification) of an hBN flake after 7 min at 100 W of oxygen plasma treatment. The crystal consists only of two atomic layers (for clarity the bilayer is shown). The inset shows a strongly contrast-enhanced image of the crystal. (e) Thickness of the SiO_2 layer on the Si substrate measured *ex-situ* after each plasma etching step. After 7 min at 100 W (O_2), the thickness changed only marginally, by less than 0.22 nm. After one additional minute at 100 (CF_4), the thickness further decreased by 0.22 nm. After three additional minutes at 500 W (CF_4) in the plasma field maximum, the thinning was substantial with 12.49 nm decrease. The error bars are shorter than the size of the symbols. A significant change in the SiO_2 thickness would change the OPL.

can be converted to physical thickness using rigorous coupled-wave analysis (RCWA) simulations[40], as shown in Figure 10.1(c). The simulations assume the refractive index of hBN to be 1.849, which was extracted by fitting an RCWA model to data pairs consisting of AFM and PSI measurements. It is worth noting that the relation between OPL and physical thickness d is nonlinear for large OPLs[18]. The data points in Figure 10.1(c) correspond to the PSI measurements (colored accordingly). Since the physical thickness of hBN is $0.4 - 0.45$ nm per layer[41], we can extract that the crystal presented here was etched layer-by-layer from 9 layers to monolayer, with an etching rate of 1 layer per 63 s. A microscope image with an artificially-enhanced optical contrast of the bilayer is shown in Figure 10.1(d). At the optimized plasma conditions, this atomic layer-by-layer etching is highly reliable, with no fails (i.e. 0 or 2 layers etched) out of 31 runs. Moreover, we used the same technique on TMDs without failures and the method was also used for precise layer-by-layer thinning of black phosphorus[42] or MoS_2[43]. Assuming the failure probability to be $\leq 0.1\%$ would reproduce our etching success of hBN with a high probability of 96.9%. Deviating from the ideal plasma conditions (63 s etching time, for all details see

Methods) results in process failures. This is evident by the fact that reducing the etching time by 10 s resulted into 2 out of 6 crystals not being etched and increasing the etching time by 10 s resulted in two layers being etched in 1 out of 3 cases (see Supporting Information, Figure S1). The reason why multiple layers can be etched without doubling the etching time is because it takes some time to start cracking the bonds, once that process starts, a faster etching rate can be achieved.

It is important to note that the plasma may damage the substrate. The OPL is dependent on the SiO_2 thickness and the RCWA simulations assume this to be fixed. We checked the thickness of a SiO_2 layer *ex-situ* after each etching step using variable angle spectroscopic ellipsometry (VASE). After 7 min at 100 W of cumulative plasma treatment, the thickness of a SiO_2 layer decreased from 262.68(1) to 262.46(1) nm (see Figure 10.1(e)), so on average the SiO_2 thinning is 0.03 nm per step. According to the RCWA simulations such substrate thickness difference results in a change of the OPL much smaller than the resolution of the PSI (0.1 nm). Therefore, we can neglect this effect. This is, however, in general dependent on the type of plasma. For a comparison: using a CF_4 plasma at 100 W for 1 min results in a thickness change of 0.22 nm of the SiO_2 and using a CF_4 plasma at 500 W for 3 min in the plasma field maximum (see Methods) etches 12.49 nm.

10.3.2 Creation of quantum emitters

The fabrication of multilayer hBN flakes for hosting single-photon emitter is similar to the procedure above. After transfer to the substrate, the flakes are treated with an oxygen plasma at different conditions and successively annealed in a rapid thermal annealer[18] (see also Methods). To locate the defects each flake is scanned in a custom-built confocal micro-photoluminescence (μPL) system with a resolution ranging from 0.2 to 1 μm. Initially, the flakes are scanned with a 1 μm grid and identified defects are located with a smaller step size of 0.2 μm, preventing accidentally missing any known defect location during subsequent scans. The pump laser, with its wavelength at 522 nm, is blocked by a long-pass filter and the emission is collected in-reflection. The defects almost exclusively occur at the edges of the host crystal flakes, due to a lower defect formation energy at these locations. Defects can, however, also form along crystal cracks within the flake. The defect formation energy there is lower as well. The spectra of three sample emitters are shown in Figure 10.2(a), which have their ZPLs at 559.78(7), 565.15(6) and 650.16(7) nm and Lorentzian linewidths of 2.24(10), 2.51(9) and 4.39(9) nm, respectively. All sample emitters presented here emit more than 80% of their photoluminescence (PL) into the ZPL, which allows for a high quantum efficiency. Time-resolved photoluminescence reveals a single-exponential decay of the excited state population for each defect with lifetimes 770(7), 549(7) and 794(13) ps, respectively (see Figure 10.2(b)). The excitation laser is pulsed at a repetition rate of 20.8 MHz and a pulse length of 300 fs. While this allows for high peak intensities, two-photon absorption of the band gap of hBN is still impossible, because $E_{\mathrm{hBN}} = 6\,\mathrm{eV} > 2 \times 2.38\,\mathrm{eV} = 2 \times E_{\mathrm{laser}}$. To prove that the localized exciton emits indeed non-classical light we utilize a Hanbury Brown and Twiss (HBT)-type interferometer, which allows for measuring the second order correlation function (see Figure 10.2(c)). We fit a three-level model with excited and meta-stable shelving state to our data. The correlation function is then given by

$$g^{(2)}(\tau) = 1 - Ae^{-|\tau|/t_1} + Be^{-|\tau|/t_2}$$

with the anti- and bunching-amplitudes A, B, and the characteristic lifetimes t_1, t_2. For the three sample emitters we find $g^{(2)}(0) = 0.142(37), 0.196(53)$ and $0.234(44)$, respectively. There was no background correction[44] necessary due to the low detector noise compared to the single-photon brightness. This also means that the observed finite multi-photon probability is not caused by detector dark counts, but rather noise sources excited by the laser. Note that the experimental data was normalized such that for infinite time delay $g^{(2)}(\tau \to \infty) = 1$. The lifetimes extracted from the correlation function measurements agree well with the lifetimes measured with time-resolved PL. As already mentioned, the literature reports ZPLs typically bunch around certain wavelengths. In fact, in our experiments we have seen this to happen around 560 nm, 590 nm and 640 nm, as the histogram in Figure 10.2(d) shows. With our fabrication method, however, we were not able to create emitters with ZPLs > 700 nm with statistical significance. In addition, sometimes we created an emitter not falling into any of the groups defined above. We believe that these are contaminating fluorescent molecules adsorbed onto the surface of hBN. Their emission is typically much weaker and their spectrum broader compared to the other emitters (see Figure 10.2(e)).

10.3.3 Atomic localization of quantum emitters

With 93 quantum emitters fabricated and characterized, we could utilize the atomic etching of hBN, removing one layer at a time. After each cumulative plasma etching step, the flakes were scanned again and we checked if the defect survived (see Supporting Information, Figure S2 for the process flow). It is possible that this etching creates new emitters, but at the layer-by-layer etching parameters, we expect the linear defect formation density to be $\sim 0.02\,\mu\text{m}^{-1}$ (i.e. one defect forms on average per $50\,\mu$m crystal edge length)[18]. Thus, it is unlikely that an emitter is removed and at the same time a new one forms at the same location. In addition, as the photophysics of the defects vary substantially, it would be even more unlikely that a newly created emitter that formed at the location of a previous emitter has similar photophysical properties (in terms of e.g. ZPL, lifetime, and dipole orientation). In fact, we did see occasionally new defects appear at new locations, but they are not counted toward the statistics in this study. The histogram of the number layer after which the defect disappeared is shown in Figure 10.3(a). The best fit to any univariate distribution reveals a Poisson distribution with a mean of 3.8. This means that the emitters are very close to the surface.

When looking at how the photophysics evolve as the top layers are successively etched, it becomes clear that the emission is stable until the emitter is removed (see Figure 10.3(b)). The photoluminescence does not decrease gradually nor change its lineshape or other photophysical properties. Rather the PL from the defects disappears suddenly entirely, and for all upon removal. This means the quantum emitters are well isolated within one layer with no appreciable inter-layer interaction. In principle, it is possible the wave function of the trapped charge carrier is spread over multiple layers, thus the defect could enter a dark state even if some layers above the layer containing the chemical defect are etched (while the defect itself is not etched yet). There is, however, no further evidence supporting this conjecture. In addition, all the emitters with ZPLs falling not into one of the categories in the histogram in Figure 10.2(d) disappeared after the first etching step. This is evidence for the fact that these emitters are indeed surface contaminants. As expected, the Raman shift after each etching step remained constant, indicating that there is not much strain in the crystal, which would relax as the layers are etched. One could

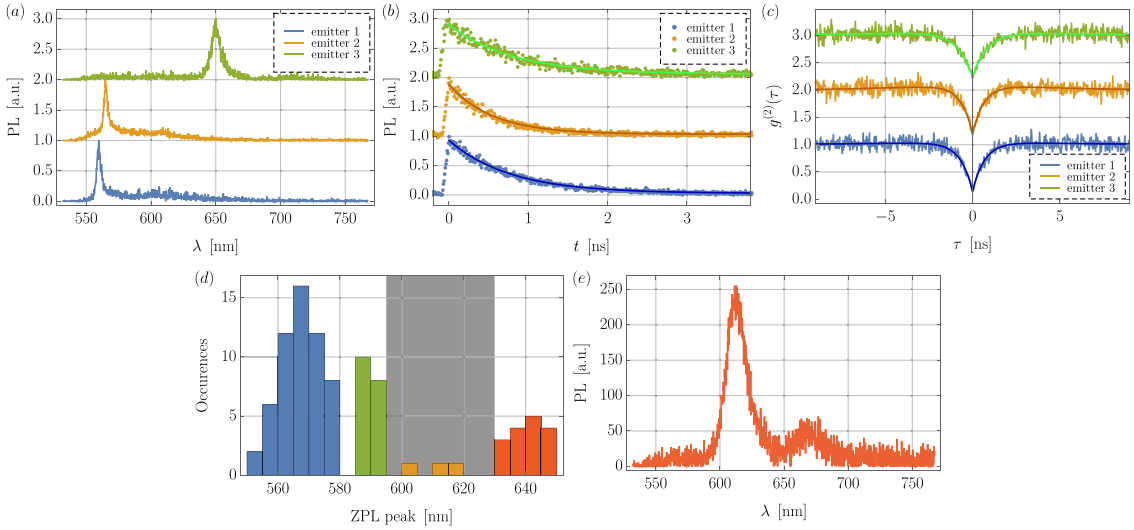

Figure 10.2: Photophysics of the emitters. (a) Normalized spectra (vertically offset for clarity) of 3 sample emitters with their ZPLs at 559.78(7), 565.15(6) and 650.16(7) nm. Their corresponding Lorentzian linewidths are 2.24(10), 2.51(9) and 4.39(9) nm, respectively. (b) Time-resolved photoluminescence reveals a single-exponential decay of the excited state population with lifetimes 770(7), 549(7) and 794(13) ps for the emitters, respectively. The data is normalized and vertically offset for clarity. (c) The second-order correlation function dips to 0.142(37), 0.196(53) and 0.234(44) at zero time delay (obtained from fits). There was no background correction applied. The re-emission peaks are present, but not visible on the scales displayed. The data is normalized such that $g^{(2)}(\tau \to \infty) = 1$ and vertically offset for clarity. (d) Histogram of the distribution of zero phonon lines from 93 defects. The ZPLs bunch around 560 nm (group 1, blue), 590 nm (group 2, green) and 640 nm (group 3, red). It is believed that defects falling into neither of these categories (excluded area, grayed out) originates from surface contaminants. (e) Sample spectrum of such an emitter from the excluded area in (d). The emission of these emitters is typically comparably weak and broad.

argue emitters that are counted as etched actually just enter a dark state temporarily. This is very unlikely, as previous experiments found during the time when the emitter is in the dark state there is still light emission from the defect, but usually it is much weaker compared to the normal emission[34, 45].

The extracted layer number is believed to be highly accurate. Assuming a failure probability $\leq 0.1\%$ (see above) results in a success probability of 77.2% that all layer numbers are correct (in total there were 258 etching steps). However, as all samples were etched at the same time, there is a chance that if one process failed, many samples would be affected. A process fail could be that it took a longer time for the plasma to ignite or to stabilize the gases (both ignition and stabilization happens at a higher plasma power, which is subsequently regulated down to the set power), so to exclude this possibility the plasma parameters are recorded *in-situ*.

The results so far prove emitters (formed by oxygen plasma treatment) are always very close to the surface. This raises a few questions: (1) Why are the emitters close to the surface? (2) Are emitters always close to the surface, or does this depend on the defect formation method? (3) Is this an explanation for the shorter excited state lifetime of the plasma treated quantum emitters?

The dominant ion species in the plasma is O^{2+} (at lower pressure and higher power O^{+}

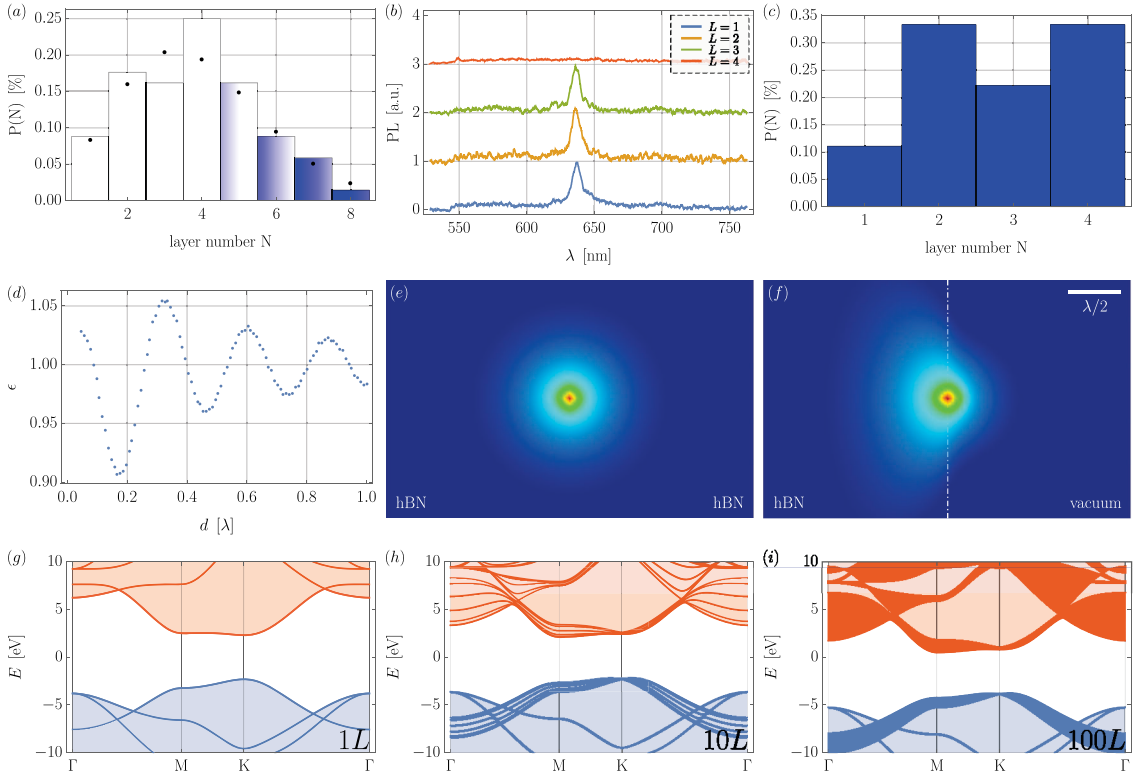

Figure 10.3: Atomic localization of quantum emitters. (a) Probability density of locating the emitters in layer N (i.e. it disappeared after N etching steps). The average value is 3.8. The black points are the best fit to any univariate distribution (here a Poisson distribution). The emitters have been created by oxygen plasma treatment. (b) Spectral evolution of one emitter as consecutive layers are removed from the top side. The emission line is relatively stable and suddenly fully disappears after the fourth etching step. (c) Probability density of locating the emitters in layer N (i.e. it disappeared after N etching steps). The emitters have been created by electron irradiation. (d) FDTD simulations of the Purcell effect of a dipole emitter close to the hBN-vacuum interface. The emitter lifetime or Purcell factor ϵ oscillates as the emitter gets moved deeper into the crystal. In the limit of $d \gg \lambda$ there is no enhancement or suppression and the electric field mode profile in this limit is shown in (e). For the limit $d \ll \lambda$ the electric field mode profile is shown in (f). The emission is stronger into the crystal than into the vacuum (as the crystal has a higher dielectric constant). (g-i) DFT calculations of the band structure routed along high-symmetry points for 1L, 10L, and 100L hBN, respectively. Due to layer-layer interactions the bands added by the layers spread, but no deep energy band appears, meaning that the interaction with surface states is likely low.

becomes more dominant). The expected ion energy during the defect formation plasma treatment is $\sim 10\,\text{eV}$. Unfortunately, this ion energy is too low for Monte Carlo methods like SRIM[46], preventing an accurate calculation of the projected ion range in matter (in this case hBN). However, in our case the plasma treatment is a chemical and not physical process. This means the process is mostly limited to the crystal surface, as the ions have only low kinetic energy and cannot penetrate deep into the crystal. The kinetic energy of the ions is similar to the defect formation energy in hBN, which is on the order of a few eV[47]. Moreover, the O_B and O_N defect have formation energies of 5.19 and 2.20 eV, respectively, so they could easily be produced by the ions[48]. The oxygen radicals are highly reactive and are thus likely producing defects. It was recently pointed out, however,

that it is unclear whether the defects are actually created using the plasma processing or one of the many other methods, or if preexisting, initially dark defects are activated via modification or restructuring of the crystal environment[49]. Both options are possible and our data so far does not allow to favor one over the other explanation.

While the oxygen plasma only acts onto the crystal surface, defect diffusion is also an important consideration. Without the exact knowledge of the chemical defect structure this is impossible to estimate, but at least a few things are known: First, hBN has strong sp^2-hybridized covalent bonds, so the defect diffusion activation energy (that is the energy required to move along the reaction path) is rather large. It is expected that diffusion is predominantly in-plane and not inter-layer due to the direct in-plane bonds, so diffusion deep into the crystal is not likely. For hBN, due to the heteronuclear structure, defect diffusion is partially suppressed, as homonuclear B-B and N-N are energetically unfavorable (these homonuclear bonds are temporarily formed as the defects moves along the reaction path)[50]. This results in a lower vacancy migration compared to homonuclear graphene. The diffusion activation energy calculated with DFT range from 2.6 to 6.0 eV at 0 K for vacancies and divacancies, with the structures often relaxing to their initial configuration[50]. This already shows the smaller defect diffusion. Furthermore, at the rapid annealing temperature of 850°C (in this experiment), only the boron vacancy has a diffusion coefficient larger than $1\,\text{Å}^2\text{s}^{-1}$[50]. Future calculations have to show how the diffusion of other point-like complexes scales. It is worth noting, that the result of the defect diffusion activation energy from DFT calculations shows a small dependency on the specifically used pseudopotential[51].

To address the second question, we repeat the experiment with emitters fabricated with electron irradiation[23,24]. The electron accelerating voltage was 10 kV with an electron fluence of $\sim 10^{18}\,\text{cm}^{-2}$. Given the thickness of the hBN flakes being $\ll 1\,\mu$m, the kinetic energy of the electrons is sufficient to fully transmit through the hBN crystals (see Supporting Information, Figure S3(a)). The energy loss of the electrons is dominated by collisions with the boron and nitrogen nuclei, as the radiative stopping power is much smaller at 10 keV kinetic electron energy (see Supporting Information, Figure S3(b)). Therefore, bremsstrahlung does not play any role. With the projected range of the electrons being $1.4\,\mu$m at 10 keV, it is expected that emitters created or activated by electron irradiation are not exclusively near the crystal surface. Monte Carlo simulations of electron trajectories through the hBN crystal (see Supporting Information, Figure S3(c,d)) also confirm this. Repeating the atomic etching on these new emitters confirms this, as none of the emitters was found within the first ten layers, and the emitters being randomly positioned within the crystal. Etching at much larger steps ($\sim$ 10s of layers at a time, even though we note this was not calibrated sufficiently) shows that defects created by electron irradiation are formed throughout the crystal (see Figure 10.3(c)). More precisely, the emitters form not exclusively at the crystal edges or dislocations anymore, in agreement with previous experiments[24]. Interestingly, the excited state lifetime of these emitters is typically longer compared to the plasma etched ones, with lifetimes ranging from $2-3$ ns (see Supporting Information, Figure S4 for a characterization of quantum emitters created under electron irradiation).

10.3.4 Theoretical modeling

Finally, we address the third question. Within the crystal, the photon density of states is decreased compared to vacuum. This is a Purcell-like effect, where the radiative lifetime

is modified as the dielectric environment changes. The Purcell factor ϵ as a function of emitter distance to the surface d is calculated using finite-difference time-domain (FDTD) simulations (see Methods) and shown is in Figure 10.3(d). The Purcell factor (and thus the excited state lifetime of an ideal dipole) oscillates and reaches 1 in the limit $d \gg \lambda$. In this limit there is no enhancement or suppression. It becomes clear that this effect only makes up a few percent in lifetime changes, so this alone cannot explain the shorter lifetime. It is still noteworthy, that there is enhancement very close to the surface, while deeper ($45 - 145$ nm) there is suppression. The electric field mode profiles in both limits show the emitter deep within hBN emits like an ideal dipole, while the emitter at the surface emits stronger into the crystal than into vacuum (see Figure 10.3(e,f)). This means the actual emitter brightness is even larger than experiments so far suggest. For emitters in cavities[52], this does not matter, as both directions are captured by the cavity. As the different lifetime is not solely due to a Purcell-like effect, we use density functional theory calculations to investigate if surface states could be the cause for the shorter lifetime. We calculate the electronic band structure of hBN for one (1L), ten (10L), and 100 layers (100L) of hBN (see Figure 10.3(g-i)). The calculations show, that as more layers are added also more energy bands are added. Due to layer-layer interactions these bands spread, but there are no genuine isolated surface bands introduced into the band gap. This implies that, unless the defect levels are very close to one of the band edges, surface states do not influence the lifetime of the defect. Therefore, we conclude that the shorter defect lifetime in our experiments is likely due to interaction with surface defects introducing additional decay pathways, or with surface phonons making existing decay pathways faster. It is worth noting, different defect structures, if involved, would most likely exhibit different lifetimes as well. Finally, the fact that the lifetime is constant during the layer-by-layer etching (see above) does not contradict our model, as the close distance to the surface makes lifetime changes too small (i.e. the lifetime change from an emitter being in layer number 2 to an emitter being in layer number 1 would be hardly measurable).

10.4 Conclusions

In this work, we have developed deterministic atomically layer-by-layer etching of hBN with an oxygen plasma. This was utilized to destructively localize quantum emitters hosted by hBN. We found that emitters fabricated by a different plasma process are always very close to the surface, within a few layers, while emitters fabricated by intense electron irradiation are located throughout the entire crystal thickness. For both creation methods, emitters are more likely to form at flake edges and grain boundaries. It is notable that they also form away from these domains, in what appears to be undistorted crystal. Creation near the surface is a likely explanation for the shorter excited state lifetime hBN quantum emitters exhibit when fabricated by plasma etching. The emitter lifetime is influenced by additional decay pathways introduced by surface defects, or interactions with surface phonons making existing decay pathways faster. In contrast, emitters deep within the crystal have lifetimes $\sim 3 - 6$ times longer, as they are well isolated from the environment and surface effects.

Considering now the implications that our observations have for the identity of the quantum emitters. Our etching study is consistent with the confinement of the emitting defect to a single layer, as per past observation of the emitters in monolayer samples[13]. The creation of deep defects away from a boundary by electron irradiation is an important observation. It implies that the defect can be a product of radiation damage and so is

further evidence that it involves a vacancy or interstitial. Specifically either a nitrogen vacancy V_N, a boron-vacancy V_B, an intralayer interstitial or an interlayer interstitial. To identify which, we need to interpret the effects of annealing.

At our annealing temperature of 850°C, it is known that the V_B is mobile, whilst V_N is not. It is reasonable to expect that the interlayer interstitials are also mobile due to the low interlayer bond energies of the material. Upon annealing, we observe improved photostability and linewidth, but no significant change in the number of emitters[18]. We attribute the improved optical properties to the removal of interstitials and single V_B, which we expect to lead to an improved charge stability and reduced electrical noise since these defects likely act as donors or acceptors. If the density of the V_B created by the radiation is low, then our annealing observation would imply that the defect does not involve V_B. This is because if the defects were single V_B, then the number of emitters would decrease with annealing, and if it were a complex involving one or more V_B, then the number of emitters would increase until saturation of the other constituents of the complex (i.e. V_N or impurities). However, we are not necessarily drawing this conclusion here, since our intense electron irradiation may have rather created a very high density of V_B, which even without annealing, could have saturated the creation of emitters (i.e. by creating V_B in close proximity to V_N or an impurity). In this case, the defect may well involve V_B. Unfortunately, we cannot determine which V_B density limit our radiation produced because there is insufficient information about the V_B creation cross-section for electron radiation. Future work should focus on establishing the V_B density created before annealing and relating this to the creation / destruction / no change of emitters during annealing to establish whether or not V_B is involved in the defect.

The creation of the defects by the oxygen plasma may imply that the defect involves oxygen impurities through their incorporation at the surface. Generalizing this hypothesis to the creation of deep emitters by electron irradiation, this would imply that oxygen is also a deep impurity in our samples. This appears reasonable given that O may also form similar sp^2 bonds as B and N if it can donate an electron to a nearby acceptor. Future work should seek to combine variation of oxygen impurity and radiation damage to ascertain whether the defect is indeed an O-V complex.

The results might also allow for a direct identification of the defect, as the knowledge of optically active defects very close to the surface might allow for imaging with high-resolution tunneling electron microscopes. A full understanding of the defect nature is required for tuning and engineering specific properties that will ultimately lead to a wider applicability in various scenarios.

10.5 Methods

Plasma etching

The oxygen plasma was generated from a microwave field (PVA TePla). Prior to any experiments, the plasma chamber was cleaned for 5 min at 500 W to remove any contaminants. We found the optimal single layer etching conditions empirically at a plasma power of 102 W for 63 s at a pressure of 0.332 mbar and a gas flow rate of 300 cm^3/min (deviating from this by 10% decreases the success probability). All experiments were carried our at room temperature. The plasma time includes about $2-3$ s during which the plasma ignites and the gases are stabilized. The plasma field is highly anisotropic and varies across the plasma chamber. Thus, for repeatable results it is crucial to place the substrates always at

the same position in the chamber. Unless stated otherwise, this position is at the plasma field minimum. It should be mentioned that the optimal parameters reported here depend on the specific gas pump, plasma generator and geometry of the chamber, which requires to optimize these parameters on every other system individually.

Fabrication and optical characterization

Thin flakes of hBN were mechanically exfoliated from bulk crystal (used as received from HQGraphene) to a viscoelastic stamp (Gel-Pak WF-40-X4) using the tape method. Crystals with thicknesses down to $\sim 5\,\mathrm{nm}$ can be identified by optical contrast with a standard optical microscope and are subsequently transferred by dry contact to a Si substrate with a 262 nm thermally grown oxide layer. For the quantum emitters, we used crystals with thicknesses ranging from $\sim 5 - 100\,\mathrm{nm}$. The emitters were created during an oxygen plasma etching step at 200 W for 1 min in the plasma field maximum (at a pressure of 0.332 mbar and a gas flow rate of $300\,\mathrm{cm}^3/\mathrm{min}$). These are harsher plasma conditions than the layer-by-layer plasma etching, but ensures a higher defect density. Moreover, the defect density is linearly proportional to the plasma power[18]. After the plasma treatment, the samples are rapidly thermally annealed at 850°C in an Ar atmosphere at a gas flow rate of $500\,\mathrm{cm}^3/\mathrm{min}$. The electron irradiated emitters have been fabricated using a scanning electron microscope in an FEI Helios 600 NanoLab, where the electrons were accelerated using a high voltage of 10 kV. The samples were irradiated with a fluence of $f = 10^{18}\,\mathrm{cm}^{-2}$, which was calculated with $f = \frac{I \cdot t}{e \cdot A}$, where I is the electron current, t is the frame time, e is the electron charge, and A is the frame area. The irradiation took place at room temperature at a pressure $< 2.2\,\mathrm{mPa}$. After electron irradiation, the emitters were not thermally annealed[24]. For emitter localization, a custom-built μPL setup was used which utilized an ultrashort-pulsed 522 nm laser with a pulse length of 300 fs at a repetition rate of 20.8 MHz. The laser was focused to the diffraction limit with a Olympus $100\times/0.9$ dry objective and the samples were scanned using Newport translation stages with a spatial resolution up to $0.2\,\mu\mathrm{m}$. The emission was collected in-reflection for 1 s through the same objective and frequency-filtered using Semrock RazorEdge ultrasteep long-pass edge filters. The light is coupled via a grating to either a CCD or a single-photon avalanche diode (SPAD) from Micro Photon Devices allowing to extract the spectrum or the temporally and spectrally resolved photoluminescence. The correlation between excitation pulse and arrival time of the fluorescence photon is given by a PicoHarp 300. For measuring the second-order correlation function we utilize another diode laser at 512 nm and two SPADs.

Finite-difference time-domain simulations

The finite difference time-domain simulations were performed using Lumerical FDTD Solutions, a commercial grade simulator based on the FDTD method[53]. To calculate the Purcell enhancement and emitter dynamics, an in-plane dipole emitter at 560 nm was defined in the center within a slab of hBN, with a dielectric constant of 3.42 at 532 nm (this was obtained from experiments). The slab was thinned down from one direction (which is equivalent to moving the emitter to the surface) and the Purcell enhancement as well as the electric field mode profile was recorded for each crystal thickness. A dynamic mesh was chosen to capture all potential emitter dynamics. The simulations assume perfectly matched layer boundary conditions, which are reflectionless or absorbing boundaries, to account for the finite memory size.

Density functional theory calculations

The DFT calculations have been performed with QuantumATK with the Virtual NanoLab front end[54, 55]. QuantumATK utilizes numerical linear combination of atomic orbitals basis sets and the density matrix for closed or periodic systems is calculated by diagonalization of the Kohn-Sham Hamiltonian. Monolayer hBN crystals have been defined using a supercell containing two atoms and the geometry has been optimized using a $21 \times 21 \times 1$ Monkhorst-Pack reciprocal space grid. The optimization converged when all forces were below $0.001\,\mathrm{eV\,\AA^{-1}}$. The electron exchange-correlation was described with the Perdew-Burke-Ernzerhof (PBE) functional in the generalized gradient approximation[56]. For all atoms a double zeta polarized basis set was chosen and band structure was routed along high symmetry points. The ten- and 100-layer hBN crystals have been constructed in a similar way, with the lattice constant c also geometrically optimized and the k-sampling in this direction chosen such that it does not influence the simulation results.

Acknowledgments

This work was funded by the Australian Research Council (CE170100012, FL150100019, DE140100805, DP180103238, DE170100169). We thank the ACT Node of the Australian National Fabrication Facility for access to their nano- and microfabrication facilities. We also thank H. Tan for access to the TRPL system and C. Corr and F. Karouta for useful discussions about plasma processing.

Supplementary information

Electronic supplementary information (ESI) available. See DOI: 10.1039/C9NR04269E or Appendix A.5.

References

[1] J. L. O'Brien, A. Furusawa, and J. Vučković, *Photonic quantum technologies*, Nat. Photon., **3** 687–695, 2009.

[2] N. Gisin, G. Ribordy, W. Tittel, and H. Zbinden, *Quantum cryptography*, Rev. Mod. Phys., **74** 145–195, 2002.

[3] A. Aspuru-Guzik and P. Walther, *Photonic quantum simulators*, Nat. Phys., **8** 285–291, 2012.

[4] T. D. Ladd, F. Jelezko, R. Laflamme, Y. Nakamura, C. Monroe, and J. L. O'Brien, *Quantum computers*, Nature, **464** 45–53, 2010.

[5] P. Tonndorf, R. Schmidt, R. Schneider, J. Kern, M. Buscema, G. A. Steele, A. Castellanos-Gomez, H. S. J. van der Zant, S. M. de Vasconcellos, and R. Bratschitsch, *Single-photon emission from localized excitons in an atomically thin semiconductor*, Optica, **2** 347–352, 2015.

[6] A. Srivastava, M. Sidler, A. V. Allain, D. S. Lembke, A. Kis, and A. Imamoğlu, *Optically active quantum dots in monolayer WSe2*, Nat. Nanotechnol., **10** 491–496, 2015.

[7] M. Koperski, K. Nogajewski, A. Arora, V. Cherkez, P. Mallet, J.-Y. Veuillen, J. Marcus, P. Kossacki, and M. Potemski, *Single photon emitters in exfoliated WSe2 structures*, Nat. Nanotechnol., **10** 503–506, 2015.

[8] Y.-M. He, G. Clark, J. R. Schaibley, Y. He, M.-C. Chen, Y.-J. Wei, X. Ding, Q. Zhang, W. Yao, X. Xu, C.-Y. Lu, and J.-W. Pan, *Single quantum emitters in monolayer semiconductors*, Nat. Nanotechnol., **10** 497–502, 2015.

[9] C. Chakraborty, L. Kinnischtzke, K. M. Goodfellow, R. Beams, and A. N. Vamivakas, *Voltage-controlled quantum light from an atomically thin semiconductor*, Nat. Nanotechnol., **10** 507–511, 2015.

[10] C. Palacios-Berraquero, M. Barbone, D. M. Kara, X. Chen, I. Goykhman, D. Yoon, A. K. Ott, J. Beitner, K. Watanabe, T. Taniguchi, A. C. Ferrari, and M. Atatüre, *Atomically thin quantum light-emitting diodes*, Nat. Commun., **7** 12978, 2016.

[11] A. Branny, G. Wang, S. Kumar, C. Robert, B. Lassagne, X. Marie, B. D. Gerardot, and B. Urbaszek, *Discrete quantum dot like emitters in monolayer MoSe2: Spatial mapping, magneto-optics, and charge tuning*, Appl. Phys. Lett., **108** 142101, 2016.

[12] J. Klein, M. Lorke, M. Florian, F. Sigger, J. Wierzbowski, J. Cerne, K. Müller, T. Taniguchi, K. Watanabe, U. Wurstbauer, M. Kaniber, M. Knap, R. Schmidt, J. J. Finley, and A. W. Holleitner, *Atomistic defect states as quantum emitters in monolayer MoS_2*, arXiv:1901.01042, 2019.

[13] T. T. Tran, K. Bray, M. J. Ford, M. Toth, and I. Aharonovich, *Quantum emission from hexagonal boron nitride monolayers*, Nat. Nanotechnol., **11** 37–41, 2016.

[14] T. T. Tran, D. Wang, Z.-Q. Xu, A. Yang, M. Toth, T. W. Odom, and I. Aharonovich, *Deterministic Coupling of Quantum Emitters in 2D Materials to Plasmonic Nanocavity Arrays*, Nano Lett., **17** 2634–2639, 2017.

[15] T. Vogl, K. Sripathy, A. Sharma, P. Reddy, J. Sullivan, J. R. Machacek, L. Zhang, F. Karouta, B. C. Buchler, M. W. Doherty, Y. Lu, and P. K. Lam, *Radiation tolerance of two-dimensional material-based devices for space applications*, Nat. Commun., **10** 1202, 2019.

[16] A. Dietrich, M. Bürk, E. S. Steiger, L. Antoniuk, T. T. Tran, M. Nguyen, I. Aharonovich, F. Jelezko, and A. Kubanek, *Observation of Fourier transform limited lines in hexagonal boron nitride*, Phys. Rev. B, **98** 081414, 2018.

[17] M. Kianinia, B. Regan, S. A. Tawfik, T. T. Tran, M. J. Ford, I. Aharonovich, and M. Toth, *Robust Solid-State Quantum System Operating at 800 K*, ACS Photonics, **4** 768–773, 2017.

[18] T. Vogl, G. Campbell, B. C. Buchler, Y. Lu, and P. K. Lam, *Fabrication and Deterministic Transfer of High-Quality Quantum Emitters in Hexagonal Boron Nitride*, ACS Photonics, **5** 2305–2312, 2018.

[19] A. W. Schell, H. Takashima, T. T. Tran, I. Aharonovich, and S. Takeuchi, *Coupling Quantum Emitters in 2D Materials with Tapered Fibers*, ACS Photonics, **4** 761–767, 2017.

[20] T. Vogl, Y. Lu, and P. K. Lam, *Room temperature single photon source using fiber-integrated hexagonal boron nitride*, J. Phys. D: Appl. Phys., **50** 295101, 2017.

[21] N. Chejanovsky, M. Rezai, F. Paolucci, Y. Kim, T. Rendler, W. Rouabeh, F. Fávaro de Oliveira, P. Herlinger, A. Denisenko, S. Yang, I. Gerhardt, A. Finkler, J. H. Smet, and J. Wrachtrup, *Structural Attributes and Photodynamics of Visible Spectrum Quantum Emitters in Hexagonal Boron Nitride*, Nano Lett., **16** 7037–7045, 2016.

[22] Z.-Q. Xu, C. Elbadawi, T. T. Tran, M. Kianinia, X. Li, D. Liu, T. B. Hoffman, M. Nguyen, S. Kim, J. H. Edgar, X. Wu, L. Song, S. Ali, M. Ford, M. Toth, and I. Aharonovich, *Single photon emission from plasma treated 2D hexagonal boron nitride*, Nanoscale, **10** 7957–7965, 2018.

[23] S. Choi, T. T. Tran, C. Elbadawi, C. Lobo, X. Wang, S. Juodkazis, G. Seniutinas, M. Toth, and I. Aharonovich, *Engineering and Localization of Quantum Emitters in Large Hexagonal Boron Nitride Layers*, ACS Appl. Mater. Interfaces, **8** 29642–29648, 2016.

[24] H. Ngoc My Duong, M. A. P. Nguyen, M. Kianinia, T. Ohshima, H. Abe, K. Watanabe, T. Taniguchi, J. H. Edgar, I. Aharonovich, and M. Toth, *Effects of High-Energy Electron Irradiation on Quantum Emitters in Hexagonal Boron Nitride*, ACS Appl. Mater. Interfaces, **10** 24886–24891, 2018.

[25] N. V. Proscia, Z. Shotan, H. Jayakumar, P. Reddy, C. Cohen, M. Dollar, A. Alkauskas, M. Doherty, C. A. Meriles, and V. M. Menon, *Near-deterministic activation of room-temperature quantum emitters in hexagonal boron nitride*, Optica, **5** 1128–1134, 2018.

[26] S. A. Tawfik, S. Ali, M. Fronzi, M. Kianinia, T. T. Tran, C. Stampfl, I. Aharonovich, M. Toth, and M. J. Ford, *First-principles investigation of quantum emission from hBN defects*, Nanoscale, **9** 13575–13582, 2017.

[27] M. Abdi, J.-P. Chou, A. Gali, and M. B. Plenio, *Color Centers in Hexagonal Boron Nitride Monolayers: A Group Theory and Ab Initio Analysis*, ACS Photonics, **5** 1967–1976, 2018.

[28] A. Sajid, J. R. Reimers, and M. J. Ford, *Defect states in hexagonal boron nitride: Assignments of observed properties and prediction of properties relevant to quantum computation*, Phys. Rev. B, **97** 064101, 2018.

[29] J. R. Reimers, A. Sajid, R. Kobayashi, and M. J. Ford, *Understanding and Calibrating Density-Functional-Theory Calculations Describing the Energy and Spectroscopy of Defect Sites in Hexagonal Boron Nitride*, J. Chem. Theory Comput., **14** 1602–1613, 2018.

[30] G. I. López-Morales, N. V. Proscia, G. E. López, C. A. Meriles, and V. M. Menon, *Toward the Identification of Atomic Defects in Hexagonal Boron Nitride: X-Ray Photoelectron Spectroscopy and First-Principles Calculations*, arXiv:1811.05924, 2018.

[31] F. Hayee, L. Yu, J. L. Zhang, C. J. Ciccarino, M. Nguyen, A. F. Marshall, I. Aharonovich, J. Vučković, P. Narang, T. F. Heinz, and J. A. Dionne, *Correlated optical and electron microscopy reveal the role of multiple defect species and local strain on quantum emission*, arXiv:1901.05952, 2019.

[32] R. Bourrellier, S. Meuret, A. Tararan, O. Stéphan, M. Kociak, L. H. G. Tizei, and A. Zobelli, *Bright UV Single Photon Emission at Point Defects in h-BN*, Nano Lett., **16** 4317–4321, 2016.

[33] T. T. Tran, C. Elbadawi, D. Totonjian, C. J. Lobo, G. Grosso, H. Moon, D. R. Englund, M. J. Ford, I. Aharonovich, and M. Toth, *Robust Multicolor Single Photon Emission from Point Defects in Hexagonal Boron Nitride*, ACS Nano, **10** 7331–7338, 2016.

[34] Z. Shotan, H. Jayakumar, C. R. Considine, M. Mackoit, H. Fedder, J. Wrachtrup, A. Alkauskas, M. W. Doherty, V. M. Menon, and C. A. Meriles, *Photoinduced Modification of Single-Photon Emitters in Hexagonal Boron Nitride*, ACS Photonics, **3** 2490–2496, 2016.

[35] G. Grosso, H. Moon, B. Lienhard, S. Ali, D. K. Efetov, M. M. Furchi, P. Jarillo-Herrero, M. J. Ford, I. Aharonovich, and D. Englund, *Tunable and high-purity room temperature single-photon emission from atomic defects in hexagonal boron nitride*, Nat. Commun., **8** 705, 2017.

[36] I. H. Abidi, N. Mendelson, T. T. Tran, A. Tyagi, M. Zhuang, L.-T. Weng, B. Ozyilmaz, I. Aharonovich, M. Toth, and Z. Luo, *Selective Defect Formation in Hexagonal Boron Nitride*, arXiv:1902.07932, 2019.

[37] M. Kianinia, C. Bradac, B. Sontheimer, F. Wang, T. T. Tran, M. Nguyen, S. Kim, Z.-Q. Xu, D. Jin, A. W. Schell, C. J. Lobo, I. Aharonovich, and M. Toth, *All-optical control and super-resolution imaging of quantum emitters in layered materials*, Nat. Commun., **9** 874, 2018.

[38] H. Park, G. H. Shin, K. J. Lee, and S.-Y. Choi, *Atomic-scale etching of hexagonal boron nitride for device integration based on two-dimensional materials*, Nanoscale, **10** 15205–15212, 2018.

[39] R. V. Gorbachev, I. Riaz, R. R. Nair, R. Jalil, L. Britnell, B. D. Belle, E. W. Hill, K. S. Novoselov, K. Watanabe, T. Taniguchi, A. K. Geim, and P. Blake, *Hunting for Monolayer Boron Nitride: Optical and Raman Signatures*, Small, **7** 465–468, 2011.

[40] J. Yang, Z. Wang, F. Wang, R. Xu, J. Tao, S. Zhang, Q. Qin, B. Luther-Davies, C. Jagadisch, and Y. Lu, *Atomically thin optical lenses and gratings*, Light Sci. Appl., **5** e16046, 2002.

[41] L. H. Li and Y. Chen, *Atomically Thin Boron Nitride: Unique Properties and Applications*, Adv. Funct. Mater., **26** 2594–2608, 2016.

[42] J. Pei, X. Gai, J. Yang, X. Wang, Z. Yu, D.-Y. Choi, B. Luther-Davies, and Y. Lu, *Producing air-stable monolayers of phosphorene and their defect engineering*, Nat. Commun., **7** 10450, 2016.

[43] S. Xiao, P. Xiao, X. Zhang, D. Yan, X. Gu, F. Qin, Z. Ni, Z. J. Han, and K. K. Ostrikov, *Atomic-layer soft plasma etching of MoS_2*, Sci. Rep., **6** 19945, 2016.

[44] A. Beveratos, R. Brouri, T. Gacoin, J.-P. Poizat, and P. Grangier, *Nonclassical radiation from diamond nanocrystals*, Phys. Rev. A, **64** 061802, 2001.

[45] X. Li, G. D. Shepard, A. Cupo, N. Camporeale, K. Shayan, Y. Luo, V. Meunier, and S. Strauf, *Nonmagnetic Quantum Emitters in Boron Nitride with Ultranarrow and Sideband-Free Emission Spectra*, ACS Nano, **11** 6652-6660, 2017.

[46] J. F. Ziegler, M. Ziegler, and J. Biersack, *SRIM - The stopping and range of ions in matter*, Nucl. Instr. Meth. Phys. Res. B, **268** 1818–1823, 2010.

[47] B. Huang and H. Lee, *Defect and impurity properties of hexagonal boron nitride: A first-principles calculation*, Phys. Rev. B, **86** 245406, 2012.

[48] N. L. McDougall, J. G. Partridge, R. J. Nicholls, S. P. Russo, and D. G. McCulloch, *Influence of point defects on the near edge structure of hexagonal boron nitride*, Phys. Rev. B, **96** 144106, 2017.

[49] M. Toth and I. Aharonovich, *Single Photon Sources in Atomically Thin Materials*, Annu. Rev. Phys. Chem., **70** 123–142, 2019.

[50] A. Zobelli, C. P. Ewels, A. Gloter, and G. Seifert, *Vacancy migration in hexagonal boron nitride*, Phys. Rev. B, **75** 094104, 2007.

[51] S. K. Estreicher, D. J. Backlund, C. Carbogno, and M. Scheffler, *Activation Energies for Diffusion of Defects in Silicon: The Role of the Exchange-Correlation Functional*, Angew. Chem. Int. Ed., **50** 10221–10225, 2011.

[52] T. Vogl, R. Lecamwasam, B. C. Buchler, Y. Lu, and P. K. Lam, *Space-compatible cavity-enhanced single-photon generation with hexagonal boron nitride*, arXiv:1902.03019, 2019.

[53] Lumerical Solutions, Inc. https://www.lumerical.com/products/fdtd-solutions/.

[54] S. Smidstrup, D. Stradi, J. Wellendorff, P. A. Khomyakov, U. G. Vej-Hansen, M.-E. Lee, T. Ghosh, E. Jónsson, H. Jónsson, and K. Stokbro, *First-principles Green's-function method for surface calculations: A pseudopotential localized basis set approach*, Phys. Rev. B, **96** 195309, 2017.

[55] Synopsys QuantumATK. version 2016.3 with the Virtual NanoLab front end, https://www.synopsys.com/silicon/quantumatk.html.

[56] J. P. Perdew, K. Burke, and M. Ernzerhof, *Generalized Gradient Approximation Made Simple*, Phys. Rev. Lett., **77** 3865–3868, 1996.

Chapter 11

Conclusions

This thesis presented advances in developing optically active defects hosted by two-dimensional hexagonal boron nitride for quantum information processing. These defects act as an idealized two-level system that, after excitation with a laser, emit a single-photon as they relax to their initial ground state. A single-photon source is a crucial key building block for optical quantum technologies, including quantum cryptography and quantum computing.

Hexagonal boron nitride as a host material for these defects has the decisive advantage of a wide band gap, which isolates the deep defect states from the energy band edges, as well as prevents non-radiative decay of the excited state. The former allows for operation at room temperature, while the latter leads to an ultrahigh single-photon luminosity and quantum yield. In addition, the 2D lattice of hBN allows for an intrinsically ideal extraction efficiency of generated single-photons.

Among the milestones achieved in this thesis is a quantum emitter attached by van der Waals force to the core of a multimode fiber. This system achieved an overall collection efficiency of 10% and was able to generate free space and fiber-coupled single-photons solely depending on the excitation direction. The fabrication process was subsequently improved through plasma etching, achieving emission linewidths $\sim 1\,\mathrm{nm}$, $g^{(2)}(0) = 0.03$ and excited state lifetimes as short as 294 ps. Furthermore, the emitters were stable over the entire duration of the experiments, with no significant changes in photophysics observed. It was also possible to transfer these emitters to arbitrary new substrates, allowing for the fabrication of on-chip single-photon sources.

A highlight of this thesis is the space qualification of 2D materials and devices based on them, including the quantum emitters in hBN, as well as atomically thin field-effect transistors. This study proved that quantum emitters in hBN can be used in orbit on satellites for quantum key distribution schemes. Moreover, the transistors survived the harsh conditions of space without degradation in performance, suggesting robust suitability for space instrumentation and satellite electronics. This was also extended to a variety of monolayered 2D materials as building blocks for future electronics and optoelectronics. Interestingly, under excess γ-radiation, monolayer WS_2 showed decreased defect densities, identified by an increase in photoluminescence, carrier lifetime and a change in doping ratio proportional to the photon flux. The underlying mechanism is traced back to radiation-induced defect healing, wherein dissociated oxygen passivates sulfur vacancies. An application of this remarkable effect could be a radiation detector.

Another highlight is the implementation of the single-photon source on a satellite platform. Due to its low size, weight and power requirements, the source is predisposed for the use on satellites or other mobile applications where strict limitations apply. The complete single-photon source was implemented on a 1U CubeSat, a picoclass satellite with

a volume of $10 \times 10 \times 10\,\mathrm{cm}^3$ and a maximal payload weight of 1.33 kg. The source was fully self-contained and ready-to-operate with the excitation laser, all driving electronics and control units, including a singleboard computer onboard the CubeSat. Therefore, this makes the source among the smallest single-photon sources in the world.

Moreover, the single-photon emission process was enhanced by an optical resonator in the Purcell regime. This increased the spontaneous emission rate, spectral and single-photon purity as well as the quantum yield and collection efficiency. The performance so far allowed one to evaluate the source for quantum key distribution protocols, thereby outperforming the most efficient decoy protocols which are conventionally used in quantum cryptography on short and medium distances. Therefore, this work provides a path toward low-cost satellite-based long-distance quantum communication networks, the backbone of a future quantum internet. Finally, efforts have been made to locate the emitters with atomic precision, with the result that the positions, at which the defects form, correlate with the fabrication method. This in turn allows one to specifically engineer the emitters and optical properties influenced by the emitter location.

Whether the emitters are indeed useful for quantum key distribution applications has yet to be demonstrated. This is left to a future experiment. The figure of merit which the experiment has to be benchmarked against is the secret key rate, and only if the single-photon source yields a higher secret key rate, it will be interesting for QKD. The simulations of the QKD experiments so far used some approximations and neglected second-order effects, but it is still expected that the advantage over decoy state protocols at short and medium distances will prevail. Further improvements can also enhance the single-photon quality even more, thus extending the usable distance the single-photon source can be used for in QKD applications. It would also be advantageous to have an electrical excitation scheme, which would reduce the complexity of the single-photon source substantially. Due to the insulating nature of hBN, however, this is not straightforward to achieve.

Another application for a satellite-based single-photon source is a fundamental test of quantum mechanics. Such experiment would search for physics beyond the standard model that could be probed with quantum optics. Examples for such theories are higher-order interference and hyper-complex quantum mechanics, expanded with a coupling strength to a gravitational field. The required single-photon interferometer has already been developed during this PhD, but the experiments are still ongoing and will continue in the future.

To summarize the work in a final remark, this thesis lays a strong foundation for future applications of single-photon sources based on hexagonal boron nitride and two-dimensional materials for space instrumentation. This predominantly applies to quantum communication, with the developed single-photon source as one of the key building blocks in a global quantum network. Further improvements of the device performance will expand the range of applications, some of which still have to be discovered and explored.

Bibliography

[1] S. Haroche and J.-M. Raimond. *Exploring the Quantum*. Oxford University Press, Great Clarendon Street, Oxford OX2 6DP, United Kingdom, 2006.

[2] M. Planck, *Über eine Verbesserung der Wienschen Spektralgleichung*, Verh. Dtsch. Phys. Ges., **2** 202–204, 1900.

[3] M. Planck, *Zur Theorie des Gesetzes der Energieverteilung im Normalspectrum*, Verh. Dtsch. Phys. Ges., **2** 237–245, 1900.

[4] A. Einstein, *Über einen die Erzeugung und Verwandlung des Lichtes betreffenden heuristischen Gesichtspunkt*, Ann. Phys., **322** 132–148, 1905.

[5] N. Bohr, *On the constitution of atoms and molecules*, Philos. Mag., **26** 1–25, 1913.

[6] R. J. Glauber, *Photon Correlations*, Phys. Rev. Lett., **10** 84–86, 1963.

[7] R. J. Glauber, *The Quantum Theory of Optical Coherence*, Phys. Rev., **130** 2529–2539, 1963.

[8] R. J. Glauber, *Coherent and Incoherent States of the Radiation Field*, Phys. Rev., **131** 2766–2788, 1963.

[9] M. Fox. *Quantum Optics*. Oxford University Press, Great Clarendon Street, Oxford OX2 6DP, United Kingdom, 2006.

[10] S. Hollands and R. M. Wald, *Quantum fields in curved spacetime*, Phys. Rep., **574** 1–35, 2015.

[11] B. T. H. Varcoe, S. Brattke, M. Weidinger, and H. Walther, *Preparing pure photon number states of the radiation field*, Nature, **403** 743–746, 2000.

[12] S. Haroche, *Nobel Lecture: Controlling photons in a box and exploring the quantum to classical boundary*, Rev. Mod. Phys., **85** 1083–1102, 2013.

[13] P. W. H. Pinkse, T. Fischer, P. Maunz, and G. Rempe, *Trapping an atom with single photons*, Nature, **404** 365–368, 2000.

[14] K. M. Birnbaum, A. Boca, R. Miller, A. D. Boozer, T. E. Northup, and H. J. Kimble, *Photon blockade in an optical cavity with one trapped atom*, Nature, **436** 87–90, 2005.

[15] T. Wilk, S. C. Webster, A. Kuhn, and G. Rempe, *Single-Atom Single-Photon Quantum Interface*, Science, **317** 488–490, 2007.

[16] S. Ritter, C. Nölleke, C. Hahn, A. Reiserer, A. Neuzner, M. Uphoff, M. Mücke, E. Figueroa, J. Bochmann, and G. Rempe, *An elementary quantum network of single atoms in optical cavities*, Nature, **484** 195–200, 2012.

[17] J. Vučković and Y. Yamamoto, *Photonic crystal microcavities for cavity quantum electrodynamics with a single quantum dot*, Appl. Phys. Lett., **82** 2374–2376, 2003.

[18] A. Badolato, K. Hennessy, M. Atatüre, J. Dreiser, E. Hu, P. M. Petroff, and A. Imamoğlu, *Deterministic Coupling of Single Quantum Dots to Single Nanocavity Modes*, Science, **308** 1158–1161, 2005.

[19] K. Hennessy, A. Badolato, M. Winger, D. Gerace, M. Atatüre, S. Gulde, S. Fält, E. L. Hu, and A. Imamoğlu, *Quantum nature of a strongly coupled single quantum dot-cavity system*, Nature, **445** 896–899, 2007.

[20] A. Wallraff, D. I. Schuster, A. Blais, L. Frunzio, R.-S. Huang, J. Majer, S. Kumar, S. M. Girvin, and R. J. Schoelkopf, *Strong coupling of a single photon to a superconducting qubit using circuit quantum electrodynamics*, Nature, **431** 162–167, 2004.

[21] K. J. Vahala, *Optical microcavities*, Nature, **424** 839–846, 2003.

[22] P. Grünwald, *What $g^{(2)}(0) < 1/2$ tells you - and what it does not*, arXiv:1711.05897, 2017.

[23] N. Gisin and H. Bechmann-Pasquinucci, *Bell inequality, Bell states and maximally entangled states for n qubits*, Phys. Lett. A, **246** 1–6, 1998.

[24] A. Einstein, B. Podolsky, and N. Rosen, *Can Quantum-Mechanical Description of Physical Reality Be Considered Complete?*, Phys. Rev., **47** 777–780, 1935.

[25] B. Hensen, H. Bernien, A. E. Dréau, A. Reiserer, N. Kalb, M. S. Blok, J. Ruitenberg, R. F. L. Vermeulen, R. N. Schouten, C. Abellán, W. Amaya, V. Pruneri, M. W. Mitchell, M. Markham, D. J. Twitchen, D. Elkouss, S. Wehner, T. H. Taminiau, and R. Hanson, *Loophole-free Bell inequality violation using electron spins separated by 1.3 kilometres*, Nature, **526** 682–686, 2015.

[26] M. Giustina, M. A. M. Versteegh, S. Wengerowsky, J. Handsteiner, A. Hochrainer, K. Phelan, F. Steinlechner, J. Kofler, J.-A. Larsson, C. Abellán, W. Amaya, V. Pruneri, M. W. Mitchell, J. Beyer, T. Gerrits, A. E. Lita, L. K. Shalm, S. W. Nam, T. Scheidl, R. Ursin, B. Wittmann, and A. Zeilinger, *Significant-Loophole-Free Test of Bell's Theorem with Entangled Photons*, Phys. Rev. Lett., **115** 250401, 2015.

[27] L. K. Shalm, E. Meyer-Scott, B. G. Christensen, P. Bierhorst, M. A. Wayne, M. J. Stevens, T. Gerrits, S. Glancy, D. R. Hamel, M. S. Allman, K. J. Coakley, S. D. Dyer, C. Hodge, A. E. Lita, V. B. Verma, C. Lambrocco, E. Tortorici, A. L. Migdall, Y. Zhang, D. R. Kumor, W. H. Farr, F. Marsili, M. D. Shaw, J. A. Stern, C. Abellán, W. Amaya, V. Pruneri, T. Jennewein, M. W. Mitchell, P. G. Kwiat, J. C. Bienfang, R. P. Mirin, E. Knill, and S. W. Nam, *Strong Loophole-Free Test of Local Realism*, Phys. Rev. Lett., **115** 250402, 2015.

[28] W. Rosenfeld, D. Burchardt, R. Garthoff, K. Redeker, N. Ortegel, M. Rau, and H. Weinfurter, *Event-Ready Bell Test Using Entangled Atoms Simultaneously Closing Detection and Locality Loopholes*, Phys. Rev. Lett., **119** 010402, 2017.

[29] N. Gisin, G. Ribordy, W. Tittel, and H. Zbinden, *Quantum cryptography*, Rev. Mod. Phys., **74** 145–195, 2002.

[30] T. D. Ladd, F. Jelezko, R. Laflamme, Y. Nakamura, C. Monroe, and J. L. O'Brien, *Quantum computers*, Nature, **464** 45–53, 2010.

[31] C. H. Bennett and G. Brassard, *Quantum cryptography: Public key distribution and coin tossing*, Theor. Comput. Sci., **560** 7–11, 2014.

[32] H.-K. Lo, X. Ma, and K. Chen, *Decoy State Quantum Key Distribution*, Phys. Rev. Lett., **94** 230504, 2005.

[33] C. Kurtsiefer, P. Zarda, S. Mayer, and H. Weinfurter, *The breakdown flash of silicon avalanche photodiodes - back door for eavesdropper attacks?*, J. Mod. Opt., **48** 2039–2047, 2001.

[34] S. Sauge, L. Lydersen, A. Anisimov, J. Skaar, and V. Makarov, *Controlling an actively-quenched single photon detector with bright light*, Opt. Express, **19** 23590–23600, 2011.

[35] L. Lydersen, M. K. Akhlaghi, A. H. Majedi, J. Skaar, and V. Makarov, *Controlling a superconducting nanowire single-photon detector using tailored bright illumination*, New J. Phys., **13** 113042, 2011.

[36] L. Lydersen and J. Skaar, *Security of quantum key distribution with bit and basis dependent detector flaws*, Quant. Inf. Comp., **10** 60–76, 2010.

[37] M. Rau, T. Vogl, G. Corrielli, G. Vest, L. Fuchs, S. Nauerth, and H. Weinfurter, *Spatial Mode Side Channels in Free-Space QKD Implementations*, IEEE J. Sel. Top. Quantum Electron., **21** 187–191, 2015.

[38] A. K. Ekert, *Quantum cryptography based on Bell's theorem*, Phys. Rev. Lett., **67** 661–663, 1991.

[39] C. H. Bennett, G. Brassard, C. Crépeau, R. Jozsa, A. Peres, and W. K. Wootters, *Teleporting an unknown quantum state via dual classical and Einstein-Podolsky-Rosen channels*, Phys. Rev. Lett., **70** 1895–1899.

[40] C. H. Bennett and S. J. Wiesner, *Communication via one- and two-particle operators on Einstein-Podolsky-Rosen states*, Phys. Rev. Lett., **69** 2881–2884.

[41] M. Żukowski, A. Zeilinger, M. A. Horne, and A. K. Ekert, *"Event-ready-detectors" Bell experiment via entanglement swapping*, Phys. Rev. Lett., **71** 4287–4290, 1993.

[42] C. Gobby, Z. L. Yuan, and A. J. Shields, *Quantum key distribution over 122 km of standard telecom fiber*, Appl. Phys. Lett., **84** 3762–3764, 2004.

[43] T. Schmitt-Manderbach, H. Weier, M. Fürst, R. Ursin, F. Tiefenbacher, T. Scheidl, J. Perdigues, Z. Sodnik, C. Kurtsiefer, J. G. Rarity, A. Zeilinger, and H. Weinfurter, *Experimental Demonstration of Free-Space Decoy-State Quantum Key Distribution over 144 km*, Phys. Rev. Lett., **98** 010504.

[44] B. Korzh, C. C. W. Lim, R. Houlmann, N. Gisin, M. J. Li, D. Nolan, B. Sanguinetti, R. Thew, and H. Zbinden, *Provably secure and practical quantum key distribution over 307 km of optical fibre*, Nat. Photon., **9** 163–168, 2015.

[45] S.-K. Liao, W.-Q. Cai, W.-Y. Liu, L. Zhang, Y. Li, J.-G. Ren, J. Yin, Q. Shen, Y. Cao, Z.-P. Li, F.-Z. Li, X.-W. Chen, L.-H. Sun, J.-J. Jia, J.-C. Wu, X.-J. Jiang, J.-F. Wang, Y.-M. Huang, Q. Wang, Y.-L. Zhou, L. Deng, T. Xi, L. Ma, T. Hu, Q. Zhang, Y.-A. Chen, N.-L. Liu, X.-B. Wang, Z.-C. Zhu, C.-Y. Lu, R. Shu, C.-Z. Peng, J.-Y. Wang, and J.-W. Pan, *Satellite-to-ground quantum key distribution*, Nature, **549** 43–47, 2017.

[46] K. Mattle, H. Weinfurter, P. G. Kwiat, and A. Zeilinger, *Dense Coding in Experimental Quantum Communication*, Phys. Rev. Lett., **76** 4656–4659, 1996.

[47] D. Bouwmeester, J.-W. Pan, K. Mattle, M. Eibl, H. Weinfurter, and A. Zeilinger, *Experimental quantum teleportation*, Nature, **390** 575–579, 1997.

[48] J.-W. Pan, D. Bouwmeester, H. Weinfurter, and A. Zeilinger, *Experimental Entanglement Swapping: Entangling Photons That Never Interacted*, Phys. Rev. Lett., **80** 3891–3894, 1998.

[49] P. Kok, W. J. Munro, K. Nemoto, T. C. Ralph, J. P. Dowling, and G. J. Milburn, *Linear optical quantum computing with photonic qubits*, Rev. Mod. Phys., **79** 135–174, 2007.

[50] J. L. O'Brien, A. Furusawa, and J. Vučković, *Photonic quantum technologies*, Nat. Photon., **3** 687–695, 2009.

[51] D. Deutsch and R. Jozsa, *Rapid solution of problems by quantum computation*, Proc. Royal Soc. Lond. A, **439** 553–558, 1992.

[52] S. Gulde, M. Riebe, G. P. T. Lancaster, C. Becher, J. Eschner, H. Häffner, F. Schmidt-Kaler, I. L. Chuang, and R. Blatt, *Implementation of the Deutsch-Jozsa algorithm on an ion-trap quantum computer*, Nature, **421** 48–50, 2003.

[53] L. K. Grover, *A fast quantum mechanical algorithm for database search*, arXiv:quant-ph/9605043, 1996.

[54] P. Shor, *Polynomial-Time Algorithms for Prime Factorization and Discrete Logarithms on a Quantum Computer*, SIAM J. Comput., **26** 1484–1509, 1997.

[55] D. P. DiVincenzo, *The Physical Implementation of Quantum Computation*, Fortschr. Phys., **48** 771–783, 2000.

[56] H. Häffner, C. Roos, and R. Blatt, *Quantum computing with trapped ions*, Phys. Rep., **469** 155–203, 2008.

[57] B. E. Kane, *A silicon-based nuclear spin quantum computer*, Nature, **393** 133–137, 1998.

[58] M. H. Devoret and R. J. Schoelkopf, *Superconducting Circuits for Quantum Information: An Outlook*, Science, **339** 1169–1174, 2013.

[59] S. Welte, B. Hacker, S. Daiss, S. Ritter, and G. Rempe, *Photon-Mediated Quantum Gate between Two Neutral Atoms in an Optical Cavity*, Phys. Rev. X, **8** 011018, 2018.

[60] P. Kok, W. J. Munro, K. Nemoto, T. C. Ralph, J. P. Dowling, and G. J. Milburn, *Linear optical quantum computing with photonic qubits*, Rev. Mod. Phys., **79** 135–174, 2007.

[61] R. Raussendorf and H. J. Briegel, *A One-Way Quantum Computer*, Phys. Rev. Lett., **86** 5188–5191, 2001.

[62] P. Walther, K. J. Resch, T. Rudolph, E. Schenck, H. Weinfurter, V. Vedral, M. Aspelmeyer, and A. Zeilinger, *Experimental one-way quantum computing*, Nature, **434** 169–176, 2005.

[63] S. Hunklinger. *Festkörperphysik*. De Gruyter Oldenburg, Genthiner Strasse 13, 10785 Berlin, Germany, 2014.

[64] C. Zhang, C. Gong, Y. Nie, K.-A. Min, C. Liang, Y. J. Oh, H. Zhang, W. Wang, S. Hong, L. Colombo, R. M. Wallace, and K. Cho, *Systematic study of electronic structure and band alignment of monolayer transition metal dichalcogenides in Van der Waals heterostructures*, 2D Mater., **4** 015026, 2016.

[65] G. D. Watkins, *Intrinsic defects in silicon*, Mater. Sci. Semicond. Process., **3** 227–235, 2000.

[66] T. Vogl, K. Sripathy, A. Sharma, P. Reddy, J. Sullivan, J. R. Machacek, L. Zhang, F. Karouta, B. C. Buchler, M. W. Doherty, Y. Lu, and P. K. Lam, *Radiation tolerance of two-dimensional material-based devices for space applications*, Nat. Commun., **10** 1202, 2019.

[67] K. S. Novoselov, A. K. Geim, S. V. Morozov, D. Jiang, Y. Zhang, S. V. Dubonos, I. V. Grigorieva, and A. A. Firsov, *Electric Field Effect in Atomically Thin Carbon Films*, Science, **306** 666–669, 2004.

[68] S. Das, J. A. Robinson, M. Dubey, H. Terrones, and M. Terrones, *Beyond Graphene: Progress in Novel Two-Dimensional Materials and van der Waals Solids*, Annu. Rev. Mater. Res., **45** 1–27, 2015.

[69] K. S. Novoselov, A. Mishchenko, A. Carvalho, and A. H. Castro Neto, *2D materials and van der Waals heterostructures*, Science, **353** aac943, 2016.

[70] M. G. Stanford, P. D. Rack, and D. Jariwala, *Emerging nanofabrication and quantum confinement techniques for 2D materials beyond graphene*, npj 2D Mater. Appl., **2** 20, 2018.

[71] S. V. Morozov, K. S. Novoselov, M. I. Katsnelson, F. Schedin, D. C. Elias, J. A. Jaszczak, and A. K. Geim, *Giant Intrinsic Carrier Mobilities in Graphene and Its Bilayer*, Phys. Rev. Lett., **100** 016602, 2008.

[72] K. S. Novoselov, A. K. Geim, S. V. Morozov, D. Jiang, M. I. Katsnelson, I. V. Grigorieva, S. V. Dubonos, and A. A. Firsov, *Two-dimensional gas of massless Dirac fermions in graphene*, Nature, **438** 197–200, 2005.

[73] A. A. Balandin, S. Ghosh, W. Bao, I. Calizo, D. Teweldebrhan, F. Miao, and C. N. Lau, *Superior Thermal Conductivity of Single-Layer Graphene*, Nano Lett., **8** 902–907, 2008.

[74] A. B. Kuzmenko, E. van Heumen, F. Carbone, and D. van der Marel, *Universal Optical Conductance of Graphite*, Phys. Rev. Lett., **100** 117401, 2008.

[75] S. J. Heerema and C. Dekker, *Graphene nanodevices for DNA sequencing*, Nat. Nanotechnol., **11** 127–136, 2016.

[76] C. Lee, X. Wei, J. W. Kysar, and J. Hone, *Measurement of the Elastic Properties and Intrinsic Strength of Monolayer Graphene*, Science, **321** 385–388, 2008.

[77] K. S. Novoselov, Z. Jiang, Y. Zhang, S. V. Morozov, H. L. Stormer, U. Zeitler, J. C. Maan, G. S. Boebinger, P. Kim, and A. K. Geim, *Room-Temperature Quantum Hall Effect in Graphene*, Science, **315** 1379–1379, 2007.

[78] Y. Zhang, T.-T. Tang, C. Girit, Z. Hao, M. C. Martin, A. Zettl, M. F. Crommie, Y. R. Shen, and F. Wang, *Direct observation of a widely tunable bandgap in bilayer graphene*, Nature, **459** 820–823, 2009.

[79] M. Dvorak, W. Oswald, and Z. Wu, *Bandgap Opening by Patterning Graphene*, Sci. Rep., **3** 2289, 2013.

[80] B. Radisavljevic, A. Radenovic, J. Brivio, V. Giacometti, and A. Kis, *Single-layer MoS_2 transistors*, Nat. Nanotechnol., **6** 147–150, 2011.

[81] H. Zeng, J. Dai, W. Yao, D. Xiao, and X. Cui, *Valley polarization in MoS_2 monolayers by optical pumping*, Nat. Nanotechnol., **7** 490–493, 2012.

[82] K. F. Mak, C. Lee, J. Hone, J. Shan, and T. F. Heinz, *Atomically Thin* MoS_2*: A New Direct-Gap Semiconductor*, Phys. Rev. Lett., **105** 136805, 2010.

[83] A. Splendiani, L. Sun, Y. Zhang, T. Li, J. Kim, C.-Y. Chim, G. Galli, and F. Wang, *Emerging Photoluminescence in Monolayer MoS_2*, Nano Lett., **10** 1271–1275, 2010.

[84] W. Zhao, Z. Ghorannevis, L. Chu, M. Toh, C. Kloc, P.-H. Tan, and G. Eda, *Evolution of Electronic Structure in Atomically Thin Sheets of WS_2 and WSe_2*, ACS Nano, **7** 791–797, 2013.

[85] N. Peimyoo, J. Shang, C. Cong, X. Shen, X. Wu, E. K. L. Yeow, and T. Yu, *Nonblinking, Intense Two-Dimensional Light Emitter: Monolayer WS_2 Triangles*, ACS Nano, **7** 10985–10994, 2013.

[86] S. Wu, S. Buckley, J. R. Schaibley, L. Feng, J. Yan, D. G. Mandrus, F. Hatami, W. Yao, J. Vučković, A. Majumdar, and X. Xu, *Monolayer semiconductor nanocavity lasers with ultralow thresholds*, Nature, **520** 69–72, 2015.

[87] K. F. Mak, K. He, C. Lee, G. H. Lee, J. Hone, T. F. Heinz, and J. Shan, *Tightly bound trions in monolayer MoS_2*, Nat. Mater., **12** 207–211, 2012.

[88] Y. You, X.-X. Zhang, T. C. Berkelbach, M. S. Hybertsen, D. R. Reichman, and T. F. Heinz, *Observation of biexcitons in monolayer WSe_2*, Nat. Phys., **11** 477–488, 2015.

[89] M. Barbone, A. R.-P. Montblanch, D. M. Kara, C. Palacios-Berraquero, A. R. Cadore, D. De Fazio, B. Pingault, E. Mostaani, H. Li, B. Chen, K. Watanabe, T. Taniguchi, S. Tongay, G. Wang, A. C. Ferrari, and M. Atatüre, *Charge-tuneable biexciton complexes in monolayer WSe_2*, Nat. Commun., **9** 3721, 2018.

[90] X. Liu, T. Galfsky, Z. Sun, F. Xia, E.-c. Lin, Y.-H. Lee, S. Kéna-Cohen, and V. M. Menon, *Strong light-matter coupling in two-dimensional atomic crystals*, Nat. Photon., **9** 30–34, 2014.

[91] N. Lundt, S. Klembt, E. Cherotchenko, S. Betzold, O. Iff, A. V. Nalitov, M. Klaas, C. P. Dietrich, A. V. Kavokin, S. Höfling, and C. Schneider, *Room-temperature Tamm-plasmon exciton-polaritons with a WSe_2 monolayer*, Nat. Commun., **7** 13328, 2016.

[92] S. Bertolazzi, J. Brivio, and A. Kis, *Stretching and Breaking of Ultrathin MoS_2*, ACS Nano, **5** 9703–9709, 2011.

[93] L. H. Li and Y. Chen, *Atomically Thin Boron Nitride: Unique Properties and Applications*, Adv. Funct. Mater., **26** 2594–2608, 2016.

[94] G. Cassabois, P. Valvin, and B.Gil, *Hexagonal boron nitride is an indirect bandgap semiconductor*, Nat. Photon., **10** 262–266, 2016.

[95] Y. Lin and J. W. Connell, *Advances in 2D boron nitride nanostructures: nanosheets, nanoribbons, nanomeshes, and hybrids with graphene*, Nanoscale, **4** 6908–6939, 2012.

[96] D. Alcaraz Iranzo, S. Nanot, E. J. C. Dias, I. Epstein, C. Peng, D. K. Efetov, M. B. Lundeberg, R. Parret, J. Osmond, J.-Y. Hong, J. Kong, D. R. Englund, N. M. R. Peres, and F. H. L. Koppens, *Probing the ultimate plasmon confinement limits with a van der Waals heterostructure*, Science, **360** 291–295, 2018.

[97] F. Cadiz, E. Courtade, C. Robert, G. Wang, Y. Shen, H. Cai, T. Taniguchi, K. Watanabe, H. Carrere, D. Lagarde, M. Manca, T. Amand, P. Renucci, S. Tongay, X. Marie, and B. Urbaszek, *Excitonic Linewidth Approaching the Homogeneous Limit in MoS_2-Based van der Waals Heterostructures*, Phys. Rev. X, **7** 021026, 2017.

[98] G.-H. Lee, X. Cui, Y. D. Kim, G. Arefe, X. Zhang, C.-H. Lee, F. Ye, K. Watanabe, T. Taniguchi, P. Kim, and J. Hone, *Highly Stable, Dual-Gated MoS_2 Transistors Encapsulated by Hexagonal Boron Nitride with Gate-Controllable Contact, Resistance, and Threshold Voltage*, ACS Nano, **9** 7019–7026, 2015.

[99] I. Jo, M. T. Pettes, J. Kim, K. Watanabe, T. Taniguchi, Z. Yao, and L. Shi, *Thermal Conductivity and Phonon Transport in Suspended Few-Layer Hexagonal Boron Nitride*, Nano Lett., **13** 550–554, 2013.

[100] T. T. Tran, K. Bray, M. J. Ford, M. Toth, and I. Aharonovich, *Quantum emission from hexagonal boron nitride monolayers*, Nat. Nanotechnol., **11** 37–41, 2016.

[101] P. Tonndorf, R. Schmidt, R. Schneider, J. Kern, M. Buscema, G. A. Steele, A. Castellanos-Gomez, H. S. J. van der Zant, S. M. de Vasconcellos, and R. Bratschitsch, *Single-photon emission from localized excitons in an atomically thin semiconductor*, Optica, **2** 347–352, 2015.

[102] A. Srivastava, M. Sidler, A. V. Allain, D. S. Lembke, A. Kis, and A. Imamoğlu, *Optically active quantum dots in monolayer WSe_2*, Nat. Nanotechnol., **10** 491–496, 2015.

[103] M. Koperski, K. Nogajewski, A. Arora, V. Cherkez, P. Mallet, J.-Y. Veuillen, J. Marcus, P. Kossacki, and M. Potemski, *Single photon emitters in exfoliated WSe_2 structures*, Nat. Nanotechnol., **10** 503–506, 2015.

[104] Y.-M. He, G. Clark, J. R. Schaibley, Y. He, M.-C. Chen, Y.-J. Wei, X. Ding, Q. Zhang, W. Yao, X. Xu, C.-Y. Lu, and J.-W. Pan, *Single quantum emitters in monolayer semiconductors*, Nat. Nanotechnol., **10** 497–502, 2015.

[105] C. Chakraborty, L. Kinnischtzke, K. M. Goodfellow, R. Beams, and A. N. Vamivakas, *Voltage-controlled quantum light from an atomically thin semiconductor*, Nat. Nanotechnol., **10** 507–511, 2015.

[106] R. V. Gorbachev, I. Riaz, R. R. Nair, R. Jalil, L. Britnell, B. D. Belle, E. W. Hill, K. S. Novoselov, K. Watanabe, T. Taniguchi, A. K. Geim, and P. Blake, *Hunting for Monolayer Boron Nitride: Optical and Raman Signatures*, Small, **7** 465–468, 2011.

[107] S. Haastrup, M. Strange, M. Pandey, T. Deilmann, P. S. Schmidt, N. F. Hinsche, M. N. Gjerding, D. Torelli, P. M. Larsen, A. C. Riis-Jensen, J. Gath, K. W. Jacobsen, J. J. Mortensen, T. Olsen, and K. S. Thygesen, *The Computational 2D Materials Database: high-throughput modeling and discovery of atomically thin crystals*, 2D Mater., **5** 042002, 2018.

[108] J. Hong, Z. Hu, M. Probert, K. Li, D. Lv, X. Yang, L. Gu, N. Mao, Q. Feng, L. Xie, J. Zhang, D. Wu, Z. Zhang, C. Jin, W. Ji, X. Zhang, J. Yuan, and Z. Zhang, *Exploring atomic defects in molybdenum disulphide monolayers*, Nat. Commun., **6** 6293, 2015.

[109] J. Shim, S.-H. Bae, W. Kong, D. Lee, K. Qiao, D. Nezich, Y. J. Park, R. Zhao, S. Sundaram, X. Li, H. Yeon, C. Choi, H. Kum, R. Yue, G. Zhou, Y. Ou, K. Lee, J. Moodera, X. Zhao, J.-H. Ahn, C. Hinkle, A. Ougazzaden, and J. Kim, *Controlled crack propagation for atomic precision handling of wafer-scale two-dimensional materials*, Science, **362** 665–670, 2018.

[110] S. Xiao, P. Xiao, X. Zhang, D. Yan, X. Gu, F. Qin, Z. Ni, Z. J. Han, and K. Ostrikov, *Atomic-layer soft plasma etching of MoS_2*, Sci. Rep., **6** 19945, 2016.

[111] J. Pei, X. Gai, J. Yang, X. Wang, Z. Yu, D.-Y. Choi, B. Luther-Davies, and Y. Lu, *Producing air-stable monolayers of phosphorene and their defect engineering*, Nat. Commun., **7** 10450, 2016.

[112] Y.-M. He, Y. He, Y.-J. Wei, D. Wu, M. Atatüre, C. Schneider, S. Höfling, M. Kamp, C.-Y. Lu, and J.-W. Pan, *On-demand semiconductor single-photon source with near-unity indistinguishability*, Nat. Nanotechnol., **8** 213–217, 2013.

[113] A. Kiraz, M. Atatüre, and A. Imamoğlu, *Quantum-dot single-photon sources: Prospects for applications in linear optics quantum-information processing*, Phys. Rev. A, **69** 032305, 2004.

[114] P. Senellart, G. Solomon, and A. White, *High-performance semiconductor quantum-dot single-photon sources*, Nat. Nanotechnol., **12** 1026–1039, 2017.

[115] H. G. Barros, A. Stute, T. E. Northup, C. Russo, P. O. Schmidt, and R. Blatt, *Deterministic single-photon source from a single ion*, New J. of Phys., **11** 103004, 2009.

[116] I. Aharonovich, D. Englund, and M. Toth, *Solid-state single-photon emitters*, Nat. Photon., **10** 631–641, 2016.

[117] M. Bock, A. Lenhard, C. Chunnilall, and C. Becher, *Highly efficient heralded single-photon source for telecom wavelengths based on a PPLN waveguide*, Opt. Express, **24** 23992–24001, 2016.

[118] M. Gould, E. R. Schmidgall, S. Dadgostar, F. Hatami, and K.-M. C. Fu, *Efficient Extraction of Zero-Phonon-Line Photons from Single Nitrogen-Vacancy Centers in an Integrated GaP-on-Diamond Platform*, Phys. Rev. Appl, **6** 011001, 2016.

[119] M. Toth and I. Aharonovich, *Single Photon Sources in Atomically Thin Materials*, Annu. Rev. Phys. Chem., **70** 123–142, 2019.

[120] C. Palacios-Berraquero, M. Barbone, D. M. Kara, X. Chen, I. Goykhman, D. Yoon, A. K. Ott, J. Beitner, K. Watanabe, T. Taniguchi, A. C. Ferrari, and M. Atatüre, *Atomically thin quantum light-emitting diodes*, Nat. Commun., **7** 12978, 2016.

[121] C. Palacios-Berraquero, D. M. Kara, A. R.-P. Montblanch, M. Barbone, P. Latawiec, D. Yoon, A. K. Ott, M. Loncar, A. C. Ferrari, and M. Atatüre, *Large-scale quantum-emitter arrays in atomically thin semiconductors*, Nat. Commun., **8** 15093, 2017.

[122] A. Branny, G. Wang, S. Kumar, C. Robert, B. Lassagne, X. Marie, B. D. Gerardot, and B. Urbaszek, *Discrete quantum dot like emitters in monolayer $MoSe_2$: Spatial mapping, magneto-optics, and charge tuning*, Appl. Phys. Lett., **108** 142101, 2016.

[123] C. Chakraborty, K. M. Goodfellow, and A. N. Vamivakas, *Localized emission from defects in $MoSe_2$ layers*, Opt. Mater. Express, **6** 2081–2087, 2016.

[124] J. Klein, M. Lorke, M. Florian, F. Sigger, J. Wierzbowski, J. Cerne, K. Müller, T. Taniguchi, K. Watanabe, U. Wurstbauer, M. Kaniber, M. Knap, R. Schmidt, J. J. Finley, and A. W. Holleitner, *Atomistic defect states as quantum emitters in monolayer MoS_2*, arXiv:1901.01042, 2019.

[125] A. Branny, S. Kumar, R. Proux, and B. D. Gerardot, *Deterministic strain-induced arrays of quantum emitters in a two-dimensional semiconductor*, Nat. Commun., **8** 15053, 2017.

[126] L. C. Flatten, L. Weng, A. Branny, S. Johnson, P. R. Dolan, A. A. P. Trichet, B. D. Gerardot, and J. M. Smith, *Microcavity enhanced single photon emission from two-dimensional WSe_2*, Appl. Phys. Lett., **112** 191105, 2018.

[127] O. Iff, N. Lundt, S. Betzold, L. N. Tripathi, M. Emmerling, S. Tongay, Y. J. Lee, S.-H. Kwon, S. Höfling, and C. Schneider, *Deterministic coupling of quantum emitters in WSe_2 monolayers to plasmonic nanocavities*, Opt. Express, **26** 25944–25951, 2018.

[128] Y. Luo, G. D. Shepard, J. V. Ardelean, D. A. Rhodes, B. Kim, K. Barmak, J. C. Hone, and S. Strauf, *Deterministic coupling of site-controlled quantum emitters in monolayer WSe_2 to plasmonic nanocavities*, Nat. Nanotechnol., **13** 1137–1142, 2018.

[129] A. L. Exarhos, D. A. Hopper, R. R. Grote, A. Alkauskas, and L. C. Bassett, *Optical Signatures of Quantum Emitters in Suspended Hexagonal Boron Nitride*, ACS Nano, **11** 3328–3336, 2017.

[130] N. Chejanovsky, M. Rezai, F. Paolucci, Y. Kim, T. Rendler, W. Rouabeh, F. Fávaro de Oliveira, P. Herlinger, A. Denisenko, S. Yang, I. Gerhardt, A. Finkler, J. H. Smet, and J. Wrachtrup, *Structural Attributes and Photodynamics of Visible Spectrum Quantum Emitters in Hexagonal Boron Nitride*, Nano Lett., **16** 7037–7045, 2016.

[131] T. Vogl, G. Campbell, B. C. Buchler, Y. Lu, and P. K. Lam, *Fabrication and Deterministic Transfer of High-Quality Quantum Emitters in Hexagonal Boron Nitride*, ACS Photonics, **5** 2305–2312, 2018.

[132] Z.-Q. Xu, C. Elbadawi, T. T. Tran, M. Kianinia, X. Li, D. Liu, T. B. Hoffman, M. Nguyen, S. Kim, J. H. Edgar, X. Wu, L. Song, S. Ali, M. Ford, M. Toth, and I. Aharonovich, *Single photon emission from plasma treated 2D hexagonal boron nitride*, Nanoscale, **10** 7957–7965, 2018.

[133] S. Hou, M. D. Birowosuto, S. Umar, M. A. Anicet, R. Y. Tay, P. Coquet, B. K. Tay, H. Wang, and E. H. T. Teo, *Localized emission from laser-irradiated defects in 2D hexagonal boron nitride*, 2D Mater., **5** 015010, 2017.

[134] S. Choi, T. T. Tran, C. Elbadawi, C. Lobo, X. Wang, S. Juodkazis, G. Seniutinas, M. Toth, and I. Aharonovich, *Engineering and Localization of Quantum Emitters in Large Hexagonal Boron Nitride Layers*, ACS Appl. Mater. Interfaces, **8** 29642–29648, 2016.

[135] H. Ngoc My Duong, M. A. P. Nguyen, M. Kianinia, T. Ohshima, H. Abe, K. Watanabe, T. Taniguchi, J. H. Edgar, I. Aharonovich, and M. Toth, *Effects of High-Energy Electron Irradiation on Quantum Emitters in Hexagonal Boron Nitride*, ACS Appl. Mater. Interfaces, **10** 24886–24891, 2018.

[136] N. V. Proscia, Z. Shotan, H. Jayakumar, P. Reddy, C. Cohen, M. Dollar, A. Alkauskas, M. Doherty, C. A. Meriles, and V. M. Menon, *Near-deterministic activation of room-temperature quantum emitters in hexagonal boron nitride*, Optica, **5** 1128–1134, 2018.

[137] T. T. Tran, C. Elbadawi, D. Totonjian, C. J. Lobo, G. Grosso, H. Moon, D. R. Englund, M. J. Ford, I. Aharonovich, and M. Toth, *Robust Multicolor Single Photon Emission from Point Defects in Hexagonal Boron Nitride*, ACS Nano, **10** 7331–7338, 2016.

[138] A. Zobelli, C. P. Ewels, A. Gloter, and G. Seifert, *Vacancy migration in hexagonal boron nitride*, Phys. Rev. B, **75** 094104, 2007.

[139] R. Bourrellier, S. Meuret, A. Tararan, O. Stéphan, M. Kociak, L. H. G. Tizei, and A. Zobelli, *Bright UV Single Photon Emission at Point Defects in h-BN*, Nano Lett., **16** 4317–4321, 2016.

[140] A. Dietrich, M. Bürk, E. S. Steiger, L. Antoniuk, T. T. Tran, M. Nguyen, I. Aharonovich, F. Jelezko, and A. Kubanek, *Observation of Fourier transform limited lines in hexagonal boron nitride*, Phys. Rev. B, **98** 081414, 2018.

[141] Z. Shotan, H. Jayakumar, C. R. Considine, M. Mackoit, H. Fedder, J. Wrachtrup, A. Alkauskas, M. W. Doherty, V. M. Menon, and C. A. Meriles, *Photoinduced Modification of Single-Photon Emitters in Hexagonal Boron Nitride*, ACS Photonics, **3** 2490–2496, 2016.

[142] A. W. Schell, H. Takashima, T. T. Tran, I. Aharonovich, and S. Takeuchi, *Coupling Quantum Emitters in 2D Materials with Tapered Fibers*, ACS Photonics, **4** 761–767, 2017.

[143] N. Mendelson, Z.-Q. Xu, T. T. Tran, M. Kianinia, J. Scott, C. Bradac, I. Aharonovich, and M. Toth, *Engineering and Tuning of Quantum Emitters in Few-Layer Hexagonal Boron Nitride*, ACS Nano, **13** 3132–3140, 2019.

[144] I. H. Abidi, N. Mendelson, T. T. Tran, A. Tyagi, M. Zhuang, L.-T. Weng, B. Özyilmaz, I. Aharonovich, M. Toth, and Z. Luo, *Selective Defect Formation in Hexagonal Boron Nitride*, arXiv:1902.07932, 2019.

[145] M. Kianinia, B. Regan, S. A. Tawfik, T. T. Tran, M. J. Ford, I. Aharonovich, and M. Toth, *Robust Solid-State Quantum System Operating at 800 K*, ACS Photonics, **4** 768–773, 2017.

[146] M. Kianinia, C. Bradac, B. Sontheimer, F. Wang, T. T. Tran, M. Nguyen, S. Kim, Z.-Q. Xu, D. Jin, A. W. Schell, C. J. Lobo, I. Aharonovich, and M. Toth, *All-optical control and super-resolution imaging of quantum emitters in layered materials*, Nat. Commun., **9** 874, 2018.

[147] X. Li, G. D. Shepard, A. Cupo, N. Camporeale, K. Shayan, Y. Luo, V. Meunier, and S. Strauf, *Nonmagnetic Quantum Emitters in Boron Nitride with Ultranarrow and Sideband-Free Emission Spectra*, ACS Nano, **11** 6652–6660, 2017.

[148] G. Grosso, H. Moon, B. Lienhard, S. Ali, D. K. Efetov, M. M. Furchi, P. Jarillo-Herrero, M. J. Ford, I. Aharonovich, and D. Englund, *Tunable and high-purity room temperature single-photon emission from atomic defects in hexagonal boron nitride*, Nat. Commun., **8** 705, 2017.

[149] G. Noh, D. Choi, J.-H. Kim, D.-G. Im, Y.-H. Kim, H. Seo, and J. Lee, *Stark Tuning of Single-Photon Emitters in Hexagonal Boron Nitride*, Nano Lett., **18** 4710–4715, 2018.

[150] P. Tamarat, T. Gaebel, J. R. Rabeau, M. Khan, A. D. Greentree, H. Wilson, L. C. L. Hollenberg, S. Prawer, P. Hemmer, F. Jelezko, and J. Wrachtrup, *Stark Shift Control of Single Optical Centers in Diamond*, Phys. Rev. Lett., **97** 083002, 2006.

[151] Y. Xue, H. Wang, Q. Tan, J. Zhang, T. Yu, K. Ding, D. Jiang, X. Dou, J.-j. Shi, and B.-q. Sun, *Anomalous Pressure Characteristics of Defects in Hexagonal Boron Nitride Flakes*, ACS Nano, **12** 7127–7133, 2018.

[152] F. Hayee, L. Yu, J. L. Zhang, C. J. Ciccarino, M. Nguyen, A. F. Marshall, I. Aharonovich, J. Vučković, P. Narang, T. F. Heinz, and J. A. Dionne, *Correlated optical and electron microscopy reveal the role of multiple defect species and local strain on quantum emission*, arXiv:1901.05952, 2019.

[153] S. A. Tawfik, S. Ali, M. Fronzi, M. Kianinia, T. T. Tran, C. Stampfl, I. Aharonovich, M. Toth, and M. J. Ford, *First-principles investigation of quantum emission from hBN defects*, Nanoscale, **9** 13575–13582, 2017.

[154] M. Abdi, J.-P. Chou, A. Gali, and M. B. Plenio, *Color Centers in Hexagonal Boron Nitride Monolayers: A Group Theory and Ab Initio Analysis*, ACS Photonics, **5** 1967–1976, 2018.

[155] A. Sajid, J. R. Reimers, and M. J. Ford, *Defect states in hexagonal boron nitride: Assignments of observed properties and prediction of properties relevant to quantum computation*, Phys. Rev. B, **97** 064101, 2018.

[156] J. R. Reimers, A. Sajid, R. Kobayashi, and M. J. Ford, *Understanding and Calibrating Density-Functional-Theory Calculations Describing the Energy and Spectroscopy of Defect Sites in Hexagonal Boron Nitride*, J. Chem. Theory Comput., **14** 1602–1613, 2018.

[157] G. I. López-Morales, N. V. Proscia, G. E. López, C. A. Meriles, and V. M. Menon, *Toward the Identification of Atomic Defects in Hexagonal Boron Nitride: X-Ray Photoelectron Spectroscopy and First-Principles Calculations*, arXiv:1811.05924, 2018.

[158] T. Vogl, M. W. Doherty, B. C. Buchler, Y. Lu, and P. K. Lam, *Atomic localization of quantum emitters in multilayer hexagonal boron nitride*, Nanoscale, **11** 14362-14371, 2019.

[159] H. Kaupp, C. Deutsch, H.-C. Chang, J. Reichel, T. W. Hänsch, and D. Hunger, *Scaling laws of the cavity enhancement for nitrogen-vacancy centers in diamond*, Phys. Rev. A, **88** 053812, 2013.

[160] T. T. Tran, D. Wang, Z.-Q. Xu, A. Yang, M. Toth, T. W. Odom, and I. Aharonovich, *Deterministic Coupling of Quantum Emitters in 2D Materials to Plasmonic Nanocavity Arrays*, Nano Lett., **17** 2634–2639, 2017.

[161] S. Kim, J. E. Fröch, J. Christian, M. Straw, J. Bishop, D. Totonjian, K. Watanabe, T. Taniguchi, M. Toth, and I. Aharonovich, *Photonic crystal cavities from hexagonal boron nitride*, Nat. Commun., **9** 2623, 2018.

[162] T. Vogl, R. Lecamwasam, B. C. Buchler, Y. Lu, and P. K. Lam, *Space-compatible cavity-enhanced single-photon generation with hexagonal boron nitride*, arXiv:1902.03019, 2019.

[163] T. Vogl, Y. Lu, and P. K. Lam, *Room temperature single photon source using fiber-integrated hexagonal boron nitride*, J. Phys. D: Appl. Phys., **50** 295101, 2017.

[164] D. Hunger, T. Steinmetz, Y. Colombe, C. Deutsch, T. W. Hänsch, and J. Reichel, *A fiber Fabry-Perot cavity with high finesse*, New J. Phys., **12** 065038, 2010.

[165] H. Kaupp, T. Hümmer, M. Mader, B. Schlederer, J. Benedikter, P. Haeusser, H.-C. Chang, H. Fedder, T. W. Hänsch, and D. Hunger, *Purcell-Enhanced Single-Photon Emission from Nitrogen-Vacancy Centers Coupled to a Tunable Microcavity*, Phys. Rev. Applied, **6** 054010, 2016.

[166] J. Benedikter, H. Kaupp, T. Hümmer, Y. Liang, A. Bommer, C. Becher, A. Krueger, J. M. Smith, T. W. Hänsch, and D. Hunger, *Cavity-Enhanced Single-Photon Source Based on the Silicon-Vacancy Center in Diamond*, Phys. Rev. Applied, **7** 024031, 2017.

[167] T. Grange, G. Hornecker, D. Hunger, J.-P. Poizat, J.-M. Gérard, P. Senellart, and A. Auffèves, *Cavity-Funneled Generation of Indistinguishable Single Photons from Strongly Dissipative Quantum Emitters*, Phys. Rev. Lett., **114** 193601, 2015.

[168] T. T. Tran, M. Kianinia, M. Nguyen, S. Kim, Z.-Q. Xu, A. Kubanek, M. Toth, and I. Aharonovich, *Resonant Excitation of Quantum Emitters in Hexagonal Boron Nitride*, ACS Photonics, **5** 295–300, 2018.

[169] A. Dietrich, M. W. Doherty, I. Aharonovich, and A. Kubanek, *Persistence of Fourier Transform limited lines from a solid state quantum emitter in hexagonal Boron Nitride*, arXiv:1903.02931, 2019.

[170] D. J. Rogers, J. C. Bienfang, A. Mink, B. J. Hershman, A. Nakassis, X. Tang, L. Ma, D. H. Su, C. J. Williams, and C. W. Clark, *Free-space quantum cryptography in the H-alpha Fraunhofer window*, Proc. SPIE, **6304** 630417, 2006.

[171] A. L. Exarhos, D. A. Hopper, R. N. Patel, M. W. Doherty, and L. C. Bassett, *Magnetic-field-dependent quantum emission in hexagonal boron nitride at room temperature*, Nat. Commun., **10** 222, 2019.

[172] R. O. Jones and O. Gunnarsson, *The density functional formalism, its applications and prospects*, Rev. Mod. Phys., **61** 689–746, 1989.

[173] W. Kohn, *Nobel Lecture: Electronic structure of matter - wave functions and density functionals*, Rev. Mod. Phys., **71** 1253–1266, 1999.

[174] K. Burke and L. O. Wagner, *DFT in a nutshell*, Int. J. Quantum Chem., **113** 96–101, 2013.

[175] J. C. Slater, *A Simplification of the Hartree-Fock Method*, Phys. Rev., **81** 385–390, 1951.

[176] P. Hohenberg and W. Kohn, *Inhomogeneous Electron Gas*, Phys. Rev., **136** B864–B871, 1964.

[177] W. Kohn and L. J. Sham, *Self-Consistent Equations Including Exchange and Correlation Effects*, Phys. Rev., **140** A1133–A1138, 1965.

[178] J. P. Perdew and M. Levy, *Physical Content of the Exact Kohn-Sham Orbital Energies: Band Gaps and Derivative Discontinuities*, Phys. Rev. Lett., **51** 1884–1887, 1983.

[179] J. Heyd, G. E. Scuseria, and M. Ernzerhof, *Hybrid functionals based on a screened Coulomb potential*, J. Chem. Phys., **118** 8207–8215, 2003.

[180] L. Hedin, *New Method for Calculating the One-Particle Green's Function with Application to the Electron-Gas Problem*, Phys. Rev., **139** A796–A823, 1965.

[181] L. Hedin and B. I. Lundqvist, *Explicit local exchange-correlation potentials*, J. Phys. C: Solid State Phys., **4** 2064–2083, 1971.

[182] J. P. Perdew and A. Zunger, *Self-interaction correction to density-functional approximations for many-electron systems*, Phys. Rev. B, **23** 5048–5079, 1981.

[183] A. D. Becke, *Density-functional exchange-energy approximation with correct asymptotic behavior*, Phys. Rev. A, **38** 3098–3100, 1988.

[184] C. Lee, W. Yang, and R. G. Parr, *Development of the Colle-Salvetti correlation-energy formula into a functional of the electron density*, Phys. Rev. B, **37** 785–789, 1988.

[185] J. P. Perdew and Y. Wang, *Accurate and simple analytic representation of the electron-gas correlation energy*, Phys. Rev. B, **45** 13244–13249, 1992.

[186] J. P. Perdew, K. Burke, and M. Ernzerhof, *Generalized Gradient Approximation Made Simple*, Phys. Rev. Lett., **77** 3865–3868, 1996.

[187] J. P. Perdew, A. Ruzsinszky, G. I. Csonka, O. A. Vydrov, G. E. Scuseria, L. A. Constantin, X. Zhou, and K. Burke, *Restoring the Density-Gradient Expansion for Exchange in Solids and Surfaces*, Phys. Rev. Lett., **100** 136406, 2008.

[188] Y. Zhang and W. Yang, *Comment on "Generalized Gradient Approximation Made Simple"*, Phys. Rev. Lett., **80** 890–890, 1998.

[189] X. Xu and W. A. Goddard, *The X3LYP extended density functional for accurate descriptions of nonbond interactions, spin states, and thermochemical properties*, Proc. Natl. Acad. Sci., **101** 2673–2677, 2004.

[190] S. Smidstrup, D. Stradi, J. Wellendorff, P. A. Khomyakov, U. G. Vej-Hansen, M.-E. Lee, T. Ghosh, E. Jónsson, H. Jónsson, and K. Stokbro, *First-principles Green's-function method for surface calculations: A pseudopotential localized basis set approach*, Phys. Rev. B, **96** 195309, 2017.

[191] Synopsys QuantumATK. Version 2016.3 with the Virtual NanoLab front end, https://www.synopsys.com/silicon/quantumatk.html.

[192] G. Kresse and J. Furthmüller, *Efficient iterative schemes for ab initio total-energy calculations using a plane-wave basis set*, Phys. Rev. B, **54** 11169–11186, 1996.

[193] G. Kresse and D. Joubert, *From ultrasoft pseudopotentials to the projector augmented-wave method*, Phys. Rev. B, **59** 1758–1775, 1999.

[194] H. R. Gutiérrez, N. Perea-López, A. L. Elías, A. Berkdemir, B. Wang, R. Lv, F. López-Urías, V. H. Crespi, H. Terrones, and M. Terrones, *Extraordinary Room-Temperature Photoluminescence in Triangular WS_2 Monolayers*, Nano Lett., **13** 3447–3454, 2013.

[195] K. Yee, *Numerical solution of initial boundary value problems involving Maxwell's equations in isotropic media*, IEEE Trans. Antennas Propag., **14** 302–307, 1966.

[196] Lumerical Solutions, Inc. https://www.lumerical.com/products/fdtd-solutions/.

[197] F. Karouta, *A practical approach to reactive ion etching*, J. Phys. D: Appl. Phys., **47** 233501, 2014.

[198] M. J. Stevens, S. Glancy, S. W. Nam, and R. P. Mirin, *Third-order antibunching from an imperfect single-photon source*, Opt. Express, **22** 3244–3260, 2014.

[199] A. Divochiy, F. Marsili, D. Bitauld, A. Gaggero, R. Leoni, F. Mattioli, A. Korneev, V. Seleznev, N. Kaurova, O. Minaeva, G. Gol'tsman, K. G. Lagoudakis, M. Benkhaoul, F. Lévy, and A. Fiore, *Superconducting nanowire photon-number-resolving detector at telecommunication wavelengths*, Nat. Photon., **2** 302–306, 2008.

[200] B. E. Kardynał, Z. L. Yuan, and A. J. Shields, *An avalanche-photodiode-based photon-number-resolving detector*, Nat. Photon., **2** 425–428, 2008.

[201] X. Ding, Y. He, Z.-C. Duan, N. Gregersen, M.-C. Chen, S. Unsleber, S. Maier, C. Schneider, M. Kamp, S. Höfling, C.-Y. Lu, and J.-W. Pan, *On-Demand Single Photons with High Extraction Efficiency and Near-Unity Indistinguishability from a Resonantly Driven Quantum Dot in a Micropillar*, Phys. Rev. Lett., **116** 020401, 2016.

[202] N. Somaschi, V. Giesz, L. De Santis, J. C. Loredo, M. P. Almeida, G. Hornecker, S. L. Portalupi, T. Grange, C. Antón, J. Demory, C. Gómez, I. Sagnes, N. D. Lanzillotti-Kimura, A. Lemaítre, A. Auffeves, A. G. White, L. Lanco, and P. Senellart, *Near-optimal single-photon sources in the solid state*, Nat. Photon., **10** 340–345, 2016.

[203] J. Storteboom, P. Dolan, S. Castelletto, X. Li, and M. Gu, *Lifetime investigation of single nitrogen vacancy centres in nanodiamonds*, Opt. Express, **23** 11327–11333, 2015.

Appendix

A.1 Physical constants

The physical constants used throughout this thesis are according to the latest 2019 SI redefinition (except for the electron mass, all these constants are exact).

- speed of light in vacuum: $c = 299792458\,\mathrm{m\,s^{-1}}$
- Planck constant: $h = 6.62607015 \times 10^{-34}\,\mathrm{Js}$ (reduced Planck constant: $\hbar = \frac{h}{2\pi}$)
- reduced Planck constant: $\hbar = \frac{h}{2\pi}$
- elementary charge: $e = 1.602176634 \times 10^{-19}\,\mathrm{C}$
- Boltzmann constant: $k_\mathrm{B} = 1.380649 \times 10^{-23}\,\mathrm{J\,K^{-1}}$

The from the SI system derived constants are

- mass of an electron: $m_\mathrm{e} = 9.10938356(11) \times 10^{-31}\,\mathrm{kg}$
- magnetic constant: $\mu_0 = 4\pi \times 10^{-7}\,\mathrm{N\,A^{-2}}$
- dielectric constant: $\epsilon_0 = \frac{1}{c^2\mu_0}$

A.2 Supplementary information: ACS Photonics 5, 2305-2312 (2018)

Supplementary information: Fabrication and deterministic transfer of high quality quantum emitter in hexagonal boron nitride

Tobias Vogl,[†] Geoff Campbell,[†] Ben C. Buchler,[†] Yuerui Lu,[‡] and Ping Koy Lam[†]

[†]*Centre for Quantum Computation and Communication Technology, Department of Quantum Science, Research School of Physics and Engineering, The Australian National University, Acton ACT 2601, Australia*

[‡]*Research School of Engineering, The Australian National University, Acton ACT 2601, Australia*

Contents

This supplementary material contains 5 pages, 3 figures and 3 tables.

S1 Correlation function parameters

This section contains all fit parameters for the correlation function parameters as defined in equation (1) in the main text in order of appearance: Defect 1 is the defect described in the section *Optical characterization*, defect 2 is the defect with the best $g^{(2)}(0)$, as described in section *Correlating optical properties*, and defect 3 is the defect before and after the chemical transfer process. The data of one channel is shifted such that μ is zero. For a comparison the table also includes the excited state lifetime τ as measured with the time-resolved photoluminescence system, which should be equal to t_1.

Table S1: **Fit parameters for the $g^{(2)}$ function for the defects described in the main text.** In addition to the fit parameters also the excited state lifetime τ as measured using time-resolved photoluminescence is shown.

defect #	A	B	t_1 [ps]	t_2 [ps]	τ [ps]
1	0.846(47)	0.176(144)	1100(134)	15441(4168)	1123(7)
2	0.976(73)	0.010(57)	1368(146)	20651(42412)	1133(18)
3 (before)	0.919(321)	0.335(336)	627(212)	2228(1762)	468(8)
3 (after)	0.776(90)	0.210(66)	399(109)	3762(3633)	375(15)

S2 Long-time stability

Table S2: **Long-time stability of photophysical properties.** The time is counted from the day of the annealing. Measured quantities are spectrum, lifetime, saturation curve and single photon purity. The bottom columns are mean value μ, standard deviation σ and relative fluctuations σ/μ.

Time [days]	$\mathrm{ZPL_{peak}}$ [nm]	γ [nm]	τ [ps]	α	$g^{(2)}(0)$
6	566.30(9)	4.38(13)	1046(30)	0.313(47)	0.395(38)
8	564.03(18)	7.26(32)	624(22)	0.714(57)	0.380(25)
59	563.92(8)	4.49(5)	1009(11)	0.641(54)	0.438(23)
91	564.71(9)	5.03(14)	897(15)	0.942(46)	0.415(43)
217	563.10(13)	5.27(21)	862(10)	0.430(53)	0.409(35)
238	568.12(14)	6.61(25)	701(7)	0.517(65)	0.396(33)
μ	565.03	5.51	857	0.593	0.406
σ	1.86	1.17	167	0.223	0.022
σ/μ	0.00328	0.213	0.195	0.376	0.054

S3 Linewidth-lifetime correlation

The only (anti-)correlation between optical properties we found was between spectral linewidth and excited state lifetime: A narrow spectral linewidth correlates with a longer excited state lifetime (see figure $S1$, linear fit). To easily compare their lifetime-bandwidth product all

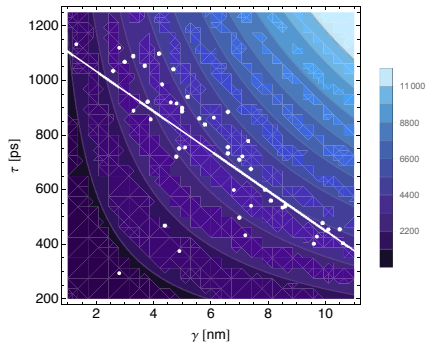

Figure S1: **Linewidth-lifetime correlation.** A narrow linewidth correlates with a longer excited state lifetime. The contour represents the lifetime-bandwidth product.

defects here have ZPLs ranging from $550-570\,\mathrm{nm}$. The contour plot represents the lifetime-bandwidth product for a constant ZPL wavelength of $562\,\mathrm{nm}$ (average value) as a function of linewidth and lifetime. Note that this introduces an error of around $4\,\%$, but this is smaller than the gradations of the contours.

S4 Extended statistics

In order to show the high quality of the emitters described in the main text we show in this section histograms of the photophysical properties (for the emitters in figure $S1$) in terms of spectral linewidth γ, excited state lifetime τ, time-bandwidth product and single photon purity $g^{(2)}(0)$ (see figure $S2$). The correlation matrix is shown in table $S3$ and graphically represented in figure $S3$. Other properties, such as crystal flake thickness or fabrication parameters are not shown for the sake of clarity. In total we studied more than 300 flakes

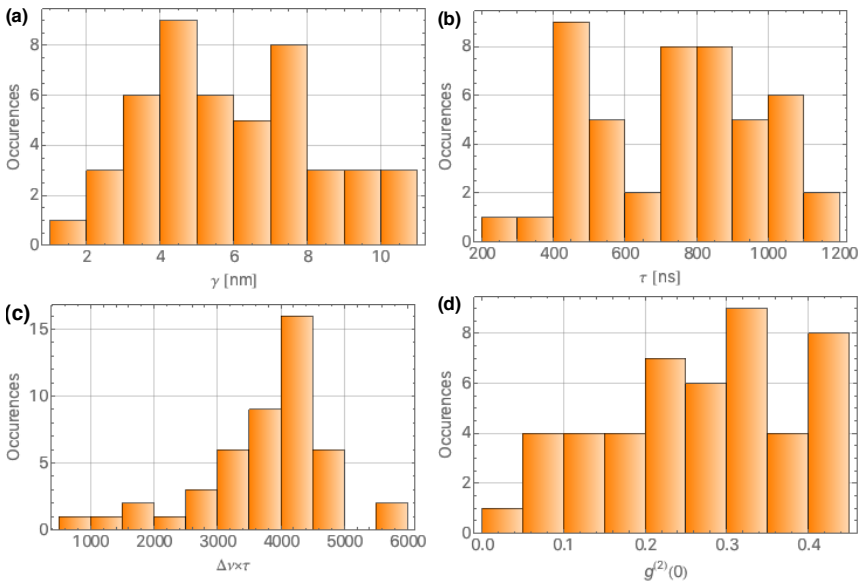

Figure S2: **Histograms of various photophysical properties.** **(a)** Spectral linewidth. **(b)** Excited state lifetime. **(c)** Time-bandwidth product. **(d)** Single photon purity.

hosting more than 200 defects. Each flake hosted between 0 and 7 defects, with the average number being 2.55 (not counting the flakes hosting no defect). In this extended statistics section only 48 defects have been taken into account, which are all from the same fabrication parameters (100 W plasma power for 1 min and consecutive annealing at 850 °C). As mentioned in the main text, there is no correlation between photophysics and the fabrication parameters.

All data is available on request from the corresponding authors.

Table S3: **Correlation matrix.** The entries for the correlations between γ and τ are close to -1, showing the anti-correlation between these parameters (consequently there are also correlations with the time bandwidth product).

	γ	λ	τ	$\Delta\nu\tau$	$g^{(2)}(0)$
γ	1	-0.0201456	-0.712732	0.546409	0.189893
λ	-0.0201456	1	0.132218	-0.0739484	0.0272105
τ	-0.712232	0.132218	1	0.0827721	-0.195027
$\Delta\nu\tau$	0.546409	-0.0739484	0.0827721	1	0.132411
$g^{(2)}(0)$	0.189893	0.0272105	-0.195027	0.132411	1

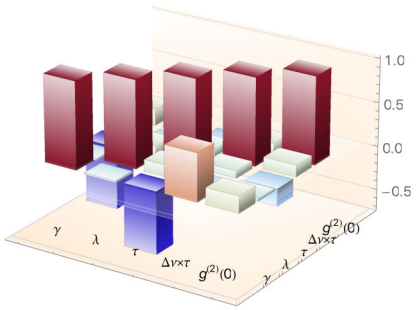

Figure S3: **Graphical representation of the correlation matrix.**

A.3 Supplementary information: Nature Communications 10, 1202 (2019)

Supplementary Information:
Radiation tolerance of two-dimensional material-based devices for space applications

Vogl et al.

1

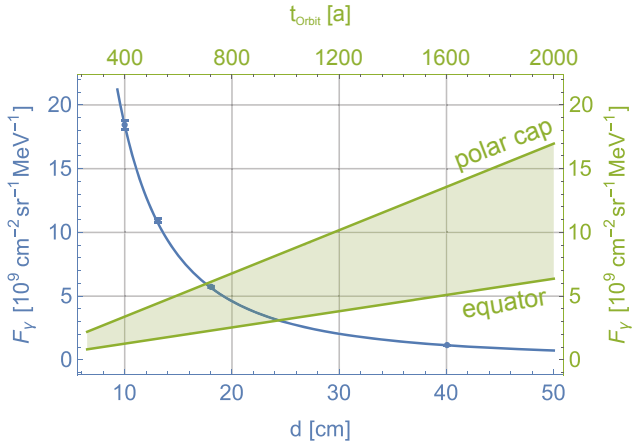

Supplementary Figure 1: Distance-dependent gamma-ray fluence. The fluence was calculated by taking the d^{-2} dependence of the photon flux into account. The data points mark the positions at which the samples were positioned during the first γ-ray test. The error bars denote the uncertainty resulting from the placement accuracy. We assume this to be ± 1 mm. The solid green lines show the integrated γ-ray flux as a function of orbit time for different geographical locations. Depending on orbital inclination, the real experienced value will be in between these lines (green shaded area). Due to a calculation error, (see main text) the simulated orbit times are 576 times higher than planned.

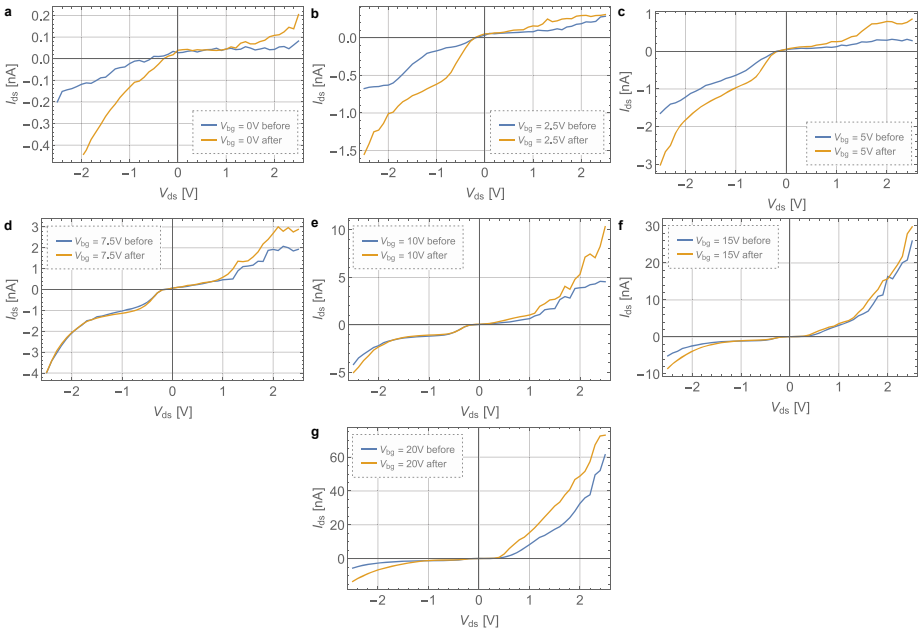

Supplementary Figure 2: Complete set of the I-V curves at different back gate voltages. **a-g** The variations in *I-V* characteristics before and after the γ-ray test were confirmed via time-dependent measurements to be most likely temporal variations, independet of any γ-ray exposure. These variations are likely due to surface adsorption, which changes the carrier mobility in such 2D materials (see main text). In addition, *I-V* characteristics in general are highly dependent on the Schottky or contact resistance which varies across different measurements. We confirmed this by measuring the same curve multiple times without irradiation at different days.

Supplementary Note 1: Averaging algorithm

The photoluminescence (PL) response typically varies across a monolayer, as can be seen from the confocal PL map in Supplementary Figure 3a. These variations are due to local contaminants on the crystal surface. We found that even by manually placing the excitation laser onto the same spot on a monolayer, the measured PL may vary. Thus, we averaged over the PL of the entire monolayer. For separating monolayer and multilayer/substrate, we first calculated the probability density function (PDF) of the entire PL map by kernel density estimation (KDE). The PDFs always show a bimodal distribution (see Supplementary Figure 3b). The first peak is attributed to substrate/multilayers and the second to the monolayer. Note that we have not truncated the PDF, resulting in a finite density below zero and above the maximal intensity I_{max} (in this case $I_{\mathrm{max}} = 690720$ a.u.). We select all data points with PL intensities between the local minimum between both peaks in the PDF and I_{max} (orange shaded area in Supplementary Figure 3b). The resulting selection mask is shown in Supplementary Figure 3c. We average over the selected data and the raw spectrum closest to the mean is assigned the average spectrum of the monolayer. For the lifetime such elaborate algorithm is not necessary. By mapping the lifetime of a crystal we found the average lifetime to be 319 ps with a standard deviation of 4 ps. Thus, the lifetime does not vary across a monolayer.

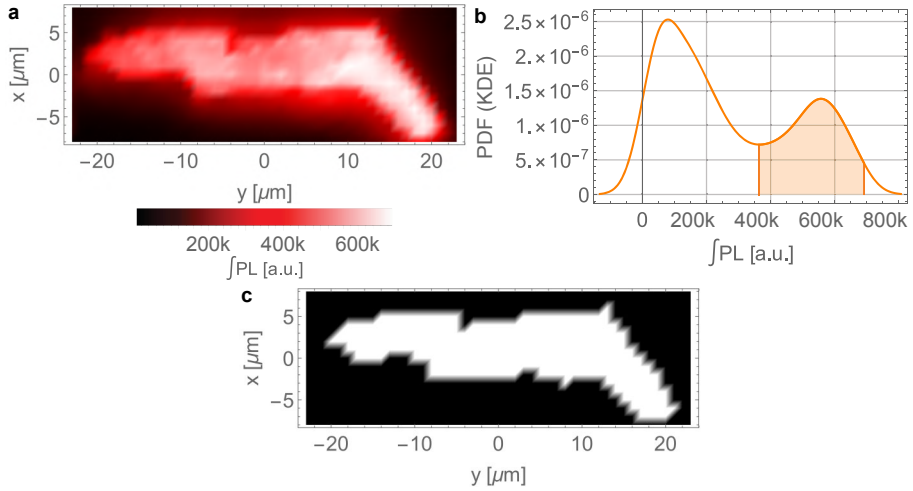

Supplementary Figure 3: Explanation of the averaging algorithm. **a** Confocal PL map of a monolayer. **b** PDF of the KDE. All scans show a bimodal distribution. The data in the orange shaded is used for averaging. **c** Map of the selection mask. All data falling into the white area is used for averaging.

Supplementary Note 2: Extended data gamma-ray tests

Note for all confocal PL maps: The black bars contain excluded data points at which the laser was re-focused during the scan. The data is shown in Supplementary Figures 4 through 8.

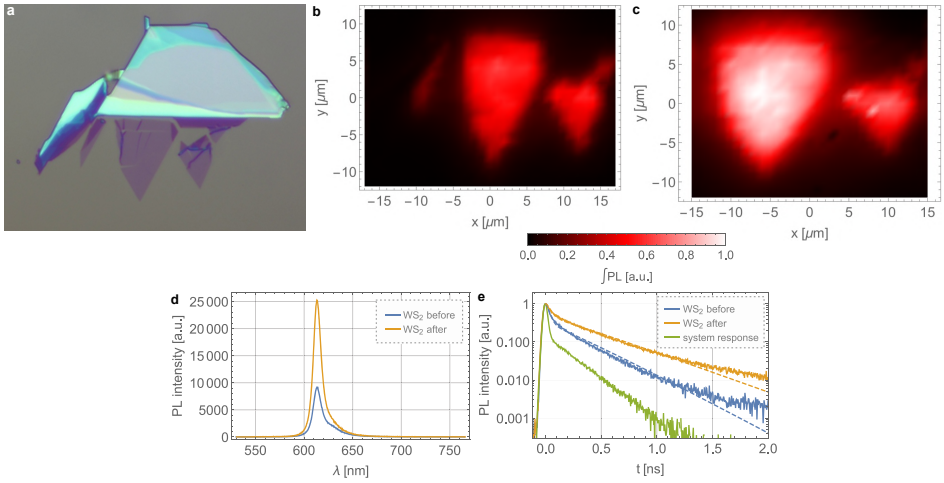

Supplementary Figure 4: Additional data set WS_2 after $F_\gamma = 10.89 \times 10^9\,\mathrm{cm}^{-2}\mathrm{sr}^{-1}\mathrm{MeV}^{-1}$. **a** Microscope image under 500× magnification. **b, c** Confocal PL map before and after irradiation. **d** The spectrum shows a PL increase of $\eta_{\mathrm{PL}} = 2.30$. **e** Carrier lifetime is increased from 272(2) to 417(3) ps ($\eta_\tau = 1.53$).

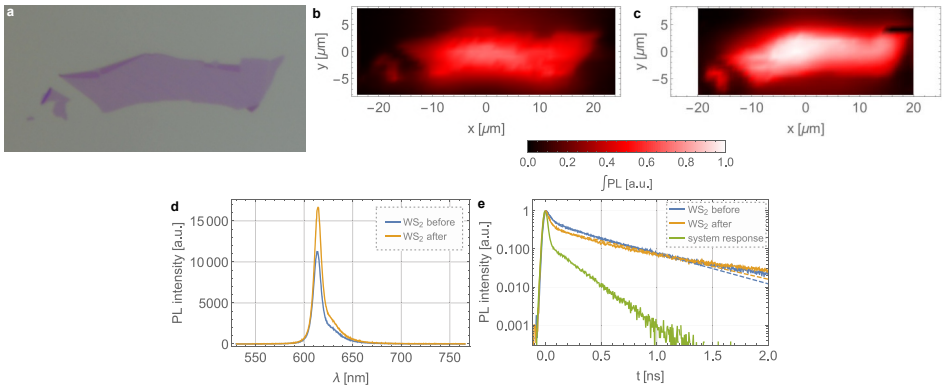

Supplementary Figure 5: Additional data set WS_2 after $F_\gamma = 5.68 \times 10^9\,\mathrm{cm}^{-2}\mathrm{sr}^{-1}\mathrm{MeV}^{-1}$. **a** Microscope image under 500× magnification. **b, c** Confocal PL map before and after irradiation. **d** The spectrum shows a PL increase of $\eta_{\mathrm{PL}} = 1.44$. **e** Carrier lifetime is increased from 542(4) to 647(6) ps ($\eta_\tau = 1.19$).

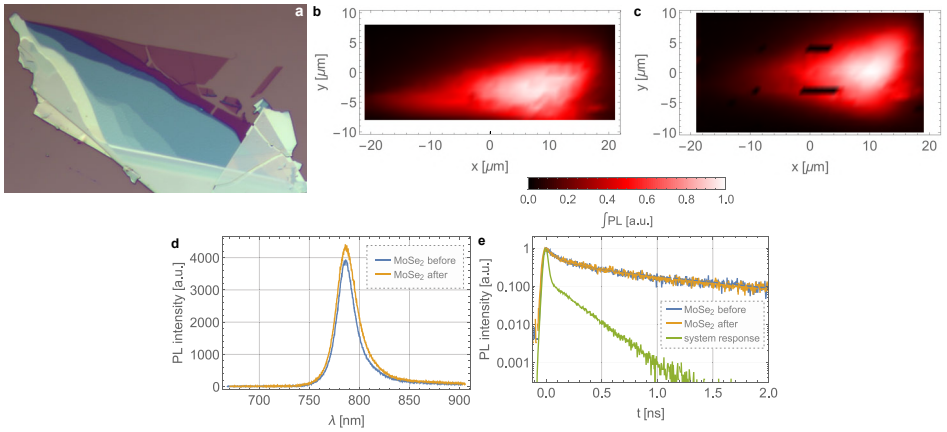

Supplementary Figure 6: Additional data set $MoSe_2$ after $F_\gamma = 10.89 \times 10^9\,\mathrm{cm}^{-2}\mathrm{sr}^{-1}\mathrm{MeV}^{-1}$. **a** Microscope image under 500× magnification. **b, c** Confocal PL map before and after irradiation. **d** The spectrum shows a PL increase of $\eta_{\mathrm{PL}} = 1.12$. **e** Carrier lifetime is decreased from 1472(61) to 1329(45) ps ($\eta_\tau = 0.90$).

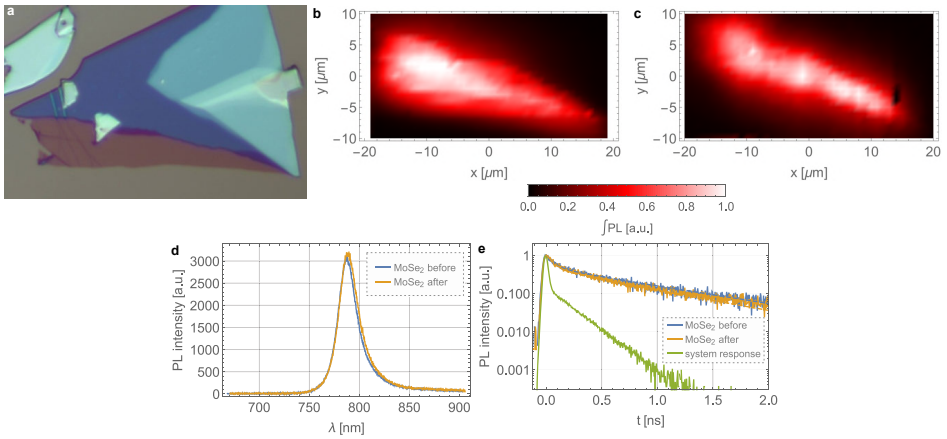

Supplementary Figure 7: Additional data set $MoSe_2$ after $F_\gamma = 1.15 \times 10^9\,\mathrm{cm}^{-2}\mathrm{sr}^{-1}\mathrm{MeV}^{-1}$. **a** Microscope image under 500× magnification. **b, c** Confocal PL map before and after irradiation. **d** The spectrum shows a PL increase of $\eta_{\mathrm{PL}} = 1.03$. **e** Carrier lifetime is decreased from 950(28) to 843(20) ps ($\eta_\tau = 0.89$).

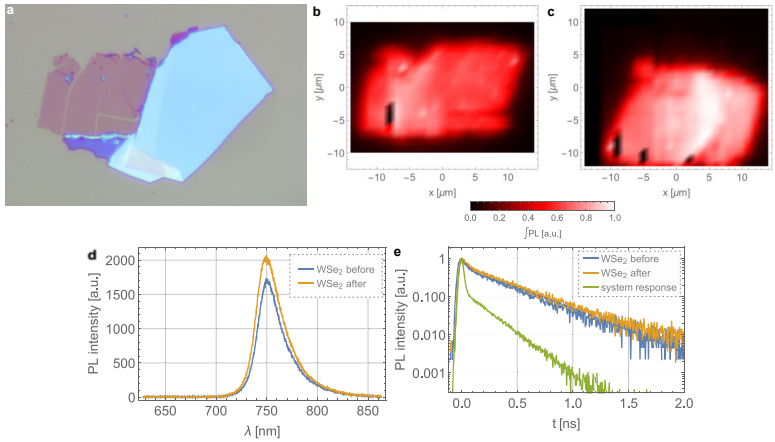

Supplementary Figure 8: Additional data set WSe_2 after $F_\gamma = 18.41 \times 10^9\,\mathrm{cm^{-2}sr^{-1}MeV^{-1}}$. **a** Microscope image under 500× magnification. **b, c** Confocal PL map before and after irradiation. **d** The spectrum shows a PL increase of $\eta_{\mathrm{PL}} = 1.25$. **e** Carrier lifetime is increased from 364(4) to 403(4) ps ($\eta_\tau = 1.11$).

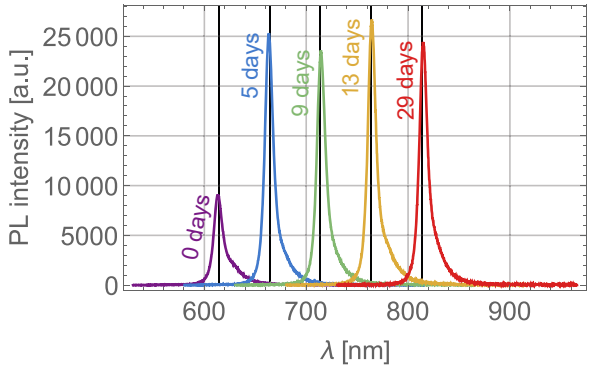

Supplementary Figure 9: Long-term stability of PL increase. The PL spectrum of the sample in Supplementary Figure 4 measured at different days. The irradiation took place at day 2. For clarity each subsequent spectra is shifted by 50 nm. The peak wavelength remained invariant (mean at 613.98 nm, visualized with black guidelines).

Supplementary Note 3: Proposed defect structures

The relaxed geometry obtained from our DFT calculations (see main text) showed that the length of the W-S bond is 2.42 Å for a pristine cell. The presence of a defect will result in relaxation of the atomic positions around the defect. Our calculations found that atoms nearest to the V_S defect move such that the nearest W-S bonds in the defect plane are 2.39 Å; the other nearby W-S bonds are 2.41 Å. In the case of the oxygen defect, the oxygen relaxes towards the transition metal, the length of the W-O bond is 2.07 Å while the other W-S bonds are roughly unchanged ($\sim$ 2.42 Å).

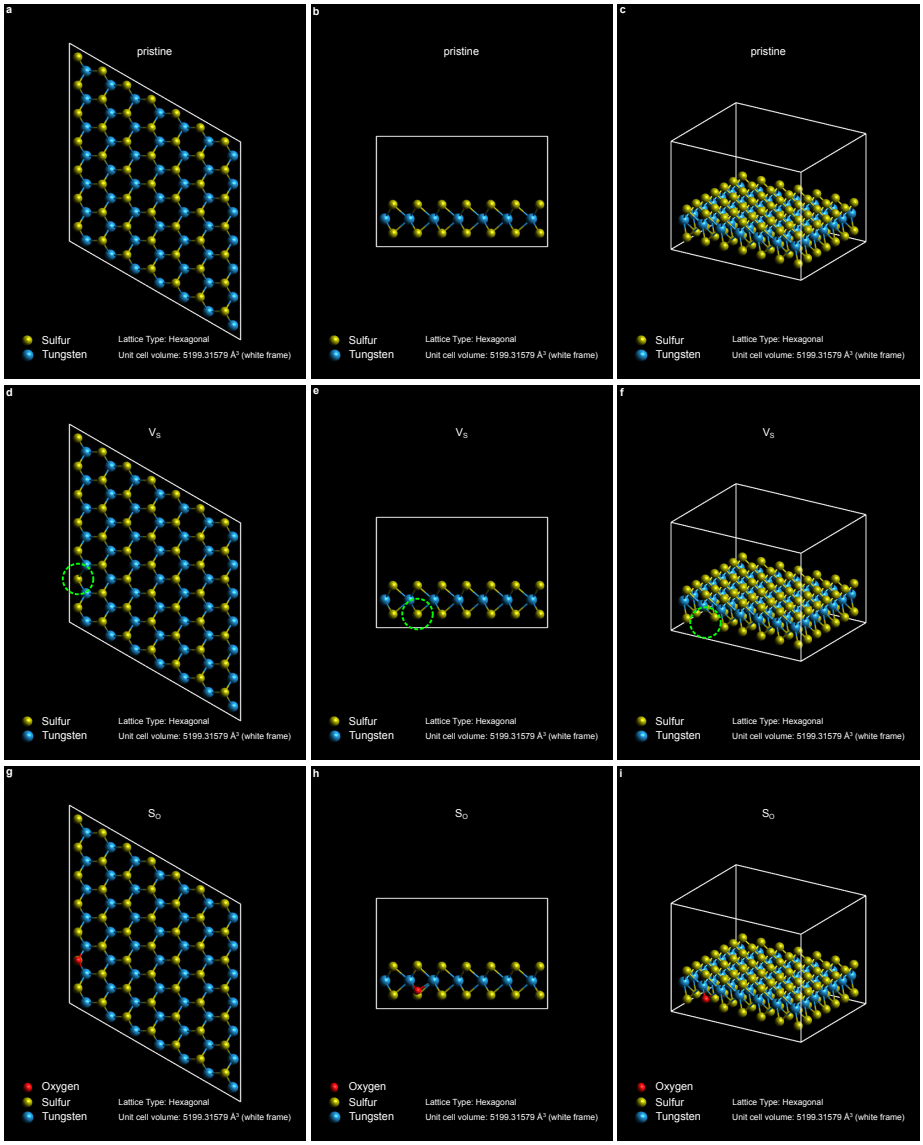

Supplementary Figure 10: Proposed defect structures in a 7×7 supercell WS_2. Pristine crystal, viewed along the Miller indices **a** $h, k, l = 0, 0, 0$; **b** $h, k, l = 0, -1, 0$; **c** $h, k, l = 1, -2, 1$. V_S defect, viewed along the Miller indices **d** $h, k, l = 0, 0, 0$; **e** $h, k, l = 0, -1, 0$; **f** $h, k, l = 1, -2, 1$. The green circle marks the position of the vacancy. S_O defect, viewed along the Miller indices **g** $h, k, l = 0, 0, 0$; **h** $h, k, l = 0, -1, 0$; **i** $h, k, l = 1, -2, 1$. For visibility, the defects shown here are at the edges of the supercell (this does not change the DFT calculations).

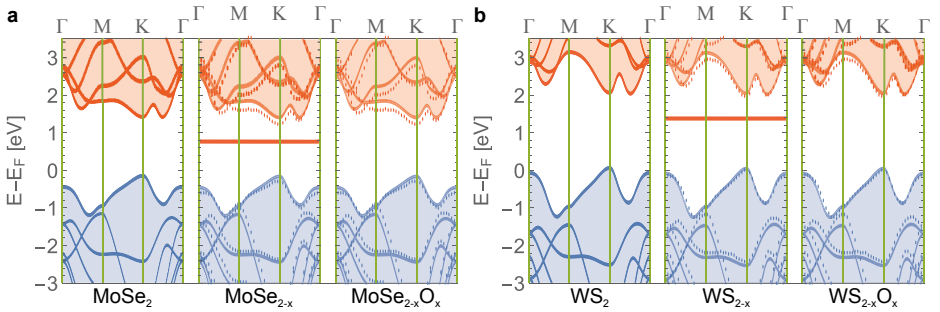

Supplementary Figure 11: DFT calculations. **a** DFT calculations of the bandstructure of pristine $MoSe_2$ (left), $MoSe_{2-x}$ (middle), $MoSe_{2-x}O_x$ (right) show that unlike the V_{Se} defect, the Se_O defect has no unoccupied deep mid-bandgap state. The middle and right bandstructure show the conduction and valence band from the primitive pristine unit cell (solid lines) overlayed with the conduction and valence band from the supercell calculations (dotted lines). **b** For a direct comparison we include the bandstructure of WS_2 here as well (see also main text). As the DFT calculations show, the defect state of the V_{Se} is closer to the conduction band ($\Delta E = 0.45\,\text{eV}$ compared to $0.56\,\text{eV}$ for the V_S defect). This means that the non-radiative charge capture cross section (CCS) of the V_S defect is smaller, as more phonons are required for the capture. For radiative charge capture this effect is reversed. With the energy difference of $0.45\,\text{eV}$ to the conduction band, the V_{Se} defect has a smaller radiative CCS. The overall capture probability is given by defect density times capture cross section, so even though the non-radiative CCS for the V_{Se} defect is higher, with the much-reduced defect density the overall capture probability is lower.

Supplementary Note 4: Interactions of charge carriers with matter

The higher energies of the annual fluence spectra calculated with SPENVIS (see main text) are not directly accessible with our particle accelerators. To assess the damage mechanism at lower energies we calculate the stopping power for protons and electrons in 2D materials. The software used are SRIM[1] for protons and ESTAR[2] for electrons. For protons the damage mechanism is dominated by nuclear energy loss via Rutherford scattering. However, with a very low collision probability, even high-energy collisions produce only local point-like defects. Electron excitation in this energy regime generally does not produce defects. At extreme electronic energy losses electron-phonon coupling can lead to local heating. This could modify the material, but on the for space relevant energy scale this does not occur (only for highly relativistic protons). Electrons are excited, but then simply relax. Ionization does only play a minor, if any role.

The nuclear stopping power (see Supplementary Figure 12a) decreases with proton energy. The stopping power of electrons (see Supplementary Figure 12b) shows a similar trend at the for space relevant energies. At low energies the stopping power is dominated by collisions and as the collision cross section decreases with electron energy, the stopping power decreases as well. However, at higher energies, due to bremsstahlung the radiative stopping power dominates. Thus, both protons and electrons with higher energies cause less damage (at least on the relevant energy scales), and the fluence must be scaled accordingly. Unfortunately, as mentioned in the main text, the minimal fluence is already above what is expected, so no further scaling down is possible. In terms of space qualification this is not an issue, as the crystals get certified for even higher radiation doses.

We note that SRIM and ESTAR have been developed for bulk materials. In the relevant energy range the radiation damage is created by collisions between the impacting particle and the atoms in the 2D material. SRIM and ESTAR can handle this reasonably well. However, the programs use various approximations, including the assumption of a mean free path between scattering events. This approximation is not valid for monolayered 2D materials. Moreover, appropriate simulations carried out by Lehtinen et al.[3,4] show, that the type of defects in 2D differs from their bulk counterparts. Complex defects are formed due to the recoil of atoms in-plane. Furthermore, the simulations show that defect production probabilities decrease with increasing energies in the MeV range. So while one has to be careful with the absolute values for the stopping power of the 2D materials (see Supplementary Figure 12), SRIM and ESTAR nevertheless reproduce the qualitative trend of a decreasing stopping power with increasing particle energy

for the relevant energy range correctly.

In addition to the stopping power of the charge carriers in 2D materials, we also provide Monte Carlo simulations of the interaction of the protons and electrons with the Al shielding material of the spacecraft. The SPENVIS calculations assume a shielding thickness of 1.853 mm Al. Supplementary Figure 13 show trajectories of the electrons and protons with varying energy through such shield, generated with Monte Carlo methods using CASINO[5] and TRIM[1], respectively. Furthermore, Supplementary Figure 14 shows the maximal range in Al of the corresponding particles as a function of energy, which determines the shielding thickness.

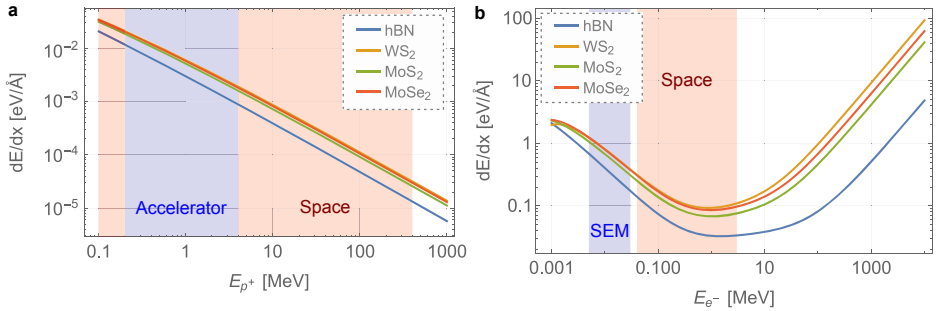

Supplementary Figure 12: Stopping power. The blue shaded areas indicate the energy range of the proton accelerator/SEM and the red shaded areas the expected proton energy range in space. **a** Nuclear stopping power for protons in various 2D materials. **b** Total stopping power for electrons in various 2D materials. At low energies, the stopping power is dominated by collisions, while at high energies it is dominated by radiation.

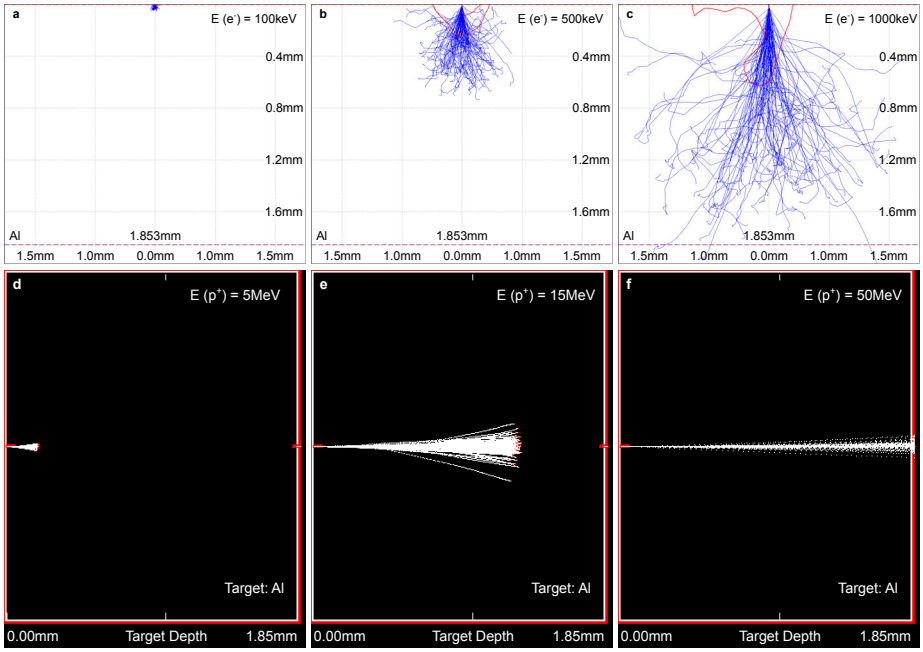

Supplementary Figure 13: Monte Carlo simulations. Electron trajectories in Al with energies **a** 100 keV, **b** 500 keV, and **c** 1 MeV, simulated with CASINO. Proton trajectories in Al with energies **d** 5 MeV, **e** 15 MeV, and **f** 50 MeV simulated with TRIM.

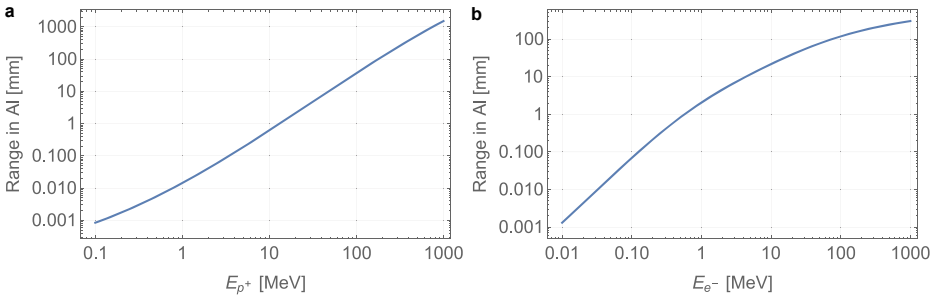

Supplementary Figure 14: Range of particles in Al. Projected range of **a** protons and **b** electrons in Al.

Supplementary Note 5: Proton irradiation

As stated in the main text, proton irradiation had no effect on any of the 2D materials at the tested fluences and energies. This was still true even after increasing the proton fluence 100-fold, to $10^{12}\,\mathrm{cm}^{-2}$. At 500 km altitude and an orbital inclination of 51.6° (which is the orbit with the highest flux) this fluence corresponds to 1386 years in orbit. Hence, we conclude that proton irradiation is no concern for 2D materials and devices in low Earth orbit (LEO). The in the following presented results (see Supplementary Figures 14 through 16) are exemplary for the full data set. We chose to show the same devices as in the main text, meaning that all samples in this section have been previously also irradiated with γ-rays. We note that we also added fresh samples to study both, isolated and combined radiation effects, but we saw no difference between these.

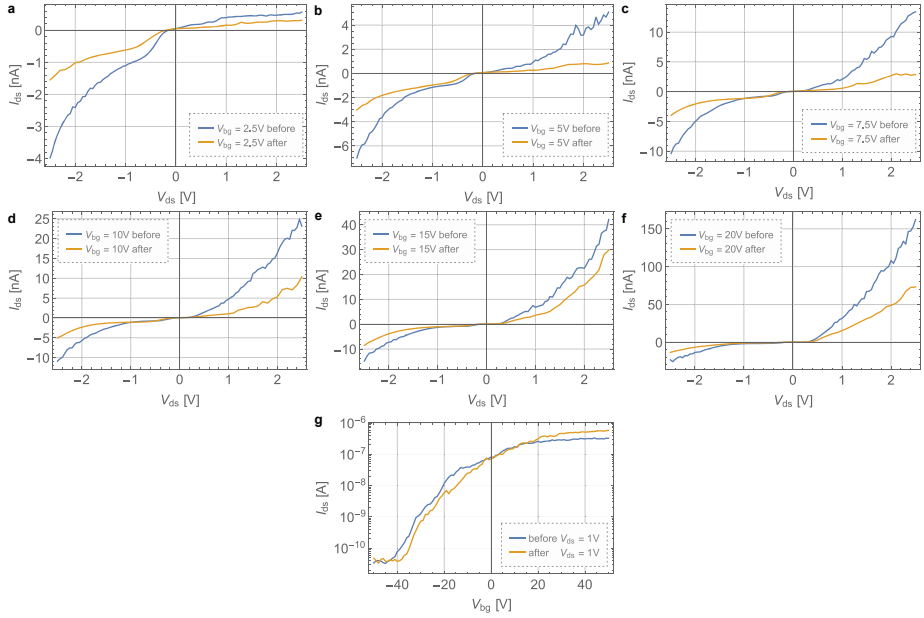

Supplementary Figure 15: Complete characterization of MoS_2 FET before / after p^+ irradiation. This sample has been previously irradiated with γ-rays (see Supplementary Figure 2). The fluence was $10^{10}\,\mathrm{cm}^{-2}$ at a proton energy of 2.5 MeV. **a-f** *I-V* curves at different back gate voltages. **g** The back gate sweep at a drain-source bias of 1 V shows no degradation in performance with the ON/OFF ratio increased from 10319 to 17479. The variations in *I-V* characteristics before and after the proton test are most likely due to temporal variations and are not actually caused by the radiation. This was confirmed by time-dependent measurements and caused by surface adsorption (see main text). In addition, *I-V* characteristics in general are highly dependent on the Schottky or contact resistance which varies across different measurements.

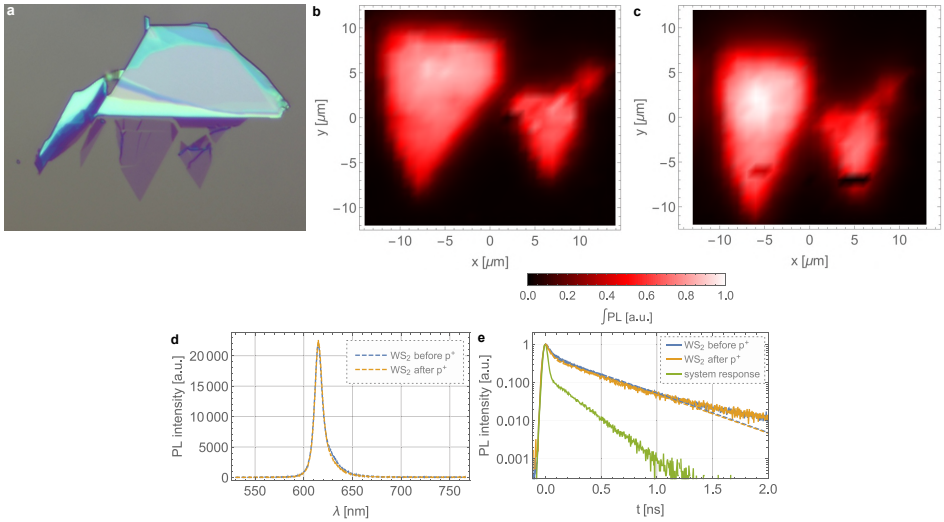

Supplementary Figure 16: WS_2 monolayer before / after irradiation with 2.5 MeV protons and a fluence $10^{10}\,\mathrm{cm}^{-2}$. This sample has been previously irradiated with γ-rays (see Supplementary Figure 4). **a** Microscope image under 500× magnification. **b, c** Confocal PL map before and after irradiation. **d** The spectrum remained invariant with $\eta_{\mathrm{PL}} = 0.96$. The exciton and trion peak positions were stable (before 614.85(2) nm and after 614.74(2) nm for excitons and before 620.99(15) and after 619.76 nm for trions), as well were the linewidths. **e** Carrier lifetime shows no change with 417(3) ps before and 425(2) ps after the proton irradiation ($\eta_\tau = 1.02$).

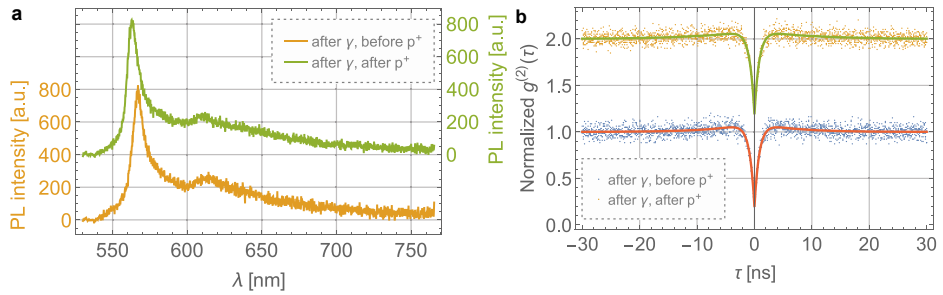

Supplementary Figure 17: Characterization of a quantum emitter in hBN before / after irradiation with 2.5 MeV protons and a fluence $10^{10}\,\mathrm{cm}^{-2}$. This sample has been previously irradiated with γ-rays (see main text Figure 3). **a** The PL spectra (vertically offset for clarity) show no changes. **b** Second-order correlation function dipping at zero time delay to 0.188(25) before and to 0.185(23) after the irradiation. The values were obtained from fitting a three-level system (for clarity the fits are differently colored).

Supplementary Note 6: Electron irradiation

As stated in the main text, electron irradiation was able to cause significant damage on the optical properties of the 2D transition metal dichalcogenides (TMDs). A scanning electron microscope (SEM) was used as an electron accelerator (see main text Methods). During the first irradiation tests at 5 kV accelerating voltage and an electron fluence of $10^{13}\,\mathrm{cm}^{-2}$, we saw a strong decrease in PL, combined with a shortening in carrier lifetime (see Supplementary Figure 18). When changing the accelerating voltage to 30 kV and keeping the fluence constant we saw this effect weaken with increased electron energy (see Supplementary Figure 19). By pushing the SEM to its minimal fluence limit of $10^{10}\mathrm{cm}^{-2}$, we saw a further reduction of this effect (see Supplementary Figure 20), even at 5 kV accelerating voltage. Note that this is still three orders of magnitude above LEO radiation levels. We also extrapolate the damage effect on TMDs to be negligible in environments comparable to LEO.

The single-photon emitter in hBN were not affected by the electron irradiation. However, at locations at which the SEM was aligned and the electron beam focused (see Supplementary Figure 21), we saw a strong increase in emitter density. The electron fluence at these positions was up to $10^{18}\mathrm{cm}^{-2}$. The fact that intense electron irradiation can catalyze the formation of quantum emitters in hBN has been reported previously[6,7].

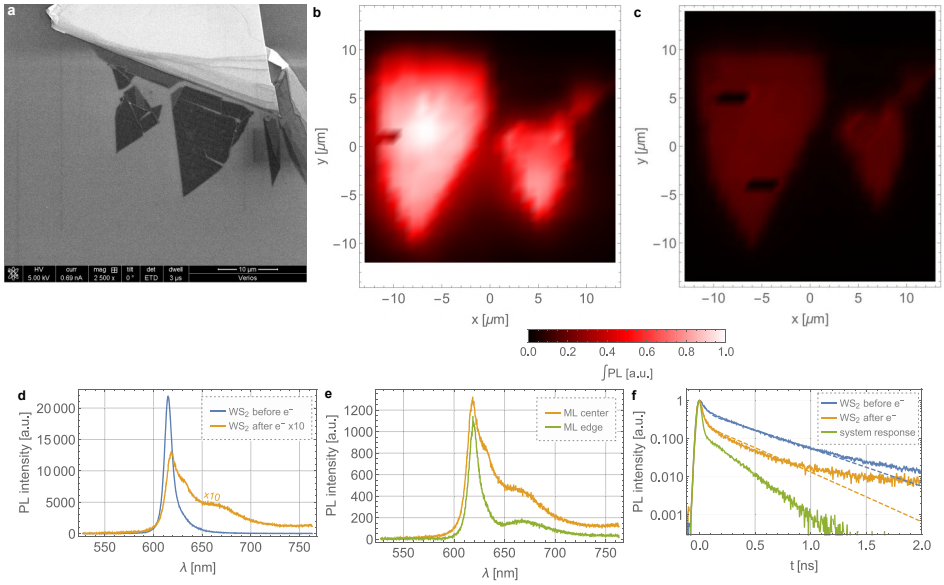

Supplementary Figure 18: WS_2 monolayer before / after irradiation with 5 keV electrons and a fluence of $10^{13}\,\mathrm{cm}^{-2}$. This sample has been previously irradiated with γ-rays (see Supplementary Figure 4) and protons (see Supplementary Figure 16. **a** SEM image under 2500× magnification. **b, c** Confocal PL map before and after irradiation. **d** The PL emission was strongly decreased as well as its shaped changed significantly. **e** Unlike for the center of the monolayer (ML), at the edges of the ML, the spectral shape was more comparable to the un-irradiated averaged spectrum. **f** The carrier lifetime was decreased from 433(2) ps before to 328(5) ps after the electron irradiation.

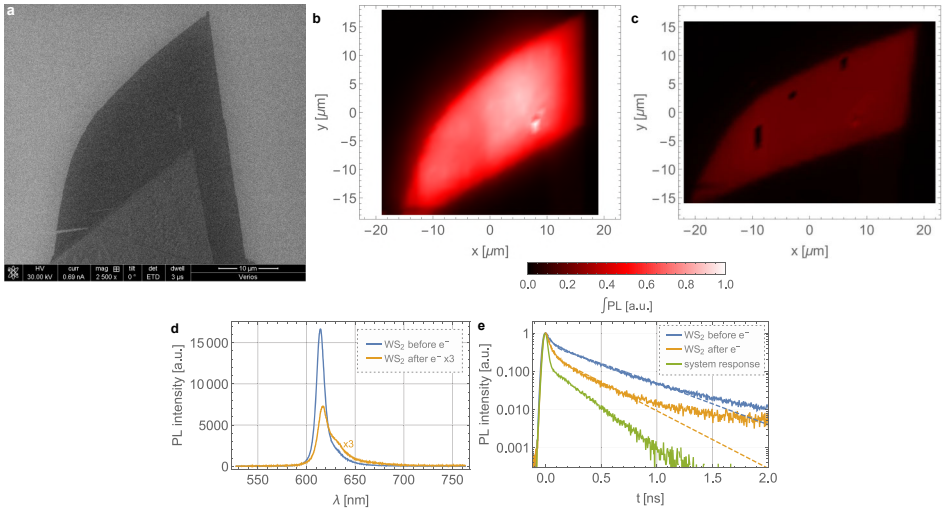

Supplementary Figure 19: WS_2 monolayer before / after irradiation with 30 keV electrons and a fluence of $10^{13}\,cm^{-2}$. This sample has been previously irradiated with γ-rays and protons. **a** SEM image under 2500× magnification. **b, c** Confocal PL map before and after irradiation. **d** The PL emission was decreased as well as its shaped changed (both change less than with 5 keV electrons). **e** The carrier lifetime was decreased from 395(2) ps before to 287(4) ps after the electron irradiation.

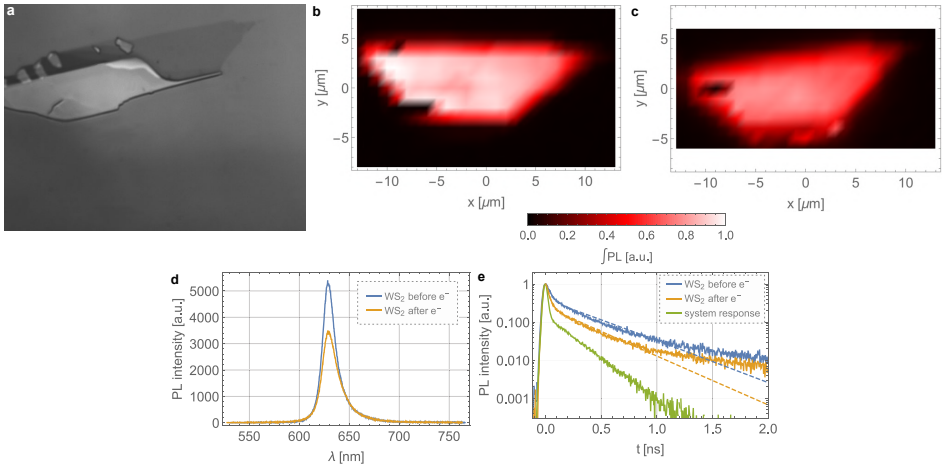

Supplementary Figure 20: WS_2 monolayer before / after irradiation with 5 keV electrons and a fluence of $10^{10}\,cm^{-2}$. This sample has been previously irradiated with γ-rays and protons. **a** Microscope image under 1000× magnification. **b, c** Confocal PL map before and after irradiation. **d** The PL emission was decreased only marginally (compared to the tests with a higher fluence), despite the lower electron energy which causes the larger damage. **e** The carrier lifetime was only decreased from 391(5) ps before to 314(5) ps after the electron irradiation.

15

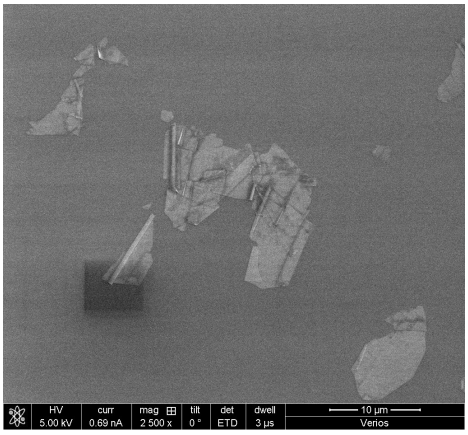

Supplementary Figure 21: SEM image of an hBN crystal. The SEM image shows a dark area at which the electron beam was aligned and focused. The electrons make the surface reactive and carbon-contaminations caused by residual organic materials in the SEM apparatus itself are bonded at areas with intense electron irradiation. At these areas the number of quantum emitters is strongly increased.

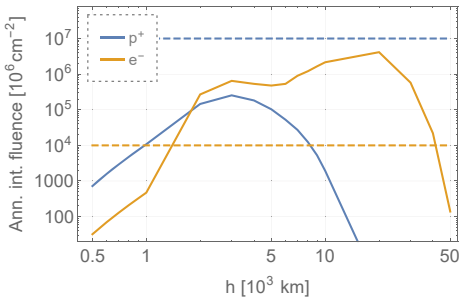

Supplementary Figure 22: Integrated annual particle fluence. The annual fluence spectra after 1.85 mm of Al shielding are integrated over the full energy range. The proton fluence always remains nearly two orders of magnitude below the damage onset threshold (dashed lines correspondingly colored). The electron fluence exceeds the observed damage onset threshold at altitudes > 1000 km. The shielding explains the leap in electron fluence at 2000 km: The electron energy increases with altitude and thus actually trapped electrons can penetrate the shielding. At lower energies the electrons originate from secondary processes of the protons interacting with the shielding material. By using an appropriate shield (5.8 mm graded Al/Ta with a Ta to Al mass ratio of 35%), the electron fluence can be kept below the damage threshold.

Supplementary References

[1] Ziegler, J. F., Ziegler, M. & Biersack, J. SRIM - The stopping and range of ions in matter. *Nucl. Instr. Meth. Phys. Res. B* **268**, 1818 – 1823 (2010).

[2] Berger, M., Coursey, J., Zucker, M. & Chang, J. ESTAR, PSTAR, and ASTAR: Computer programs for calculating stopping-power and range tables for electrons, protons, and helium ions (2005). http://physics.nist.gov/Star, National Institute of Standards and Technology, Gaithersburg, MD.

[3] Lehtinen, O. et al. Effects of ion bombardment on a two-dimensional target: Atomistic simulations of graphene irradiation. *Phys. Rev. B* **81**, 153401 (2010).

[4] Lehtinen, O. et al. Production of defects in hexagonal boron nitride monolayer under ion irradiation. *Nucl. Instrum. Methods Phys. Res. B* **269**, 1327 – 1331 (2011).

[5] Drouin, D. et al. CASINO V2.42 - A Fast and Easy-to-use Modeling Tool for Scanning Electron Microscopy and Microanalysis Users. *Scanning* **29**, 92–101 (2007).

[6] Choi, S. et al. Engineering and localization of quantum emitters in large hexagonal boron nitride layers. *ACS Appl. Mater. Interfaces* **8**, 29642–29648 (2016).

[7] Ngoc My Duong, H. et al. Effects of high-energy electron irradiation on quantum emitters in hexagonal boron nitride. *ACS Appl. Mater. Interfaces* **10**, 24886–24891 (2018).

A.4 Supplementary information: arXiv:1902.03019 (2019)

Supplementary Information: Space-compatible cavity-enhanced single-photon generation with hexagonal boron nitride

Tobias Vogl,[1] Ruvi Lecamwasam,[1] Ben C. Buchler,[1] Yuerui Lu,[2] and Ping Koy Lam[1]

[1] *Centre for Quantum Computation and Communication Technology, Department of Quantum Science, Research School of Physics and Engineering, The Australian National University, Acton ACT 2601, Australia*

[2] *Centre for Quantum Computation and Communication Technology, Research School of Electrical, Energy and Materials Engineering, The Australian National University, Acton ACT 2601, Australia*

CONTENTS

This Supplementary Information contains 7 pages and 5 figures.

S1. HEMISPHERE FABRICATION

The borosilicate glass substrates (Fisherbrand) have been coated with nominal 100 nm gold using electron-beam thermal evaporation. During the milling the edges of the substrate (or rather the conductive coating) have been grounded using copper tape. This prevents substrate charging effects, where the ion beam is deflected as more and more charge carriers accumulate in the insulating glass. The Ga^+ ions are accelerated with a voltage of 30 kV, at which our FIB (FEI Helios 600 NanoLab) has sub-nm resolution. We limited the current to ≤ 0.28 nA, this way there were no charging effects for milling times of 6 min or less. During the milling process we add I_2-gas, which ensures a smooth surface. The dose rate is encoded in the RGB color of a hemispherical pixel map. The dose rate to RGB value was carefully calibrated, however, we note that this is strongly dependent on the material and conductive coating as well as the state of the ion source. For the calibration we milled squares with edge lengths of 10 μm and measured the resulting depth as a function of pixel value. Figure S1(a) shows the trace of the depth scanned through a number of squares. After the milling the layer of gold is dissolved in a custom-made potassium iodide solution (KI:I_2:H_2O with ratio 4:1:40 by weight). By comparing the height profile before and after the KI-etching we can extract the actual gold thickness, which for us was 102.7 nm.

We characterized each hemisphere in terms of radius of curvature, ellipticity ϵ, and surface roughness or deviation from an ideal hemisphere. We define the latter as

$$r_q = \sqrt{\frac{1}{N}\sum_i^N |z_i - f(x_i)|^2} \tag{1}$$

where f is the fit function, and $\epsilon = |R_x - R_y|/(R_x + R_y)$ as the relative difference of radii in arbitrarily chosen orthogonal axes and determine R_x, R_y from fits. Figure S1(b) shows that hemispheres with smaller radii become more elliptical. Furthermore, the surface roughness also increases for these hemispheres (not shown in Figure S1(b)). This limits the the minimal radius of curvature to $> 2.3\,\mu$m.

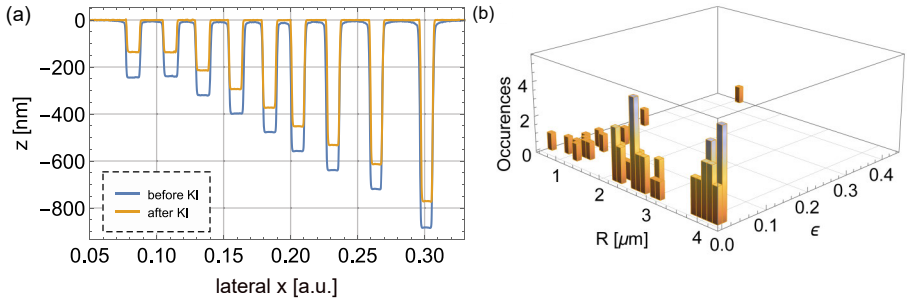

FIG. S1: Hemisphere fabrication. (a) Trace of the height profile etched using the FIB and scanned through a number of milled squares (different dose rate used for the squares). (b) The statistics show that for small radii of curvature below 2.3 μm, the hemispheres become more elliptical. In addition, while there are a few non-elliptical hemispheres with a tiny radius, all of these hemispheres suffer of a higher surface roughness.

S2. SPIN SPEED CURVES PDMS SOLUTION

We used the Sylgard 184 Silicone Elastomer kit as basis for the PDMS solution. The PDMS and curing agent were mixed in a 10:1 ratio. The solution was diluted using tert-Butyl alcohol (TBA). This allows us to achieve thin and uniform films while at the same time preventing swelling[1]. All substrates were plasma cleaned and substrate and solution were pre-baked at 40°C (TBA is a solid at room temperature). After spin coating, the PDMS films are cured at 125°C for 20 min. To measure the spin speed curves we coated Si substrates with the solution at varying spin speeds and dissolved the PDMS film on about half of the Si chip using chemical etching (acetone and isopropyl alcohol). The chemical etching took place prior to the heat curing. Using a surface profiler (Bruker Dektak) we measured the

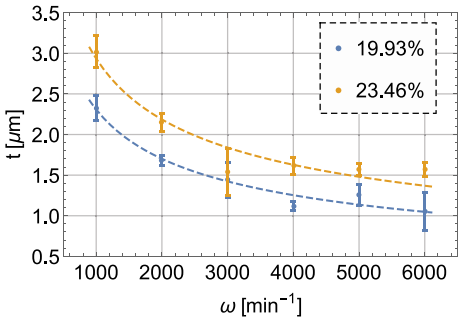

FIG. S2: Spin speed curves for different PDMS concentrations in TBA (error bars are σ as defined in the text).

height of the PDMS film. We used a large stylus diameter (12.5 μm) and minimal force (1 mg) to reduce the pressure on the PDMS film, thereby getting an accurate measurement of the film thickness with a resolution of 1.1 nm. We repeated the measurement at multiple locations on each chip. We define the total deviation of the mean $\bar{t}$ as

$$\sigma = \sqrt{\sigma(\bar{t})^2 + \overline{\sigma(t)}^2} \tag{2}$$

where $\sigma(\bar{t})$ is the standard deviation of the mean of all measurements and $\overline{\sigma(t)}$ is the mean of the standard deviation of each measurement. Thus, the first term describes the roughness on large length scales, while the latter describes the local roughness. We fit the data with

$$t(\omega) = \frac{t_0}{\omega^\alpha} \tag{3}$$

For PDMS concentrations of 19.93% and 23.46% (by weight) and static dispense we find the experimentally derived constants $t_0 = 48.41\,\mu$m, $\alpha = 0.441$ and $t_0 = 55.45\,\mu$m, $\alpha = 0.425$, respectively. The corresponding spin speed curves are shown in Figure S2. Calculating the required spin speed allows us to hit the target thickness within 1%. Note that for dynamic dispense the results become less accurate and reproducible.

S3. PHOTOGRAPHS OF THE DEVICE

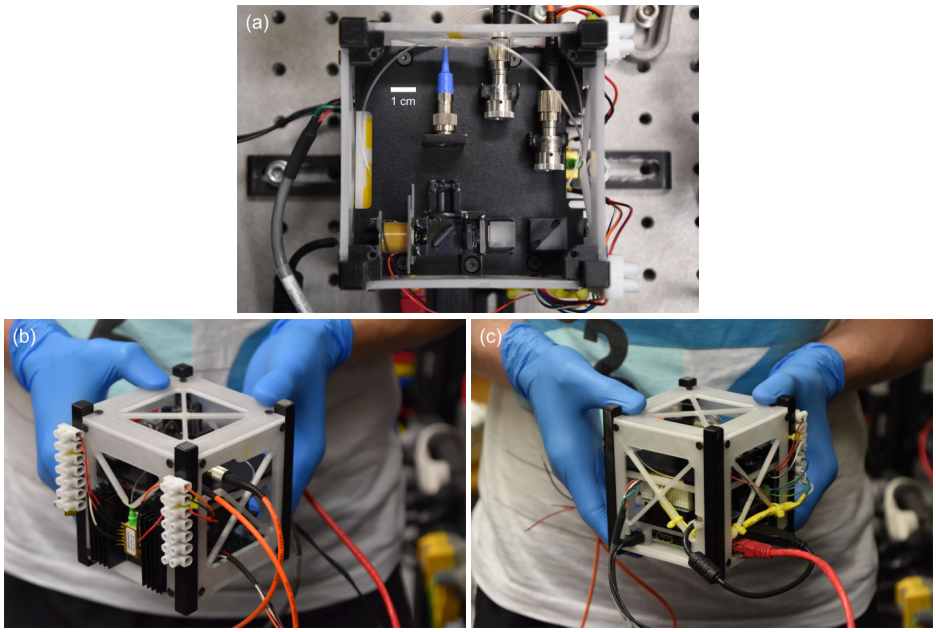

FIG. S3: Photographs of the device. (a) Top view optics platform. The satellite has an edge length of 10 cm (including 3D printed skeleton). (b),(c) Side-view satellite.

S4. TRANSVERSE MODE SPACING

The cavity modes (Hermite-Gaussian modes) are solutions to the Helmholtz equation in the paraxial approximation. The analytical solution for the resonant frequency of longitudinal mode q and transverse mode m, n is

$$\nu^q_{m,n} = \frac{c}{2L}\left(q + \frac{1+m+n}{\pi}\arccos\left(\sqrt{g_1 g_2}\right)\right) \tag{4}$$

with the cavity parameters $g_i = 1 - L/R_i$ depending on the radii of curvature of the spherical mirrors. For a flat mirror $g_1 = 1$, so the product of the cavity parameters in our case simplifies to $1 - L/R$. The transverse mode spacing in wavelength space is thus

$$\frac{c}{\nu^8_{0,1}} - \frac{c}{\nu^8_{0,0}} = 22.7\,\text{nm} \tag{5}$$

which is much larger than the observed peak spacing in the spectrum (see main text).

S5. FDTD SIMULATIONS

The finite-difference time-domain (FDTD) simulations were performed using Lumerical FDTD Solutions, a commercial-grade simulator based on the FDTD method[2]. To calculate the Purcell enhancement of a dipole emitter

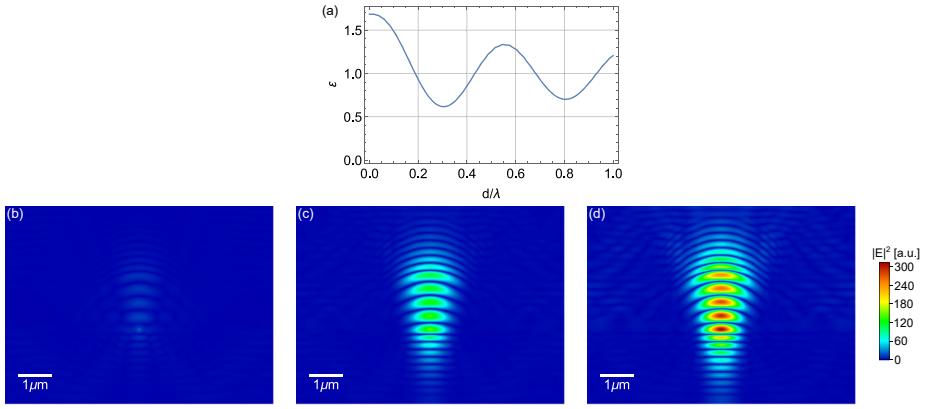

FIG. S4: FDTD simulations. (a) Purcell enhancement of a dipole emitter in close vicinity of a dielectric surface (mirror). As the distance d of the dipole to the dielectrics increases, the spontaneous emission rate oscillates and reaches 1 (no enhancement) for $d \gg \lambda$. (b) Intracavity electric field in the plano-concave cavity, with the cavity detuned. As the cavity length is scanned towards resonance, the intracavity field increases (c) and reaches its maximum on resonance (d).

due to the substrate, we define the mirror as 9 stacks of alternating SiO_2/TiO_2 layers, with the SiO_2 layer terminating the mirror. For the refractive indices we use the experimentally derived constants $n_{SiO2} = 1.521$, $n_{TiO2} = 2.135$ (see main text) and set the thickness to 92.9 nm for SiO_2 and 66.2 nm for TiO_2. To capture all dynamics we choose the mesh size much smaller than the size of the features. We define a dipole source at the SiO_2-vacuum interface with an emission wavelength of 565 nm and its axis oriented in-plane with the dielectrics. The simulation uses PML (perfectly matched layer) boundary conditions, which are reflectionless or open boundaries. We sweep the distance d of the dipole emitter to the dielectric stack and record the Purcell enhancement ε at each position (see Figure S4(a)). As d increases, the spontaneous emission rate oscillates and reaches unity (no enhancement or suppression) for $d \gg \lambda$.

We also model the plano-concave cavity by adding the hemispherical mirror to the simulation. Here, we leave the dipole at a fixed position and sweep the position of the hemispherical mirror. We record the intracavity electric field among other properties. The cavity is on resonance with the dipole when the intracavity power is maximal. Figure S4(b)-(d) show the electric field intensity as the mirror position is scanned: First, the cavity is detuned and the emission is suppressed (see Figure S4(b)). As the cavity length increases towards resonance, the intensity increases (see Figure S4(c)). Finally, at resonance the intensity is maximal (see Figure S4(d)).

S6. QKD SIMULATIONS

The extractable secret bit per signal[3] for practical BB84-like protocols is

$$S \geq q \max\left\{-Q_\mu f(E_\mu) h_2(E_\mu) + \Omega\left(1 - h_2\left(e_1\right)\right), 0\right\} \tag{6}$$

For BB84 $q = 1/2$, because only in half of all cases the basis choice of sender and transmitter coincide. In the asymptotic limit of infinite qubits, however, q can be chosen more efficiently (as high as 1). Q_μ and E_μ is the gain and quantum bit error ratio of the signal state, respectively. $f(E_\mu)$ is the error correction efficiency, which is in general dependent on the error ratio that has to be corrected. In the GYS experiment this is 1.22 for an error of $E_\mu = 3.3\%$[4]. The binary Shannon entropy is defined as $h_2(p) = -p\log_2(p) - (1-p)\log_2(1-p)$. Ω is the fraction of detection events originating from single-photon events and e_1 is the error ratio on the single-photon state. The latter two are difficult to estimate, so one has to assume the worst case scenario that a photon-number splitting attack occurred on every multi-photon state and all errors originate from single-photon states. A better way to estimate these, however, is by using additional decoy states, whose statistics we measure, allowing us to find better bounds on Ω and e_1[3]. In the asymptotic limit the fraction of decoy states can also be as low as 0, so that the protocol is maximally efficient.

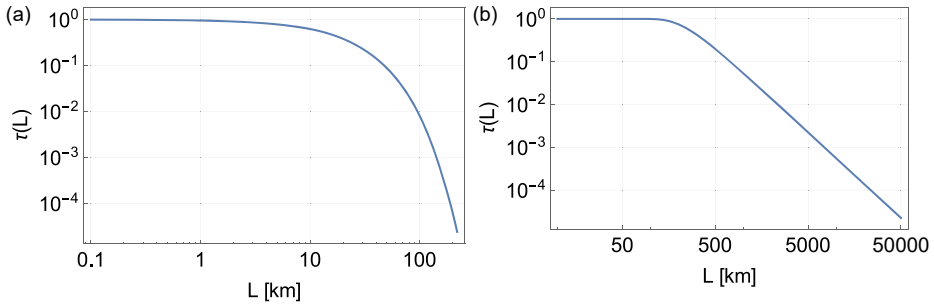

FIG. S5: Link transmission (a) for a fiber channel with losses of 0.21 dB/km and (b) for a free space channel with diffraction losses only, assuming a 5 and 60 cm telescope on the satellite and ground station, respectively. The wavelength is 565 nm.

We implemented both protocols for a fiber channel of length L with its transmission defined as

$$\tau(L) = 10^{-\alpha L} \tag{7}$$

with $\alpha = 0.21\,\mathrm{dB/km}$, and for a free space channel with its transmission (taking only diffraction losses into account) defined as

$$\tau(L) = 1 - e^{-2r^2/w^2(L)} \tag{8}$$

with r being the radius of the telescope of the ground station and

$$w(L) = \sqrt{w_0^2 + \frac{L^2\lambda^2}{\pi^2 w_0^2}} \tag{9}$$

is the evolving beam width along L. w_0 is the radius of the telescope onboard the satellite. Our simulations assume a 5 cm telescope on the satellite (which is still CubeSat sized) and a 60 cm telescope on the ground station. The resulting transmissions through the fiber and free space link are shown in Figure S5. As the link efficiency decreases, the received signal decreases as well, which results in a lower signal-to-noise ratio. At some point the detector dark counts contribute significantly to the quantum bit error ratio and thus the extractable secret bit per signal hits zero.

For our single-photon source the extractable secret bit per signal is given by

$$S \geq q \max\left\{-f(E_\mu)h_2(E_\mu) + (1-\Delta)\left(1 - h_2\left(\frac{E_\mu}{1-\Delta}\right)\right), 0\right\} \tag{10}$$

where we again set $q = 1$ and

$$\Delta = \frac{g^{(2)}(0)}{\tau(L)\eta_{\mathrm{det}}(1-\eta)} \tag{11}$$

is the probability that a multi-photon is emitted divided by the probability that any emitted photon is detected. η is the quantum efficiency of the single-photon source and η_{det} is the single-photon detector efficiency. For an ideal single-photon source of course $\Delta = 0$. It should be mentioned that the sifted key rate (i.e. the rate that the receiver detects and this times S is the secret key rate) scales with the mean photon number μ for the conventional protocols and with the quantum efficiency η for our single-photon source. Again, for an ideal single-photon source $\eta = 1$.

[1] J. H. Koschwanez, R. H. Carlson, and Deirdre R. Meldrum, "Thin PDMS Films Using Long Spin Times or Tert-Butyl Alcohol as a Solvent," PLoS ONE **4**, e4572 (2009).

[2] Lumerical Solutions, Inc., https://www.lumerical.com/products/fdtd-solutions/.
[3] Hoi-Kwong Lo, Xiongfeng Ma, and Kai Chen, "Decoy State Quantum Key Distribution," Phys. Rev. Lett. **94**, 230504 (2005).
[4] C. Gobby, Z. L. Yuan, and A. J. Shields, "Quantum key distribution over 122 km of standard telecom fiber," Appl. Phys. Lett. **84**, 3762–3764 (2004).

A.5 Supplementary information: Nanoscale 11, 14362-14371 (2019)

Supporting Information: Atomic Localization of Quantum Emitters in Multilayer Hexagonal Boron Nitride

Tobias Vogl,[†] Marcus W. Doherty,[‡] Ben C. Buchler,[†] Yuerui Lu,[¶] and Ping Koy Lam[†]

[†]*Centre for Quantum Computation and Communication Technology, Department of Quantum Science, Research School of Physics and Engineering, The Australian National University, Acton ACT 2601, Australia*

[‡]*Laser Physics Centre, Research School of Physics and Engineering, The Australian National University, Acton, ACT 2601, Australia*

[¶]*Centre for Quantum Computation and Communication Technology, Research School of Electrical, Energy and Materials Engineering, The Australian National University, Acton ACT 2601, Australia*

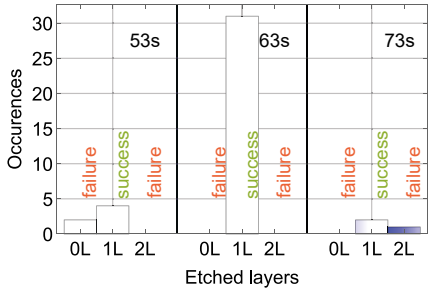

Figure S1: Histogram of single-layer etching failures and successes for various plasma etching times. A failure is if 0 or 2 layers have been etched, while in a successful process only 1 layer is etched.

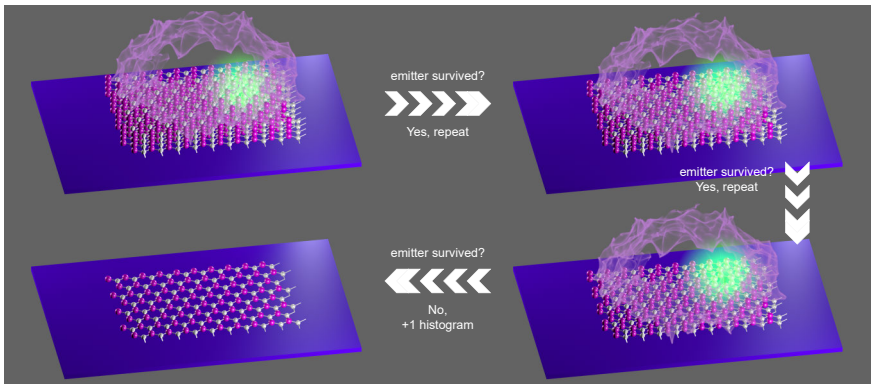

Figure S2: The process cycle shows the experimental procedure. An hBN crystal hosting a quantum emitter is treated with an oxygen plasma. After exactly one atomic layer is etched we verify if the emitter survived. If so, the plasma treatment is repeated, if not, we add a count in the corresponding layer bin in the histogram.

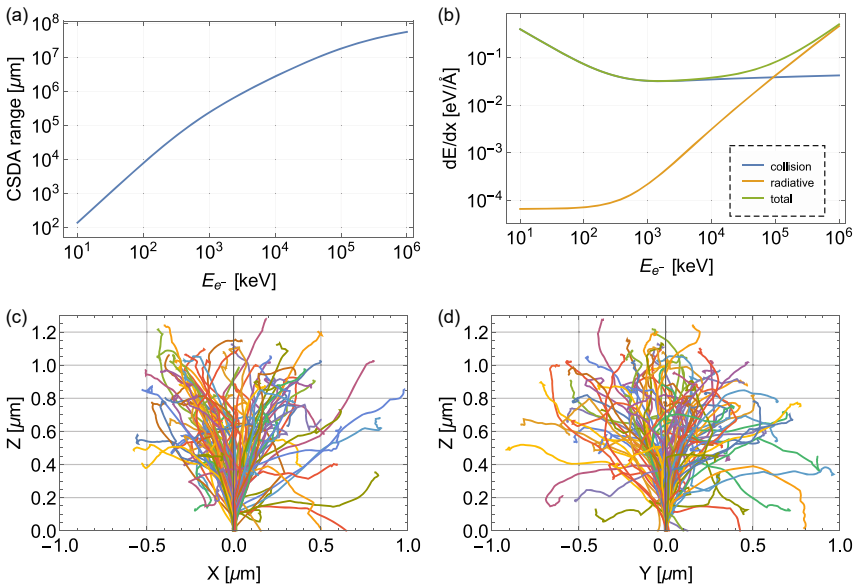

Figure S3: Simulations of electron interactions with hBN. (a) Projected range of electrons in hexagonal boron nitride in the continuous slowing down approximation (CSDA). (b) Stopping power of hBN for electrons. At low energies the total stopping power is dominated by collisions, while at high energies it is dominated by bremsstrahlung. The calculations of the range and stopping power have been performed using ESTAR.[1] (c, d) XZ- and YZ-projection of Monte Carlo trajectories of 10 keV (the same energy used in the experiments) electrons through hBN (101 trajectories, differently colored for clarity), simulated with CASINO.[2] This shows defects are created throughout the material. All simulations in (a-d) assume boron and nitrogen in a stoichiometric ratio of 1:1 and a material density of 2.1 g cm^{-3} as a target.

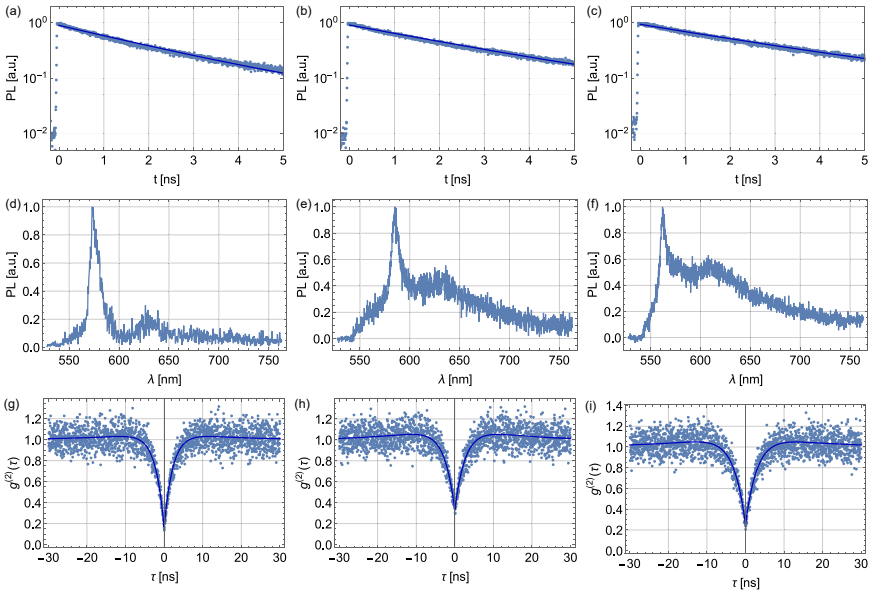

Figure S4: Photophysics of sample quantum emitters in multilayer hBN created with electron irradiation. The lifetimes in (a-c) are 2.223(6), 2.758(7), and 3.084(9) ns, respectively. This makes these emitters $3-6$ times slower compared to the plasma treated ones (see main text). The spectra are shown in (d-f). The Debye-Waller factor for emitters created by radiation damage are usually lower compared to the emitters created by the plasma treatment. The second-correlation function dips to 0.17(3), 0.33(3), and 0.25(7) at zero time delay, respectively (g-i).

References

1. Berger, M.; Coursey, J.; Zucker, M.; Chang, J. ESTAR, PSTAR, and ASTAR: Computer Programs for Calculating Stopping-Power and Range Tables for Electrons, Protons, and Helium Ions. http://physics.nist.gov/Star (National Institute of Standards and Technology, Gaithersburg, MD, 2005).

2. Drouin, D.; Couture, A. R.; Joly, D.; Tastet, X.; Aimez, V.; Gauvin, R. CASINO V2.42 - A Fast and Easy-to-use Modeling Tool for Scanning Electron Microscopy and Microanalysis Users. *Scanning* **2007**, *29*, 92–101.